2015

Lasers processing of ultra-hard materials

Ammar Abdulghani Melaibari
Iowa State University

Lasers processing of ultra-hard materials

by

Ammar Abdulghani Melaibari

A dissertation submitted to the graduate faculty

in partial fulfillment of the requirements for the degree of

DOCTOR OF PHILOSOPHY

Major: Mechanical Engineering

Program of Study Committee:
Pranav Shrotriya, Major Professor
Reza Montazami
Ganesh Balasubramanian
Wei Hong
Alan Russell
Scott Chumbley

Iowa State University

Ames, Iowa

2015

TABLE OF CONTENTS

LIST OF FIGURES

LIST OF TABLES

ACKNOWLEDGEMENTS

I would like to express my gratitude to everyone was involved in any of the projects that make this dissertation. I would like to thank my major professor, Dr. Pranav Shrotriya, for the opportunity to work with him. He has offered his support through his knowledge, expertise, and time. The success of my projects would not have been possible without his professional experience and valuable inputs.

I also would like to thank all my committee members: Dr. Scott Chumbley, and Dr. Wei Hong for teaching me in the courses I took with them that prepared me with the needed knowledge for my work in these projects; Dr. Alan Russell for his support in using the pulsed laser deposition and his inputs and expertise with BAM material; Dr. Ganesh Balasubramanian and Dr. Reza Montazami for their comments and valuable suggestions on these projects.

Special thanks to all my collaborators for their support and contributions to this work. I greatly treasure the experience of working with Dr. Pal Molian and Dr. Volodymyr Bushlya. Also, I would like to thank all the fellow students I worked with or shared thoughts with: Zhuoru Wu, Jingnan Zhao, Austin Shaw, Anthony Fontanini, Mansour Manci, and Roslyn Melookaran.

In addition, I would like to send special thanks to my family: my parents, my wife, my sisters, and my kids. They have provided the love and support I needed to pass through my difficult times. This dissertation is proof of their support.

Finally, I would like to acknowledge the support provided by the National Science Foundation (under the grants CMMI-1000035 and 1067894), and the scholarship provided

by King AbdulAziz University, Jeddah, Saudi Arabia. Also, I would like to thank Diamond Innovations, Inc, and Dr. Volodymyr Bushlya for the BN samples. In addition, a thank you note for Fianium Ltd. for the picosecond laser testing.

ABSTRACT

Laser processing of ultra-hard materials is a relatively new field that have the potential to improve variety of products and different industries. This dissertation explores specific new development in this field through three main subjects: laser machining, laser deposition of thin film, and laser treatment. In laser machining of ultra-hard material, controlled crack propagation mechanism -as opposed to the typical ablation mechanism- was investigated, and micromachining of ultra-hard thin film was also observed. For the laser deposition of ultra-hard thin film, designing new microstructured materials was explored, and the utilization of the inherent particulate formation associated with the pulsed laser deposition process was proposed for the first time. After that, a novel laser/waterjet treatment process to increase the hardness of certain ceramic materials was studied. Also, laser shock processing was investigated. Analytical and experimental approaches was conducted through all of these studies, and different analysis techniques were applied. The results indicate the feasibility of these processes when applied on ultra-hard materials, and provide a better understanding of the governing mechanisms.

CHAPTER 1: GENERAL INTRODUCTION

Ultra-Hard Materials

New materials facilitate the development of new technologies. Engineering systems and products are required to perform more complex tasks than ever before as well as to function under more severe operational conditions. In many fields, engineering ceramics are emerging as the most desirable alternative for various high performance applications such as cutting tools in manufacturing applications, heat resistance shield in aerospace applications, and anti-oxidant in refractories [1]. The desirability comes from the superior properties such as low density, wear resistance, hardness, stiffness, chemical inertness, and thermal stability. These characteristics make shaping these materials for their applications difficult, and limit the ability to shape them for more applications.

Engineering ceramics can be divided to two groups: 1) hard ceramics with Vickers hardness less than 35 GPa such as alumina, zirconia, and silicon nitride; 2) ultra-hard ceramics with Vickers hardness greater than 35 GPa such as diamond and boron nitride. Generally, hard ceramics substitute metals when high wear resistance parts are needed or extreme operational conditions are applied (high temperature or corrosive environment). Ultra-hard ceramics are used as abrasives, cutting and drilling tools, and protective layers.

For many engineering ceramics, conventional processes such as drilling, milling, turning, and honing can be used. On the other hand, ultra-hard ceramics cannot be shaped effectively using conventional processes. This drawback had limit the machining of ultra-hard ceramics to unconventional processes such as electro discharge machining (EDM), lasers processing, and water-jet machining. Even though these processes are currently being used in

industries to machine the ultra-hard ceramics, they still face variety of limitations such as low process efficiency and high cost. As an example for some of these limitations: not all ultra-hard ceramics are electrically conductive to utilize EDM, nor can be efficiently machined with lasers or water-jet since they require high power and long machining time. More often, these materials are either produced in their final shape directly from powdered materials using high pressure high temperature process (HP-HT) or are applied as thin film on other materials using chemical or physical vapor deposition techniques.

Laser processing and Ultra-Hard Materials

Among all the current processes of ultra- hard materials, laser processing is in unique position for the future of these materials. It is the only process that can be applied as cutting process, thin film deposition process, and treatment process. Therefore, the utilization and machinability of ultra-hard ceramics will be addressed in this dissertation with emphasis on laser processing through these three main topics: machining, thin film deposition, and treatment of ultra-hard materials. The emphasis of laser processing in each of these topics comes from the unique advantages of lasers in dealing with ultra-hard materials as described in each of these topics below.

1.1. Laser Machining of Ultra-hard Material

Laser-alone and laser-based hybrid processes show more potential in processing ceramics [2] because the machining efficiency is primarily dependent on the thermal and optical properties instead of the mechanical properties of the workpiece material. Lasers have been used in conjunction with other conventional processes to cut ceramics and produce better

quality cut surfaces. For example, in laser-assisted turning; the laser is focused on the workpiece in front of the cutting tool to heat up the workpiece locally. The heated material just in front of the cutting tool becomes softer and can be easily removed. This increases the performance of the process since it allows the turning process to cut hard to machine brittle materials. Laser-assisted turning also requires lower magnitude of cutting forces leading to high workpiece surface quality and dimensions accuracy with low energy and cost [3]. According to Dubey et al [4] laser-assisted turning of silicon nitride and alumina ceramics is economically effective since it reduces the surface roughness, cutting forces, and tool wear.

For ultra-hard ceramics, lasers are used to perform machining and micromachining through ablation, melting, and evaporation [5]. Since ultra-hard ceramics are often needed in high precision applications, these mechanisms of material removal do not meet some of the high industries requirements. In laser machining using these mechanisms, heat affected zone, low speed, and high energy are some of the main limitations. However, due to the unique mechanical properties of ultra-hard materials an alternative cutting mechanism can be used. The novel controlled crack propagation mechanism would minimize heat and energy required for laser machining and increase the cutting speed. The work done on investigating this cutting mechanism is reported in four scientific peer reviewed papers (Chapter 2, 3, 4 and 5). These investigations addressed the role of the fluid medium in Laser/Water-Jet (LWJ) process with respect to controlled crack propagation mechanism, and modeling the mechanism to optimize for the process parameters. Also, a change of the crack direction was investigated.

As in laser machining, laser micromachining of ultra-hard materials face the same problems of low precision and large heat affected zone; however, controlled crack propagation mechanism cannot be applied due to the high precision requirement. We addressed these

limitations through the investigation of material removal through ablation mechanism, but using smaller wavelength laser and smaller pulse duration to minimize the heat and the area affected by laser.

1.2. Pulsed Laser Deposition and Ultra-hard Material Thin film

One of the ways to utilize ultra-hard materials is to apply them as thin films using chemical (CVD) or physical (PVD) vapor deposition techniques. This makes shaping and utilizing these materials much easier. Thin films of ultra-hard materials are used in different applications and products such as dielectric protective layer in semiconductors industry, or hard protective layer in tooling industry. Each of CVD and PVD techniques has its own challenges when it comes to deposition of ultra-hard materials. Some limitations related to the substrate materials, deposition conditions, and process efficiency/cost. For the PVD techniques in specific, the main challenge that shared by all PVD techniques is preserving the chemical stoichiometry of the deposited material. Femtosecond Pulsed Laser Deposition (PLD) among all PVD techniques, on the other hand, is proposed by many researchers to overcome this drawback [6].

Using PLD to deposit ultra-hard material is not a new topic even though only a few work was done in this field; however, the extension of the possible applications in using it is not explored yet. For example, such advantage of PLD opens the door in material design to utilize ultra-hard materials in building new structured materials. We attempt to mimic the Nacre microstructure of brick, bridge, and mortar system using PLD to incorporate ultra-hard materials in the microstructure system. The results not only explored the potential of using ultra-hard materials in this field, but also introduced for the first time -based on our knowledge-

the utilization of the inherent problem of particulate formation associated with PLD to create controlled textured surfaces. The study of this topic is presented in chapter 5.

1.3. Laser Treatment of Ultra-hard Material

Laser treatment of metals is a very well established field, and it has been used in many industries for precise controlled surface treatment. On the other hand, laser treatment of ceramic materials has been established recently and especially with some certain ceramic materials - Boron Nitride (BN) - this process was never addressed.

Based on our work on BN in the laser machining and PLD of ultra-hard materials, we noticed the potential of laser treatment of BN. Improving the hardness of BN using laser treatment would open the door for unlimited opportunities in many industries. Especially in the tooling industry, this opportunity would have a huge impact. Diamond is the hardest material but suffers from low thermal and chemical stability when used in machining of ferrous materials, and cubic boron nitride is thermally and chemically stable but has half the hardness of Diamond. We addressed this issue through investigating hardness improvement of cubic boron nitride material through two approaches: 1) Laser shock processing (LSP), and 2) Laser waterjet (LWJ) heat treatment. The first approach used shock waves to embed nano diamond particles on the surface of PCBN tools in order to increase the hardness of the tool. The second approach used LWJ surface heat treatment to increase the hardness of BN tools. The approaches in both projects were initiated for the first time in the field of ultra-hard ceramics to the best of my knowledge. The detailed studies are presented in chapter 7, 8, 9, and 10. Also, a patent application was filed for the LWJ heat treatment process [7].

Dissertation Organization

This dissertation is organized in the journal paper format that includes ten papers (Chapters 2 to 11). Chapter 1 provides the motivation and background for these studies. Chapter 2-6 addresses two special topics in the field of laser machining of ultra-hard materials: hybrid laser water-jet (LWJ) machining, and micromachining of thin film. Chapter 2 discusses an experimental investigation of the effect of different fluid media on continuous wave CO_2 laser machining with respect to ablation and controlled fracture mechanism. Chapter 3 and 4 include the work conducted to identify the mechanism governing the cutting of BN using LWJ and controlled fracture mechanism through experimental and analytical approach. Chapter 5 addresses the difficulties encountered in the change of the crack direction in multi-axis cutting. A preliminary qualitative model is also presented to explain the observed experimental results. Chapter 6 addresses laser micromachining of $AlMgB_{14}$ (BAM) thin films using picosecond laser. The micromachining of ultra-hard ceramics was performed and analyzed to explore the potential of picosecond laser in this area.

Chapter 7 is a comparison study on PLD of ultra-hard ceramics with nano and femto-second lasers. The work done in chapter 7 and 6 explore the possibility of making a superior bio-inspired structured material that expected to outperform most of the known materials in its mechanical properties. The work in chapter 7 also explore the possibilities of utilizing PLD to build textured surfaces without the need for additional processes.

Chapter 8-11 addresses two special topics in the field of laser treatment of ultra-hard material: LSP, and LWJ treatment of BN. Chapter 8 is the paper on LSP where the surface of PCBN tool was tested and analyzed with and without diamond nano powders. The results show an improvement in PCBN hardness of 15% with LSP, and 12% with nano diamond and LSP.

Chapter 9 includes the preliminary results of LWJ heat treatment where the hardness improvement was around 100% in dual phase BN and 40% in single phase. Chapter 10 and 11 are on the investigation of the hardness improvement mechanism in LWJ treatment of BN.

Chapter 12 presents general conclusions observed in all of these studies and describes future research ideas to move forward with these projects.

Note

Chapter 2, 3, 6 and 10 are peer reviewed conference papers that published in the proceedings of each conference. Chapter 4, 5, 7, 8, 9, and 11 are peer reviewed journal papers. Chapter 4 and 11 journal papers are extensions of the work done in the conference papers in chapter 3 and 10 respectively. So, they include a new sections in addition to a modified version of the work in these two conference papers.

I designed and carried out all the experimental work and analysis in these publications except in chapter 8. In chapter 8, I did some of the analysis and helped in the writing of the manuscript. Also, all the first drafts of the papers were done by me except chapter 3, 4 and 8. In chapter 3 and 4, I performed the experiments and some of the analysis.

References

[1] Bar-Cohen, Yoseph. “High Temperature Materials and Mechanisms”, Boca Raton, FL: CRC Press by Taylor & Francis Group, LLC. (2014), p 6

[2] J.K.S. Sundar, S.V. Joshi, “Laser cutting of materials”, Centre for Laser Processing of Materials, International Advance Research Centre for Powder Metallurgy and New Materials, Hyderabad

[3] Rozzi, J.C., Pfefferkorn, F.E., Y.C. Shin, F.P. Incropera, “Experimental evaluation of the laser assisted machining of silicon nitride ceramics”, ASME Journal of Manufacturing Science and Engineering 122 (2000) 666–670

[4] Dubey, A., Yadava, V., “Laser beam machining—A review”, International Journal of Machine Tools & Manufacture 48 (2008) 609–628

[5] Meijer, J., “Laser beam machining (LBM), state of the art and new opportunities”, Journal of Materials Processing Technology 149 (2004) 2–17

[6] Loehman, Ronald E. “Characterization of Ceramics”, New York, NY: Momentum Press®, LLC, (2010), p 44

[7] Melaibari, A., “Method of increasing the hardness of wurtzite crystalline materials” USPTO patent case number 20140210139 filed in 2011 and published in 2014.

CHAPTER 2: EFFECT OF FLUID MEDIUM ON LASER MACHINING OF POLYCRYSTLINE CUBIC BORON NITRIDE TOOL

A modified version from a paper published in the conference proceedings of *The 44th CIRP Conference on Manufacturing Systems* June 1-3, 2011

Ammar Melaibari[1,2,3], Pal Molian[1,4], and Pranav Shrotriya[1,4]

Abstract

Polycrystalline cubic boron nitride (PCBN) tools are currently fabricated through Nd:YAG laser machining, electric discharge machining, and water-jet, all of which suffer from thermal damage and low speed. A hybrid CO^2 laser-water-jet machining (LWJ) was able to overcome these deficiencies. In order to understand the role of water-jet and its effects in laser machining, a study was undertaken to identify the effect of various fluid media (argon, nitrogen, oxygen, air and water) on kerf geometry, surface roughness, phase transition and recast layer of PCBN tools. Scanning electron microscopy, Raman spectroscopy, and optical profilometer were used to characterize the machined regions. The effect of each fluid medium on the outcomes of the experimental investigation is discussed.

Keywords: laser, water-jet, PCBN tool

[1] Laboratory for Lasers, MEMS and Nanotechnology, Dept. of Mechanical Engineering, Iowa State University, Ames, IA 50011, USA
[2] Dept. of Mechanical Engineering, King AbdulAziz University, Jeddah, Saudi Arabia
[3] Primary researcher and lead author
[4] Co-author

2.1. Introduction

Polycrystalline cubic boron nitride (PCBN) is the second hardest known material, diamond being the hardest. Unlike diamond, PCBN is not found in nature, but is a man-made material. It is hailed as the best performance cutting tool material for machining hard cast iron, high chrome alloy steels, high-strength nickel super alloys and powder metal alloys because of its advantages over diamond in terms of thermal and chemical stability. PCBN is manufactured by sintering fine particles of c-BN with the aid of ceramic matrix typically TiN or AlN under high pressure and high temperature conditions. PCBN not only possesses the outstanding mechanical properties such as extreme hardness and wear resistance but also exhibits high thermal conductivity, high Young's Modulus, low coefficient of friction, and chemical inertness (less reactive to metals like titanium) [1]. In recent years, PCBN tools are increasingly used in micro-manufacturing of a variety of precision components because PCBN is able to keep its nature when scaling down the end mills from conventional to microscopic sizes. In addition, PCBN meets the high demands of form accuracy, surface quality and low subsurface damage in ductile machining of brittle materials. Thus, PCBN is currently employed in the industry for cutting 'difficult-to-machine' materials because of its superior characteristics [1]. However the same properties limit the ability to shape the PCBN tools for various geometries.

Many machining techniques have been developed to shape PCBN that ranged from water-jet to electric discharge machining (EDM), and pulsed Nd:YAG laser. Due to the shortcomings in the water-jet process such as time consumption, wide kerf, poor surface finish and taper water-jet was not acceptable. In EDM, the process has been used to fabricate all insert shapes with good quality, but the material removal rates remained low. Lasers, on the other hand, have excellent prospects for machining PCBN. However, the central issues like

formation of recast layer, phase transition, and kerf geometry require a secondary process like honing. Also, the material removal rate is low. Thus the existing processes for the fabrication of PCBN tools are inefficient with respect to cost, time, and energy consumption.

The current processes used to produce PCBN tool inserts are pulsed Nd:YAG laser and EDM, both of which suffer from thermal damages and long machining time. We have recently demonstrated a novel, hybrid continuous wave CO^2 laser/ water-jet process (LWJ) for machining hard ceramic materials that seems to eliminate many of the deficiencies associated with pulsed Nd:YAG laser and EDM [2, 3]. It may be noted that LWJ uses an entirely different mechanism than conventional laser machining where a laser beam causes the material removal by heating up and evaporating the material. In LWJ, thermal stresses induced by temperature gradient and phase transition provide controlled crack initiation and propagation that in turn offers a fast, cheap, and low energy method to cut PCBN. The LWJ process begins with rapid laser heating leading to localized damage and phase transformation of surface layers; this is followed by water-jet (fast quenching of the surface layers) resulting in a stress field in the transformed material. The stress fields propagate the localized cracks through the thickness with the end result of material separation. Small kerfs, less taper and high-speed cutting are the beneficial effects of LWJ process. Drawbacks include the presence of recast layer and chemically-induced products on the top of kerf that increase the surface roughness [4].

In this work, a study was undertaken to identify the material removal mechanisms in laser machining under different fluid media including LWJ. A 500 W continuous wave CO^2 laser was used to examine the effects of argon, nitrogen, oxygen, air and water-jet on the cutting of PCBN substrates. Evaporation, ablation, melting, erosion, oxidation, graphitization and controlled crack fracture mechanisms were elucidated. The laser-cut surfaces were

analyzed using scanning electron microscopy, Raman spectroscopy and optical profiliometer to determine the role of each medium on the cut quality.

2.2. Experimental Details

Equilateral triangular inserts of PCBN without carbide backup, prepared by EDM, were offered by Diamond Innovations, Worthington, Ohio, USA for the experiments. The triangles have 7 mm side length and 1.6 mm thickness. The average particle size is 4 μm with a composition of 75% of c-BN and 25% of Ti based matrix containing carbon, by volume (BZN 9000 of Diamond Innovations). Surface roughness (Ra) of the top (polished) and the side (EDM machined) were 0.3 and 3 μm respectively.

Five triangular inserts were used, one for each fluid medium. Laser machining was accomplished at two different cutting speeds 42.3 and 84.6 mm/sec (100 and 200 in/min) for each insert. All fluid media pressure was kept at 140 kPa (20 psi) except for the water-jet. Since the abrasive-free water-jet was used in the work, the pressure was kept higher at 5.5 MPa (800 psi).

A continuous wave CO^2 Laser (Model 820 Spectra Physics) of 10.6 μm wavelength and 500 W power was used in all experiments. The laser beam was focused to a spot size of 0.2 mm on the sample surface using a 127 mm focal length lens. For the laser/water-jet experiment, the water-jet followed the laser beam with a spacing of 4 mm to avoid the absorption of laser power by direct contact with water. See Figure 1 for laser head description. It may be noted that water absorbs about 70% of CO^2 laser energy. Details of laser-water-jet setup are described elsewhere [5].

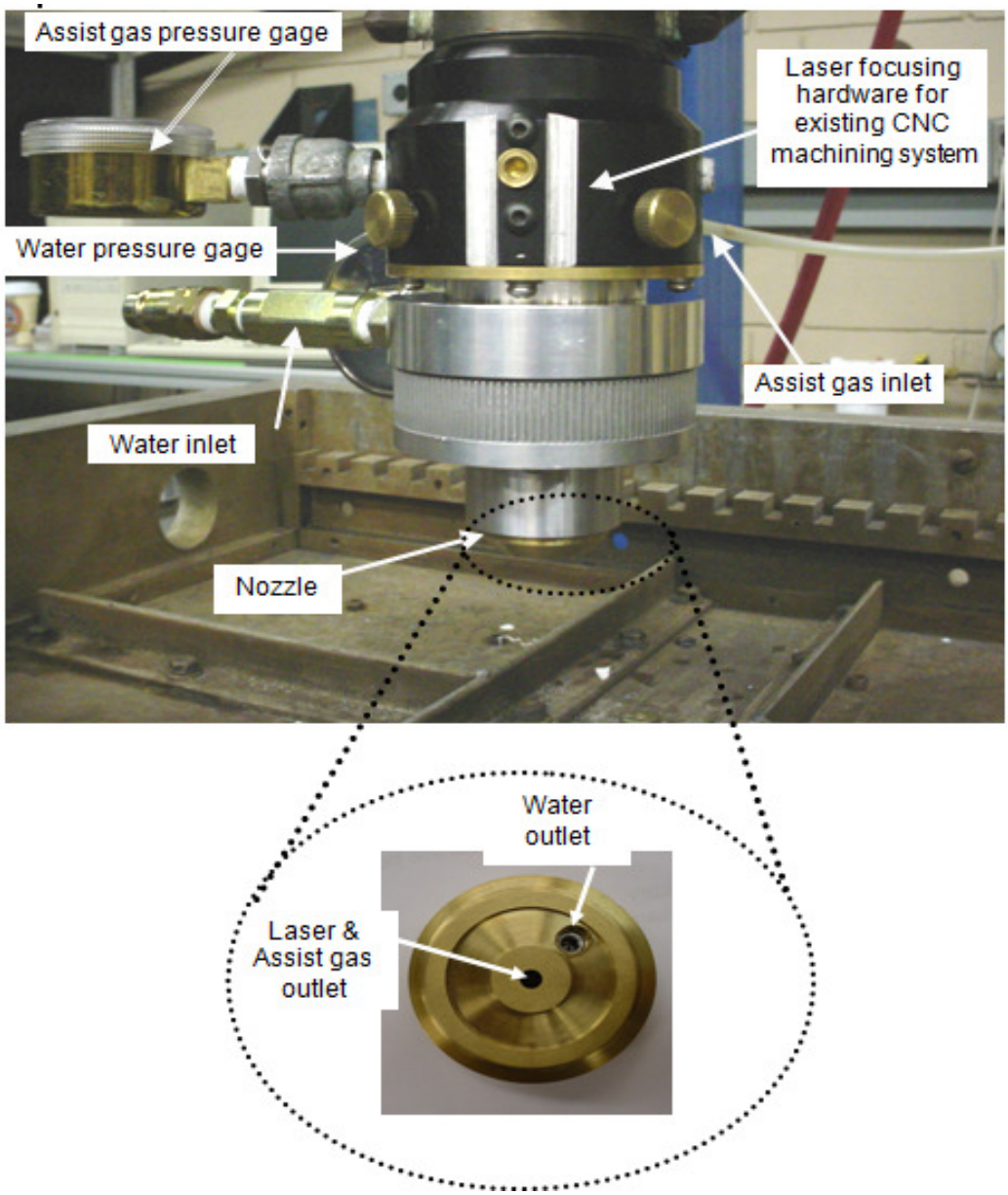

Figure 1: Laser head description with the assist fluids inlets and outlets.

Measurements of kerf geometries and surface roughness profiles were carried out using an optical profilometer (Zygo NewView 7100) with 5X and 20X magnifications. The roughness readings were taken from the kerf side of those samples that were completely cut through. In those samples that were only scribed, roughness was measured from a region very close to the top edge of the kerf. Scanning electron microscopy (SEM Model JEOL JSM-

606LV at 20 kV) was used to make secondary electron image of the machined surfaces in order to identify the growth of the recast layer and the characteristics of phase transition regions. Phase transition was determined using Dispersive Raman spectroscopy (Renishaw-inVia Raman Microscopy). Ar-ion laser at 488 nm wavelength was used for excitation.

2.3. Results and Discussion

The assist gas plays a key role in laser machining. In general, the assist gas serves four main purposes:

1. It can cause a chemical reaction depending on its reactivity and produces or absorbs heat.
2. It provides a mechanical force to eject the melt from the cut zone. However inefficient removal of the molten layer can lead to deterioration of cut surface.
3. It cools the cut zone by forced convection causing a potential loss in heat penetration.
4. It protects the lens from the contamination by evaporated species.

The efficiency and overall quality of laser machining is thus strongly dependent on the interaction of the assist gas with the sample. Table 1 summarizes the data on kerf geometry and surface roughness of laser machined PCBN with different fluid media; these are average values based on many data points. At the cutting speed of 42.3 mm/sec, complete separation was achieved when using air, O_2, N_2, and Ar. For the same speed, water-jet caused only scribing suggesting that water-jet forced significant convection and also changed the material removal mechanism to more of cracking. However mechanical snapping of the scribed samples enabled complete separation. At a cutting speed of 84.6 mm/sec, only scribing was made possible in all samples. The effect of doubling the speed on kerf depth is quite striking with all gas media.

Direct sublimation or melting of PCBN by laser irradiation is a challenge. In order to machine PCBN, high laser intensity and phase transition from c-BN to h-BN (surface reconstruction) are required. The process begins with the conversion of sp^3 to sp^2 phase transition followed by gasification of sp^2-bonded BN [6]. In the oxygen environment, both oxidation and phase transition govern. First, c-BN oxidizes to a protective layer of B_2O_3, and then this layer evaporates allowing c-BN to transform to sp^2-bonded BN phases on the surface. Then, these phases will melt and evaporate. In addition, the oxidization of the binder material and all the gaseous products will continue to yield fine particulates with different sizes. Thermal expansion mismatch between c-BN and h-BN leads to thermal stresses that in turn create crack formation. The crack growth is caused by stresses induced by thermal gradients and phase changes. The effect of each fluid medium on oxidation, and phase transition is discussed below along with the material removal mechanism.

Table 1: Kerf geometry and surface roughness of laser machined PCBN

Fluid medium	Kerf Width, µm	Kerf Depth, µm	Taper angle, degrees	Surface Roughness (Ra), µm	
				Machined area	Cracked area
Ar (42.3 mm/s)	complete separation (1600 µm)			-	2.5
Ar (84.6 mm/s)	211	60	30	6	-
N_2 (42.3 mm/s)	complete separation (1600 µm)			5	3
N_2 (84.6 mm/s)	177	450	11	5	-
Air (42.3 mm/s)	complete separation (1600 µm)			4	1.2
Air (84.6 mm/s)	185	100	42	6	-
O_2 (42.3 mm/s)	complete separation (1600 µm)			5	1.8
O_2(84.6 mm/s)	172	360	13	4	-
Water-jet (42.3 mm/s)	200	185	14	7	-
Water-jet (84.6 mm/s)	190	85	24	4	-
Original PCBN	Side machined with EDM			3	-

2.3.1. Argon

The complete separation of PCBN at 42.3 mm/sec is illustrated by its transverse section in Figure 2(a) while the scribing at 84.6 mm/sec is shown by its top view in Figure 2(b). A thin layer is melted and evaporated followed by crack formation and propagation through the thickness (Figure 2(a)). The kerf in the complete-cut sample is characterized by two regions: machined area (melts and evaporates) and cracked area (fractured zone). Figure 2(b) shows a shallow but wider kerf compared to all other gases. The temperature-induced phase change makes a thermally insulating h-BN layer which reduces the machined depth in argon environment [6]. It may be noted that in a flow of high purity argon gas, PCBN can be heated up to about 2800°C without any oxidation although its surface blackens, possibly due to the phase change beginning at ~1600°C [7] where c-BN transforms to h-BN, and the carbon in the binder matrix to graphite, or h-BNC. Another possible reason is the oxidization of nitrogen to form NO and/or NO_2 due to air exposure after machining since no boron oxide protective layer is formed; this led to the creation of boron carbide (B_4C) on the surface. The kerf is rough with a chipped zone at the start and end points of laser cutting that could be attributed to thermal expansion mismatch stresses between c-BN and h-BN phases at the edge and also to the pre-existing cracks from EDM machining.

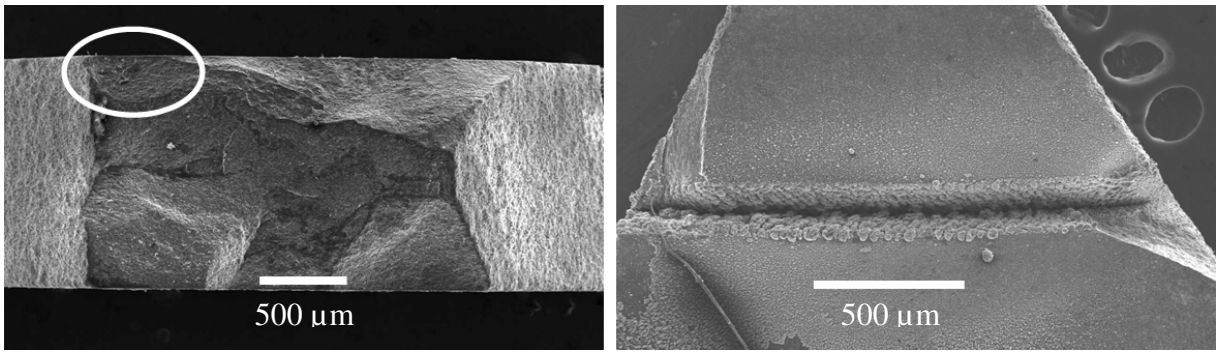

(a) (b)

Figure 2: (a) Transverse section of laser-cut PCBN at 42.3 mm/s with argon as assist gas, the machined area is inside the circle; (b) Top view of laser-scribed PCBN at 84.6 mm/s with argon assist gas.

The surface roughness of the machined area in Figure 2(b) was difficult to measure because the region was very small and the light from optical profilometer was completely absorbed there. Raman spectroscopy revealed the presence of h-BNC and other BN phases in the machined area (Figure 3) which could be the reason for the light absorption. The as-received PCBN has the distinct 1307 cm^{-1} peak characteristic of longitudinal optical (LO) Raman active mode for c-BN. In contrast, the machined area exhibits two peaks, one at 1377 cm^{-1} and the other at 1585 cm^{-1}. The 1377 cm^{-1} peak could belong to sp^2 bonding between N-B in the rhombohedral phase (r-BN) or in plane vibrations of the hexagonal phase (h-BN) [8]. The shift to higher frequency in h-BN Raman line –which is ~1366 cm^{-1} – can be attributed to the effect of impurities like carbon in the matrix material on h-BN and/or to the decrease in the crystalline size of h-BN. Nemanich *et al.* [9] indicated that the Raman line for h-BN can be shifted to higher frequency, broadened, and became asymmetric as the crystalline size decreases. The Raman features around ~1585 cm^{-1} can be attributed to h-BNC [10] or B_4C [11]. The formation of rhombohedral BN and/or of well-crystallized h-BN layers was observed along grain boundaries. Rapid heating and cooling associated with the process will cause the more probable c-BN transformation to h-BN, h-BNC and/or rhombohedral phase. Furthermore, the fact that phase transition takes place at the grain boundaries implies that finer grain size grades (as in the present case) would provide a large number of sites for the formation of these phases.

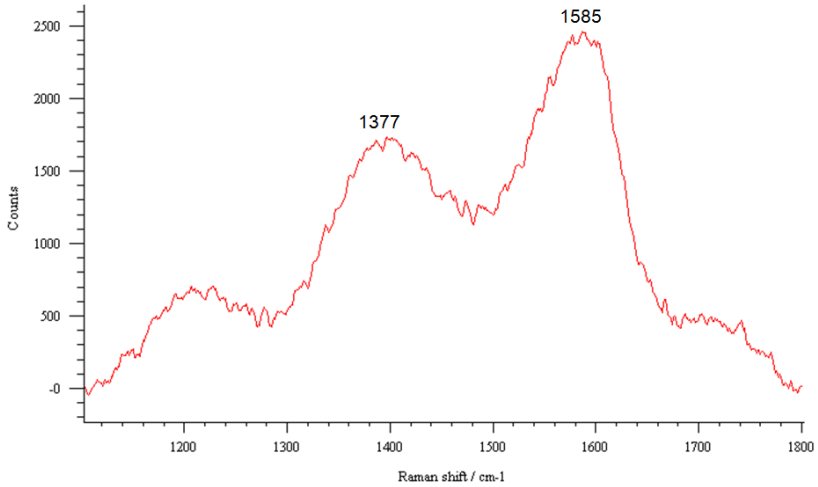

Figure 3: Raman spectrum of the machined area in laser-cut PCBN with argon gas.

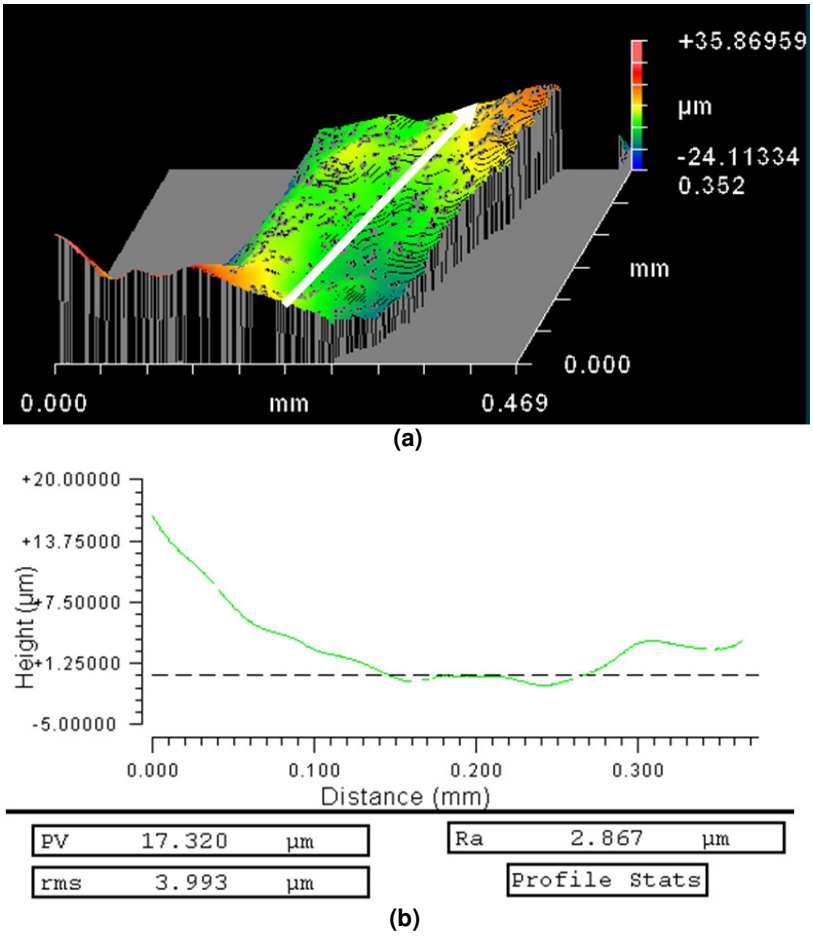

Figure 4: Waviness in the cracked area when argon assist gas was used; (a) 3D topography of the transverse section, the arrow indicate the locations of the profiles taken; (b) Surface Profile.

In contrast to the machined area, the cracked area has low surface roughness but exhibited high waviness (Figure 4). The waviness effect is explained by a stress-induced explosion mechanism caused by a) the phase change where the lattice structure changes from c-BN to r-BN and then h-BN decreasing grain size and inducing high stresses [6]; and b) thermalization of the lattice because argon has the lowest heat conduction coefficient.

2.3.2. Nitrogen

Figure 5 shows the scanning electron micrographs of the transverse section of complete-cut (Figure 5(a)) and scribed (Figure 5(b)) PCBN tools. The kerf in complete-cut sample consists of two regions: a) machined area near the top showing a particulate structure 'debris' unlike that of argon; this structure contributed to roughness peaks in the kerf and on the edge. Collision interaction between the nitrogen molecules and the sputtered particles from ablation and evaporation modes in the PCBN which make up the recast layer may account for high degree of surface roughness. This interaction has been recorded between diamond and different gases in a research conducted by Gloor *et al.* [12]; and b) cracked area which is rougher than those produced by other gases. The roughness is believed to result from the different depths of the machined area that in turn created sub-micro cracks with different orientations. When the crack propagates it needs space; the absence of space means roughening. For the scribed sample (Figure 5(b)), the kerf was deepest and narrowest among all assist gases. Surface roughness is same as that obtained in the machined area (Figure 5(a)). It appears that nitrogen facilitates improving laser ablation of PCBN and thereby increased the machined depth. Nitrogen gas enhances the reactivity of PCBN that is partially responsible for the improved CO_2 laser ablation.

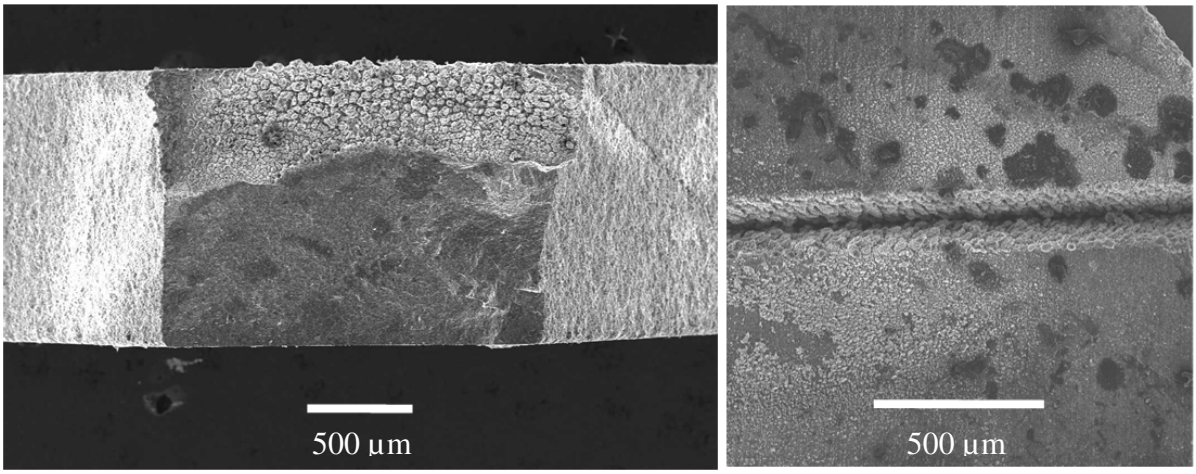

Figure 5: Transverse section of laser-cut PCBN at 42.3 mm/s with nitrogen as assist gas, the machined area is near the top; (b) Top view of laser-scribed PCBN at 84.6 mm/s with nitrogen as assist gas.

Raman spectroscopy analysis revealed many phases including the h-BNC or B_4C, h-BN and/or r-BN, as shown in Figure 6. The 1710 cm^{-1} peak, which is close to the theoretical carbonyl peak, could be an indication for the addition of oxygen, upon air exposure, to the (C=N) band as in Aramid. Using nitrogen gas with PCBN increases the tendency for the previously stated phase transitions and creates some kind of fibers.

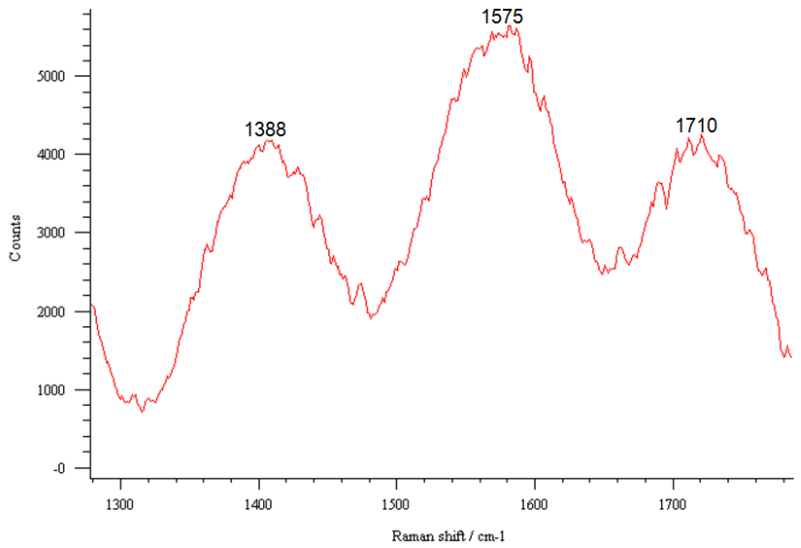

Figure 6: Raman spectrum of machined area in laser-cut PCBN with nitrogen gas.

An intriguing feature of nitrogen assist gas is the formation of particulate structures (various sizes) in both machined and scribed areas. These fine particulate matters ranging in size from nanometers to few micrometers can be attributed to the chemical reaction of nitrogen and carbon binder with oxygen right after laser machining. Thus, nitrogen assist gas in CO_2 laser cutting of PCBN promotes the initial phase change to h-BN, which creates thermal expansion mismatch stresses sufficient to fracture the sample, and improves the laser energy absorption leading to evaporation and condensation of vapour phases leading to fibres formation.

2.3.3. Air

Unlike argon and nitrogen, the air assist gas produced a heavy recast layer (Figure 7) in the laser-cut PCBN. The machined surface was rough due this layer. This recast layer also affect the depth of the machined area as in nitrogen assist gas which roughen the cracked area too. Electron dispersive X-ray analysis indicated that the recast layer was composed of TiB_2 and TiO_2 because of the variety of chemical reactions that could occur among PCBN, binder (Ti matrix) and different impurities in air and the Oxidization temperature of materials other than PCBN are below the oxidization temperature of PCBN e.g. Ti starts to oxidize at 600°C and carbon at 700°C. Raman spectroscopy revealed c-BN, fiber phases and unknown phases which could be attributed to stretching in the h-BN and h-BNC bonds (Figure 8).

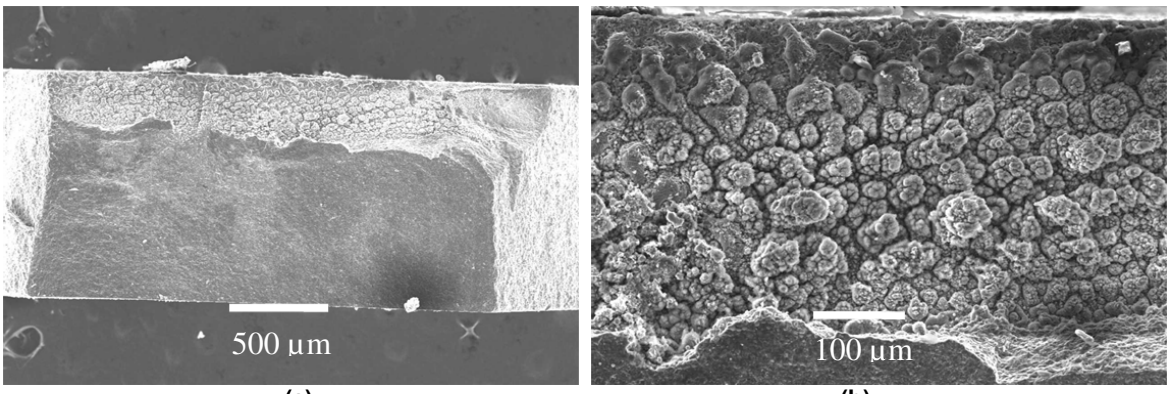

Figure 7: (a) Transverse section of laser-cut PCBN at 42.3 mm/s with air as assist gas; (b) Structure of the machined area near the top.

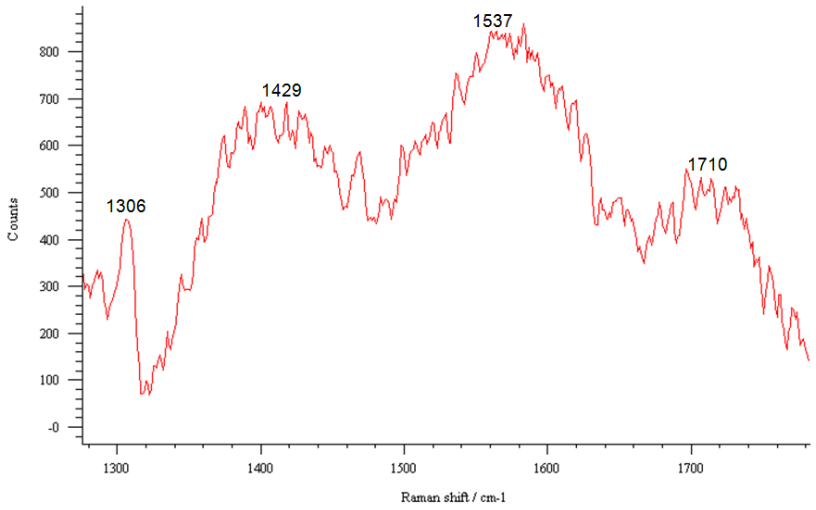

Figure 8: Raman spectrum of machined area in laser-cut PCBN with air as the assist gas.

It is well known that a protective layer of B_2O_3 will cover c-BN when heated to 300°C, and no further oxidization will occur until heated over 1300°C in air or oxygen; the released Nitrogen will form NO and/or NO_2 [13]. The first reaction is not likely to protect the sample in our case due to the fast elevated temperature to ~3000°C. In contrast, the second reaction is more likely to happen in the heat affected zone; machined area, inside the kerf, and around the kerf. The oxidization of nitrogen will leave the oxidized area with rich boron content which is in good agreement with the black heat affected zone and black recast layer. Having more boron

will blacken the area and create boron clusters [14] or boron rich phase of c-BN [6]. Therefore, the high temperature will sublimate the material in the machined zone and oxidize the heat affected zone. Although PCBN oxidation and phase transition are connected phenomena, they are not fully understood. We propose that PCBN undergoes oxidization first which create rich phase of c-BN_{1-x} and form NO_x gases. Then, a reaction/phase transition to h-BNC or B_4C, and some kind of fiber will take place. Recast layer is essentially the binder material oxidation.

2.3.4. Oxygen

Using oxygen as an assist gas showed a recast layer in the complete-cut similar to that of water on one side and similar to that of argon on the other side. This indicates that the cutting mechanism is more complicated and the resulting chemical reactions are also complex. The c-BN starts to change to h-BN as well as h-BNC. Then a strong chemical reaction occurs between oxygen and BN phases as well as with the binder to remove the debris Figure 9(a). The cracked area, on the other hand, was similar to that of nitrogen.

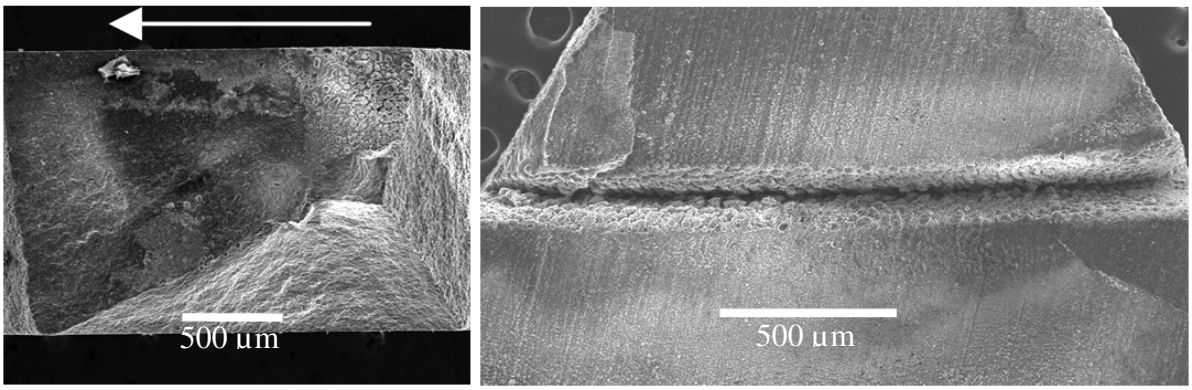

Figure 9: (a) Transverse section of laser-cut PCBN at 42.3 mm/s with oxygen assist gas. The arrow shows the machining direction; (b) Top view of laser-scribed PCBN at 84.6 mm/s with oxygen assist gas.

Scribing with oxygen assist gas (Figure 9(b)) tends to reduce the phase change area on the sample even though the oxidized particles were sputtered all around the surface. In

addition, no peaks of debris were observed along the kerf edge due to the effect of the high weight of oxygen compared to nitrogen in the collision interaction between the oxygen and the sputtered particles [12].

Raman spectrum shown in Figure 10 indicates that the peaks were similar to that of argon medium since the cutting area in that case was exposed to air very fast which resulted in binder material oxidization; however, in the case of rich oxygen environment the oxidized particles are very fine and small due to the pure oxidization effect. It should be noted that the increased shift in the Raman peak of BN is connected to the reduction in the crystal size [6]. On the other hand, cutting with 42.3 mm/sec does not show a lot of debris which is a result of further oxidization or the increased blowing effect corresponds to the lower cutting speed. The lower cutting speed allows the gas stream to force melted and evaporated material away from the machined area. It may be concluded that laser machining of PCBN samples under oxygen is more stable with respect to oxidization than phase change.

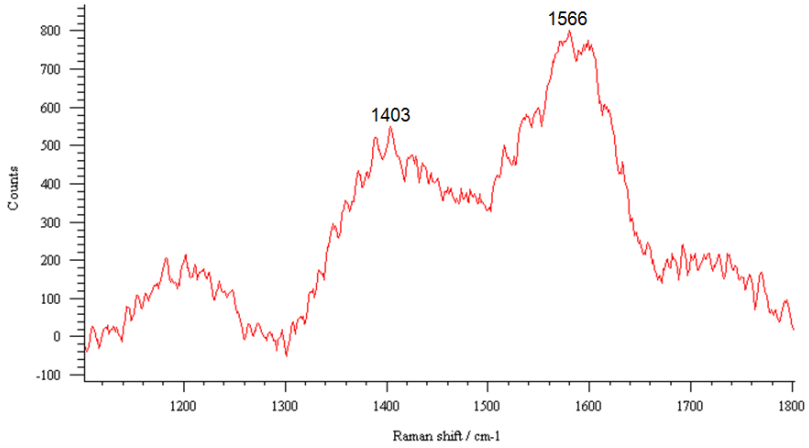

Figure 10: Raman spectrum of machined area in laser-cut PCBN with oxygen assist gas.

2.3.5. Water-Jet

The coupling between the laser and water-jet produced a recast layer similar to that obtained using oxygen assist gas. At the same time, other reactions are expected to occur due to the presence of hydrogen in water. Hidaiw and Tokura [15] observed a c-BN reaction with water and steam in laser machining which produce NH_4^+ or NH_4^+-N and boric acid. Products from these reactions are free to escape. However, the extent of oxidation was very severe because water reacts with sample material violently releasing gases and forming heavy recast layer (Figure 11). Even at low speed, there was an oxidized layer that resulted from high heat dissipation allowing the oxidized layer to form on the surface. The recast layer also increased the roughness. Furthermore the heat dissipation was so fast that the heat penetration (kerf depth) was quite low. Raman spectrum of the zones around laser-cut was mixture of those of oxygen and argon (Figure 12). Despite such drawbacks, easy mechanical separation after scribing was achieved. The phase transition (machined area) layer was very thin. In addition, kerf and taper were attractive. The best candidate fluid between oxygen and water is found to be water because by virtue of its rapid quenching effect, the crack propagation was much better controlled. Furthermore, the sputtered particles below the recast layer were very insignificant.

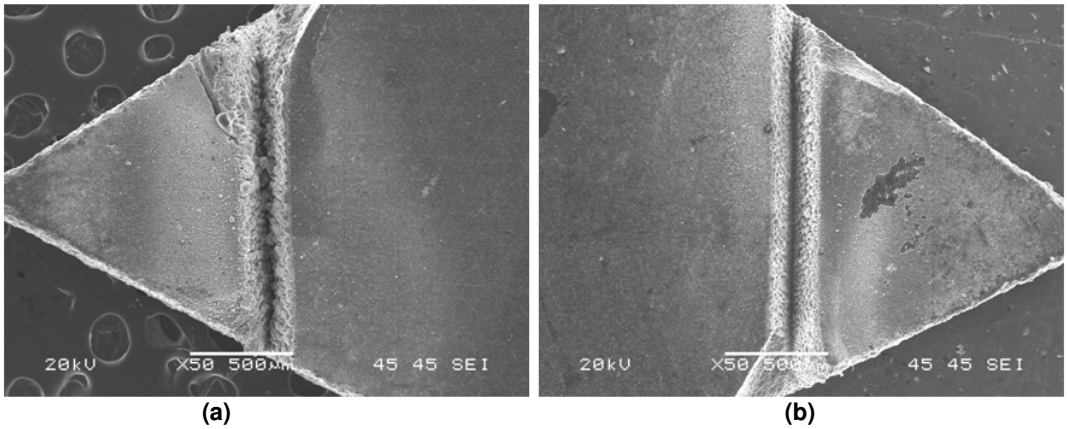

(a) (b)

Figure 11: (a) Top views of the LWJ cutting area at 42.3 mm/s; (b) Top views of the LWJ cutting area at 84.6 mm/s.

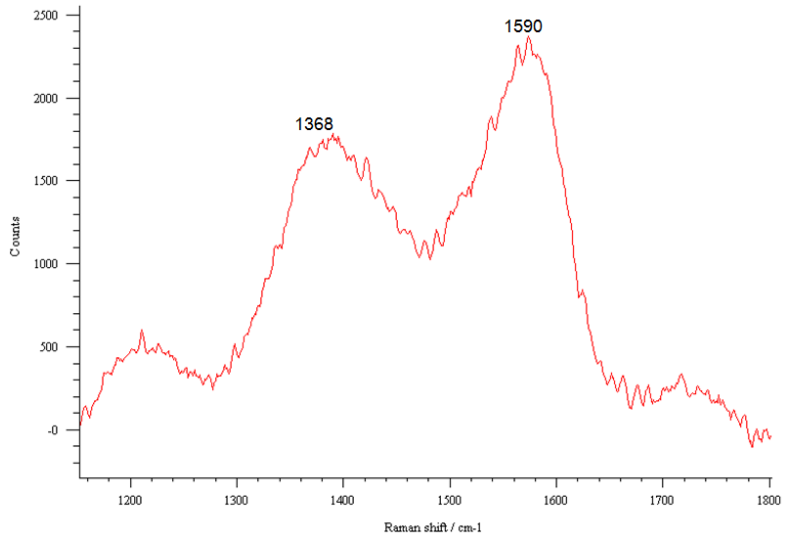

Figure 12: Raman spectrum of machined area in laser-cut PCBN with water as the assist fluid.

2.4. Summary

The effect of assist gas (Ar, N_2, air, O_2) and water in CO_2 laser machining of polycrystalline cubic boron nitride (75% c-BN and 25% Ti based matrix) was investigated. Different material removal mechanisms were observed depending on the type of fluid medium. Analysis of the observation revealed a two-step process consisting of: 1) phase transition of a thin surface layer of PCBN (melting, evaporation, oxidation (c-BN_{1-x} and B_4C) and phase change (h-BN and h-BNC)); 2) crack formation and propagation. In all cases, the cut surfaces can be characterized by two regions: machined area and cracked area (Table 2). The machined area had different phases of boron nitride while the cracked area retained the original c-BN structure (Figure 13). Argon enhanced the phase change but did not offer controlled fracture mechanism due to the explosion effects. Nitrogen, air and oxygen are more effective for removing material through ablation/evaporation. However, the surface roughness and unfavourable phase transitions do not make these assist gases suitable for the controlled crack separation mechanism. Water is an excellent candidate in producing very thin phase transition

layer as well as controlled cracking. Optimization of LWJ process is in order to further improve the process.

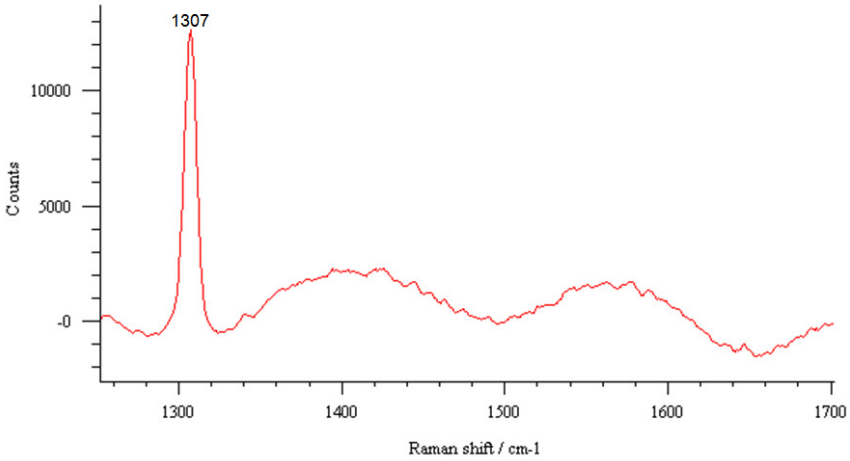

Figure 13: Raman spectrum of cracked area in laser-cut PCBN with water as the assist fluid.

Note, the broad peak around 1200 cm^{-1}, which has been detected only when using nitrogen and air, could be attributed to a new boron-doped phase [16]. Amorphous boron which has a peak around 1150 cm^{-1}, boron carbide which has a peak around 1251 cm^{-1}, or w-BN phase which has broad peaks around 1248 and 1106 cm^{-1} are the closest peaks to the unidentified peak [14]. These peaks are also under consideration to identify the broad peak around 1200 cm^{-1} since the shift in the raman peak can be affected by the presence of different impurities in the sample [14], the increase of temperature by the laser [17], the change of the crystallite size due to the phase transformation [17], and the induced stresses between the boundaries of the phases [17] which all occurred in our case. When using argon, oxygen, and water, this peak is very small and unidentifiable by the Raman program as a peak.

Table 2: Summary for the results of laser machined PCBN

Fluid	Machined area	cracked area
Argon	Shallow + Large affected zone	Rough + waviness
Nitrogen	Deep + Large affected zone	Rough
Air	Average + Large affected zone	Smooth
Oxygen	deep	Smooth + waviness
Water	shallow	Smooth

2.5. Acknowledgments

This material is based upon work supported by the National Science Foundation under Grant No. CMMI-1000035, and the scholarship provided by King AbdulAziz University. The authors gratefully acknowledge the polycrystalline cubic boron nitride tool inserts donated by Diamond Innovations, Inc, Worthington, OH.

2.6. References

[1] Spriggs, G. E., 2002, 13.5 Properties of diamond and cubic boron nitride. Beiss, P., Ruthardt, R., Warlimont, H. (ed.). SpringerMaterials - The Landolt-Börnstein Database.

[2] Chen S.-L., 1999, The effects of high-pressure assistant-gas flow on high-power CO_2 laser cutting, Materials Processing Technology, 88:57–66.

[3] Kalyanasundaram D., Shrotriya P., Molian P., 2009, Obtaining a relationship between process parameters and fracture characteristics for hybrid CO_2 laser/water-jet machining of ceramics, Engineering Materials and Technology, 131/1: 011005.1-011005.10.

[4] Kalyanasundaram D., 2009, Mechanics Guided Design of hybrid laser/water-jet system for machining hard and brittle materials, Iowa State University, PhD dissertation.

[5] Kalyanasundaram D., Shehata G., Neumann C., Shrotriya P., Molian P., 2008, Design and validation of a hybrid laser/water-jet machining system for brittle materials, Laser Applications, 20/2:127-34.

[6] Sachdev H., Haubner R., Nöth H., Lux B., 1997, Investigation of the c-BN/h-BN phase transformation at normal pressure, Diamond and Related Material, 6:286-292.

[7] Solozhenko V., Turkevich V., Holzapfel W., 1999, Refined phase diagram of boron nitride, Journal of Physical Chemistry, 103/15:2903-2905.

[8] Liu J., Vohra Y., Tarvin J., Vagarali S., 1995, Cubic-to-rhombedral transformation in boron nitride induced by laser heating: In situ Raman-spectroscopy studies, Physical Review B, 51/13:8591-8594.

[9] Nemanich R, Solin S., Martin R., 1981, Light scattering study of boron nitride microcrystals, Physical Review B, 23/12:6348-6356.

[10] Ci L., Song L., Jin C., Jariwala D., Wu D., Li Y., Srivastava A., Wang Z., Storr K., Balicas L., Liu F., Ajayan P., 2010, Atomic layers of hybridized boron nitride and graphene domains, nature materials, 9:430-435.

[11] Kuhlmann U., Werheit H., 1994, Raman effect of boron carbide (B4.3C to B10.37C), Journal of Alloys and Compounds, 205:87-91

[12] Gloor S., Pimenov S.M., Obraztsova E.D., Luthy W., Weber H.P., 1998, Laser ablation of diamond films in various atmospheres, Diamond & Related Materials, 7:607-611.

[13] Lavrenko V., Alexeev A., 1986, High-Temperature Oxidation of Boron Nitride, Ceramics International, 12:25-31.

[14] Sachdev H., 2003, Influence of impurities on the morphology and Raman spectra of cubic boron nitride, Diamond and Related Materials, 12:1275–1286.

[15] Hidaiw H., Tokura H., 2006, Hydrothermal-Reaction-Assisted Laser Machining of Cubic Boron Nitride, Journal of the American Ceramic Society, 89/5:1621-1623.

[16] Zinin P.V., Kudryashov I., Konishi N., Ming L.C., Solozhenko V.L, Sharma S.K., 2005, Identification of the diamond-like B–C phase by confocal Raman spectroscopy, Spectrochimica Acta Part A, 61: 2386–2389

[17] Bergman L., Nemanich R.J., 1996, Raman Spectroscopy Characterization of hard, wide-bandgap for Semiconductors: Diamond, GaN, GaAlN, AlN, BN, Annu. Rev. Mater. Sei., 26:551-79

CHAPTER 3: MECHANISM GOVERNING CUTTING OF POLYCRYSTALLINE CUBIC BORON NITRIDE (PCBN) WITH TRANSFORMATION INDUCED FRACTURE

A paper published in the conference proceedings of *the 41st NAMRI/SME conference*, Vol. 41, June 10-14 (2013)

Zhuoru Wu[5,6], Ammar A. Melaibari[1,7,8], Pal Molian[1,4] and Pranav Shrotriya[1,4]

Abstract

A combined experimental and analytical approach is undertaken to identify mechanism governing the cutting of polycrystalline Cubic Boron Nitride (pCBN) sample by a hybrid CO_2 laser/waterjet (CO_2-LWJ) manufacturing process. In CO_2-LWJ machining, a high power laser was used for local heating followed by waterjet quenching of the sample surface leading to fracture propagation along the sample surface. Cutting results indicate two fracture behaviors: scribing and through fracture. Raman spectroscopy analysis of the cut surface indicates that laser heated PCBN undergoes chemical phase transformation from sp^3-bonded cubic Boron Nitride (c-BN) into hexagonal Boron Nitride (h-BN) and other sp^2-bonded phases. Surface profile was experimentally measured using profilometer and compared with analytical predictions in order to estimate the expansion strain and dimensions of transformation region associated with CO_2-LWJ induced transformation. FEM calculation was used to determine

[5] Laboratory for Lasers, MEMS and Nanotechnology, Dept. of Mechanical Engineering, Iowa State University, Ames, IA 50011, USA
[6] Primary researcher and lead author
[7] Dept. of Mechanical Engineering, King AbdulAziz University, Jeddah, Saudi Arabia
[8] Co-author

stress fields generated in the workpiece based on the strain and volume measured experimentally in order to determine the feasibility of crack propagation.

Keywords: Laser/waterjet machining (LWJ), cubic boron nitride, phase transformation, crack propagation.

3.1 Introduction

Cubic Boron Nitride (CBN) is the second hardest material on earth, inferior only to diamond. It is not found in nature but can be synthesized by application of high temperature and pressure [1]. Polycrystalline cubic boron nitride (PCBN) blank are produced through sintering of CBN powders with ceramic matrix such as titanium nitride (TiN) or aluminum nitride (AlN). Since its discovery, PCBN has been used in industry as a substitute for diamond due to the superior thermal and chemical stability. The advantages that PCBN does not react with ferrous metals and has a high resistance to oxidation[2] makes it ideal tool material for machining hard cast iron, high chrome alloy steels, high-strength nickel super alloys, powder metal alloys and metal matrix composites[3].

CBN Tool inserts are traditionally cut from the compact blanks by either diamond sawing, electric discharge machining (EDM) or Nd:YAG laser cutting and finished by diamond grinding, lapping, and polishing. A variety of tool geometries such as square, triangle, circle and rhombus are fabricated for use in various machining operations. The main requirements of a manufacturing process in cutting the desired geometry of tool inserts are: capabilities to generate smooth surface, parallel and narrow kerf, minimal heat affected zone and excellent dimensional tolerance enabling precision; and high cutting speed. In tool production, high speed, low cost and fine resolution are the main consideration for industrial

productivity. However, none of the current machining processes perform the combination of these features due to the extreme hardness of PCBN materials. Traditional manufacturing methods for producing tool inserts in PCBN are slow and cost-inefficient.

Given the limitations of conventional material removal mechanisms, a number of recent reports have focused on non-conventional mechanisms for cutting and machining of pCBN. Hidai and Tokura [4] investigated the hydrothermal-reaction assisted laser drilling of pCBN in steam environment based on measurements of mass loss at high temperatures. CBN film deposited on copper substrate, binder-containing sintered pCBN, and binderless sintered pCBN were irradiated with an Ar-ion laser in water and steam as well as in different gas atmospheres. Single-crystal and binderless sintered CBN reacted very well with steam and thus hydrothermal-reaction-assisted laser machining was effective. However the technique failed in machining the binder-containing sintered CBN.

Swiss Federal Institute of Technology in Lausanne, Switzerland has developed Laser-Microjet® [5], a hybrid technology based on waterjet-guided Nd:YAG laser for machining of pCBN. In this unique laser cutting technique, a free laminar waterjet is used as an optical waveguide to direct the Nd:YAG laser beam onto the sample. The Laser-Microjet® allows precise cutting of pCBN materials with smaller kerf and better surface finish. A Q-switched pulse laser (up to 300 W) of 532 nm wavelength and water pressure of 2-10 MPa was employed for the process. The waterjet prevented any thermal damage and permitted parallel beam transmission through the sample leading to taper-free and narrow kerf features. The tolerances are much smaller than those obtained with conventional laser and EDM processes. However the process suffers from very slow cutting speeds as it reports 70 passes with each pass at a speed of 7 mm/min to cut 3.25 mm thick pCBN sample.

Crack propagation provides an energy and cost efficient method for cutting of ceramics because hardness and brittleness of ceramics lead to low material removal rates and slow cutting speeds during conventional machining processes. In low thermal conductivity ceramics such as alumina thermal shock induced fracture has been successfully utilized for energy efficient cutting [6, 7]. However in high thermal conductivity ceramics such as polycrystalline cubic boron nitride (pCBN), thermal shock is not feasible. In this paper, we investigate fracture based material separation of pCBN due to synergistic interactions between laser heating and subsequent waterjet quenching through "score and snap" mechanism — laser heating leads to localized damage and oxidation of surface layers; and subsequently, stress fields developed due to constrained expansion of transformed material and waterjet quenching act on the laser-produced "score" to propagate crack through the thickness. A CO_2-Laser/waterjet machining (CO_2-LWJ) [6-9] system was used to investigate a novel mechanism for cutting of pCBN compacts through controlled fracture rather than energy intensive erosion or ablation of material. Cut surfaces were analyzed to identify the mechanism governing material separation. Stress fields induced due to volumetric expansion associated with oxidation of pCBN and binder were determined.

3.2 Experimental Procedure

A continuous wave CO_2 Laser (Model 820 Spectra Physics) of 10.6 μm wavelength and 1.5 kW rated power was used for the experiments. The laser head has been modified to accommodate the low-pressure waterjet (< 1000psi or < 8MPa) to realize CO_2-LWJ machining. The working principle of the CO_2-LWJ system is presented in Figure 14 and has been previously reported [6-8]. The workpiece is irradiated with a CO_2 laser beam for localized heating and subsequently, the heated spot is rapidly quenched with the trailing waterjet.

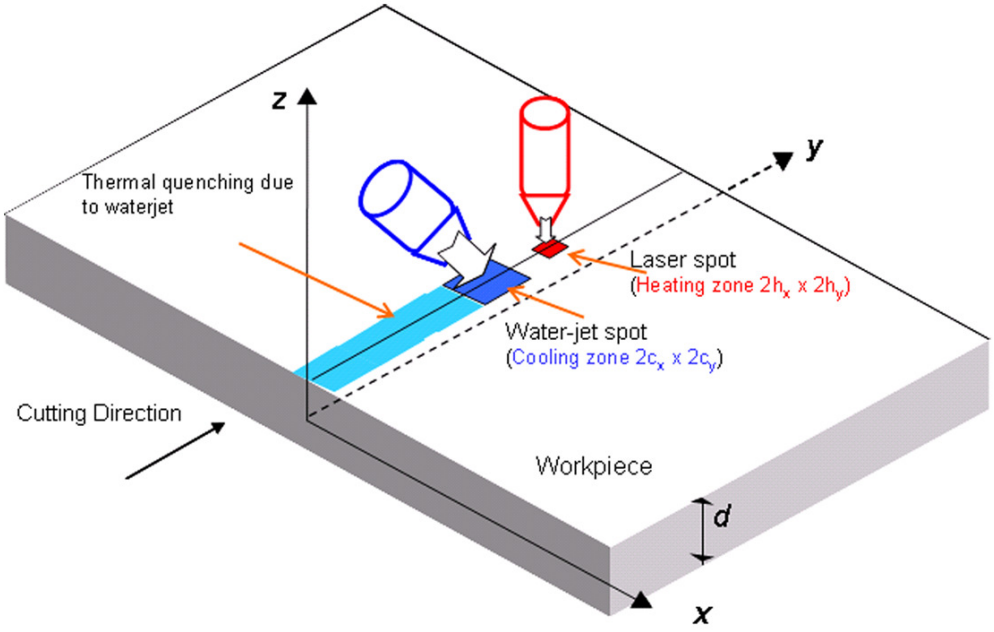

Figure 14: Schematic representation of CO_2-LWJ machining setup.

CO_2-LaserWaterjet cutting experiments were carried on the commercial Polycrystalline Cubic Boron Nitride (PCBN) produced by Diamond Innovations, Inc. (Worthington, Ohio). Two different sets of experiments were performed on PCBN samples: the first set was conducted to determine the effect of processing parameters on the fracture behavior; the other set was conducted to obtain the size of phase transformed zone as well as associated expansion strain associated with machining. The sample in first set was a triangular PCBN insert with dimension of 7mm side length and 1.6mm thickness. It is a member of BZN 9000 series with a composition of 75% CBN (particle size of 4 μm) and 25% of Ti matrix and other impurities. Surface roughness (Ra) was 0.3 μm of the polished faces and 3 μm of the side. The sample used in the second set was 4.8mm in thickness.

A continuous wave CO_2 Laser of 10.6 μm wavelength was used in all the cutting experiments. Laser beam was focused on the sample surface to a spot size of 0.2 mm using a 127mm (5 in.) focal length lens. Pressure of water-jet was maintained at 800 psi as to apply rapid quenching on the heated region. The Distance between laser beam and water-jet was set up to be 2 mm to prevent direct interaction between them. During the experiments, laser beam was irradiated outside the PCBN sample, then translated into it and stopped at the other side. After each cutting test, the sample surface was carefully examined and characterized based on the fracture behaviors.

It has been shown in our previous publications that the different fracture behavior of LWJ machining of alumina [8] was a function of line energy (ratio of laser power to cutting velocity). Therefore, the aim of the first set of cutting experiments was to study how the crack behavior affected by the line energy (P/v) in PCBN sample. Three single pass cuttings were carried out with different cutting speed at laser power of 500W. The details of cutting parameters are shown in Table 3.

Table 3: Parameters of experiment set 1.

Number of cutting	Cutting speed(in/min)	Power(W)	Line Energy P/v(J/m)
1	50	500	23622
2	100	500	11811
3	200	500	5905

The second set of cutting was conducted for measuring expansion strain due to phase transformation and predicting dimensions of the phase transformation zone. Thick specimen was used to generate distinct surface scribing without material separation. Three single pass cuttings were carried out with parameters given in Table 4. Surface profiles around each

scribing line were measured using optical profilometer (Zygo NewView 7100) and statistical analysis was applied on these data aim to reduce variance. The measured surface profiles cut by different line energy values were compared with FEM displacement result calculated from different expansion strain values and various dimensions of transformed zone. The best match result indicated the actual expansion strain and revealed the relationship between line energy and dimensions (depth and width) of transformation region.

Table 4: Parameters of experiment set 2.

Number of cutting	Cutting speed(in/min)	Power(W)	Line Energy P/v(J/m)
1	50	800	37795
2	100	800	18898
3	200	800	9448

After the cutting experiments, scanning electron microscopy (SEM Model JEOL JSM-606LV at 20 kV) was used to inspect the cut surface in order to identify the depth of transformation zone. Raman spectroscopy (Renishaw-inVia Raman Microscopy) with Ar-ion laser at a wavelength of 488nm was utilized to identify the phases present in the laser irradiated zone.

3.3 Numerical Modeling

3.3.1 Finite Element Analysis for Determination of Transformation Induced Stress Field

Similar to carbon, boron nitride exits both diamond-like sp^3 bonded phases (cBN and wBN) and graphite-like sp^2 phases (hBN and rBN) and transformation between these phases would happen under high temperature or high pressure conditions [10]. It was reported that the

sp^2-bonded structure occupies much more volume than sp^3-bonded structure [11], therefore transformed material has a tendency to expand the original material. Based on experimental observations of cutting and Raman analysis of cut surfaces, we hypothesize that laser irradiated zone of the pCBN workpiece undergoes a phase transformation during cutting process that results in volume expansion of the transformed region. The volumetric change initiates a tensile stress field in the surrounding material that lead to propagation of crack through thickness direction. The hypothesis of the crack propagation mechanism is schematically represented in Figure 15. A finite element model is developed to investigate the validity of the proposed hypothesis.

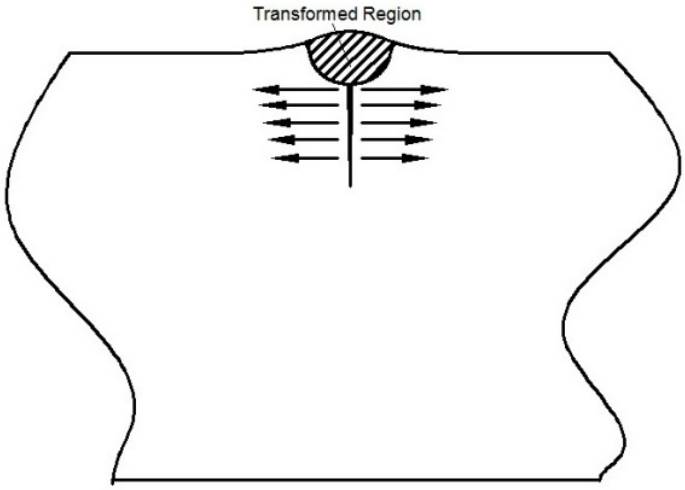

Figure 15: Hypothesis for Crack propagation mechanism.

The pCBN workpiece subjected CO_2-LWJ machining was modeled in finite element analysis package ABAQUS (Simulia, Providence, RI). A transformation zone undergoing uniform expansion was utilized to model the influence of material transformation along the cutting path. Volume of the transformed material will be estimated based on the comparison of predicted surface deformation and experimental measurements. Crossectio of the transformation region was modeled as a semi-ellipse since laser intensity follows a gaussian

distribution. A schematic diagram of the finite element model of the workpiece indicating the transformed zone is presented in Figure 16. Due to the symmetry, only one half of the workpiece was analyzed with fixed boundary condition in horizontal direction on the axis of symmetry. Fixed boundary condition in vertical direction was applied on outer edge to simulate the support of the table. The dimensions of the transformation zone in XZ plane (comparable to laser spot size ~ 0.1mm) are significantly smaller than the length along laser path direction (comparable to sample size ~ cm). Therefore plane strain state can be applied to this model to obtain stress field in XZ plane.

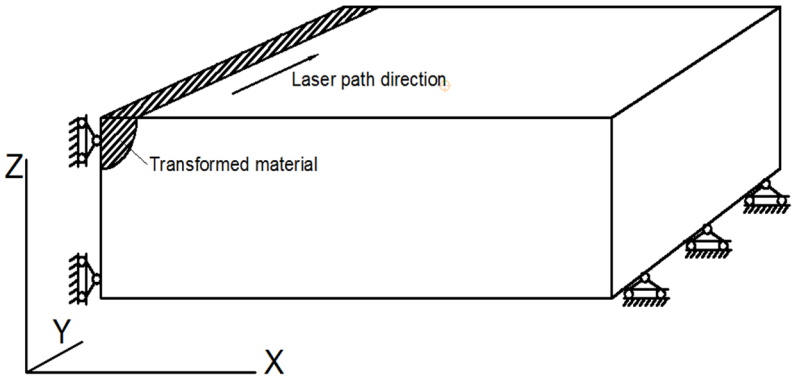

Figure 16: Finite Element model and boundary conditions.

3.4 Results and Discussion

3.4.1 Experimental Results

For the first set of cutting experiments, fracture behavior were studied depend on the line energy (expressed in J/m). Observed fracture characteristics for the PCBN sample are plotted as a function of the line energy in Figure 17 for CO_2-LWJ machining. Three different fracture behaviors at different line energy were discovered. At the highest line energy (23622 J/m), a through cut was observed, indicating that the energy input was above the threshold value of through cutting. At the middle line energy (11811 J/m), a straight groove was found

along the cutting path. Subsequently, the cracked sample could be completely separated with application of hand pressure with clean fracture surface and straight crack line. The energy input at this level was at the threshold of through cutting over the thickness of this sample. At the lowest line energy (5905 J/m), only groove was observed on the sample surface. The grooved sample could not be separated on application of hand pressure after experiments.

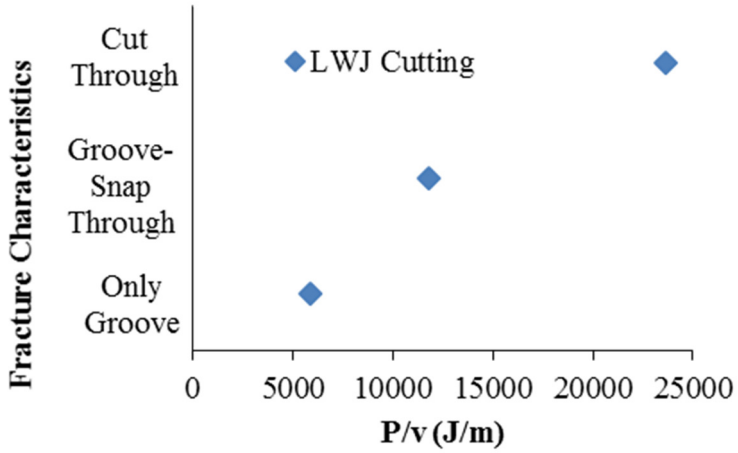

Figure 17: Experimental results of fracture behaviour

SEM image of the through cut cross-section of LWJ machining at line energy of 23622J/m (500 W laser power and at 50 inches/min) is shown in Figure 18(a). Top views of scribing at line energy of 11811 J/m (500 W laser power and at 100 inches/min) before snapping and 5905J/m (500 W laser power and at 200 inches/min) are shown in Figures 18(b) and (c) respectively. In the through-cut case shown in Figure 18(a), two different regions can be clearly observed. The top region near the surface is the transformation zone that undergone phase transformation as well as material evaporation.

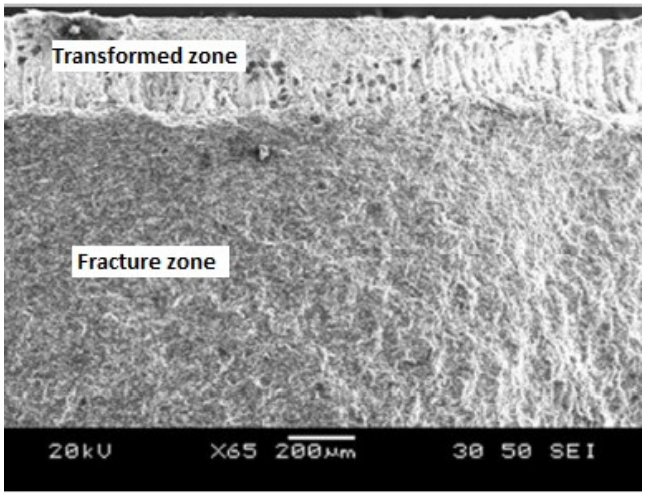

(a)

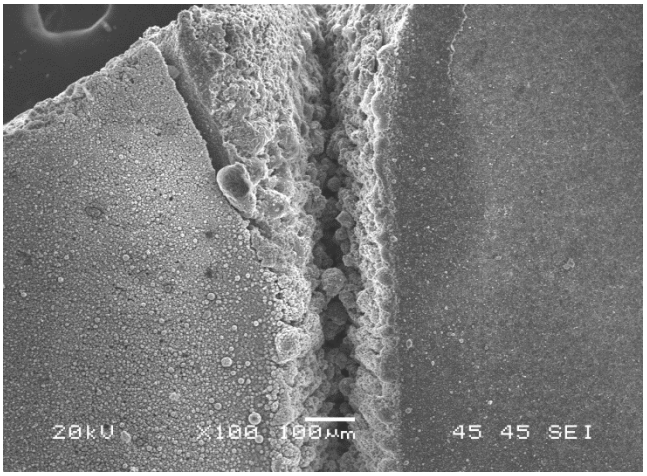

(b)

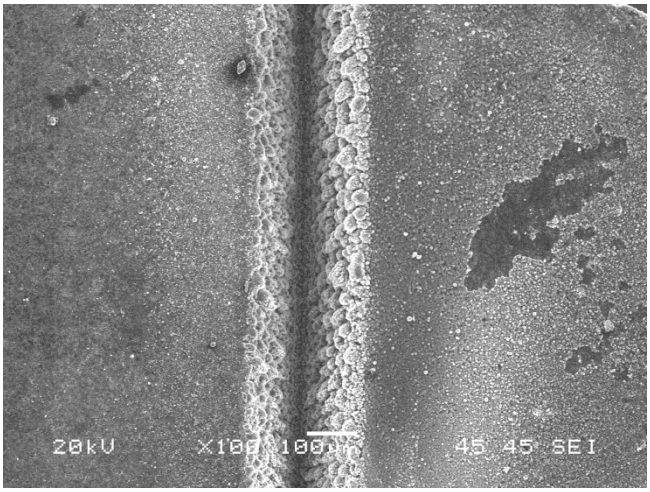

(c)

Figure 18: SEM images of (a) Fracture cross section at line energy of 23622J/m (b) Top view of scribing at line energy of 11811 J/m (c) Top view of scribing at line energy 5905J/m.

The bottom region is the fracture zone resulted from propagation of cracks through the thickness due to transformation strain. As shown in the image, the depth of transformation layer for through cutting is roughly 200 μm. In the scribing cases shown in Figure 18(b) and (c), recast layer along scribing line can be observed. Because of the rapid heat dissipation by water, narrow kerfs was produced and kerfs depth was found to be quite shallow. Furthermore, no visible lateral cracks were generated during LWJ cutting and sputtered particles below the recast layer were very insignificant.

Raman spectroscopy result of both the fracture zone and the transformation zone on the crack cross section is shown in Figure 19. The Raman specrtrum of the as-received material is found to be similar to the fracture zone. On the fracture region, c-BN is the only peak that can be detected reveals that there is no phase transformation happened here. However, on the transformation region, no c-BN peak but two other phases was discovered. The peak of h-BN around 1370 cm^{-1} proved that laser heating and water quenching has transformed PCBN into h-BN. The peak around 1580-1590 cm^{-1} was reported to be a graphite-like sp^2-B-C-N atomic hybridization [12]. In both types of phase transformation, the volume of the original PCBN was expanded that helped in the material separation.

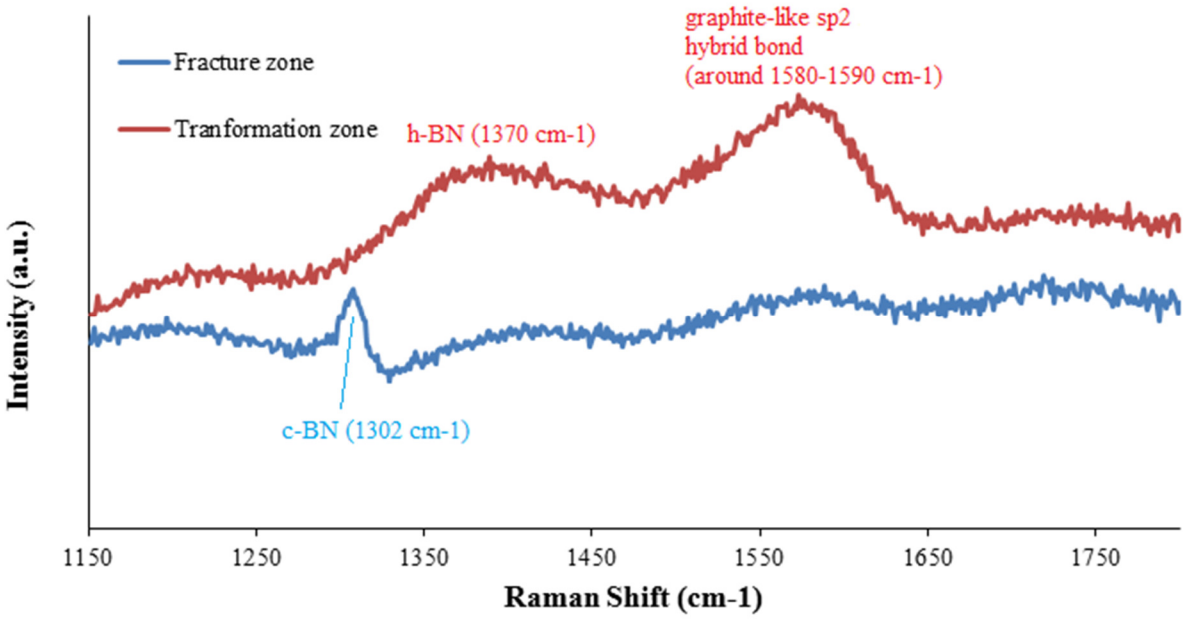

Figure 19: Raman spectrum of transformed zone and fracture zone.

From the structure study and chemical testing of machined sample, our understanding of the cutting mechanism is: (1) The sp^3 bonded c-BN transformed into sp^2-bonded BN phases between 1000 and 1800°C in the heat affected region; (2) These sp^2-bunded phases melted and evaporated at temperature beyond 1000°C; (3) deposition of crystalline h-BN and BN whisker formation occurs resulted in the recast layer [10]. All these reactions mix up with each other and happened instantaneously that lead to the crack propagation under stresses due to phase transformation expansion. This hypothesis is tested using the finite element model.

3.4.2 Validation of Finite Element Model

Due to the accuracy limitation of FEM especially in describing functions with sharp change, we validated FEM solution with the exact solution in an axis-symmetric case of a spherical region of dilatation in a finite elastic plate [13]. For axis-symmetric problem,

Galerkin [14] introduced a stress function φ satisfying $\nabla^4 \varphi=0$ such that displacement components can be written as

$$u_r = -\frac{1}{2G}\frac{\partial^2 \varphi}{\partial r \partial z}, \quad u_z = \frac{1}{2G}[2(1-\nu)\nabla^2 \varphi - \frac{\partial^2 \varphi}{\partial z^2}]$$

And stresses are

$$\sigma_r = \frac{\partial}{\partial z}\left[\nu\nabla^2 \varphi - \frac{\partial^2 \varphi}{\partial r^2}\right],$$

$$\sigma_\theta = \frac{\partial}{\partial z}\left[\nu\nabla^2 \varphi - \frac{1}{r}\frac{\partial \varphi}{\partial r}\right],$$

$$\sigma_z = \frac{\partial}{\partial z}\left[(2-\nu)\nabla^2 \varphi - \frac{\partial^2 \varphi}{\partial z^2}\right],$$

$$\sigma_{r\theta} = \frac{\partial}{\partial z}\left[(1-\nu)\nabla^2 \varphi - \frac{\partial^2 \varphi}{\partial z^2}\right]$$

Where ∇^2 is Laplace operator, G is the shear modulus and ν is the poison ratio.

Yu and Sanday [13] introduced Galerkin stress function and a method of integrating infinite virtual images to solve the boundary value problem of a finite plate with boundary conditions $\sigma(z=0) = \sigma(z=h) = 0$. By substituting φ in the equation with their proper integrated Galerkin stress function, the final stress and displacement field can be obtained. We computed the analytical solution presented by Yu and Sanday [13] for radial stress outside an expanding spherical cavity. In addition, the finite element model was also utilized to compute the stress distribution. Comparison of FEM solution with analytical solution of reduced σ_r along z axis is presented in Figure 20.

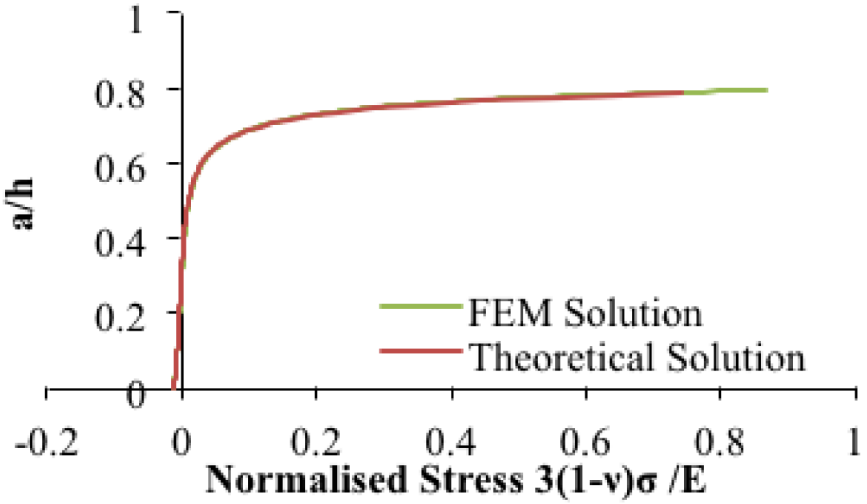

Figure 20: Comparison of FEM with theoretical solution

Mesh of the finite element model was refined till the computed stress became independent of the mesh size. The analytical and numerically computed stress distribution follow each other indicating that the finite element model can accurately determine the stresses induced due to expansion of the transformed zone.

3.4.3 Transformation Strain and Dimensions Measurement Results

In the second set of cutting experiments performed on thicker CBN samples, scribing was found in cuttings with all the parameters. It was observed from the sample side that the depth of the groove with the highest line energy of 37795J/m (800 W laser power and at 50 inches/min) was the deepest while the lowest line energy (9448J/m) produced the shallowest groove. The kerfs widths of the three scribing lines were found to be roughly the same size as the laser spot size (0.2 mm) from profilometer measurement results.

Surface profile of the workpiece was measured along lines normal to cutting path using optical profilometer for the three different line energy values. Measured profiles along

25 different lines were averaged to determine the surface deformation along the z direction. Average surface deformation as function of distance from the laser-cutting path is plotted for the three different line energy values in Figure 21. In order to determine the depth of transformation zone and effective transformation strain, numerical predictions of surface deformation were compared to measurements plotted in Figure 21.

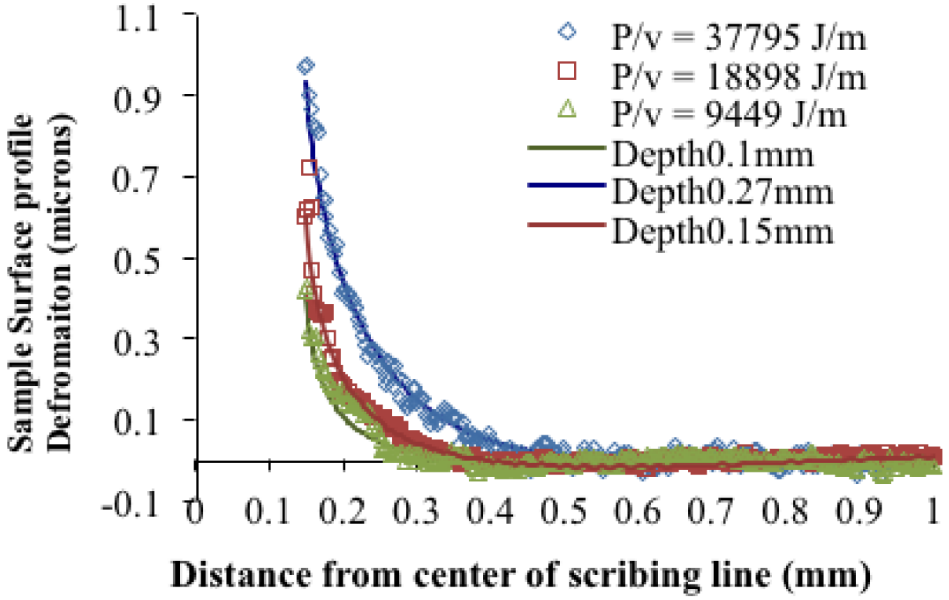

Figure 21: Comparison of measured surface deformation and FEM based prediction.

The surface deformation was predicted assuming that the expansion strain in the transformed zone is constant and is independent of the laser line energy used during cutting. The effect of the line energy was approximated by assuming that the depth of the transformation zone increases with increasing line energy values. Based on the assumption that all material heated above a threshold temperature is transformed, dimensions of the transformed material will be a linear function of heat input. Heat input is proportional to line energy. Hence dimensions of transformation region should be roughly a linear function with

line energy. In addition, transformation width was assumed to be constant due to the fact that the kerfs width was measured same of the three line energy values.

FEM calculations were performed for different values of expansion strain values and various dimensions of transformed zone were compared with the experimental measurement of surface deformation. FEM solutions that best describe the experimental results are shown in Figure 21. These solutions corresponded to expansion stain of 0.006 and transformation zone width of 0.15mm. Depths of transformation zone were 0.27mm, 0.15mm and 0.1mm for line energy values of 37795 J/m, 18898 J/m and 9449 J/m, respectively. The relationship between line energy and depth of transformation zone is plotted in Figure 22. The linear relation between the line energy value and depth of transformation indicates that the depth of transformation for different line energy values may be estimated using the linear relationship.

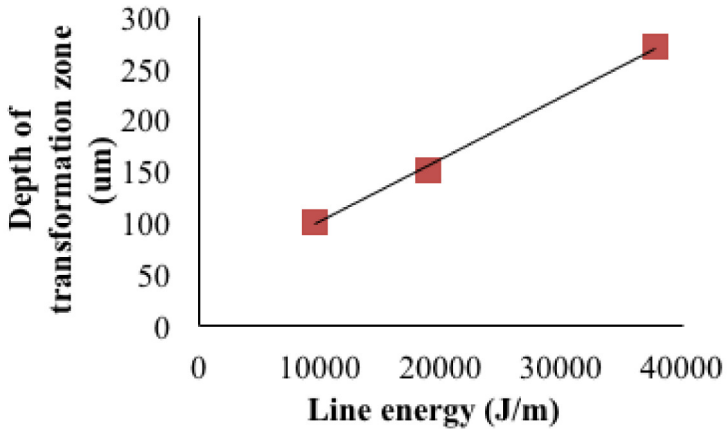

Figure 22: Relationship between line energy with depth of transformation zone

3.4.4 Transformation Stress Results

The linear relationship between line energy values and depth of transformation zone determined in Figure 21 was used to approximate the transformation depth for pCBN specimens of 1.6 mm that were used for first set of cutting experiments. For the line energy

value of 23622J/m, the depth of transformation zone obtained from Figure is 181μm, while the SEM image of the cut surface (see Figure 18(a)) shows that transformed zone thickness is roughly 200 μm. The comparison shows that linear relationship may be used for estimating the transformed zone thickness for other line energy values. The small discrepancy between them may come from inaccurate modeling assumptions. The assumption of constant expansion stain and constant width of transformation zone is probably the main resource for the discrepancy.

Transformation depth of the three cutting line energies in first set of experiment were found to be 75 μm for 5905J/m (500 W laser power and at 200 inches/min), 110 μm for 11811J/m (500 W laser power and at 100 inches/min) and 181 μm for 23622J/m (500 W laser power and at 50 inches/min). Transformation width was still assumed to be 0.15mm due to the observation of similar kerfs width. The transformation zone was assumed to undergo an expansion strain of 0.006 in all the cases and stress distribution in the remaining workpiece was determined using the Finite element model. Computed stress distribution along the mid-plane of the workpiece for different line energy values is plotted in Figure 23. The numerical results indicate that the volume expansion of the transformed zone can lead to significant magnitude of tensile stresses in the workpiece material outside the transformed zone. These tensile stresses lead to propagation of cracks from the transformed zone along the thickness of the workpiece and may result in material separation. The magnitude of the stress increases with line energy values indicating that workpiece will increasingly susceptible to fracture and material separation as the line energy values are increased.

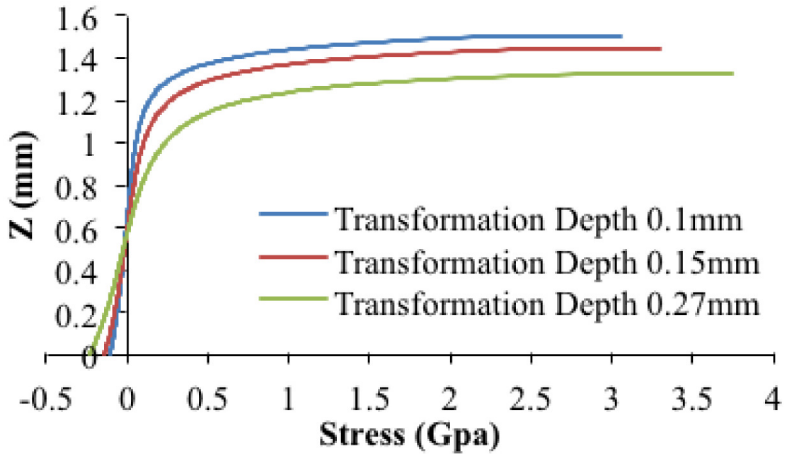

Figure 23: Stress distribution across the thickness for three line energies.

The computed stress distribution may be used to determine the crack driving force for different line energy values. Laser irradiation caused the non-stable phase transformation which lead to crack nucleation and propagate under transformation stress towards both thickness direction and laser moving direction. This phenomenon indicated two kinds of crack configurations: plane strain crack through vertical direction and channeling crack along laser path (schematically represented in Figure 24). At the beginning of a cut, laser beam was irradiated outside the sample, then moved in and created a crack at the edge across the thickness. This crack was a plane strain crack which may be utilized to estimate initial cut depth. As the laser went further, the existing plane strain crack propagated following the laser path which may be considered to be the channeling crack.

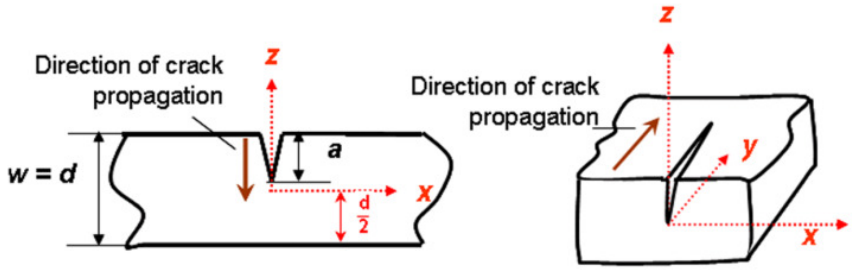

Figure 24: (a): Plain strain cracking (b): Crack channeling

Driving forces (energy release rate) of plane strain crack can then be obtained from stress intensity factors by

$$G(a') = \frac{K_I(a')^2}{E'}$$

The channeling of the edge crack is a three-dimensional problem. In our experiment, material separation along the cutting path due to may be treated as steady-state crack propagation [15]. It is assumed that the crack propagated at a fixed depth and constant tip shape. Then the channeling process that the crack tip advances a unit distance is equal to removing a unit slice far ahead of the crack tip and attaching a unit slice with plane strain crack far behind the crack tip. The difference of energy stored in these two unit slice is the released energy U for crack propagates unit length. Apparently, it is just the released energy of the plane strain crack propagation and can be obtained by integration as

$$U = \int_0^a G(a')\,da'$$

And then, by definition, the energy release rate for the channeling crack is

$$G_{channeling} = \frac{U}{a} = \frac{1}{a}\int_0^a G(a')\,da'$$

The crack driving forces determined on the basis of the computed stress distribution may be compared to the critical energy rates for pCBN to determine the feasibility of crack

propagation. The high magnitude of stresses computed for the volume transformation suggest that computed energy release rates will be sufficient for material separation.

3.5 Conclusion

Cutting experiments are conducted on two different thicknesses of PCBN blank insert to achieve different purposes: study the effect of processing parameters on the fracture behaviors and obtain the size of phase transformed zone as well as associated expansion strain after laser heating. Three different fracture behavior observed from the first type of experiment indicate the threshold line energy for through cutting. Chemical testing results indicate that laser heated PCBN undergoes chemical phase transformation and material separation takes place due to propagation of cracks along the machining path. Based on the experimental observations and material properties, material separation is hypothesized to occur through crack propagation under the stress fields imposed due to the volumetric expansion associated with transformation of c-BN to h-BN and other sp^2 phases. Measurement of transformation strain and dimensions of transformation region reveals a linear relationship between cutting line energy and size of transformation zone. Transformation stress based on the experimental result of expansion strain and transformation volume was obtained from FEM calculation. Future work is currently focused on calculating energy release rate in order to demonstrate the feasibility of proposed mechanism of material separation through controlled crack propagation.

3.6 References

[1] Wentorf, R.H., Synthesis of Cubic Form of Boron Nitride. Journal of Chemical Physics, 1961. 34(3): p. 809-&.

[2] Mirkarimi, P.B., K.F. McCarty, and D.L. Medlin, Review of advances in cubic boron nitride film synthesis. Materials Science & Engineering R-Reports, 1997. 21(2): p. 47-100.

[3] Ding, X., W.Y.H. Liew, and X.D. Liu, Evaluation of machining performance of MMC with PCBN and PCD tools. Wear, 2005. 259(7-12): p. 1225-1234.

[4] Hidai, H. and H. Tokura, Hydrothermal-reaction-assisted laser machining of cubic boron nitride. Journal of the American Ceramic Society, 2006. 89(5): p. 1621-1623.

[5] Sibailly, O.D., F.R. Wagner, L. Mayor, and B. Richerzhagen. High precision laser processing of sensitive materials by Microjet. in Fourth International Symposium on Laser Precision Microfabrication. 2003. SPIE.

[6] Kalyanasundaram, D., G. Shehata, C. Neumann, P. Shrotriya, and P. Molian, Design and validation of a hybrid laser/water-jet machining system for brittle materials. Journal of Laser Applications, 2008. 20(2): p. 127-134.

[7] Kalyanasundaram, D., P. Shrotriya, and P. Molian, Obtaining a relationship between Process parameters and Fracture energy for CO2 Laser/Waterjet Machining of Ceramics. Journal of Engineering Materials and Technology, 2009. 131(1): p. 011005-10.

[8] Barnes, C., P. Shrotriya, and P. Molian, Water-assisted laser thermal shock machining of alumina. International Journal of Machine Tools & Manufacture, 2007. 47(12-13): p. 1864-1874.

[9] Kalyana-sundaram, D., J. Wille, P. Shrotriya, and P. Molian. CO2 Laser/Waterjet machining of Polycrystalline Cubic Boron Nitride. Transactions of the North American Manufacturing Research Institute 2008 May 20-23 [cited 36; 517-524].

[10] Sachdev, H., R. Haubner, H. Noth, and B. Lux, Investigation of the cBN/h-BN phase transformation at normal pressure. Diamond and Related Materials, 1997. 6(2-4): p. 286-292.

[11] Robertson, J., Diamond-like amorphous carbon. Materials Science & Engineering R-Reports, 2002. 37(4-6): p. 129-281.

[12] Mannan, M.A., H. Noguchi, T. Kida, M. Nagano, N. Hirao, and Y. Baba, Growth and characterization of stoichiometric BCN films on highly oriented pyrolytic graphite by radiofrequency plasma enhanced chemical vapor deposition. Thin Solid Films, 2010. 518(15): p. 4163-4169.

[13] Yu, H.Y. and S.C. Sanday, Center of Dilatation and Thermal-Stresses in an Elastic Plate. Proceedings of the Royal Society of London Series a-Mathematical Physical and Engineering Sciences, 1992. 438(1902): p. 103-112.

[14] Galerkin, B., Contribution to the general solution to the problem of the elasticity theory in the case of three dimensions. Comptes Rendus Hebdomadaires Des Seances De L Academie Des Sciences, 1930. 190: p. 1047-1048.

[15] Ho, S. and Z. Suo, Tunneling Cracks in Constrained Layers. Journal of Applied Mechanics-Transactions of the Asme, 1993. 60(4): p. 890-894.

CHAPTER 4: HYBRID CO_2 LASER/WATERJET (CO_2-LWJ) CUTTING OF POLYCRYSTALLINE CUBIC BORON NITRIDE (PCBN) BLANKS WITH PHASE TRANSFORMATION INDUCED FRACTURE

A paper published in *the journal of Optics & Laser Technology*, Volume 70, P. 39-44 (2015)

Zhuoru Wu[9,10], Ammar A. Melaibari[1,11,12], Pal Molian[4],[13] and Pranav Shrotriya[1,4]

Abstract

The present paper investigates a transformation induced fracture mechanism for the cutting of Polycrystalline Cubic Boron Nitride (PCBN) sample by a hybrid CO_2 laser/waterjet (CO_2-LWJ) manufacturing process. In CO_2-LWJ machining, a laser was used for local heating followed by waterjet quenching leading to fracture propagation along the sample surface. Cutting results indicate that as line energy of the laser was increased the sample response transitioned from scribing to through cutting. Raman spectroscopy analysis of the cut surface indicates that laser heated PCBN undergoes chemical phase transformation from sp^3-bonded cubic Boron Nitride (cBN) into hexagonal Boron Nitride (hBN) and other sp^2-bonded phases. The sp^2-bonded structure occupies more volume than sp^3-bonded structure such that the transformed material has a tendency to expand the original material and leads to surface deformation around the cutting path. Surface profile of the cut samples were experimentally

[9] Laboratory for Lasers, MEMS and Nanotechnology, Dept. of Mechanical Engineering, Iowa State University, Ames, IA 50011, USA
[10] Primary researcher and lead author
[11] Dept. of Mechanical Engineering, King AbdulAziz University, Jeddah, Saudi Arabia
[12] Co-author
[13] Dept. of Mechanical and Manufacturing Engineering, St. Cloud State University, St. Cloud, MN 56301, USA

measured using profilometry and compared with numerical predictions in order to estimate the expansion strain and dimensions of transformation region. Based on the obtained expansion strain and transformation zone, stress fields and crack driving forces were computed for channeling cracks that result in material separation. Comparison of the crack driving forces with fracture toughness of PCBN shows that transformation induced crack propagation is the feasible mechanism for cutting during CO_2-LWJ machining.

Keywords: CO_2 laser/waterjet machining (CO_2-LWJ), cubic boron nitride, controlled crack propagation

4.1. Introduction

Cubic Boron Nitride (CBN) is the second hardest material on earth, inferior only to diamond. It is not found in nature but can be synthesized by application of high temperature and pressure [1]. Polycrystalline cubic boron nitride (PCBN) blank are produced through sintering of CBN powders with ceramic matrix such as titanium nitride (TiN) or aluminum nitride (AlN). Since its discovery, PCBN has been used in industry as a substitute for diamond due to the superior thermal and chemical stability. The advantages that PCBN does not react with ferrous metals and has a high resistance to oxidation[2] make it ideal tool material for machining hard cast iron, high chrome alloy steels, high-strength nickel super alloys, powder metal alloys and metal matrix composites [3].

CBN Tool inserts are traditionally cut from the compact blanks by either diamond sawing or electric discharge machining (EDM) or Nd:YAG laser cutting and finished by diamond grinding, lapping, and polishing. However, traditional manufacturing methods for

producing tool inserts are slow and cost-inefficient due to the extreme hardness of PCBN materials. Given the limitations of conventional material removal mechanisms, a number of recent reports have focused on non-conventional mechanisms for machining of PCBN. Hidai and Tokura [4] investigated the hydrothermal-reaction assisted laser drilling of PCBN in steam environment based on measurements of mass loss at high temperatures. Swiss Federal Institute of Technology in Lausanne, Switzerland has developed Laser-Microjet® [5], a hybrid technology based on waterjet-guided Nd:YAG laser for machining of PCBN. The Laser-Microjet® allows precise cutting of PCBN materials with smaller kerf and better surface finish but the process suffers from very slow cutting speeds as it reports 70 passes with each pass at a speed of 7 mm/min to cut 3.25 mm thick PCBN sample.

Crack propagation provides an energy and cost efficient method for cutting of ceramics because hardness and brittleness of ceramics lead to low material removal rates and slow cutting speeds during conventional machining processes. In low thermal conductivity ceramics such as alumina thermal shock induced fracture has been successfully utilized for energy efficient cutting [6,7]. However in high thermal conductivity ceramics such as polycrystalline cubic boron nitride (PCBN), thermal shock may not be feasible. In this paper, we investigate fracture based material separation of PCBN due to synergistic interactions between laser heating and subsequent waterjet quenching. Cut surfaces were analyzed to identify chemical and phase changes of the PCBN due to LWJ machining. Height profiles of the machined PCBN samples were measured to determine the phase transformation induced deformation. Finite element analysis was used to estimate the stress fields associated with the deformation and predict the crack driving forces for channeling cracks that result in material separation in order to determine the mechanism governing material separation.

4.2. Experimental Procedure

A continuous wave CO2 Laser (Model 820 Spectra Physics) of 10.6 µm wavelength and 1.5 kW rated power was used for all the cutting experiments. The laser head has been modified to accommodate the low-pressure waterjet (< 8 MPa (1000 Psi)) to realize CO2-LWJ machining. The modified laser head of the CO2-LWJ system is shown in Figure 25 and details of its design have been previously reported [6-8]. The laser head that incorporates the waterjet ensures that the workpiece is first irradiated with a CO2 laser beam for localized heating and subsequently, the heated spot is rapidly quenched with the trailing waterjet.

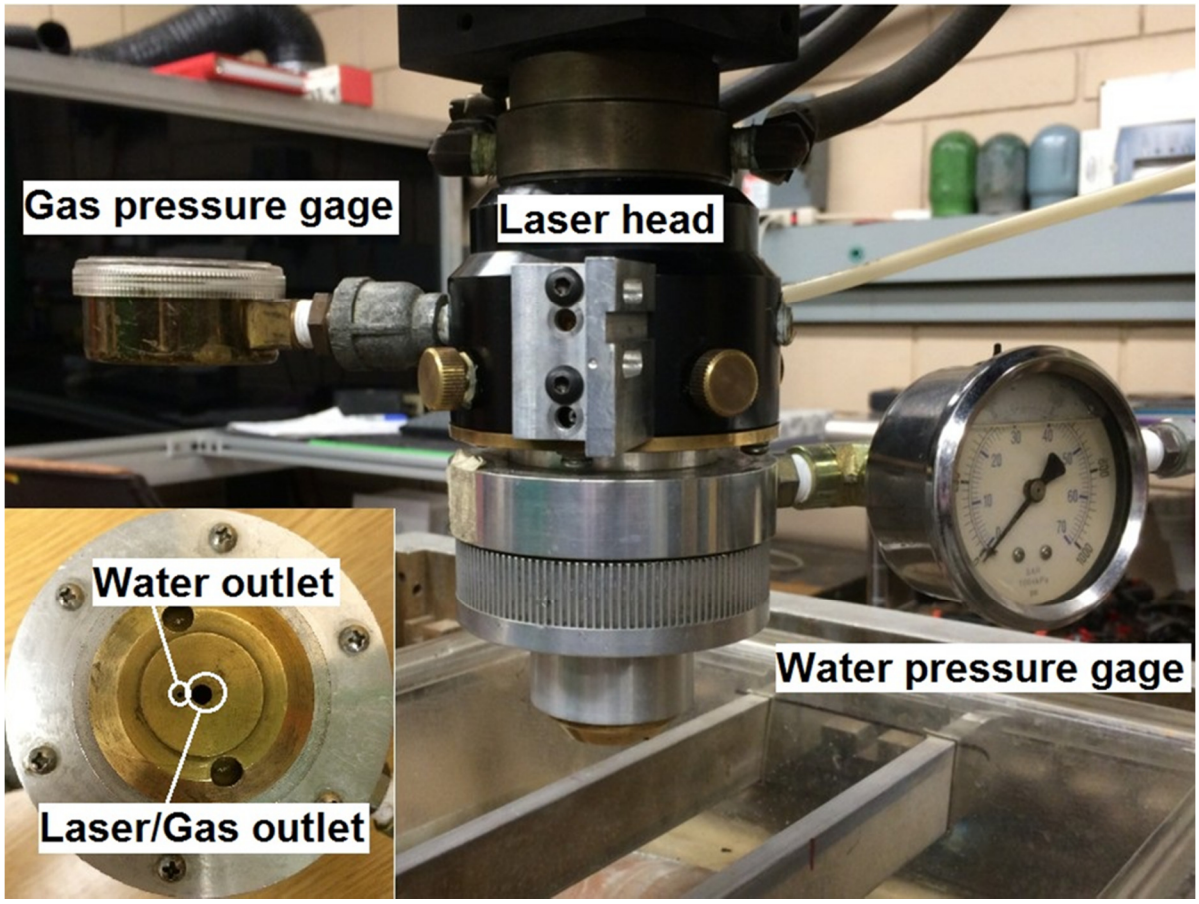

Figure 25: Experiment setup of CO_2-LWJ machining system

Two different sets of experiments were carried out on the commercial Polycrystalline Cubic Boron Nitride (PCBN) tool samples (Diamond Innovations, Inc. (Worthington, Ohio)) that have a composition of 82% CBN (average particle size of 15 μm). The first set was conducted to determine the effect of the laser line energy (ratio of laser power to cutting velocity) on fracture characteristics of PCBN samples; and the second set of experiments was conducted to characterize the surface deformation of samples associated with Laser/waterjet machining.

Triangular PCBN inserts (BZN 7000 series) with dimensions of 7 mm side length and 1.6 mm thickness were used for the first set of experiments. The inserts had a surface roughness (Ra) of 0.3 μm on the polished faces and 3 μm on the side. Single-pass straight-line cutting experiments were carried out at the same laser power (P) of 500W but with three different cutting speeds (v) of 21.2 (50), 42.4 (100) and 63.5 (200) mm/sec (in/min) in order to investigate PCBN machining at line energies (P/v) of 23.6, 11.8, and 5.9 J/mm, respectively.

The second set of experiments was carried out on thick PCBN circular blanks (50 mm in diameter and 4.8mm in thickness) with same composition as the triangular inserts. Single-pass straight cutting experiments were carried out at a fixed laser power (P) of 800W with different cutting speeds to achieve line energies from 5.9 to 37.8 J/mm. The reason for using thick specimens was to ensure that samples does not undergo material separation and thus enable characterization of the surface deformation over the similar range of line energies as the first set of experiments.

In all the experiments, laser beam was focused on the sample surface to a spot size of 0.2 mm using a 127mm (5 in.) focal length lens. Pressure of water-jet was maintained at 5.5 MPa (800 psi) to apply rapid quenching on the heated region. Assist gas flow at a pressure of

69 kPa (10 psi) surrounding the laser beam was maintained during experiments to protect the lens from damage due to spatter. Payne et al. [9] have reported that water has very high absorption for CO_2 laser energy and therefore , the laser/water-jet was designed such that the water-jet trailed the laser beam with a spacing of approximately 2 mm in order to minimize absorption of laser power by direct contact with water.

Machined surfaces of the PCBN specimens were imaged by JEOL JSM-606LV Scanning Electron Microscope (SEM) at an acceleration voltage of 20 kV. Raman spectroscopy (Renishaw InVia Raman Microscope) with Ar-ion laser at a wavelength of 488nm was utilized to determine the PCBN phases in different regions of the transverse surfaces and the as-received samples. For the scribed thicker samples in the second set of experiment, surface profiles around each scribing line were measured using optical profilometer (Zygo NewView 7100) to characterize the surface deformation.

4.3. Numerical Modeling

4.3.1. Finite Element Analysis for Determination of the Transformation Induced Surface Deformation

Boron nitride exits both in diamond-like sp3-bonded phases – cubic (cBN) or wurtzite (wBN) phases -- and graphite-like sp^2 phases – hexagonal (hBN). The transformation between these phases may take place under high temperature or high pressure conditions [10] and is associated with volumetric changes [11]. During the cutting experiments, the laser irradiated sample surface may undergo a phase transformation from sp^3 to sp^2 bonded phases and induce volumetric expansion that may lead to deformation and development of stress field in the

surrounding material. Finite element analysis was utilized to predict the stress fields and surface deformation of the sample due to the expansion of the transformed material.

The PCBN workpiece was modeled in finite element analysis package ABAQUS (Simulia, Providence, RI). A transformation zone undergoing uniform expansion was utilized to model the influence of material transformation along the cutting path. Material properties of hBN were assigned to the transformation zone while material outside was modeled as PCBN. Cross-section of the transformation region was modeled as a semi-ellipse since laser intensity follows a Gaussian distribution. A schematic diagram of the workpiece indicating the transformed zone and cutting path is presented in Figure 26(a). The dimensions of the transformation zone in XZ plane (comparable to laser spot size ~ 0.1mm) are significantly smaller than the length along laser path (comparable to sample size ~ cm). Therefore plane strain state was applied to this model as shown in Figure 26(b) to obtain stress field in XZ plane. Given the symmetry of the sample, one half of the workpiece was analyzed with zero displacement in x direction (U_x=0) along the axis of symmetry. On outer edge of model, zero displacement in z direction (U_z=0) was applied to simulate the support of table during cutting. Mesh was refined to ensure that numerical results are independent of element size. Final refined mesh was composed of about 15000 quadratic elements with 8 nodes. Finally, the numerical predictions of surface deformation were compared to experimental measurements in order to estimate the transformation strain and dimensions of the transformed zone corresponding to the different line energies used in the CO_2-LWJ cutting.

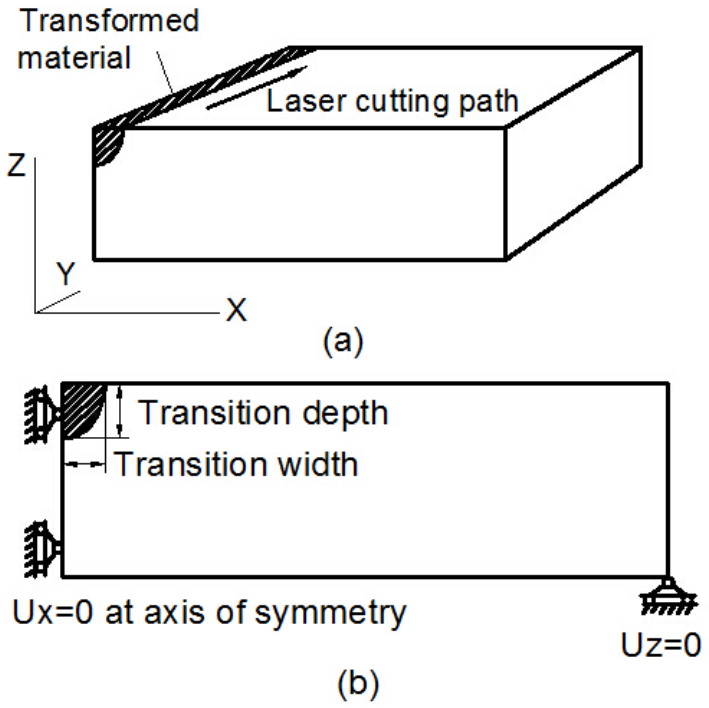

Figure 26: (a) Schematic diagram of the workpiece machined by LWJ beam (b) Plane strain finite element model and boundary conditions for predicting sample deformation

4.3.2. Fracture Mechanics Analysis of Crack

Energy release rates for two different crack configurations – a plane strain crack along the thickness of the sample and channeling cracks along laser path, schematically shown in Figure 27 (a) and (b), respectively – were determined using the finite element analysis. The path independent J-integral [12-14] was computed to determine the energy release rate to characterize the crack propagation. Due to the extremely brittle nature of PCBN, the material response can be regarded as linear elastic such that J-integral equals energy release rate. Figure 28 shown the plane strain finite element model used to determine the J-integral values. The transformation zone size and expansion strain estimated from the deformation model were utilized to determine the energy release rate for crack propagation at different line energies. J-integral values were calculated for 10 contour layers around crack tip and achieved path-

independence at out layers of elements. Energy release rates for plain strain cracks as a function of depths was obtained by modeling cracks of different depths starting below the transformation zone to the rest of whole thickness.

Material separation along the cutting path can be treated as steady-state propagation of a channeling crack. Following Ho and Suo [15], energy release rate of channeling crack propagating with a constant tip shape at fixed depth (indicated by the shaded area in Fig 3(b)) was computed from the difference of energy stored in the configurations before and after crack advance. Consequently, the energy release rate for channeling cracks, $G_{\text{channeling}}$, for crack depth, a, was computed by integrating and averaging plain strain energy release rates, G_{plain}, over the crack depth:

$$G_{\text{channeling}} = \frac{1}{\text{a}} \int_0^{\text{a}} G_{\text{plain}}(\text{a}')\, \text{da}' \qquad (1).$$

The channeling energy release rates were compared to the fracture toughness of PCBN to determine the feasibility of crack propagation along the cutting path due to CO_2-LWJ induced transformation.

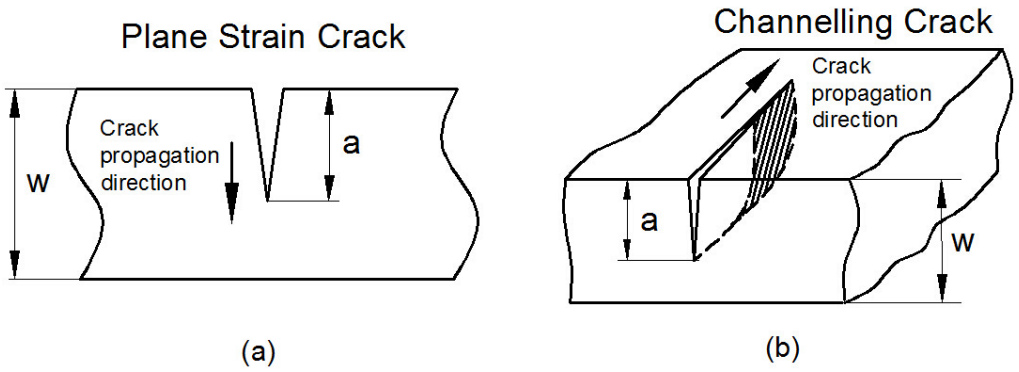

Figure 27: Crack configurations: (a) Plain strain crack (b) Crack channeling

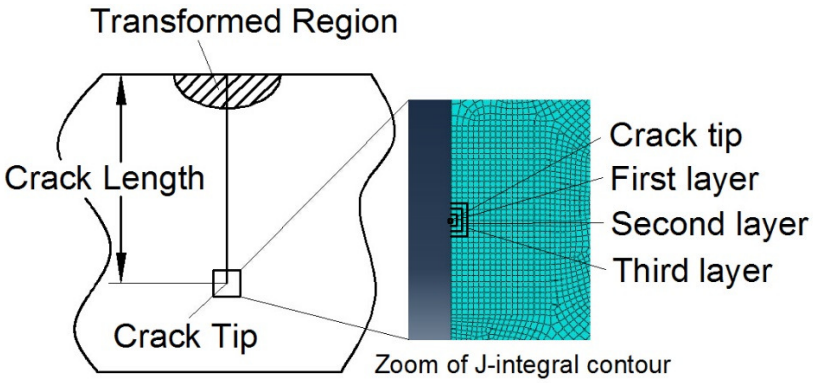

Figure 28: Finite element model and crack tip mesh configuration for calculating energy release rate

4.4. Results and Discussion

4.4.1. Experimental Results

For the first set of cutting experiments, observed fracture characteristics of the PCBN samples are summarized in Table 5. At the highest line energy (23.6J/mm), PCBN samples were separated with a through cut, indicating that the energy input was above the threshold value for through cutting. At the middle line energy (11.8J/mm), a straight groove was found along the cutting path. Subsequently, the cracked samples could be snapped by hand pressure with clean fracture surface and straight crack interface. The energy input at this level was at the threshold of through cutting over the thickness. At the lowest line energy (5.9J/mm), only groove was observed on the sample surface. The grooved sample could not be separated on application of hand pressure after experiments.

Table 5: Experimental cutting results of fracture behaviours at different line energies

Line energy (J/mm)	5.9	11.8	23.6
Fracture characteristics	Groove only	Deep groove snapped by hand pressure	Cut through

The scribed sample was cut at line energy of 5.9 J/mm and the SEM image of the sample top surface is shown in Figure 29(a). Because of the rapid heat dissipation by water, narrow kerfs were produced and kerfs depth was found to be quite shallow. Recast layer inside the groove can be observed. No visible lateral cracks were generated during LWJ cutting and sputtered particles around the groove were insignificant. The transverse cross-section of the sample cut at line energy of 23.6 J/mm is shown in Figure 29(b). As shown in Figure 29(b), the cross-section of through-cut sample is divided into two different zones with different surface morphologies. Raman spectroscopy results of the two different zones are shown in Figure 30. The Raman spectrum of the top zone shows no cBN peak but two other peaks corresponding to different BN phases. The peak around 1370 cm^{-1} corresponds to hBN phases [16] while the peak around 1580-1590 cm^{-1} is reported to be a graphite-like sp^2 B-C-N phases [17]. While the Raman spectrum of the lower zone away from laser irradiated surface was found to be similar to the as-received material with a peak at 1302 cm^{-1} [18] corresponding to cBN phases. The SEM and Raman spectroscopy results showed that the top region near surface has undergone phase transformation as well as material ablation. This zone is labeled as the transformation zone in the SEM image in Figure 29(b). While the bottom region has the same composition with the original material is labeled as the fracture zone.

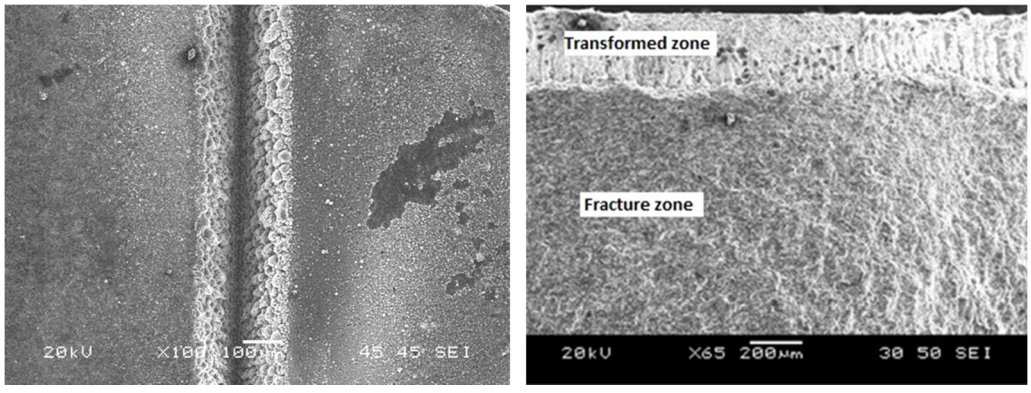

Figure 29: SEM images of (a) Top view of scribed sample at line energy of 5.9kJ/m. (b) Fracture cross-section at line energy of 23.6kJ/m

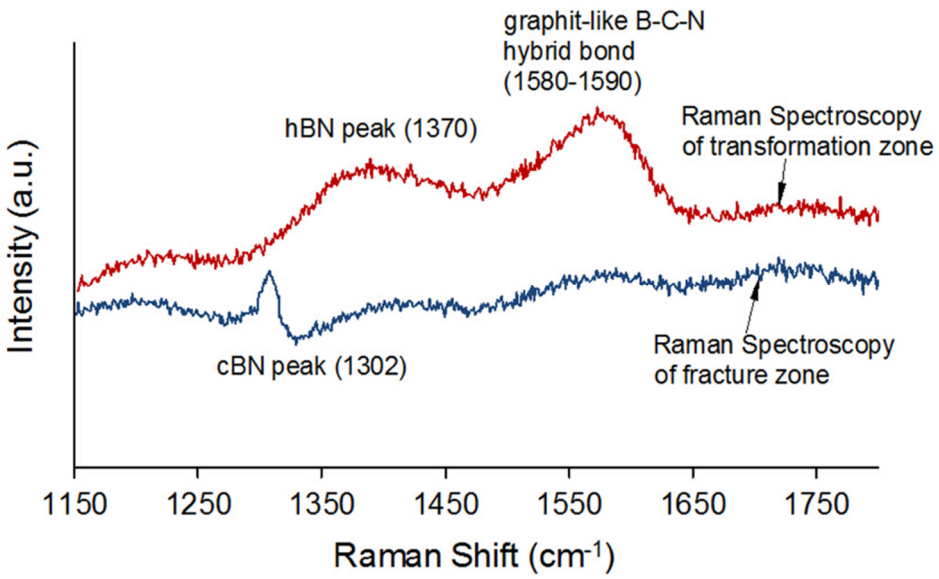

Figure 30: Raman spectrum of transformed zone and fracture zone

4.4.2. Surface Deformation

In the second set of cutting experiments performed on the thicker cBN samples, only scribing was observed for all the three cutting parameters. Surface profile of the specimens adjacent to the kerf of each scribed cut were measured using optical profilometry and height distribution perpendicular to the scribed cut was averaged to determine the representative surface deformation. The surface profiles were found to be nearly symmetric about the cut center and averaged value of the two sides are plotted in Figure 31 along with error bars for the three line energies. The error bars are equal to one standard deviation of the measured height values and represent the variations in the surface profile along the cut direction. The kerf widths of the three scribing lines were found to be roughly the same as the laser beam diameter of 0.2 mm. For all three line energies, surface deformation is highest near the kerf and decays monotonically with distance from the scribed cut. The magnitude of surface deformation is dependent on line energy and is found to increase as the line energies are increased.

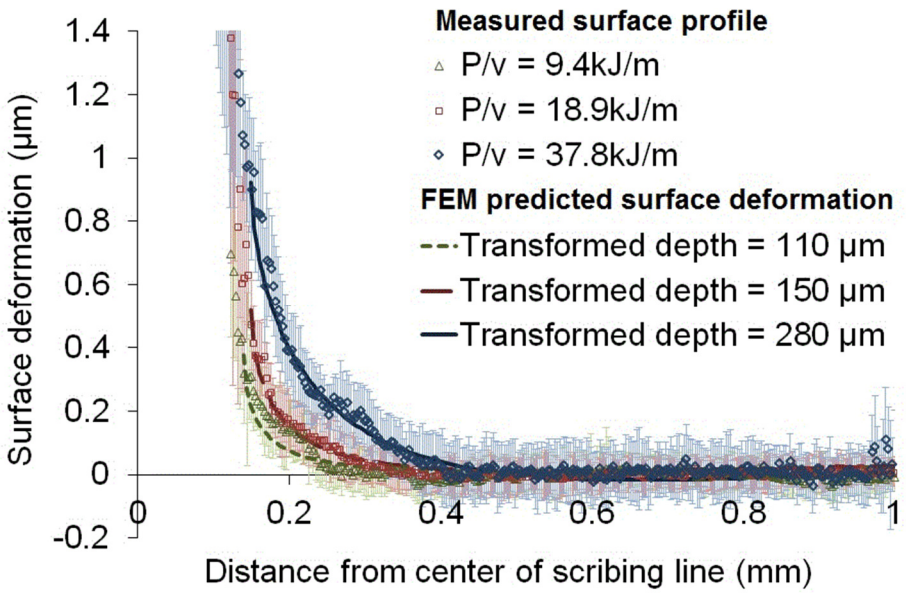

Figure 31: Comparison of measured surface deformation with FEM model prediction. Measured surface profile including error bars of first standard deviation were presented in the data

4.4.3. Numerical Modeling of Laser Cutting Induced Phase Transformation

The experimental observations suggest that the material separation during the cutting experiments is through a "score and snap" mechanism: (1) laser irradiation led to scribing as well as heating and transformation of the material from sp3-bonded cBN to sp^2-bonded BN phases in the transformation zone along the cutting path [10]; (2) the constrained volumetric expansion of the material in transformation resulted in deformation and development of stress field in the material surrounding the transformation zone; (3) The transformation induced stress fields lead to propagation of cracks formed during scribing that result in the material separation. In order to validate the "score and snap" mechanism, numerical modeling is utilized to determine if the scribed initial cracks can propagate through the thickness under transformation induced stress field. The numerical modelling is performed in two steps: firstly, FEA deformation models are used to predict the surface deformation of thick specimens. The

numerical predictions are compared to experimentally measurements to estimate the transformation zone size and expansion strains as a function of line energy. In the second step, the estimated transformation zone size and expansion strains are utilized in the FEA fracture models of thin specimen with different crack depths to determine the energy release rates as a function of crack depth. Finally, the computed energy release rates are compared to the fracture toughness of PCBN in order to determine the propensity of crack propagation under different line energies.

Numerical predictions of surface deformation that best describe the measured surface deformation are also plotted as smooth lines in Figure 31. The numerical results for all the laser line energies corresponded to a constant expansion strain of 1.3% and transformation zone width of 0.15mm. The width of transformation zone was assumed to be constant based on the observation of similar kerf widths for all the line energies. Depths of transformation zone depend on laser line energy and were found to follow a linear relationship that is plotted in Figure 32.

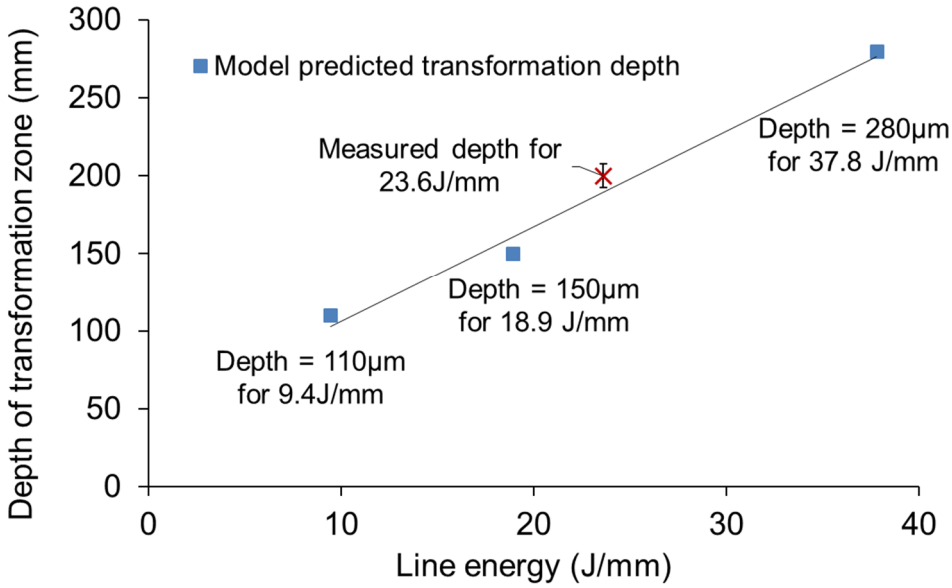

Figure 32: Relationship between line energy and depth of transformation zone

The linear relationship between line energy values and depth of transformation zone can also be used to approximate the transformation depth for PCBN specimens of 1.6 mm that were used in the first set of cutting experiments. On the through-cut specimen cut with line energy of 23.6J/mm, depth of transformed zone measured from transverse SEM image (see Figure 29(b)) is plotted in Figure 32.

Two different numerical predictions of the finite element model - surface deformation and transformation depth - were compared to experimental results from two independent sets of experiments. Good agreement between the measured and predicted response in both cases indicates that numerical model can describe the transformation induced deformation and consequently relate the LWJ cutting parameters (line energy) to the size of the transformation depth and expansion strain. The small discrepancy between them may come from inaccurate modeling assumptions. The assumption of constant expansion stain and constant width of transformation zone is probably the main source for the discrepancy.

4.4.4. Energy Release Rates for Channeling Cracks

In the first set of experiments, laser radiation is initially incident over the specimen boundary resulting in damage across the whole thickness and therefore, equilibrium depth of a channeling crack is most appropriate for approximating the CO_2-LWJ induced cut depth in the specimens. In order to compute the energy release rates for channeling cracks, FEA fracture model shown in Figure 28 was first utilized to predict the plane strain energy release rate of the PCBN specimen. In this model, the transformation zone depth was estimated using the linear relationship obtained in Figure 32 for each line energy. The transformation zone width and expansion strain were kept 0.15 mm and 1.3% as found from the deformation model.

Finally, the computed energy release rates for plain strain cracks were used in equation (1) to determine the energy release rates for channeling cracks as a function of the crack depth.

The energy release rates corresponding to the three line energies used in cutting experiments are plotted as function of channeling crack depth in Figure 33. Energy release rates reach the highest for cracks that are approximately twice the depth of the initial crack due to the large tensile stresses outside the transformation region induced from material expansion. Critical energy release rates ($G_{critical}$) range based on reported fracture toughness of BZN7000 as 7.7-10 MPa$\sqrt{m}$ [19] was also plotted in Figure 33 in order to explain the fracture characteristics observed in the cutting experiments. Channeling energy release rates for all crack depths corresponding to line energy of 5.9J/mm are lower than the critical range suggesting that under this processing condition laser irradiation induced damage results in scribing of samples and the transformation induced stress field is not sufficient to propagate the channeling cracks. Channeling energy release rates corresponding to cutting line energy of 11.8J/mm lies right between the critical range, indicating that this processing condition is threshold for transition between scribing cuts to through the thickness cuts. Channeling energy release rates at all crack depths for the highest cutting line energy of 23.6J/mm is higher than $G_{critical}$ suggesting that cracks are expected to propagate along the laser path through the whole thickness. The numerical prediction based on comparison between computed energy release rates with $G_{critical}$ agrees well with fracture characteristics observed in the cutting experiments.

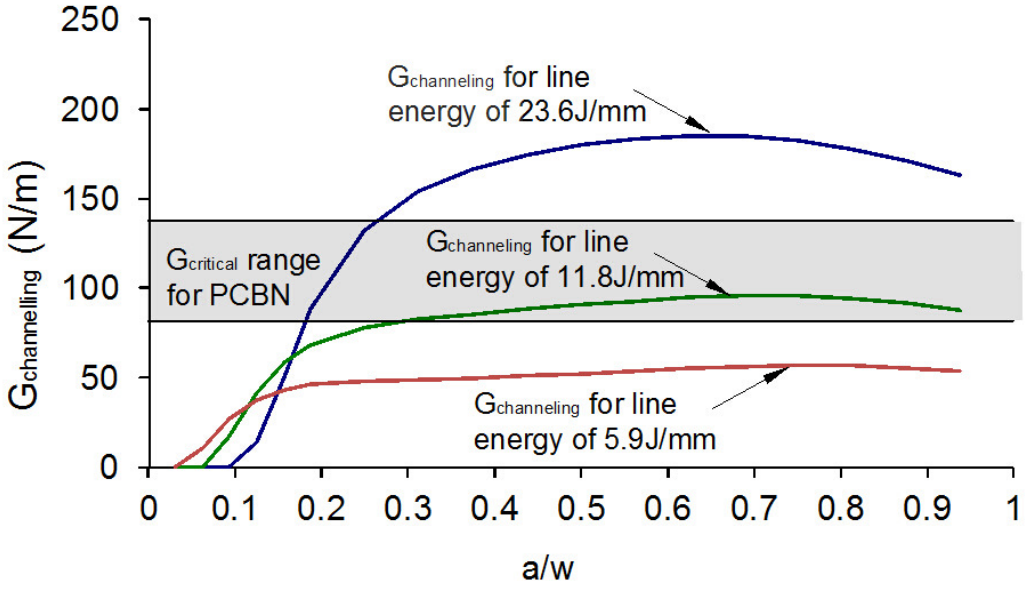

Figure 33: Energy release rate for channeling crack

Results of numerical modeling based on "score and snap" cutting mechanism for material separation are able to describe the experimentally observed transition from scribing to through-cut of PCBN specimens. Our assumptions of uniform expansion strain associated with PCBN transformation and shape of transformation zones are simplistic but can adequately describe the mechanism governing material separation. The numerical model may be used to determine the line energy values required for scribing and through cutting of PCBN specimen with different thicknesses and different geometries.

4.5. Conclusions

The hybrid CO_2-LWJ machining system is used for cutting experiments on two different thicknesses of PCBN blank samples in order to study the effect of processing parameters on the fracture behaviors and to estimate the size of phase transformed zone as well as associated expansion strain. Three different fracture behaviors were observed in cutting

experiments on thinner PCBN blanks indicating a transition from scribing to through-cut at threshold value of laser line energy. Surface analyses of the cut samples indicate that laser-heated PCBN undergoes phase transformation. Based on the experimental observations, a "score and snap" cutting mechanism is proposed for material separation. Laser irradiation of the sample surface leads to scoring and phase transformation of the PCBN from sp^3 to sp^2 hybridized BN phases along the cutting direction. Constrained volumetric expansion of transformed material leads to development of tensile stresses in the surrounding material and propagation of laser-scored cracks along the thickness. Finite element modeling of the transformation induced surface deformation and energy release rates for cracks is utilized to validate the "score and snap" mechanism for PCBN cutting. Numerical modeling of the transformation induced surface deformation indicates that transformation zone depth increases linearly with laser line energy used for cutting and volumetric changes associated with transformation may be modeled using an uniform volumetric expansion strain. Comparison of the computed energy release rate for channeling cracks with reported values of PCBN fracture toughness indicate that "score and snap" cutting mechanism describes the experimental observations. These results suggest that controlled crack propagation is an efficient mechanism for separation of PCBN materials.

4.6. Acknowledgements

The authors would like to gratefully acknowledge the financial support provided by the US National Science Foundation under the grant CMMI -1000035. The authors would also like to thank Diamond Innovations, Inc. (Worthington, OH) for providing the Polycrystalline Cubic Boron Nitride samples.

4.7. References

[1] Wentorf RH. Synthesis of Cubic Form of Boron Nitride. J Chem Phys. 1961;34:809-&.

[2] Mirkarimi PB, McCarty KF, Medlin DL. Review of advances in cubic boron nitride film ynthesis. Mat Sci Eng R. 1997;21:47-100.

[3] White CC, VanLandingham MR, Drzal PL, Chang NK, Chang SH. Viscoelastic characterization of polymers using instrumented indentation. II. Dynamic testing. Journal of Polymer Science Part B: Polymer Physics. 2005;43:1812-24.

[4] Hidai H, Tokura H. Hydrothermal-reaction-assisted laser machining of cubic boron nitride. Journal of the American Ceramic Society. 2006;89:1621-3.

[5] Sibailly OD, Wagner FR, Mayor L, Richerzhagen B. High precision laser processing of sensitive materials by Microjet. Fourth International Symposium on Laser Precision Microfabrication. 1 ed: SPIE; 2003. p. 501-4.

[6] Kalyanasundaram D, Shehata G, Neumann C, Shrotriya P, Molian P. Design and validation of a hybrid laser/water-jet machining system for brittle materials. J Laser Appl. 2008;20:127-34.

[7] Kalyanasundaram D, Shrotriya P, Molian P. Obtaining a relationship between Process parameters and Fracture energy for CO2 Laser/Waterjet Machining of Ceramics. Journal of Engineering Materials and Technology. 2009;131:011005-10.

[8] Barnes C, Shrotriya P, Molian P. Water-assisted laser thermal shock machining of alumina. Int J Mach Tool Manu. 2007;47:1864-74.

[9] Payne BP, Nishioka NS, Mikic BB, Venugopalan V. Comparison of pulsed CO2 laser ablation at 10.6 mu m and 9.5 mu m. Lasers in Surgery and Medicine. 1998;23:1-6.

[10] Sachdev H, Haubner R, Noth H, Lux B. Investigation of the cBN/h-BN phase transformation at normal pressure. Diam Relat Mater. 1997;6:286-92.

[11] Robertson J. Diamond-like amorphous carbon. Mat Sci Eng R. 2002;37:129-281.

[12] Bueckner HF. A Novel Principle for Computation of Stress Intensity Factors. Z Angew Math Mech. 1970;50:529-&.

[13] Rice JR. A Path Independent Integral and Approximate Analysis of Strain Concentration by Notches and Cracks. J Appl Mech. 1968;35:379-+.

[14] Anderson TL. Fracture mechanics: fundamentals and applications: CRC press; 2005.

[15] Ho S, Suo Z. Tunneling Cracks in Constrained Layers. J Appl Mech-T Asme. 1993;60:890-4.

[16] Song L, Ci LJ, Lu H, Sorokin PB, Jin CH, Ni J, et al. Large Scale Growth and Characterization of Atomic Hexagonal Boron Nitride Layers. Nano Lett. 2010;10:3209-15.

[17] Mannan MA, Noguchi H, Kida T, Nagano M, Hirao N, Baba Y. Growth and characterization of stoichiometric BCN films on highly oriented pyrolytic graphite by radiofrequency plasma enhanced chemical vapor deposition. Thin Solid Films. 2010;518:4163-9.

[18] Sachdev H. Influence of impurities on the morphology and Raman spectra of cubic boron nitride. Diam Relat Mater. 2003;12:1275-86.

[19] DEvelyn MP, Zgonc K. Elastic properties of polycrystalline cubic boron nitride and diamond by dynamic resonance measurements. Diam Relat Mater. 1997;6:812-6.

CHAPTER 5: TWO-DIMENSIONAL CONTOUR CUTTING OF POLYCRYSTALLINE CUBIC BORON NITRIDE USING A NOVEL LASER/WATER-JET HYBRID PROCESS

A paper published in *The International Journal of Advanced Manufacturing Technology*, DOI: 10.1007/s00170-012-3945-2 (2012)

Ammar Melaibari[14, 15, 16], Pal Molian[1, 17] and Pranav Shrotriya[1, 4]

Abstract

In the laser/water-jet hybrid machining (LWJ), a novel process applicable to brittle materials, the laser beam creates a groove through evaporation and causes solid-state phase transition through heating and shock waves while the water-jet performs quenching. Both laser and water-jet induce stresses and phase changes that lead to cutting via crack formation and controlled fracture mechanism through the rest of the thickness. While LWJ is very well documented by our group for one-dimensional cutting, it remains as a challenge for two-dimensional cutting because of the changing direction of the crack in relation to the laser beam path. In this paper, a focused continuous wave CO_2 laser (400 W) was combined with abrasive-free water-jet 0.4-1.4 MPa (60-200 psi) to generate and steer the controlled crack in two-directions in Polycrystalline Cubic Boron Nitride (PCBN) tool blanks. A 42.33 mm/sec (100 in/min) cutting speed was used in all the tests. The direction of the cracks generated by LWJ was changed to 60, 108, 120, 135 degrees and made to follow a curve with 1 mm radius in

[14] Laboratory for Lasers, MEMS and Nanotechnology, Department of Mechanical Engineering, Iowa State University, Ames, IA 50011.
[15] Dept. of Mechanical Engineering, King AbdulAziz University, Jeddah, Saudi Arabia
[16] Primary researcher and lead author
[17] Co-author

accordance with the standard tool shapes. The cut quality was investigated at the point of change in the crack direction using optical profilometer, Raman spectroscopy, and scanning electron microscopy (SEM). Results indicated that successful cuts were made with obtuse angles (120, and 135 degrees) in contrast to acute angles (60 degree). The crack propagation in the heat affected zone where the phase transition from c-BN to a new phase has occurred is responsible for the inability to obtain good quality cuts in the acute angle cases. A preliminary graphical representation that explains the observed experimental results is formulated.

Keywords: Two-dimensional cutting, cubic boron nitride, tool, laser, water-jet

5.1. Introduction

Polycrystalline cubic boron nitride (PCBN) is the second hardest material on earth with outstanding mechanical properties such as extreme hardness, high Young's Modulus, low coefficient of friction, and superior wear resistance. PCBN also offers greater thermal and chemical stability than polycrystalline diamond. These characteristics make PCBN as an ideal material for tool inserts used to machine hard cast iron, high chrome alloy steels, high-strength nickel super-alloy, and powder metal alloys. At the same time, these characteristics limit the ability to shape the PCBN tools for various geometries. PCBN is available in two forms: one is in the form of thin layer backed on tungsten carbide substrate and the other is in free form, solid cylindrical compact. Carbide backing provides the high impact resistance.

PCBN tool inserts are traditionally produced by cutting a master blank using wire-EDM and Nd:YAG, both of which suffer from deficiencies that in turn require finishing by diamond grinding, lapping, or polishing. PCBN tools having low electrical conductivity are better cut

by the laser than wire-EDM. However PCBN on WC substrate has sufficient electrical conductivity to be cut by wire EDM. The material removal rates in wire-EDM and Nd:YAG pulsed laser are low. Such processes also consume very high energy. Among these techniques, Nd:YAG laser cutting seems to be widely used because of the following benefits: high speed, precision, minimal thermal damage and flexibility. For example, a 300 W average power Nd:YAG laser is capable of cutting 1.6 mm thick PCBN 30 times faster than wire cutting [1]. The cut width was also three times narrower than achieved by wire cutting. The location error is on the order of few micrometers. The laser easily evaporates PCBN but the carbide substrate is more difficult to cut. Nitrogen gas assist was utilized to overcome this problem.

PCBN tool makers are seeking for novel material removal methods and mechanisms to overcome the deficiencies associated with traditional laser and wire-EDM cutting. Consequently hybrid machining processes were developed. Swiss Federal Institute of Technology in Lausanne, Switzerland has developed a Laser-Microjet® technology [2] that uses water to guide the Nd:YAG laser beam for machining of PCBN. Although it has a number of benefits, it still suffers from very slow cutting speeds and utilizes the same material removal mechanism as in traditional laser cutting. For example, it has been reported that it took 70 passes at the rate of 7 mm/min per pass to cut 3.25 mm thick PCBN blank [2].

Another potential approach is the use of dual laser beams that were effectively used to cut ceramics such as aluminum oxide through a controlled fracture mechanism [3]. The first laser beam is used to create a groove while the second laser beam is used to induce tensile stresses that can propagate the crack. While this mechanism offers the opportunity to solve the problems of laser cutting of PCBN, the high hardness and low thermal expansion coefficient of PCBN limit the stresses required form the crack. Our group has recently developed a novel

process of continuous wave CO_2 laser/water-jet (LWJ) to improve the machining of PCBN [4]. In this process, controlled fracture mechanism was utilized rather than energy-consuming evaporation mechanism as in laser cutting and taper-causing erosion mechanism as in water-jet cutting. LWJ process begins with rapid laser heating leading to localized damage and phase transformation of surface layers, followed by water-jet (fast quenching of the surface layers) resulting in a stress field in the transformed material. The stress fields propagate the localized cracks through the thickness where the end result is material separation. The controlled fracture mechanism led to the achievement of a complete cut through the thickness of the workpiece with less energy and time. LWJ is well proven for one-dimensional cutting of PCBN with the following benefits: very small kerf width determined by the size of crack, little taper, higher speed and minimal thermal damage.

The standard tool shape for PCBN is round. Other shapes such as rectangle, triangle, rhombus and square are less frequently used. In order to implement LWJ technique for PCBN tool blanks, it is imperative that LWJ should cut regular and irregular shapes needed for tool inserts. This implies that crack direction should be made to follow the laser beam path in contour cutting which remains as formidable challenge. In addition, PCBN backed on WC substrate poses difficulties in controlling the crack through the thickness. In this work, we have studied the effect of changing the direction of the controlled crack in LWJ process using four different angles commonly encountered in solid and WC-backed PCBN tool inserts. Accuracy, surface roughness and phase transformation around the corners were investigated.

5.2. Experimental Details

PCBN tool blanks were acquired from Diamond Innovations, Inc. (Ohio) both in solid and WC-backed forms. The thickness of solid form PCBN was 1.6 mm. The WC-backed PCBN had the following thicknesses: PCBN = 0.8 mm, WC = 0.8 mm; and PCBN = 0.8 mm, WC = 4 mm. The CBN content of the grades varied from 50% to 75% with additives and binders like TiN, AlN, Ti-matrix etc. Higher CBN content provides increased fracture toughness, resistance to abrasion and higher thermal conductivity.

Figure 34 shows the LWJ head where the nozzle at the bottom left shows two holes. The central hole is to pass the laser beam while the smaller hole is to transmit the water. The nozzle is configured such that the laser beam is ahead of the water-jet by 2 mm under focused condition and 6 mm under defocused condition to prevent the direct interaction of the laser beam with the water-jet stream. The tool blank was held on a fixture mounted on a cutting box and made to move by a positioning table in X-Y plane. The laser head can also be rotated such that the beam and water-jet are made always in tandem. A continuous wave CO_2 laser of 10.6 μm wavelength and 400 W power was used in all experiments. The laser beam was focused to a spot size of 0.2 mm on the sample surface using a 127 mm focal length lens. In one set of experiments of PCBN on thin carbide substrate, multiple passes were performed; the laser beam was focused in the first pass, and then defocused to a spot size of 0.5 mm in the other passes. The water-jet followed the laser beam in the focused mode with a spacing of 2 mm to avoid the absorption of laser power by direct contact with water. The spacing was increased to 6 mm in the last set of experiments of the defocused passes for the same reason. The water-jet pressure in the experiments was 1.4 MPa (200 psi) and 0.4 MPa (60 psi) for solid PCBN and WC-backed PCBN substrate respectively. The air was flown with the laser beam at a pressure

of 35 kPa (5 psi) to keep the lens from contamination with water. The angles used were 60, 108, 120, and 135 degrees typical of common insert angles. All the angle cuts were performed by turning the LWJ head while moving the sample. The 60 degree cut was also performed by making intersection between two straight line cuts.

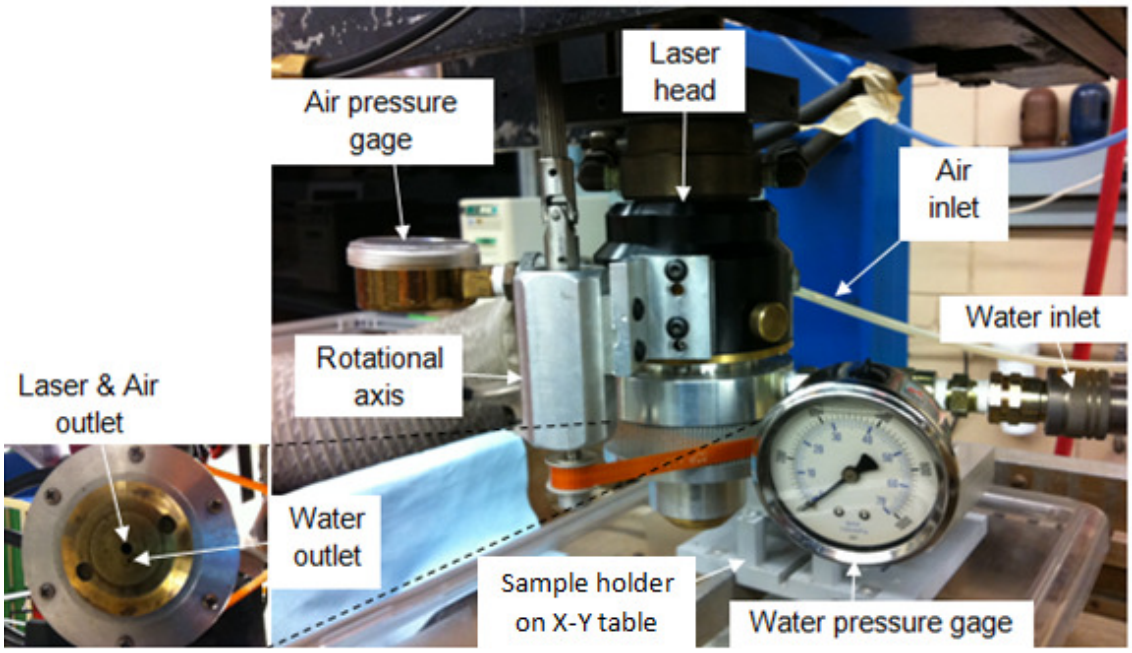

Figure 34: Laser head description with the assist fluid inlets and outlets.

Scanning electron microscopy (SEM Model JEOL JSM-606LV at 20 kV) was used to obtain secondary electron images of the cut surfaces in order to analyze the machined and cracked regions before and after the turns. The kerf geometry and the surface roughness were analyzed using optical profilometer (Zygo NewView 7100) with 5X and 20X magnifications. The extent of phase transition around the corners and intersections were examined using Dispersive Raman spectroscopy (Renishaw-inVia Raman Microscopy) with Ar-ion laser at 488 nm wavelength.

5.3. Results and Discussion

In the investigation of the two-axis cutting of PCBN, the governing factors for the successful cutting of the free-standing PCBN samples are phase change and turning point position. For PCBN samples, backed with carbide substrate, there are three additional factors: carbide substrate thickness, thermal characteristics of WC, and water-jet pressure.

5.3.1. LWJ Cutting of Free-Standing PCBN Segments

Cuts of 120 and 135 degree angles were performed successfully on free-standing PCBN segments (50% c-BN, 50% Ti matrix) with 1.6 mm thickness (Figure 35). The transverse section of LWJ cut typically contains a shallow machined region that is close to the surface, and a cracked region throughout the rest of the thickness; this is typical of what was observed in one-dimensional cutting [5, 6]. Each region has different cut qualities. The surface of the cracked area exhibited a low waviness at the bottom, and a roughness that is almost the same before and after the turn, with an average Ra= 8 μm (Figure 35). The waviness could be attributed to the small distance between the laser path and the cracked path which cause crack instability which will be shown later in the model formulation section. The taper angle, in the machined area, was 15 degrees along the cut; before and after the turn. However, in the cracked area, the taper angle was different after the turn. It was 0 degrees before the turn, but it started as 30 degrees after the turn and then reduced to 0 degrees along the cut (Figure 35). This behavior will be explained in the model formulation section as well.

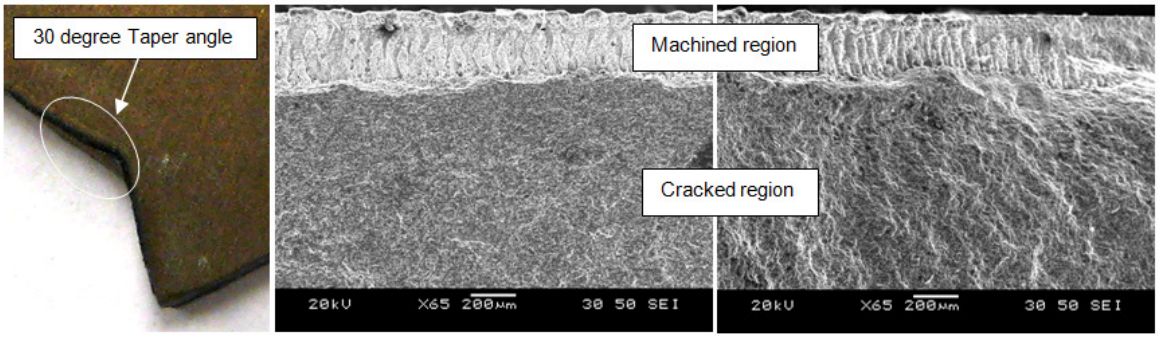

Figure 35: On the left, a taper angle appeared after a 120 degree turn on free standing PCBN sample. In the centre, a SEM image of the transverse section of PCBN before the turn in LWJ cutting. On the right, a SEM image of the transverse section of PCBN after the turn in LWJ cutting.

In addition, an attempt to make a curve with a 1 mm radius was performed successfully. The cut quality was the same as those of 120 and 135 degree angles, except for the absence of a corner. Consequently, there was no taper angle in the cracked area at/around the curve; however, the taper appears after the curve (Figure 36). This taper is a result of the turning point position and not the turning itself, since the taper started to form at some distance after the curve. When the turning point position is close to the edge, the crack tends to deviate from the laser beam path and takes a shorter path to the edge.

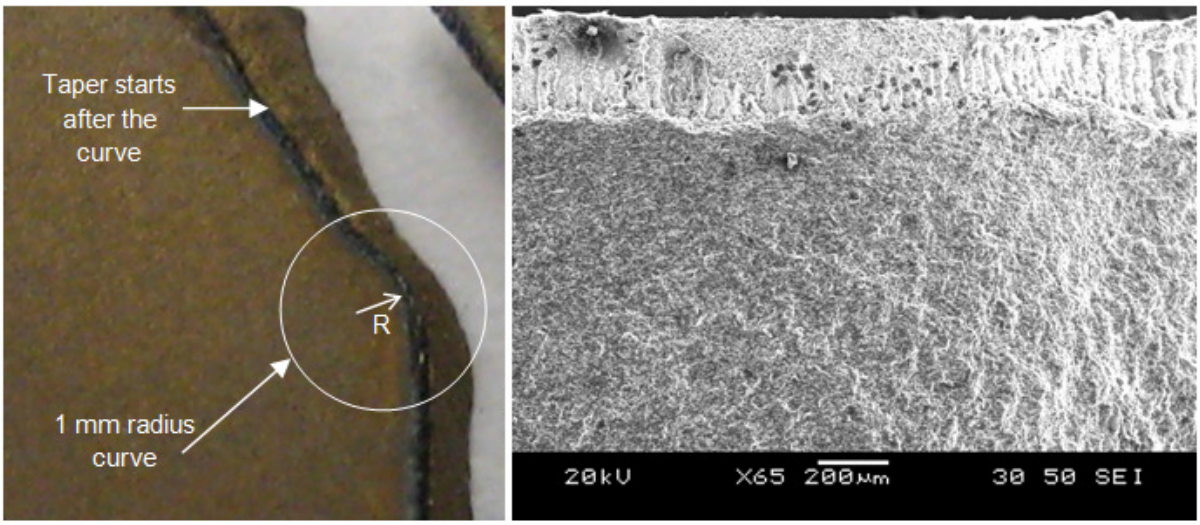

Figure 36: In the left, angular top view of LWJ cut of a curve with 1mm radius on free-standing PCBN sample showing the taper. In the right, a SEM image of the transverse view of the turn.

The attempt to cut at 108 degrees on a segment with the same composition produced a groove only. In other words, the groove was performed in two-axis, but the crack did not propagate through the third dimension, thickness. Another trail to cut a 108 degree angle with a turning point position close to the sample edge was performed. The crack propagated through the thickness before the turn and when it reached the turning point, the crack propagated in an uncontrolled fashion to the sample edge (Figure 37).

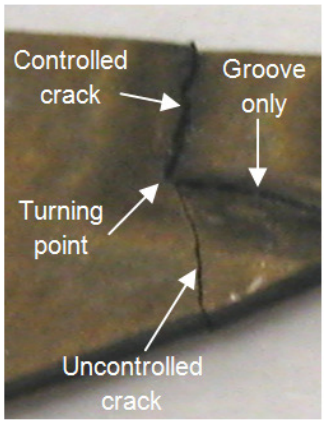

Figure 37: An uncontrolled crack propagated at the turning point when the turn is close to the edge.

The attempts to produce 60 degree cuts were also unsuccessful. Turning the cut to acute angle seems to produce a lot of heat which destroys the sample with uncontrolled fracture to small pieces. Therefore, the 60 degree angle was performed in an alternative fashion by performing an intersection between two straight line cuts. In this trail, the first line cut was all the way through as expected, but the second line did not cut all the way through because the laser beam was passed over the heat affected area from the first cut suggesting the important role played by phase transition. A groove of varying depth was created along the second cut (Figure 38). Another experiment was performed to further prove this result, in which two parallel straight grooves were made so that their heat affected zones overlap, then a third

straight groove was made perpendicular to the parallel lines. The third groove line was shallow at the overlap of heat affected zone (Figure 39).

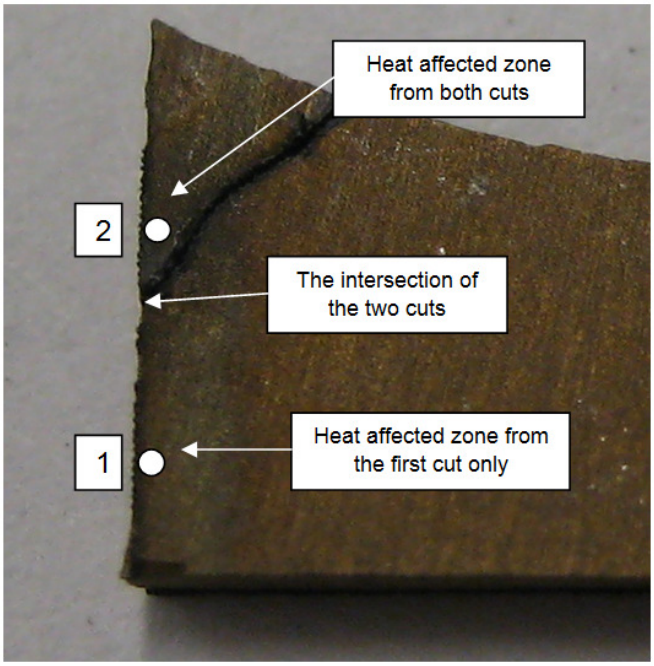

Figure 38: An intersection of two straight line cuts where the first line cut the free standing PCBN sample while the other line did not propagate through the whole thickness due to the phase change effect.

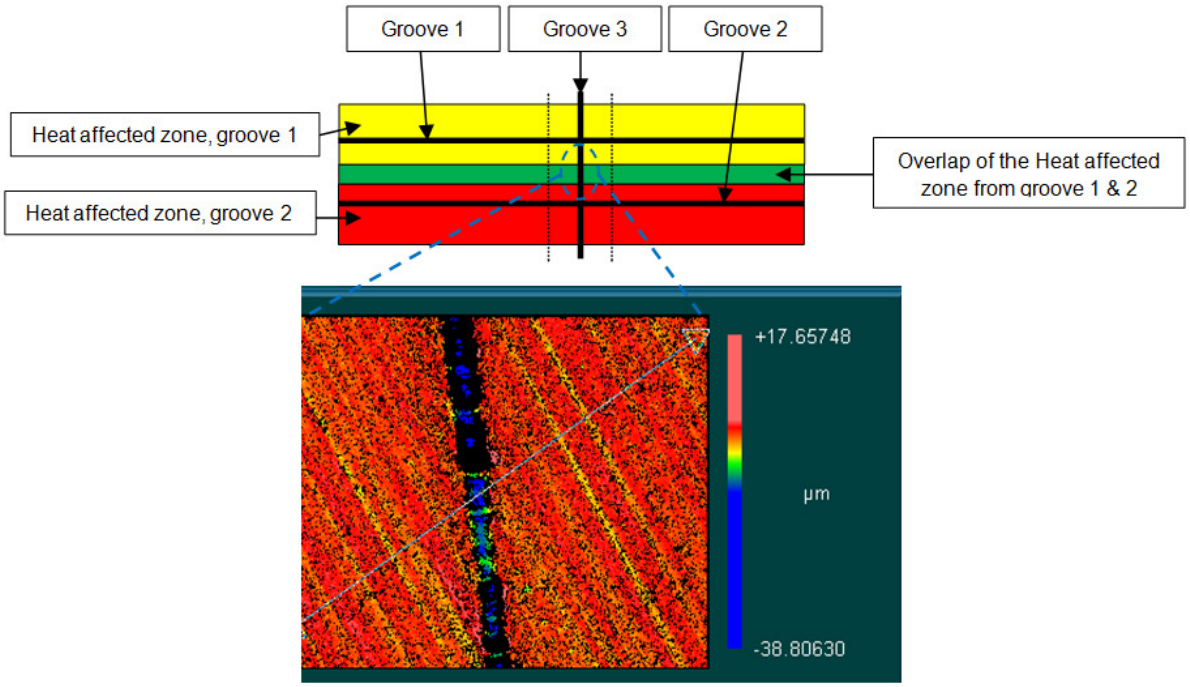

Figure 39: Optical profilometer trace showing the change in depth of the third groove.

It is clear from this experiment that the extent of phase change has a huge effect on the groove depth which in turn controls the initial crack length needed to propagate the crack through the thickness. This means the phase change plays a vital role in the ability to turn a crack in the LWJ process. Turn cuts up to 108 degrees are not possible because of the overlap between the heat affected zones of the two sides of the angle. Inside the area between these lines, the phase change is enhanced that in turn prevented the crack from taking the turn.

Let us now understand the four main different phases associated with BN: hexagonal (h-BN), rhombohedral (r-BN), cubic zincblende (c-BN), and wurtzite (w-BN) depending on the pressure and temperature (Figure 40). Both h-BN and r-BN have layer structures (sp^2 bonding) and lower densities compared to c-BN and w-BN (sp^3 bonding). Although it was accepted for a long time that h-BN is the most stable structure at ambient conditions, recent experimental investigations and *ab initio* calculations affirm that c-BN is the most stable structure at ambient conditions [7]. Using the Raman spectroscopy, we identified phase changes from c-BN to all phases in LWJ samples. An increase in a new phase (1198 cm^{-1}) is particularly noted in the acute angle area (Figure 41 and 42). This increase in the new phase at the corners can be attributed to the high pressure emerging from the transformation of c-BN to the h-BN phase before and after the turn, and the additional heat at the corner, due to the long laser exposure in that area. This new phase can be attributed to a new boron-doped phase which has a peak around 1210 cm^{-1} [8] or amorphous boron which typically has a peak around 1150 cm^{-1} since the shift of these peaks can be explained by the presence of different impurities in the sample [9], the increase of temperature by the laser [10], the change of the crystallite size due to the phase transformation [10], and the induced stresses between the boundaries of the phases [10] which all occurred in this experiment. It may be noted the composites of c-BN and

w-BN exhibit higher fracture toughness in the range of 13 to 16 MPa $m^{1/2}$ compared to 7 MPa $m^{1/2}$ for c-BN [11]. Consequently the critical initial crack length for propagation needs to be much longer. Hence, it can be argued that the propagation of a crack through the new phase will be much more difficult. Thus it may be concluded that increasing the cutting angle will decrease the transformation to this new phase at the corner and produce a nicer cut.

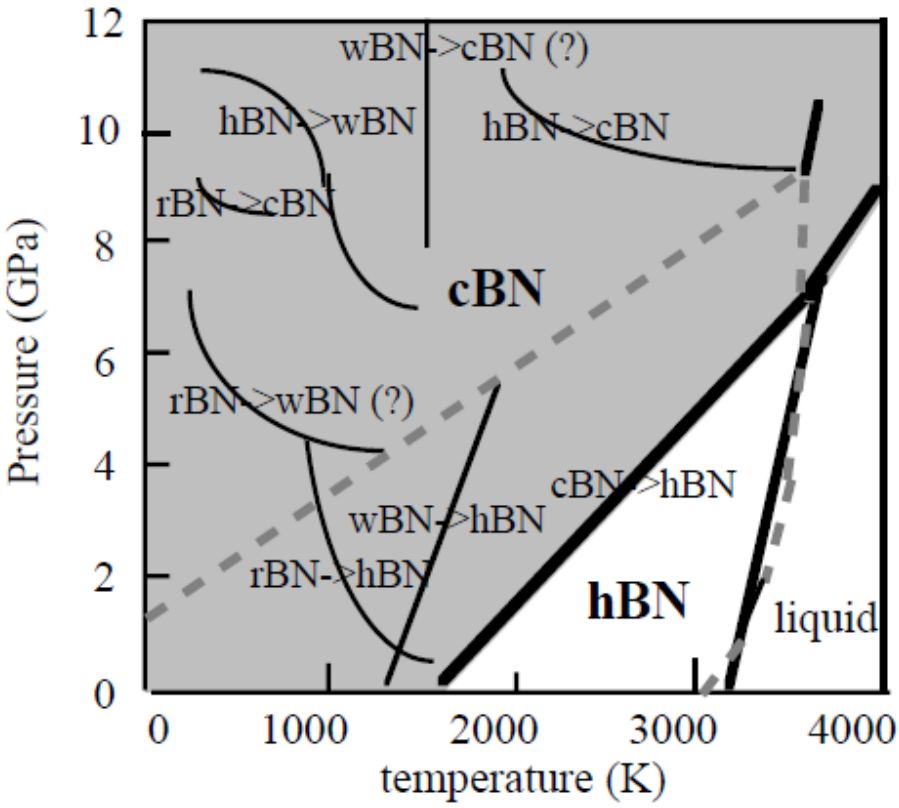

Figure 40: Phase diagram of BN (Source: Reference 7 in chapter 5)

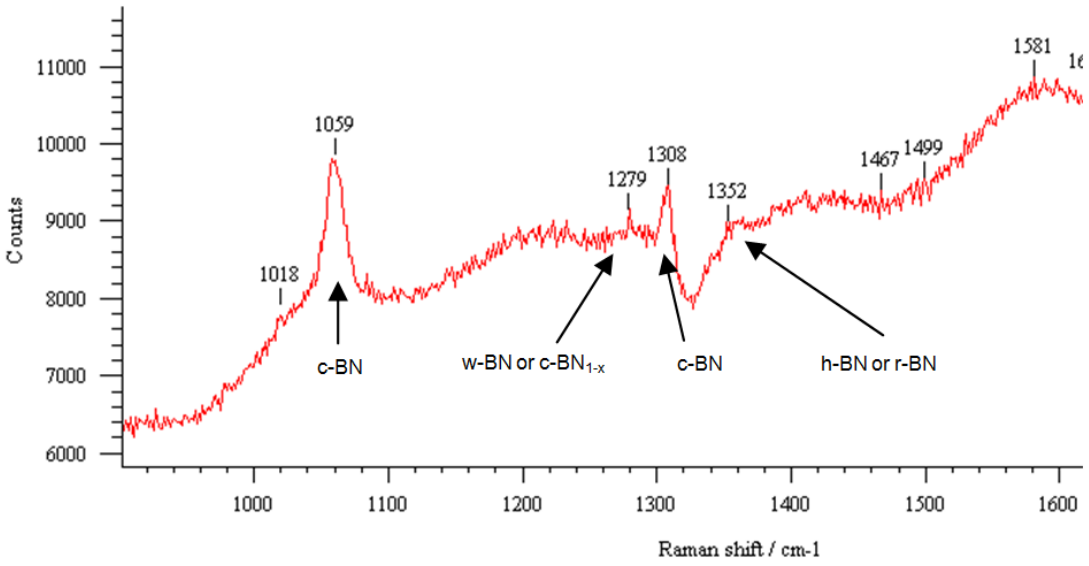

Figure 41: Raman spectrum at point (1) in Figure 5 where different peaks of different phase can be observed (c-BN1-x , c-BN, h-BN, w-BN and r-BN)

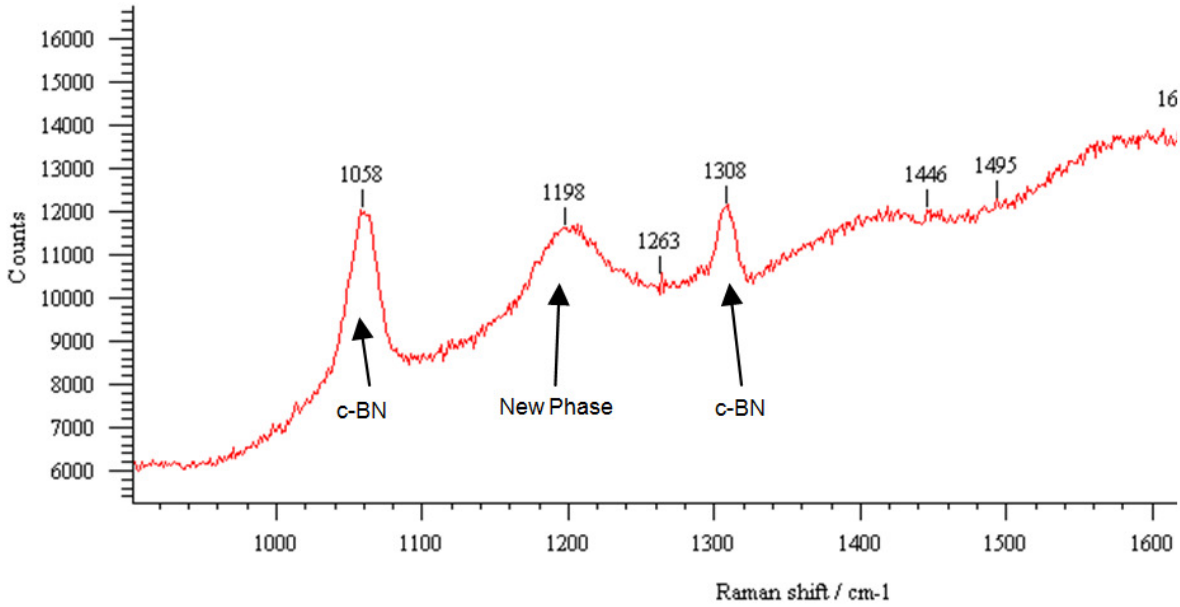

Figure 42: Raman spectrum at point (2) in Figure 5 where different peaks of different phases can be observed like in point (1); the peak at 1198 cm−1 is attributed to a new phase.

5.3.2. LWJ Cutting of PCBN Backed with Carbide Substrate

In the case of two-axis cutting of PCBN on thin carbide substrate (PCBN thickness = 0.8 mm, carbide substrate thickness = 0.8 mm) with controlled fracture, the crack propagates through the whole thickness after multiple passes (4 passes) of the defocused beam followed with water-jet, and 120 degree angle cut was successfully performed (Figure 43). In this cut, the surface roughness, waviness, and taper angle were different before and after the turning point. Before the turning point, the average surface roughness in the cracked area and the carbide substrate area was Ra = 4 µm with no taper. In the machined area before the turn, the machined surface was chipped off at the top, which added more taper to the machined area. At the turn, the whole surface was chipped off, which provides a low surface roughness (Ra = 4 µm) with no corner (Figure 43 and 44). After the turn, the machined area had an average surface roughness Ra = 9 µm with a 15 degree taper angle. The PCBN cracked area, after the turn, had a very high waviness while the carbide substrate cracked area had low waviness (Figure 43).

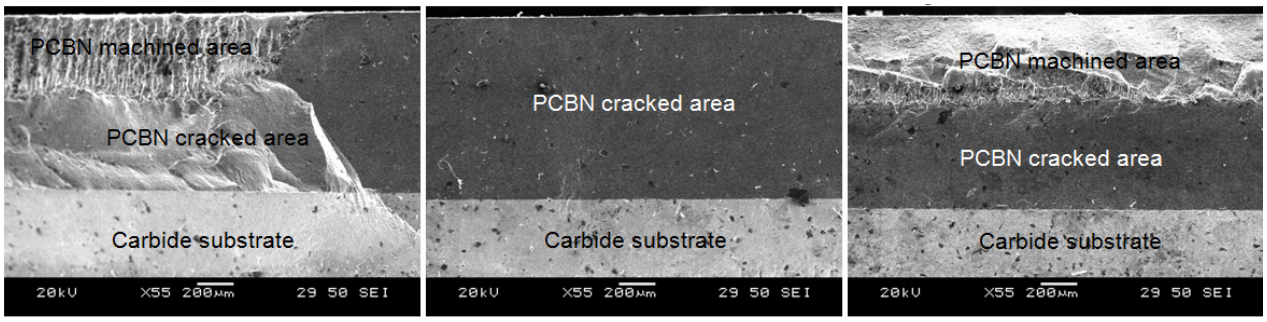

Figure 43: SEM images of LWJ cuts of PCBN on thin carbide substrate. Before the turn (right), the PCBN and the substrate cracked areas have low surface roughness values and almost no waviness while the machined area with multiple passes has high values of surface roughness. At the turning point (middle) only cracked surface with low surface roughness values. After the turn (left), high surface roughness and waviness in the cracked and machined areas.

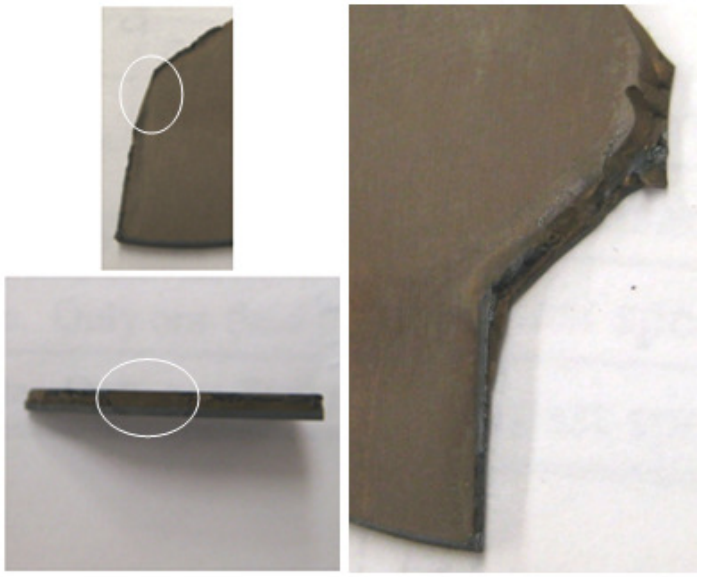

Figure 44: On the left (top), top view of a 135 degree angle cut where the crack turned before the laser beam turning point, (bottom) transverse section of the cut shows the chipped area around the turning point in the circle. On the right, a taper angle appeared after the turn on PCBN for carbide substrate sample.

The crack in the cutting of thick carbide substrate (PCBN thickness = 0.8 mm, carbide substrate thickness = 4 mm) did not propagate through the thickness. In addition, there were lateral cracks along the whole cut (Figure 45 left). Reducing the water-jet pressure from 200 psi to 60 psi (the minimum) reduced the lateral cracks, but did not eliminate them. Multiple defocused passes with the water-jet were performed until the PCBN around the cutting area was destroyed completely by lateral cracks, yet the crack did not propagate through the carbide substrate. Thus, PCBN backed with thick carbide substrate is not suited for LWJ process.

Even in the LWJ cuts of PCBN on thin carbide substrate, the cut was only attractive for about the first half inch and then the crack became uncontrolled with appearance of lateral cracks (Figure 45 right). This could be attributed to the built-up temperature in the carbide substrate and its effect on the interface between the PCBN and the carbide substrate. The heat produced by the laser will transfer to both materials while the heat conductivity and the heat expansion coefficient of PCBN and the carbide substrate are different. This will accumulate

the heat in the carbide substrate making it like a heat sink. This accumulated heat will expand the carbide more than the PCBN creating a high tension in the PCBN. This high tension creates the lateral cracks on the PCBN side.

Figure 45: On the left, LWJ on PCBN blank with thick carbide substrate where extensive lateral cracks can be observed. On the right, a complete straight cut of PCBN blank with thin carbide substrate where the cut was controlled for half inch then become uncontrolled and lateral cracks start to appear from the built up temperature in the carbide substrate.

5.3.3. The Model Formulation

In LWJ machining, when the laser beam impinges the surface material, it starts to transform to h-BN and causes an increase in volume; this will make compressive stresses around the initial crack. When the water-jet acts on the material, the laser heated area will start to shrink due to the quenching effect around the h-BN which will change the stresses to tensile mode around the initial crack. This will allow the crack to propagate and move a distance away from the laser spot. After the crack propagates through the thickness, residual stresses will be left along the crack tip since no phase transformation occurred deep inside the material but a new surface is generated (Figure 46).

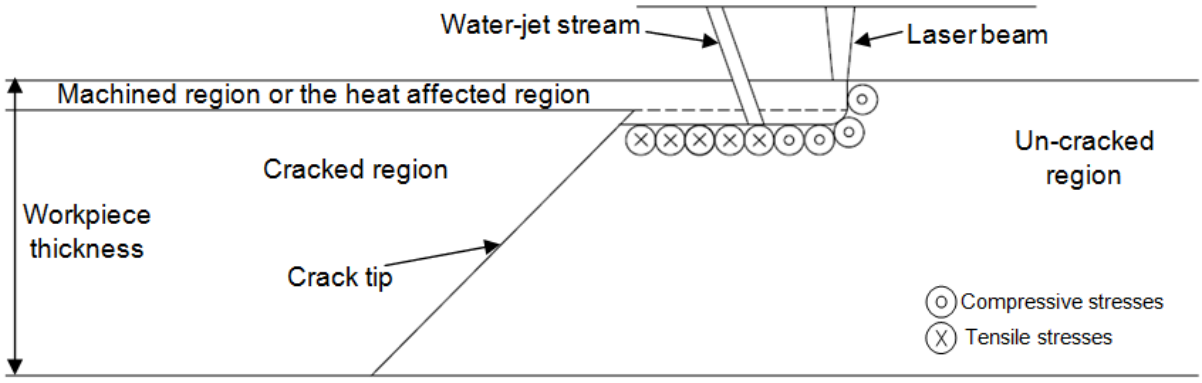

Figure 46: Schematic representation for LWJ machining for a straight line. The big circles represent the stress field inside the material; small circles (compressive) and cross (tensile).

Therefore, when making a turn with the LWJ head, the crack tip will not follow the laser beam path. It will make the turn right away, which will create the observed taper. The phase transformation to the new phase around the corner requires a longer crack size to propagate the crack through it. So, the crack tip will make a shorter path to the laser beam path and reconnect with it after it passed the new phase area (Figure 47).

In order to prove this hypothesis, we conducted the following experiment; PCBN segments (65% c-BN, 35% TiN) with 1.6 mm thickness were used to make a groove with a 135 degree angle using LWJ. In this case, the sample was snapped by applying a small bending force (by hand) to see whether the crack path follows the groove path with no taper. The crack actually propagated in a longer distance path due to the direction of the applied force. However, it did not go through the area of rich new phase, which confirms the model (Figure 47).

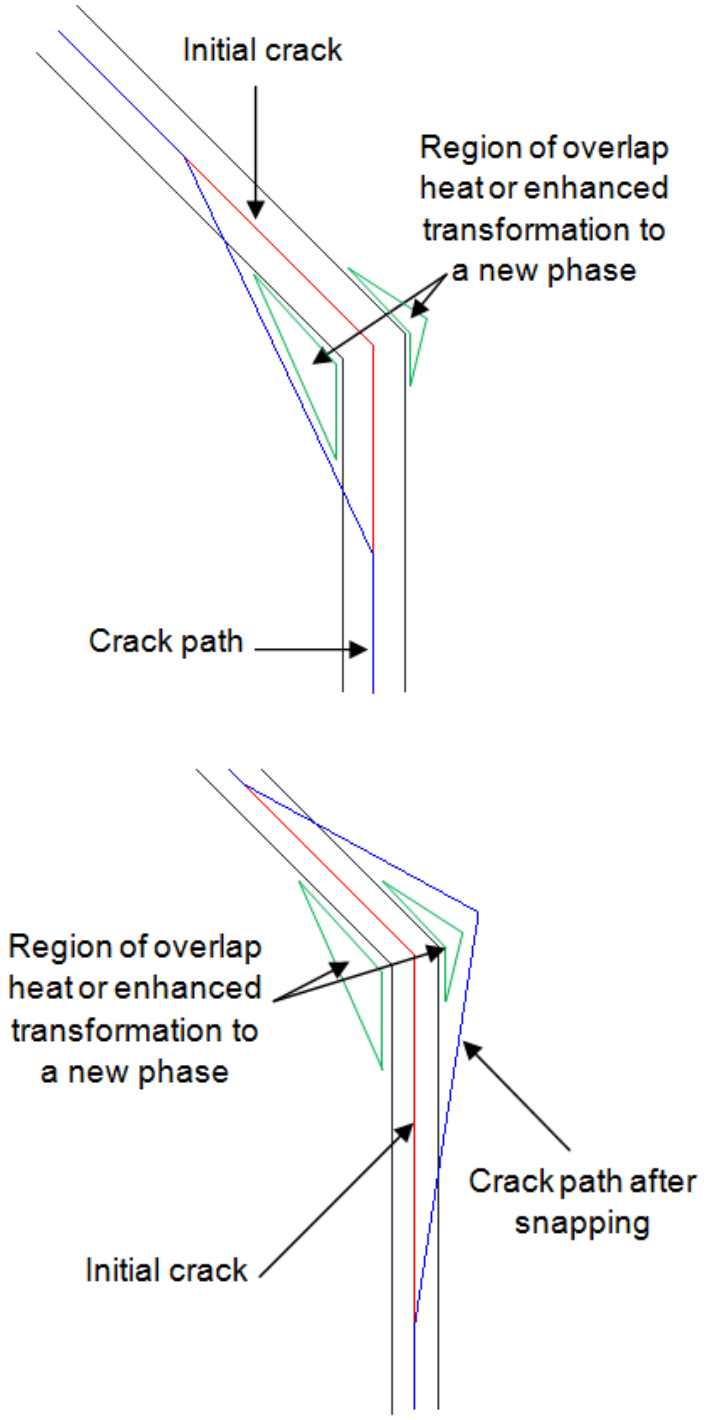

Figure 47: Schematic representation for LWJ machining at the turning point (top view). On the top, the model is for complete separation using LWJ machining on PCBN. On the bottom, the representation is for a groove made on PCBN using LWJ and a complete separation is then performed by snapping the sample.

The change of taper angle and waviness after the turn in the obtuse angle can be explained as shown in Figure 48. In the case of small thickness, the distance between the crack tip and the laser beam spot will be smaller; this will reduce the taper angle and the waviness. In other words, the sample thickness and the distance between the crack tip and the laser beam are limitations in two-dimensional LWJ cutting.

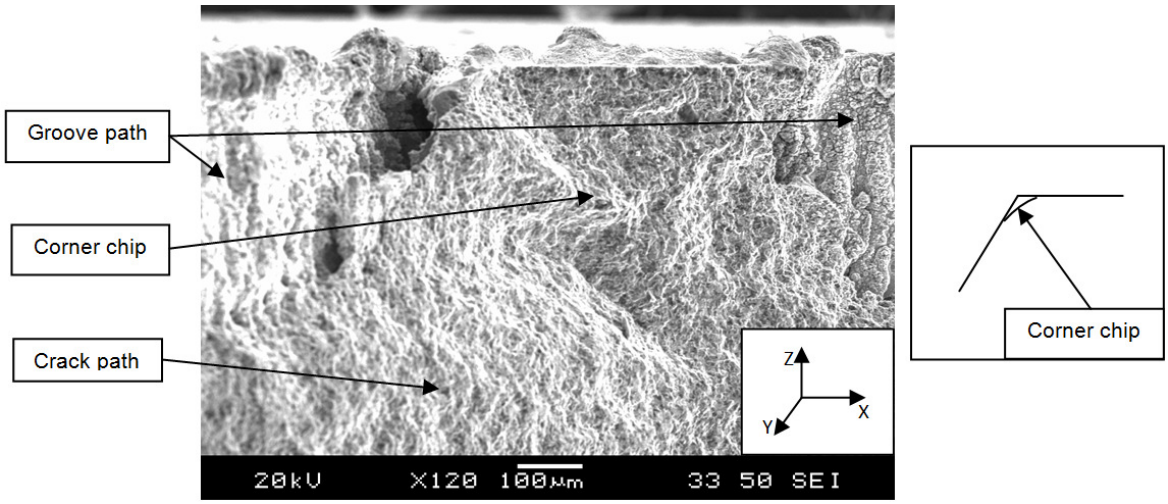

Figure 48: On the left, SEM image of the transverse section of the corner in LWJ cut which shows the crack path and groove path. On the right, schematic top view shows the corner chip due to the mismatch between the groove path and the crack path at the corner.

5.4. Conclusion

Two-dimensional cutting with 120 and 135 degrees have been successfully conducted on PCBN tool blanks using LWJ. Also, 1 mm radius cut was performed which means that the contour cutting is possible. Multiple passes of defocused laser beam can propagate the initial crack of PCBN samples on thin carbide substrate to provide a complete cut. The cut geometry and roughness are acceptable before the turn. After the turn there are some problems with taper and waviness in the cracked area. However, PCBN samples on thick carbide substrate resulted in numerous lateral cracks making the process limited to only thin carbide substrates.

The governing parameters for the successful two-axis cutting with controlled crack propagation mechanism of PCBN using LWJ were phase change, turning point position, sample thickness, substrate thickness, substrate thermal characteristics, and water-jet pressure. A preliminary qualitative model of the two-axis cutting with controlled crack propagation mechanism confirms the observations.

5.5. Acknowledgments

This material is based upon work supported by the National Science Foundation under Grant No. CMMI-1000035 and the scholarship provided by King AbdulAziz University. The authors gratefully acknowledge the polycrystalline cubic boron nitride blanks donated by Diamond Innovations, Inc, Worthington, OH.

5.6. References

[1] http://qs-diamondtechnology.com/LDMachines.aspx, tapped on o5/15/2011

[2] O. Sibailly, F. Wagner, L. Mayor, B. Richerzhagen, 2003, High precision laser processing of sensitive materials by Microjet, Proceedings of the Society of Photo-optical Instrumentation Engineers (SPIE), Vol. 5063/501-504

[3] Tsai C.-H., Liou C.-S., 2003, Fracture Mechanism of Laser Cutting With Controlled Fracture, Journal of Manufacturing Science and Engineering, Vol. 125/519-528

[4] Kalyanasundaram D, Shrotriya P., Molian P., 2009, Obtaining a Relationship Between Process Parameters and Fracture Characteristics for Hybrid CO_2 Laser/Water-jet Machining of Ceramics, Journal of Engineering Materials and Technology, Vol. 131/011005

[5] D. Kalyan-Sundaram, J. Wille, P. Shrotriya, P. Molian, 2008, CO_2 Laser/Water-jet Cutting of Polycrystalline Cubic Boron Nitride, Transactions of NAMRI/SME, Vol. 36/517-524

[6] Melaibari, P. Shrotriya, P. Molian, 2011, Effect of Fluid Medium on Laser Machining of Polycrystalline Cubic Boron Nitride Tool, 44th CIRP conference on manufacturing systems.

[7] Pui K. Lam, 1999, Phase diagram, cluster stability, and growth mechanism of boron nitride, Science and technology of high pressure: proceedings of the AIRAPT-17, Vol, 1/935-938

[8] Zinin P.V., Kudryashov I., Konishi N., Ming L.C., Solozhenko V.L, Sharma S.K., 2005, Identification of the diamond-like B–C phase by confocal Raman spectroscopy, Spectrochimica Acta Part A, 61: 2386–2389

[9] Sachdev H., 2003, Influence of impurities on the morphology and Raman spectra of cubic boron nitride, Diamond and Related Materials, 12:1275–1286.

[10] Bergman L., Nemanich R.J., 1996, Raman Spectroscopy Characterization of hard, wide-bandgap for Semiconductors: Diamond, GaN, GaAlN, AlN, BN, Annu. Rev. Mater. Sei., 26:551-79

[11] C. Divakar, S. Bhaumik, A. Singh, High pressure and high temperature processing and performance of wBN-cBN composite tools, Advances in High Pressure Science and Technology, Editor: A. K. Singh, Tata McGraw-Hill, New Delhi, pp. 281-302, 1991, also from http://nal-ir.nal.res.in/4827/1/67high-pressure.PDF tapped on o5/15/2011

CHAPTER 6: PICOSECOND LASER MICROMACHINING OF ULTRA-HARD ALMGB$_{14}$ THIN FILMS

A paper published in *the Advanced Materials Research* Vol. 804, pp 17-22, DOI: 10.4028/www.scientific.net/AMR.804.17 (2013)

Ammar Melaibari[18, 19, 20], and Pal Molian[1, 21]

Abstract

Ultra-hard $AlMgB_{14}$ (30-50 GPa) thin films were deposited on silicon substrate for a nominal thickness of 100 nm using a pulsed excimer laser and then subjected to direct micromachining using a 532 nm, 30 picosecond pulsed Nd:YAG laser. The application is targeted towards synthesizing an artificial nacre material composed of hexagonal bricks and particle bridges of superhard $AlMgB_{14}$ thin film and mortars of Ti thin film that biomimic the hierarchical architecture of natural nacre. The effects of pulse energy (0.1 to 1 μJ) and laser scanning speed (0.5 to 1.5 m/sec) on ablation depth and quality of scribed channels were evaluated. The morphology of the channels was characterized using confocal microscope and optical profilometer. Results indicated a clean material removal process characterized by absence of heat affected zone, high-speed scribing and small feature size. The energy fluence for the removal of 100 nm thin film without affecting the silicon substrate was 0.3 J/cm^2. An interesting observation is that particulate matter present in the thin film was not ablated

[18] Laboratory for Lasers, MEMS and Nanotechnology, Department of Mechanical Engineering, Iowa State University, Ames, IA 50011.
[19] Dept. of Mechanical Engineering, King AbdulAziz University, Jeddah, Saudi Arabia
[20] Primary researcher and lead author
[21] Co-author

suggesting a size effect. Analysis of thermal transport reveals that the material removal has occurred via spallation and phase explosion mechanisms. The picosecond laser thus offers a high-speed energy source for precisely ablating ultra-hard thin films that in turn will allow the potential for fabrication of novel artificial nacre with exceptional strength and toughness.

6.1. Introduction

Picosecond (ps) pulsed lasers are rapidly emerging as high-performance manufacturing tools for scribing, micromachining and cutting all types of materials (silicon, metal, glass and plastic) with feature sizes ranging from 1 μm to 50 μm. For example, via drilling of silicon by the laser beam in both percussion and trepanning modes resulted in extremely smooth side walls [1]. In general, ps-lasers are preferred to nanosecond (ns) and femtosecond (fs) pulsed lasers from both ends of pulse width spectrum for a number of reasons such as higher reliability, less maintenance, more compactness and higher speed over fs-lasers; and higher resolution, superior edge quality, and little collateral thermal damage over ns-lasers. The broad uses of ps-lasers depend on the amount of pulse energy that ranges from micro to millijoules. In the area of manufacturing where the applications include microelectronics, photovoltaics, displays and medical devices, ps-lasers are superior to industrially-proven ns-lasers because the material is removed more by optical absorption rather than thermal diffusion in a precise, controlled manner.

One grand success story of ps-lasers is micromachining of multiple layers of thin films used in solar cells and flat panel displays. The ps-pulses precisely control the scribe depth and selectively ablate thin films by a combination of linear and nonlinear (multiphoton) absorption associated with high intensity and short pulse time. Scribing of interconnections in thin films

of amorphous silicon (α-Si), cadmium telluride (CdTe) and Cu (In1-xGax)S_{e2} (CIGS) was successfully achieved to obtain minimal thermal damage, high spatial resolution, low contamination, high efficiency and low overall device manufacturing costs [2, 3]. For example, a 355 nm ps-laser was able to scribe P1 layer without heat affected zone (HAZ), interdiffusion layer of the melt and mixing of Mo with CIGS, and micro-cracks [4]. Traditionally P2 and P3 laser scribes, which require the removal of CdTe and amorphous silicon (a-Si) layers respectively, are performed by ns-pulsed lasers [5, 6]. However these scribes exhibited undesirable sidewall non-uniformity, cracking and excessive debris. Additional problem was the beam positioning particularly when the pulse repetition rate was scaled to 200 kHz or higher. Picosecond pulsed lasers were able to overcome these deficiencies [7]. Baird et al evaluated CdTe and a-Si thin film photovoltaic device P2 and P3 scribe process performance and quality produced by 532 nm, 30 ps pulses at 200 kHz employing a square flat-top spatial beam profile and found channels with less taper, fewer defects and faster speed than achievable with a Gaussian beam [8]. Picosecond laser pulses also offered a one step, dry process for patterning indium tin oxide (ITO) films for high throughput, highest edge quality, superior resolution and reduced linewidth which are well suited for the fabrication of touch screens and other displays [9]. In another area of microelectronics, selective removal of SiN and SiO_2 dielectric passivation and anti-reflection coatings from textured crystalline Si wafers was demonstrated using a ps-fiber laser [10]. Both flat-top square beam profile and conventional Gaussian beam profile were used to remove these dielectric layers. The shaped beam profile improved material removal capability particularly at the edges of the scribes. Thus, ps-laser scribing of thin film devices benefit from absence of delamination, very low debris, minimal HAZ and high die fracture strength.

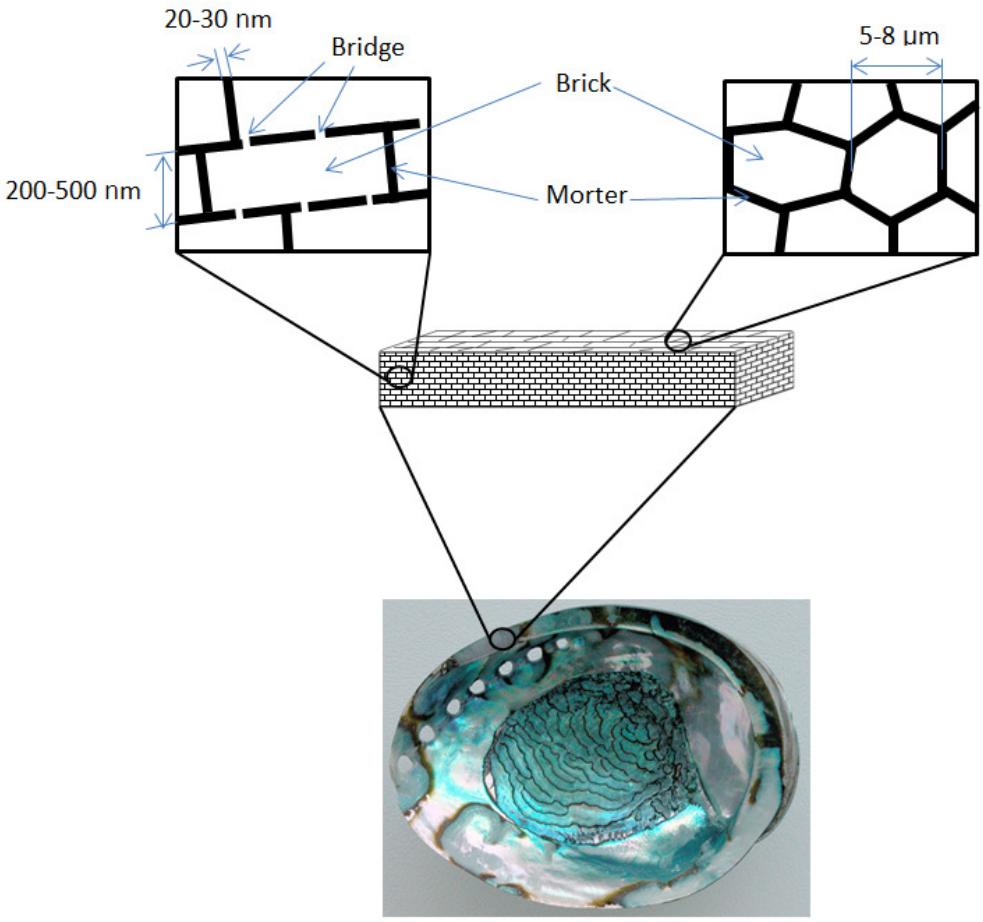

Figure 49: Hierarchical architecture of Nacre

Ultra-hard intermetallic borides such as $AlMgB_{14}$ belong to the class of diamond materials by offering extreme hardness, wear resistance and chemical stability [11]. $AlMgB_{14}$ also provides crack blunting and deflection for increased fracture resistance. $AlMgB_{14}$ in the form of thin film or bulk material exhibits exceptional abrasive wear resistance sometimes superior to that of polycrystalline diamond. In this paper, the objective is to determine the feasibility of a picosecond laser to scribe ultra-hard $AlMgB_{14}$ (30-50 GPa) thin films for fabricating the hierarchical micro/nanoscale structures of artificial nacre shown in Fig.49. Essentially the ps-laser must be capable of creating clean, high resolution hexagonal “brick” structures in $AlMgB_{14}$ thin films.

6.2. Experimental Details

Picosecond lasers are available in both free space and fiber configurations. However the free space form is often bulky, complex and expensive. The fiber based, ps-laser is limited to pulse energy less than 10 μJ but is excellent for ablation of thin films and polymers. In this work, a 5 μJ Fianium Model HE1064/532 picosecond fiber master oscillator power amplifier laser producing 532 nm, 30 picosecond pulses with a pulse repetition frequency of 70 KHz was employed [12]. The laser beam profile is Gaussian with an M^2 factor of less than 1.2. The laser system has also a modulation capability that enables selection of pulse repetition rate from single-shot to 1 MHz. A workstation comprised of a hybrid galvanometer scanner (Scanlab HurrySCAN II-14) and linear stage beam positioning system was utilized to fabricate arbitrary patterns with feature sizes under 10 μm at speeds up to 10 m/sec. The laser output was directed through an 8x beam expander and then steered through the scanner with a 100 mm focal length telecentric objective lens to produce a spot size of 6-8 μm on the surface of thin film. The laser and scanner were synchronously controlled. Super-hard thin films of $AlMgB_{14}$ were prepared on 25 mm diameter silicon wafer by the standard excimer (248 nm) pulsed laser deposition technique described elsewhere [13]. The film thickness was about 100 nm with few particulates and a surface roughness of 1 nm in Ra scale.

The silicon samples deposited with $AlMgB_{14}$ thin film were first scribed in straight lines with increasing pulse energy and increasing speed to identify the window of operating parameters. Results showed that pulse energies and scanning speeds in the range of 0.1 to 1 μJ and 500 mm/sec to 1500 mm/sec respectively were found to be optimum that would not meet the criteria of “no ablation” or “excessive cutting”. Using this window of parameters, two-dimensional plus sign patterns were carved out on the thin films to investigate how the

operating parameters affected the scribe morphology. The beam overlap along a line was governed by the scanning speed and pulse repetition rate. Single pass scribing was employed in all cases. Following laser scribing, a 3D confocal optical microscope and an optical surface profilometer were used to determine the ablation depth and quality of the scribed channels.

6.3. Results and Discussion

Figure 50 shows 2D confocal images of laser scribed plus signs as a function of pulse energy for two scanning speeds. The following observations are made: 1) $AlMgB_{14}$ thin film has been cleanly removed without any damage to the underlying silicon substrate; 2) the scribe channels are mostly straight and free of defects such as cracking and residual debris; 3) the shape of the scribed zone resembles teardrop despite the beam exhibiting Gaussian energy distribution. Such a teardrop shape is attributed to the scanning speed and thermal transport properties of thin film; 4) the size of scribed zone changes in a more pronounced manner with pulse energy than scanning speed implying that the geometry of channel is best controlled by pulse energy; 5) higher pulse energies resulted in possibly some recast layer (Fig.50a, b) within the scribed zone probably caused by the re-melting of silicon; 6) the particulate matter in thin films is not removed in most cases (Fig.50c-f) partly due to the size effect; 7) there is no overlap of laser pulses in cases of higher scanning speeds due to the fact that the beam velocity (spot size times pulse repetition rate) is slower than the galvanometer scanning speed; and 8) pulse energy 0.6 μJ/pulse and scanning sped of 1500 mm/sec are the most optimum in removing the film with almost no heat affected zone.

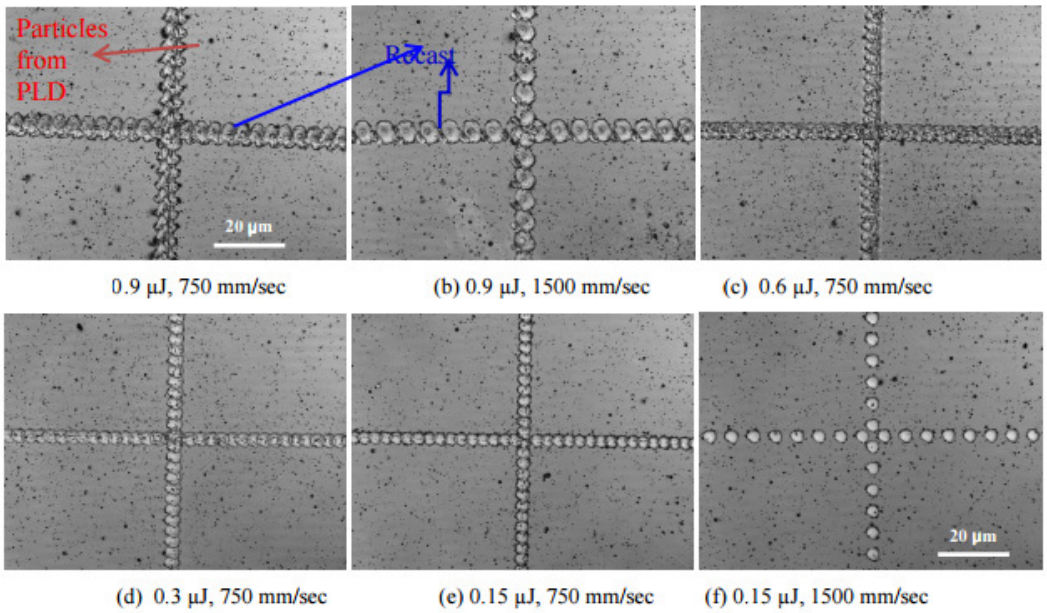

Figure 50: Confocal microscope images of plus sign scribed on Ultra-hard thin film

Detailed characterization and analysis of four scribed layers was made to ascertain the effect of pulse energy and scanning speed on ablation depth, ablation threshold, HAZ and overall quality of scribing. At higher pulse energy and lower scanning speed (0.9 µJ and 500 mm/sec, Fig.51a), there is a large HAZ and significant recast layer indicating the dominance of thermal diffusion. The ablation depth, given by the peak-to-valley (PV) distance, is about 0.8 µm, inferring that silicon is also removed along with the thin film. A three times increase in speed eliminated HAZ and reduced the ablation depth to 0.28 µm (Fig.51b). However the scribe is not continuous. In addition, recast layer could not be eliminated. When pulse energy was reduced to 0.15 µJ, only ablation of thin film has occurred (Fig.52a,b). The energy fluence for the removal of 100 nm thin film of $AlMgB_{14}$ is calculated to be about 0.3 J/cm^2 ; this is similar to the ablation of solar cell thin films such as ITO and Mo where ablation threshold lies in the range 0.1 to 0.5 J/cm^2 [3-10].

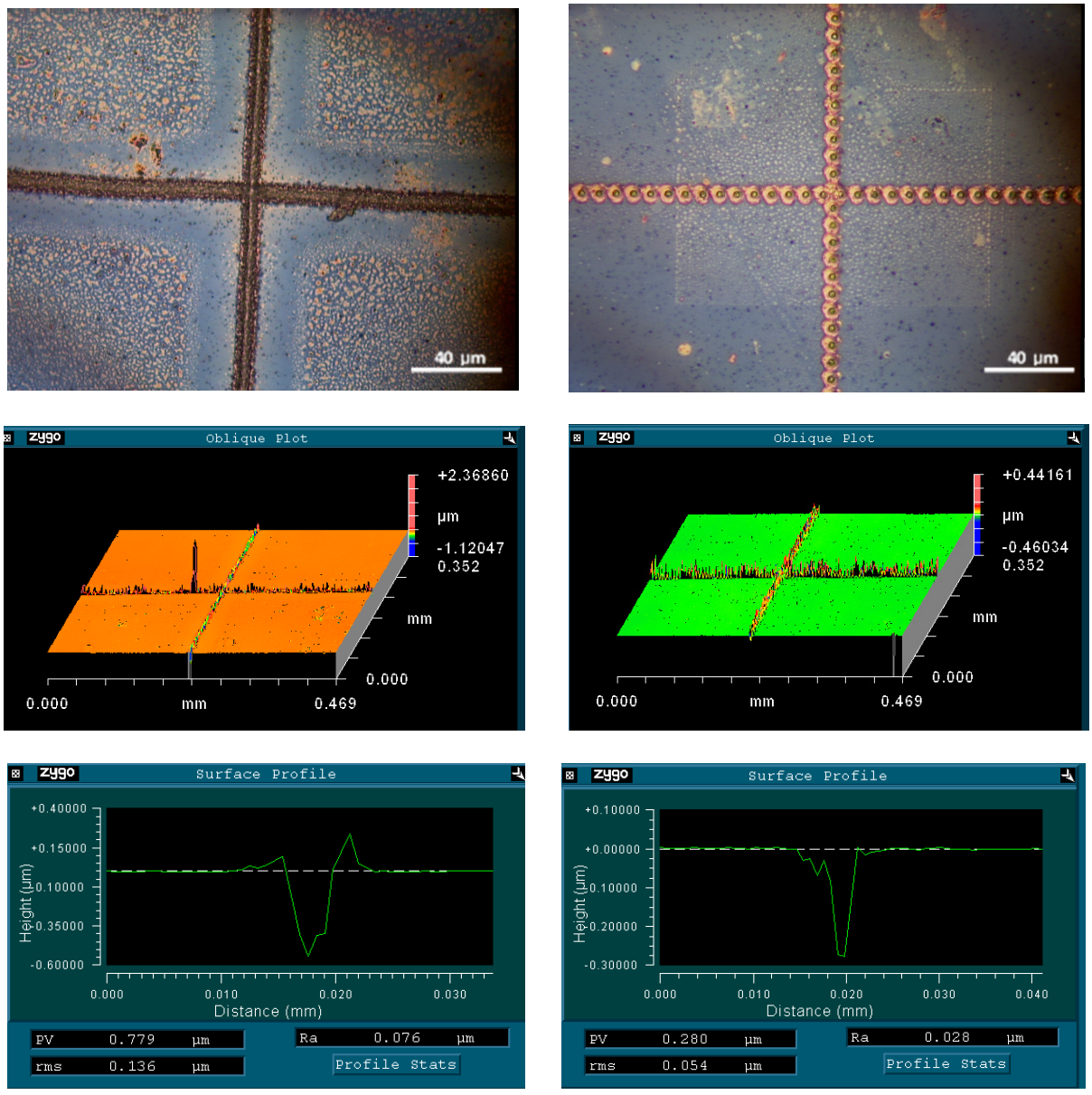

(a) 0.9 µJ, 500 mm/sec (b) 0.9 µJ, 1500 mm/sec

Figure 51: Optical images and profiolometer traces of scribed channels on $AlMgB_{14}$ thin films at high pulse energy

The benefits of ps-laser micromachining for the $AlMgB_{14}$ thin film can be realized through a fundamental understanding of ultrafast laser-material interaction phenomena. The optical absorption characteristics of $AlMgB_{14}$ at 532 nm are unknown; however, due to the

$AlMgB_{14}$ alloy's similarity to most metals, the absorption depth can be assumed to be few nanometers. In addition, multiphoton absorption can occur due to the extreme intensity and picosecond time scale and can significantly decrease the absorption depth. Thus, the multiphoton absorption phenomenon allows the photon absorption to occur mostly at the surface of $AlMgB_{14}$.

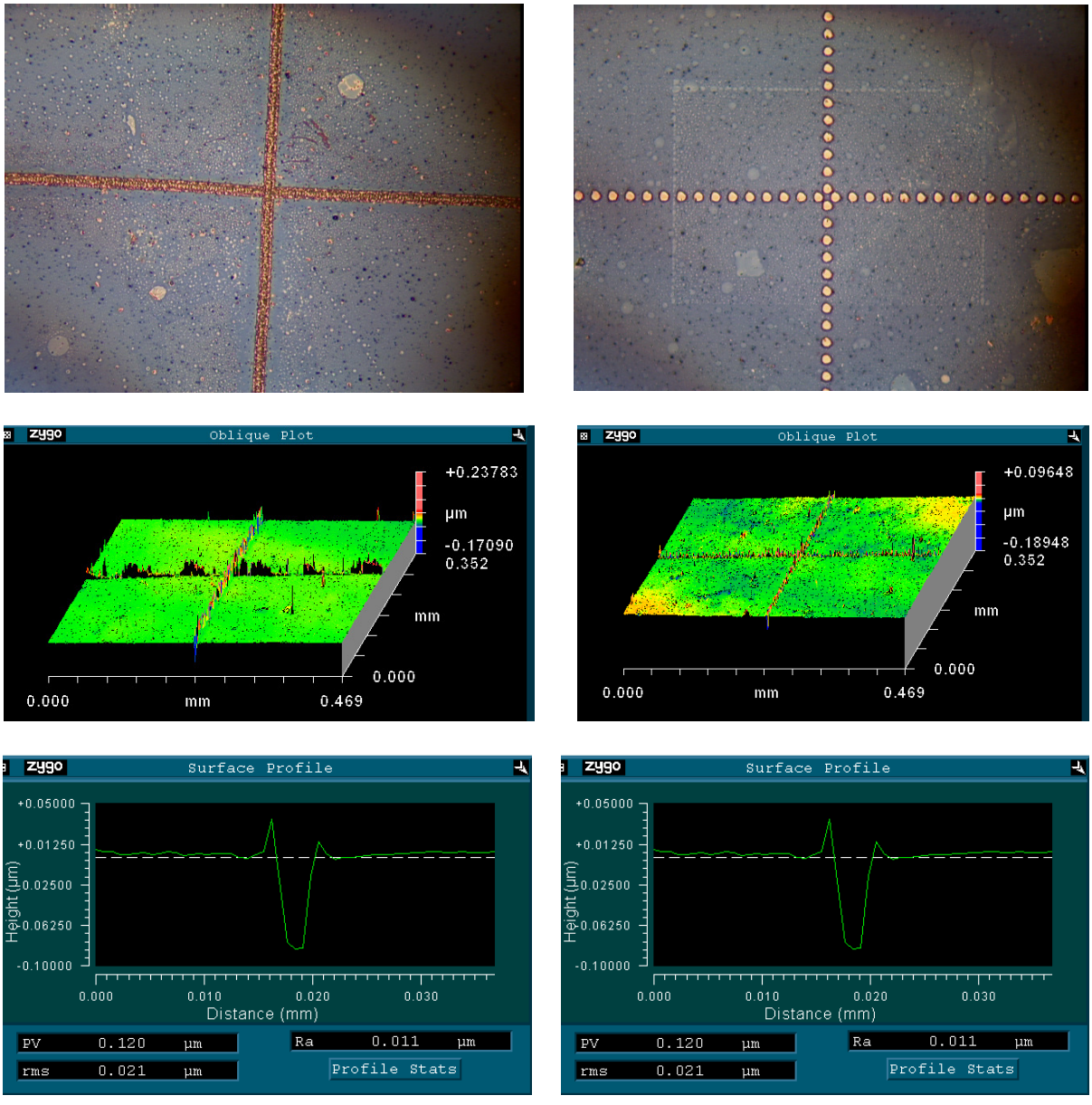

(c) 0.15 µJ, 500 mm/sec (d) 0.15 µJ, 1500 mm/sec

Figure 52: Optical images and profiolometer traces of scribed channels on $AlMgB_{14}$ thin films at low pulse energy

In ultrafast laser–material interactions, the electrons are heated to extreme temperatures by the absorption of photons and the high temperature electrons in turn exchange energy with the lattice. The electrons and the lattice reach a thermal equilibrium on a time scale that depends on the specific material. For most metals, this thermalization time is in picoseconds while for non-metals it is on the order of microseconds. Since $AlMgB_{14}$ is closer to metal and the pulse duration of laser used in our study is 30 ps, we can assume that thermalization will occur prior to ablation. As a result photothermal mechanisms of ablation govern the material removal. Thermal effects such as local heating and cooling rates, maximum temperatures and temperature gradients can all be extreme leading to enhanced diffusion rate, chemical decomposition, rapid phase transformation, highly non equilibrium structure, thermal stress and thermoelastic excitation of acoustic waves. Photothermal ablation mechanisms such as spallation, phase explosion, critical point phase separation, hydrodynamic expulsion and vaporization may vary depending on the energy fluence used [14-17]. For the 0.3 to 2 J/cm^2 used in the present work, the likely ablation mechanisms are photomechanical spallation and phase explosion. Spallation is driven by the compressive stresses and the hot-electron blast force generated by non-equilibrium hot electron gas [14]. Phase explosion occurs when a superheated metastable liquid undergoes an explosive liquid-vapor phase transition [15].

6.4. Conclusion

The effect of a picosecond pulsed laser on the ablation of ultra-hard $AlMgB_{14}$ thin film deposited on silicon substrate was investigated. Results are similar to those of semiconductor thin films used in solar cell and flat panel displays where high quality scribes free of contamination and heat affected zone, minimal damage to the underlying silicon substrate, and

complete removal of thin film were obtained at high speed and low energy fluence. As a result, new advances in the applications of ultra-hard materials for tools and bioinspired structures can be expected.

6.5. Acknowledgements

The authors sincerely acknowledge the financial support provided by the National Science Foundation under Grant No. CMMI-1067894. The authors thank Dr. Tim Gerke and Fianium, Inc for providing the picosecond laser used in this work.

6.6. References

[1] C. Dorman and M. Schulze: LTJ September 2008 No.4 (WILEY-VCH Verlag GmbH & Co. KGaA, Weinheim)

[2] S. Selleri, A. Cucinotta, F. Poli and D. Passaro: IEEE, (2009), p.1.

[3] H. Booth: Journal of Laser Micro/Nanoengineering, 5(3) (2010), p.183

[4] P. Gecys, G. Raciukaitis, M. Gedvilas, A. Braun and S. Ragnow: Laser Institute of America, Anaheim, CA, United States, 3 (2010), p.1210

[5] J. Su, D. Tanner, and C. Eberspacher, Proceedings of 23rd European Photovoltaic Solar Energy Conference, Valencia, Spain (2008), p.2479.

[6] J. Bonse, R. Patel, S. Manuef, R. Desailly, C.Devasia and D. Clark: Proceedings of 23rd European Photovoltaic Solar Energy Conference, Valencia, Spain (2008), p. 2325

[7] B. Baird, Proc. of SPIE, 7580 (2010), pp. 75800Q-1-75800Q-9

[8] B. Baird, T. Gerke, K.Wieland and N. Paudel: 26th European Photovoltaic Solar Energy Conference and Exhibition, (2011), p.2470

[9] www.Coherent.com, A Unique Laser Process for Rapid Patterning of Thin Films (2009)

[10] T.Gerke and B.Baird: ICALEO Conference Proceedings (2011), LIA, Florida

[11] B. Cook, J. Harringa, T. Lewis and A. Russell : Scripta Materalia 42 (6), (2000) p.597

[12] http://www.fianium.com/pdf/he-1064-532(v1.1).pdf

[13] A. Melaibari and P. Molian: J. Appl. Phys. 112 (2012), p. 104303

[14] E. Leveugle, D. Ivanov and L. Zhigilei: Applied Physics A: Materials Science & Processing 79 (2004) p.1643

[15] C. Cheng and X. Xu: Physical Review B 72 (2005) p.165415.

[16] F. Vidal, T. Johnston, S. Laville, O. Barthélemy, M. Chaker, B. Le Drogoff, J.Margot and M. Sabsabi: Physical Review Letters 86 (2001) p. 2573.

[17] N.N. Nedialkov, S. Imamova and P. Atanasov: Journal of Physics D: Applied Physics, 37 (2004) p. 638.

CHAPTER 7: PULSED LASER DEPOSITION TO SYNTHESIZE THE BRIDGE STRUCTURE OF ARTIFICIAL NACRE: COMPARISON OF NANO- AND FEMTOSECOND LASERS

A paper published in *the Journal of Applied Physics,* Vol. 112, 104303, (2012)
DOI: 10.1063/1.4765734

Ammar Melaibari[22, 23, 24], and Pal Molian[1, 25]

Abstract

Nature offers inspiration to new adaptive technologies that allow us to build amazing shapes and structures such as nacre using synthetic materials. Consequently we have designed a pulsed laser ablation manufacturing process involving thin film deposition and micro-machining to create hard/soft layered 'brick-bridge-mortar' nacre of $AlMgB_{14}$ (hard phase) with Ti (soft phase). In this paper, we report pulsed laser deposition (PLD) to mimic brick and bridge structures of natural nacre in $AlMgB_{14}$. Particulate formation inherent in PLD is exploited to develop the bridge structure. Mechanical behavior analysis of the $AlMgB_{14}$/Ti system revealed that the brick is to be 250 nm thick, 9 μm lateral dimensions while the bridge (particle) is to have a diameter of 500 nm for a performance equivalent to natural nacre. Both nanosecond (ns) and femtosecond (fs) pulsed lasers were employed for PLD in an iterative approach that involves varying pulse energy, pulse repetition rate and target-to-substrate

[22] Laboratory for Lasers, MEMS and Nanotechnology, Department of Mechanical Engineering, Iowa State University, Ames, IA 50011.
[23] Dept. of Mechanical Engineering, King AbdulAziz University, Jeddah, Saudi Arabia
[24] Primary researcher and lead author
[25] Co-author

distance to achieve the desired brick and bridge characteristics. Scanning electron microscopy (SEM), X-ray photoelectron spectroscopy (XPS), and optical profilometer were used to evaluate the film thickness, particle size and density, stochiometry and surface roughness of thin films. Results indicated that both ns-pulsed and fs-pulsed lasers produce the desired nacre features. However, each laser may be chosen for different reasons: fs-pulsed laser is preferred for much shorter deposition time, better stoichiometry, uniform-sized particles and uniform film thickness while ns-pulsed laser is favored for industrial acceptance, reliability, ease of handling and low cost.

7.1. Introduction

Mimicking the structures of natural composites creates enormous interest in the development of composite materials as it leads to a number of benefits: energy conversion, energy production, self-assembly, hydrophobicity, adhesion, and improved mechanical properties (Ref.1). Teeth, bones, and seashell structures were mimicked specifically for improving the strength and toughness properties. Nacre, the iridescent inner layer of seashells, is composed of approximately 95% calcium carbonate and 5% polysaccharides and proteins. Nacre exhibits a three-dimensional, hierarchical "brick-bridge-mortar" structure, where the microscale bricks and nanoscale bridges are made of $CaCO_3$ cemented together by nanoscale layers of organic mortar material (Fig.53). Nacre exhibits toughness 1000 times greater than monolithic $CaCO_3$ (Ref.2). Nacre's high toughness is attributed to the energy-dissipating configuration of the $CaCO_3$ bricks and organic 'glue', and to the interlocking of hard bricks by bridges and asperities on their surfaces. Thus, the biologically controlled growth of nacre leads to highly organized, hierarchical configuration that spans from the molecular level up to the final macroscopic structure.

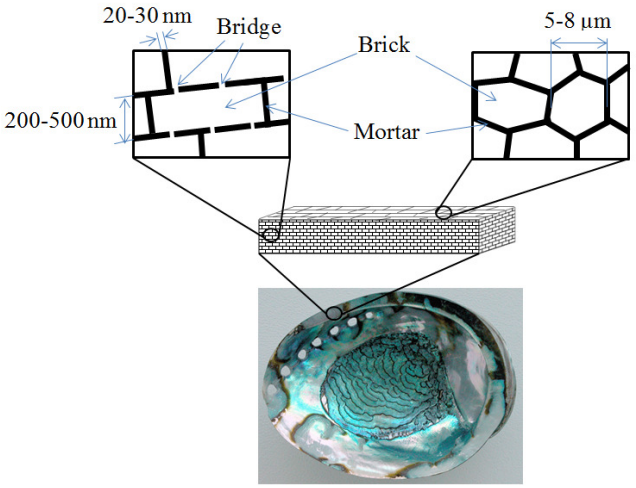

Figure 53: Schematic illustration of the structure of nacre showing salient features

Many attempts were performed to mimic the nacre's microstructure using a variety of bottom-up nanomanufacturing methods that include: (1) freeze casting, (2) layer-by-layer deposition, (3) electrophoretic deposition, (4) mechanical assembly and (5) chemical self-assembly (Ref.2-6). In all these attempts, a mineral and an organic material were used to build the 'brick-and-mortar' structure. However, these methods suffer from limitations such as long processing time, use of organic binder and the inability of the process to fabricate orderly and oriented bricks as well as achieve the desired property improvements. In the present work, a pulsed laser ablation method was utilized with a combination of inorganic materials that is capable of overcoming the above deficiencies while enabling the material to achieve the exceptional properties seen in nature. Laser is a manufacturing tool that can provide high spatial resolution, minimal contamination and high throughput in both top-down (laser micro/nano-machining) and bottom-up (laser deposition) fabrication of multi-scale materials with nano-to macro-structures. Laser has potential to overcome the challenges faced in the bottom-up only method where there may be material limitations, an inability to form complex geometries, and month-long processing times found in nature.

In this work, we considered femtosecond (fs) and nanosecond (ns) pulsed lasers to achieve the complex hierarchical structure of nacre in synthetic boron-based materials at a rapid rate. A manufacturing system employing a vacuum processing station with subtractive and additive material capabilities is being developed for this purpose. The innovation of the work also includes a high-performance synthetic composite. In order to achieve higher strength and fracture toughness than the recorded values of the other attempts to mimic nacre, ultra-hard intermetallic ($AlMgB_{14}$ designated as BAM) was combined with titanium where BAM provides strength while titanium serves as interlayer binder. Titanium is a ductile metal that can deform easily under shear stress. Successfully fabricated BAM/Ti nano-composite with nacre architecture is expected to provide unprecedented strength, toughness and lubrication for the following reasons (Ref.7-10): 1) BAM is a super-hard material (hardness of 28 to 46 GPa) while Ti is soft with strong affinity to BAM. It may be noted that BAM is the third hardest material on earth developed at Iowa State University; 2) BAM is chemically inert, thermally stable and electrically conductive as well as capable of serving as an excellent self-lubricant by forming boric acid film through oxidation and reaction with ambient water vapor; 3) The strength ratio of hard and soft phases in abalone shell ($CaCO_3$ compressive strength: 1 GPa, organic glue strength: 50 MPa (Ref.2)) is roughly 20. The selected BAM and Ti strength ratio is about 23–30; and 4) Previous study revealed that Ti interlayer with BAM resulted in strong chemical bonds (Ref.10). In addition, Ti acted as a flux material, caused in situ cleaning and resulted in substantially improved adhesion strength (Ref.10).

The method to prepare the nacre-like structure is depicted in Fig. 54 that involves three main tasks: (1) Pulsed laser deposition (PLD) of BAM to form the brick surface with nano-bridges; (2) Laser micro/nano-machining of BAM to form hexagonal bricks; (3) Sputtering of

titanium to form the mortar layer. Such a process will be repeated several times to build layer-by-layer composite. In this paper, we present the results of the first task; PLD of BAM.

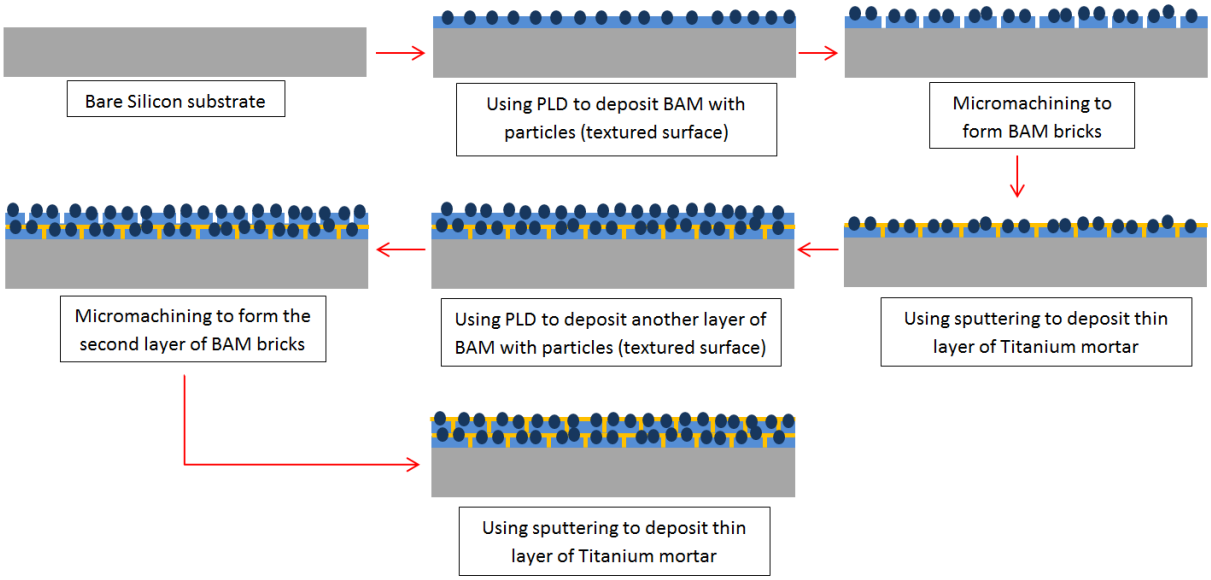

Figure 54: Flow chart of the sequence processes to create nacre-like structure

In PLD, a pulsed laser beam strikes the surface of solid target and the strong absorption of the electromagnetic radiation by the surface leads to rapid evaporation of the target material consisting of highly excited and ionized species (Ref.11, 12). A glowing, highly forward-directed plasma plume forms in front of the target surface and controls the film characteristics. The advantages of PLD include: stoichiometric deposition of complex materials; simple, inexpensive experimental setup; high-density thin films; less contamination; and capability to produce multi-layered films of different materials. The shortcomings of PLD include particulate formation, target roughening, and small area deposition. The quality, thickness, and area of the deposited film in PLD are governed by a number of variables that include: laser wavelength, pulse energy, spot size, pulse repetition rate, density and composition of target, target-to-substrate distance, vacuum or gaseous environment and film growth mechanics. In this work, laser parameters (pulse energy and repetition rate) and process variable (target-to-

substrate distance) were varied through an iterative approach to deposit BAM thin film with desired characteristics suitable for nacre-like structure.

7.2. Mechanics Approach

The approach in mimicking the nacre is to establish the appropriate dimensions of the brick and bridge structures for BAM/Ti system using mechanics of natural nacre and then use the PLD process to attain these dimensions. The mechanical performance improvements observed in natural nacre are used as the basis.

7.2.1. Calculations of Film Thickness for Nacre-like Structure:

To achieve the nacre structure's superior mechanical properties, the BAM bricks should have a specified thickness and exhibit rough surface (asperities or bridges). The brick thickness can be estimated based on the critical aspect ratio for efficient stress transfer criteria between neighboring bricks (BAM) via shear deformation in the matrix (Ti) (Ref.13):

$$\rho_n = \frac{L}{h} = 2\sqrt{\frac{2(1-\varphi_n)\Theta_n E_n}{\tau_n \varphi_n}} \qquad (1)$$

Where L is the lateral dimension of the brick, and h is the thickness of the brick. τn and Θn are, respectively, the shear strength and failure shear strain of titanium, while En and ϕn are Young's modulus and volume fraction of BAM. The shear strength of titanium, estimated as 80% of the tensile strength (Ref.14), is 265 MPa, while the failure shear strain at one level of hierarchy as in our method (n=1) can be approximated to be 35% (Ref.13). Young's modulus of BAM is 365 GPa, and the volume fraction of BAM is set at 75%. Note that the volume fraction of the hard phase in natural nacre is 95%; however, in our method we

have to reduce the volume fraction of BAM due to the limitations in depositing Ti in the spaces between the bricks (third task in Fig. 54), which are 20 nm wide and 500 nm deep. Hence, the distance between the bricks in our method is increased to account for the decreased volume fraction of BAM. Using equation (1), the critical aspect ratio for the brick dimension is determined as 36. For lateral dimensions of 5 μm and 9 μm, the thickness of brick is to be 139 nm and 250 nm respectively.

7.2.2. Calculation of Particle Size and Density of Particles for Nacre-like Structure

Nacre is stiffer, stronger and tougher than many synthetic composites. A key structural feature that enables nacre to exhibit superior properties over its harder component ($CaCO_3$) is the formation of aspirates or bridges. Meyers et al. (Ref.15) investigated the cause of failure in nacre structure. They found that the failure occur in the inter-tile region (sliding between bricks). Then, they discussed the main models suggested by other researchers before they presented their own model. The three models are; interlayer formed by (1) aspirates (Ref.16), (2) organic layer acting as viscoelastic glue (Ref.17), (3) mineral bridges (Ref.15). Based on their discussion we believe the mineral bridges model is the best model to describe the failure mechanism in the nacre structure. Therefore, we incorporated it in our design. Generating these bridges could be performed using the same PLD process that used to make the film (bricks). PLD is inherently associated with particulate formation that could be exploited to generate the bridges eliminate the laser texturing step.

It has been discovered that the improvement of compressive strength is five folds and fracture toughness (KIC) is eight folds in the direction perpendicular to the layers when nacre and monolithic $CaCO_3$ are compared (Ref.5). In this work, since the particles in thin films

produced by PLD will perform the same function as bridges in nacre, the size of these particles is estimated for our nacre-like BAM/Ti system. First, the goal is to set the expectation that our technique must improve the BAM strength and fracture toughness with the same number of folds as in natural nacre structure. BAM has a modulus of elasticity (E) of 365 GPa fracture toughness (KIC) of 4 MPa . $m^{1/2}$, and hardness (H) of 37 GPa (3773 VHN). The theoretical strength can be assumed to follow the fundamental principles (Ref.18):

$$\sigma_{th} = \frac{E}{30} \qquad (2)$$

The relation between the yield strength and hardness of BAM can be represented by the modified Tabor's expression as (Ref.19):

$$\sigma_y = \frac{VHN}{3}\,(0.1)^{m-2} \qquad (3)$$

Where VHN is Vicker's hardness number and m is Meyer's hardness coefficient. Since BAM is a brittle intermetallic material where the tensile strength (σ_t) is almost equal to the yield strength (σ_y), m can be approximated to be 2 (Ref.20). Therefore, the yield strength (σ_y) is estimated as 1258 MPa.

Assuming the material will fail by fracture of the bridges, the diameter of the bridges (D) must be equal to or larger than twice the flaw size (a). This assumption is based on the design for the worst case scenario. If the flaw size is more than half the particle size then the bridge cannot handle any force and will count as already broken. If the flaw size is less than half the particle size, the bridge would handle more force than a bridge that have a flaw equal to half of its size. Thus, the particle size ($D \geq 2a$) can be estimated from the fracture mechanics equation:

$$\sigma_{th} = \frac{K_{Ic}}{\sqrt{\pi a}} \qquad (4)$$

The fracture toughness (KIC) of BAM with nacre-like structure can be approximated as 32 MPa. $m^{1/2}$ following the eight folds increase from the original value, and the strength (σ_{th}) will be set as 60 GPa to follow the five folds increase in the theoretical strength of BAM. The critical flaw size (a) will then become 90 nm. This suggests that the particle size should be equal to 180 nm or larger. By considering that at least one third of the particle will be contained in the bricks (Fig. 55), the particle size should be around 540 nm.

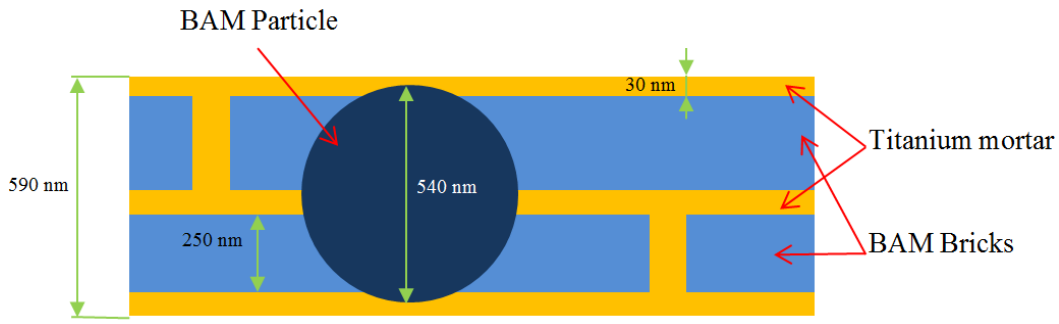

Figure 55: Schematic showing the bridge (particle) between two layers of bricks with the dimensions of nacre-like structure

The particles are contained in the bricks in the top and bottom layers. The design for at least two third of the particle to be covered by each layer for the particles to function, which will leave 300 nm gap between layers that need to be filled with the mortar layer. However, reducing the gap distance will only enforce the particles role in supporting the system. The size of the particles is very large in comparison with the brick thickness, which is a result of using different materials (more brittle than calcium carbonate) and different proportions of hard to soft phase – in our model it is 75% hard phase while artificial nacre have 95% hard phase.

The number of particles per brick can be calculated using the following equation reported in (Ref.15):

$$n = \frac{\sigma_t \, A_B}{\sigma_{th} \, A_P} \qquad (5)$$

Where AB is the brick surface area and AP is the particle cross-sectional area. In this analysis, the areas are calculated based on brick lateral dimension and particle diameter as AB= 63.6 μm^2 and AP= 0.23 μm^2 respectively. The result is 6 particles per brick which could be translated to a particle density of 1/ 10 μm^2. Thus, our goal is to find the laser parameters and other process variables in PLD that would give rise to a 250 nm thin film embedded with 0.5 µm particles for a density of one particle per ten μm^2.

7.3. Experimental Details

The first task in the preparation of nacre-like structure is the use of PLD, a bottom-up nano-manufacturing method, to deposit a 250 nm thin film of $AlMgB_{14}$ (BAM) on silicon substrate. PLD is particularly attractive for $AlMgB_{14}$ due to its potential for reproducing the multi-component target stoichiometry in the film by congruent ablation. The target used was 12-mm diameter $AlMgB_{14}$ prepared by powder metallurgy technique. Powders of $AlMgB_{14}$ phase were produced by mechanically alloying charges of aluminum, magnesium, and boron powder in the proper atomic ratios using planetary milling. One-half inch targets were made by loading about three grams of mechanically alloyed powder in a graphite die and hot uniaxially pressing the powder under an argon atmosphere. Iron and oxygen impurities react with the $AlMgB_{14}$ material to form FeB and $MgAl_2O_4$ spinel phase. After pressing, the target was ground using 45-µm diamond slurry to obtain flat and uniform surfaces.

Two types of pulsed lasers – nanosecond (ns) pulsed and femtosecond (fs) pulsed – were employed to synthesize BAM thin films since pulsed lasers are capable of heating only a

very thin layer (<100 nm) of target material, generating high energy/velocity, fine particles (ionized and excited species) (Ref.21, 22). The ns-laser used was a 248 nm, 23 ns KrF excimer (Lambda Physik Model 110). The laser being the industrial standard for PLD is capable of emitting a beam with maximum pulse energy of 300 mJ and maximum pulse repetition rate of 100 Hz. The fs-laser used was a 800 nm, 100 fs Ti:sapphire (Spectra-Physics Solstice) with a maximum pulse energy of 2.3 mJ and maximum pulse repetition rate of 1000 Hz. The ns-laser beam was focused to a rectangular spot with an area of 0.8 mm^2 while the fs-laser was focused to a circular spot with an area of 0.02 mm^2 on the target surface.

Fig. 56 is a photograph of the PLD chamber where the 12 mm diameter BAM target disc was secured. The laser beam was fired at 45o to the target. The target was spun on its axis while continuously being irradiated with the beam to provide fresh surfaces that in turn aid in uniform ablation. In the case of fs-laser ablation, the target material was rotated as well as the beam raster scanned to prevent deep ablation inside the target and to sustain the bright plasma throughout deposition. The ablated material was deposited on 25 mm diameter and 300 μm thick p-type silicon substrates. The substrate was also rotated during the deposition to allow for uniform film thickness. The vacuum chamber features an ultrahigh vacuum (10-7 torr or better), a mounting fixture for target and substrate and a resistance heating device for heating the substrate up to 773 K. Heating provides better adhesion of the film (Ref.11). Controlling vacuum chamber quality to 10-7 torr or better during PLD is essential to prevent oxide buildup at the interfaces, which would render the interfaces incoherent. In our PLD technique, the film thickness was precisely controlled by controlling the number of pulses because each pulse deposited only a minute amount (angstroms) of target material. The deposition process was facilitated by a computerized control system in which laser parameters

(i.e. energy, pulses, etc.), target rotation, target-to-substrate distance, and substrate temperature were controlled. Tables 6 and 7 show the PLD parameters for ns- and fs-lasers respectively. The effects of pulse energy, pulse repetition rate, and target-to-substrate distance on PLD of BAM were investigated to produce films suited for nacre-like configuration.

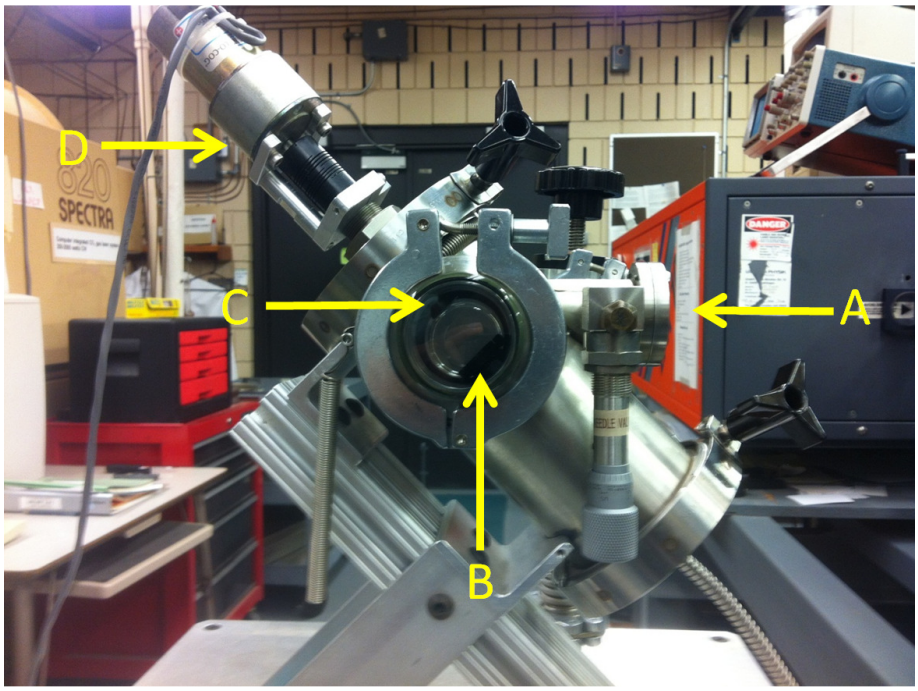

Figure 56: The PLD system where: (A) the focus lens where the laser beam passes through; (B) the substrate holder inside the vacuum chamber; (C) the target material (AlMgB14); (D) motor for target and substrate holder rotations.

Table 6: PLD parameters for samples a to g using the nanosecond pulsed laser

Sample	Pulse energy, mJ	Energy fluence, J/cm^2 [Spot size = 0.8 mm^2]	Repetition rate, Hz	Number of pulses [time duration =1 hour]	Target-to-substrate distance, cm
a	180	22.5	5	18000	5
b	150	18.75	5	18000	5
c	100	12.5	5	18000	5
d	200	25	5	18000	2.8
e	200	25	10	36000	2.8
f	180	22.5	5	18000	2.8
g	100	12.5	10	36000	2.8

Table 7: PLD parameters for samples h and i using the femtosecond pulsed laser

Sample	Pulse energy, mJ	Energy fluence, J/cm^2 [Spot size =0.02 mm^2]	Repetition rate, Hz	Time duration, min	Number of pulses	Target-to-substrate distance, cm
h	2.3	11.5	1000	10	600000	5
i	2.3	11.5	1000	20	1200000	5

Following the deposition of BAM thin films on silicon, the samples were characterized for the deposition rate, stoichiometry and particulate size/density. Fig. 57 shows an example of BAM film on the silicon substrate. Film thickness, a measure of deposition rate, was measured using an optical profilometer (Zygo NewView 7100) with 5X and 20X magnifications and accuracy of ±10 nm. The roughness readings were taken as an average for 0.5mm x 0.4mm area. Particulates were examined using a scanning electron microscope (SEM Model JEOL JSM-606LV). Stoichiometry of the films was obtained using X-ray photoelectron spectroscopy (XPS). The analysis was performed with a PHI 5500 spectrometer using Al Kα1 radiation with a 45° electron collection angle. Survey spectra were acquired in the range from 0 to 1100 eV at pass energy of 187.85 eV. The high resolution spectra of the surface constituents were acquired from samples i and g with 58.7 eV pass energy.

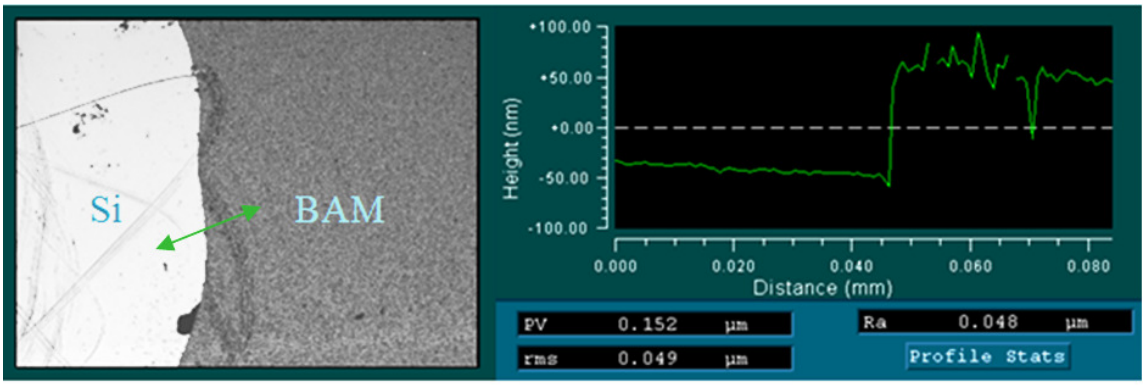

Figure 57: (a) The intensity map of the surface of sample g where the bright area is the bare Si substrate and the gray area is the BAM film; the green line is the line profile in (b) across the two areas which show the thickness of the film.

7.4. Results and Discussion

Thin film deposition by PLD consists of essentially six steps: (1) ablation of the target through mechanisms such as collisional, thermal and electronic excitation, Coulomb explosion, phase explosion, exfoliation and hydrodynamics leading to the formation of a plasma that consists of species such as atoms, molecules, electrons, ions, clusters, particulates, and molten globules; (2) bombardment of the ablated flux on the substrate surface, causing both condensation and sputtering depending on the kinetic energy and velocity of species; (3) deposition of adatoms (vapor atoms) on substrates through chemisorption (chemical bonding) and physisorption (short-range van der Waals forces); (4) surface diffusion and mobility of the adatoms, governed by the substrate temperature, through several atomic distances before becoming incorporated into the film; (5) nucleation and growth of the film leading to two-dimensional, layer-by-layer (Frank–van der Merwe) or three-dimensional, island (Stranski–Krastanov) deposition depending on lattice matching of substrate and film; and (6) development of topography and crystallography.

An iterative approach involving four parameters - pulse energy, pulse repetition rate, target-to-substrate distance and pulse width/wavelength – is applied to find the best possible combination that would control the deposition in such a way that the desired film thickness (250 nm), particle size (500 nm) and particle density (one per 10 μm^2) could be achieved. The effects of these four parameters on film thickness, surface roughness, particulate size/density and stoichiometry are described below while keeping in perspective of thin film deposition events elucidated in the previous paragraph.

7.4.1. Effects of Nanosecond Pulsed Laser

7.4.1.1. Pulse Energy

Pulse energy or energy fluence (pulse energy/spot area) is the most dictating parameter in PLD affecting the film thickness and surface morphology. Table 8 shows the film thickness and surface roughness of PLD samples. Film thicknesses are under 200 nm for the typical one hour deposition and surface roughness data are well within nanoscale. As expected surface roughness increases with an increase in pulse energy. Fig. 58 (a, b, and c) shows the effect of pulse energy on particulate formation. Increasing the pulse energy from 150 mJ to 180 mJ almost doubled the particle size and density while reducing the pulse energy from 150 mJ to 100 mJ almost eliminated the particulate matter implying the strong role played by pulse energy. In contrast to particulate formation, there is only minimal effect on film thickness when pulse energy was increased from 150 mJ to 180 mJ. The slight decrease in film thickness in the 180 mJ (sample a) is attributed to the creation of large-sized particles.

Table 8: Average thickness and surface roughness of films

Sample	Surface roughness (Ra), (nm)	Film thickness, (nm)
a	13	100
b	7	110
c	1	-
d	80	120
e	9	150
f	93	130
g	1	85
h	7	100
i	7	220

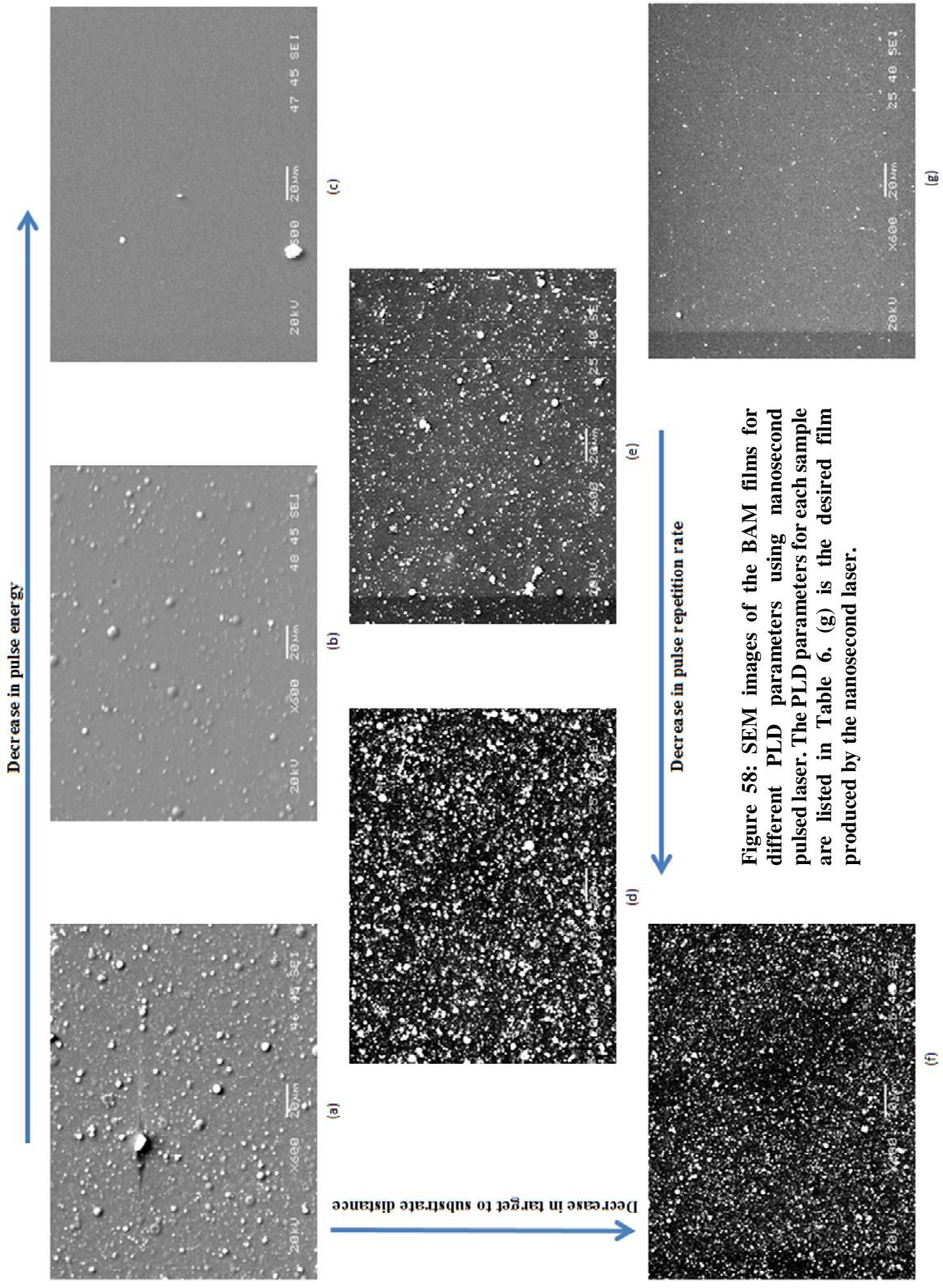

Figure 58: SEM images of the BAM films for different PLD parameters using nanosecond pulsed laser. The PLD parameters for each sample are listed in Table 6. (g) is the desired film produced by the nanosecond laser.

Pulse energy is the leading parameter in the generation of adatoms and particles from the target material (Ref.23). For the pulse energies used in this work, a mixture of adatoms and particles is generated through thermal ablation. An increase in pulse energy increased the ablated mass, the ablated depth, and the target surface temperature leading to an increase in the ablated material in the plume; this enhances the collisions among atoms and condensed particles resulting in the formation of thicker films and micro-sized particles. Similar findings were observed in many other studies [Ref.24, 25]. The particulate formation is enhanced by the kinetic energy associated with the ablated material prior to deposition (Ref.26) and by inhomogeneous laser heating that causes segregates (Ref.27), or phase explosion (Ref.28). The ns-laser ablation is known to produce large numbers of molten droplets by hydrodynamic sputtering. During the ns-pulse, a sizable depth of material expands rapidly as it is heated and liquefies. When the deeper regions of the molten irradiated area solidify and contract, liquid droplets of the surface can be ejected. Films produced at high energies invariably had many particles on their surfaces that were at least as large as 10 μm across. Low pulse energies were, however, found to be effective at reducing the number of micro particles (molten droplets). It may be inferred that the formation of such droplets can affect the stoichiometry of the film (Ref.26).

7.4.1.2. Pulse Repetition Rate

Although not common, pulse repetition rate can be effectively used to reduce the particulate density. In Fig. 58 (d and e), the number of micro particles is reduced significantly by increasing the pulse repetition rate. The film thickness and surface smoothness were increased by increasing the repetition rate from 5 Hz to 10 Hz (Table 8). However the particle

size remained more or less the same. Such findings agree well with a recent study (Ref.24) that the relation between the pulse repetition rate and the particle size was independent while there was a close correlation between the mass concentration of particles and the pulse repetition rate.

The effect of pulse repetition rate can be explained through its effect on the density of the ablated materials in the plume (Ref.24, 26), and the time interval it takes the adatoms to condense on the surface (Ref.29, 30). Increasing the density of the ablated material will increase the number of nucleation sites in the film resulting in smaller particles (Ref.31), increased particle density in the film (Ref.24), and increased film thickness as well (Ref.26). The time interval between pulses affects the film morphology during the film growth process. If the time interval is too long (low repetition rate), the adatoms from each pulse will set at the nucleation sites separately from the adatoms generated from the next pulse which degrade the bonding between each layer in the deposited film; this will also limit the diffusion of the new adatoms to fill the voids in the film. If the time interval is too short (high repetition rate), the adatoms will not have enough time to reach the right position in the nucleation sites due to the rapid formation of the next layer.

High repetition rate can also accumulate energy on the target surface, causing an increase in surface temperature and lowering ablation threshold. Such accumulation of energy from many pulses leads to strong ablation of materials. Film growth in PLD process shows that the island density is governed by the pulse repetition rate. At low rates, there is such a longer interval between pulses enabling the islands to ripen thus reducing the total island density. In contrast, with increased rates, the islands will be dispersed resulting a much higher island density. One problem related to high repetition rates is the overall increase in target

temperature, which favors material segregation. In the case of $AlMgB_{14}$, segregation of $MgAl_2O_4$ spinel phase may occur due to the differences in melting temperatures.

7.4.1.3. Target-to-Substrate Distance

The target-to-substrate distance (TSD) is another major factor that affects the characteristics of thin films during deposition. Fig. 58 (a and f) shows a decrease in TSD leads to an increase in particle density - should be in number per area while Table 8 shows an increase in film thickness and surface roughness with decreasing TSD. Also, decreasing TSD increases the variation in film thickness between the center of the sample and the edges. Sample (a) has a uniform gray color on the whole surface, while sample (f) has a dark color in the center and reddish color on the edges indicating optical transparency effects of film thickness variations. It has also been previously reported that the variation in film thickness increases with decreasing TSD (Ref.32). This can be illustrated by considering laser plasma as a sprayer with a cone angle; using a small distance between the sprayer and a surface will result in small covered area. Therefore, increasing TSD will assist in obtaining a uniform film thickness.

When TSD increases the surface roughness decreases as a result of the change in surface morphology. Serhiy et al (Ref.33) explained the effect of TSD based on the reaction time of adatoms. In the case of small TSD, the reaction time is very short for the highly energetic adatoms resulting in an incomplete coalescence that will create voids between the growing grains. If the density of the voids is high enough, each group of voids will merge together creating valleys which in turn increase the roughness. With large TSD, the ablated material will have more chances to coalesce in the plume along the way creating larger particles. At the same time, this will reduce the number of micro particles since they are

accumulating together. The overall film surface is smoother even with the larger particles. On the other hand, the kinetic energy associated with the particles upon impingement on the substrate surface will change with the changes in TSD. If the particle energy is high enough, the particles will bounce back out of the film surface or will break the weak bonds in the large particles when it hit the surface, and that's why large particle (≥5 μm) are absent in Fig. 58 (f). Using smaller or larger TSD from the optimal one will affect the crystallinity. The incomplete coalescence leads to a weak bonding in small TSD while the insufficient kinetic energy in large TSD leads to high strain in the bonding which degrades the crystallinity (Ref.33).

While large TSD is attractive for many reasons, the major drawback is the low deposition rate that in turn reduces film thickness. Zheng and Kwok found that the deposition rate varies inversely with square of TSD (Ref.34); this effect is attributed to the possible collisions among atoms, ions and clusters with the ambient environment that could be expressed as PD^2 = constant where P is the ambient pressure and D is TSD (Ref.35). If the substrate is far away, the surface activation by moderately energetic ions and atoms will not be available and consequently the deposition rate, particle size and density will be low.

7.4.1.4. Particulate and Particulate-free Thin Film

Deposition of particulates on thin film is one of the key issues in PLD. The particulates are classified as: nanoparticles and clusters (<100 nm), growth and coalescence of clusters to form sub-μm particles, solidified melt droplets with diameters between 0.1 and 3 μm (due to hydrodynamic instabilities), irregularly shaped solid grains with diameters between 1 μm and 10 μm (due to thermal stresses), and solidified splash droplets with diameters > 10 μm (due to superheating and liquid-phase expulsion). The physical mechanisms include the target sub-

surface boiling, expulsion of the liquid layer by shock wave, and segregation and coalescence in the collision region. Such particulates will affect the growth of the subsequent layers, locally degrade the microstructure, increase the surface roughness, reduce the minimum width of features in micromachining and affect optical, electronic and mechanical properties. As a result, many efforts were undertaken to eliminate the particulates or, at least, reduce their size and density. The density of coarse particulates can be drastically reduced by selecting the proper target material (density, outgassing, surface smoothness) and increasing the aspect ratio (length to width) of the plume through larger laser spot sizes and/or higher fluences. Other techniques are: inserting a shadow mask to block off the large particulates; keeping a large distance between target and substrate; rotating both the target and substrate to produce uniform films.

In order to obtain a smooth and almost particle-free surface (Fig. 58 (c)), lower pulse energy, higher pulse repetition rate, and larger TSD must be employed. Since there are no particles formed through the coalescence of atoms in the plume at low pulse energy in this study, there was no difference in using either 5 Hz or 10 Hz. This can be explained by the collision mechanism as: even with less ablated material in the plume and the larger mean free path between the ablated material in the plume, the ablated species do not have enough energy to coalesce more than a few times and the binding energy between the condensed particles in the plume are so weak that it will break when it hits the substrate surface. The few large particles exist on the surface could be a result of different particle formation mechanism such as segregates. For example the spinel phase of BAM ($MgAl_2O_4$) could be the reason for these segregates. Elimination of these large particles is important since it will affect the micromachining of the tablets in the nacre-like material.

The best set of process parameters that provided controlled particle size in the range of 0.5~1 μm are pulse energy of 100 mJ, repetition rate of 5 Hz and 2.8 cm TSD (Fig. 58 (g)). However the film thickness was only 80 nm for one hour of deposition time; this can be increased to 250 nm by increasing either pulse repetition rate or deposition time or both.

7.4.2. Effects of Femtosecond Pulsed Laser

Ultrashort (<picosecond) pulsed lasers are emerging tools for PLD because pulse width can significantly change plasma dynamics and accordingly affect film thickness, particulate size and its density, crystallinity and stoichiometry. Experimental trials shown in Table 7 using the 100 fs-pulsed Ti:sapphire laser produced fairly uniform particles of 0.5 μm (Fig. 59) for a film thickness of 100 nm in 10 minutes and 220 nm in 20 minutes (Table 8, samples h and i). It is important to note that the deposition rates in nm/sec are much higher than obtained with the ns-pulsed laser. A comparison with ns-pulsed excimer laser shows that fs-pulsed laser could deposit films six times faster and, that too, at lower energy fluences. The surface roughness was also comparable to those of ns-pulsed laser (Fig. 60). The most interesting observation was the uniformity in film thickness that could be attributed to the larger plasma plume developed in fs-pulsed ablation. X-ray photoelectron spectroscopy results of the film stochiometry for two selected films (samples g and i) from ns- and fs-PLD are shown in Table 9. The stoichiometry of BAM films produced by ns-pulsed laser and fs-pulsed laser was 1:1:7 and 1:1:10 respectively for Al:Mg:B indicating that there is deviation in the ratios among the elements from the original 1:1:14 stochiometry.

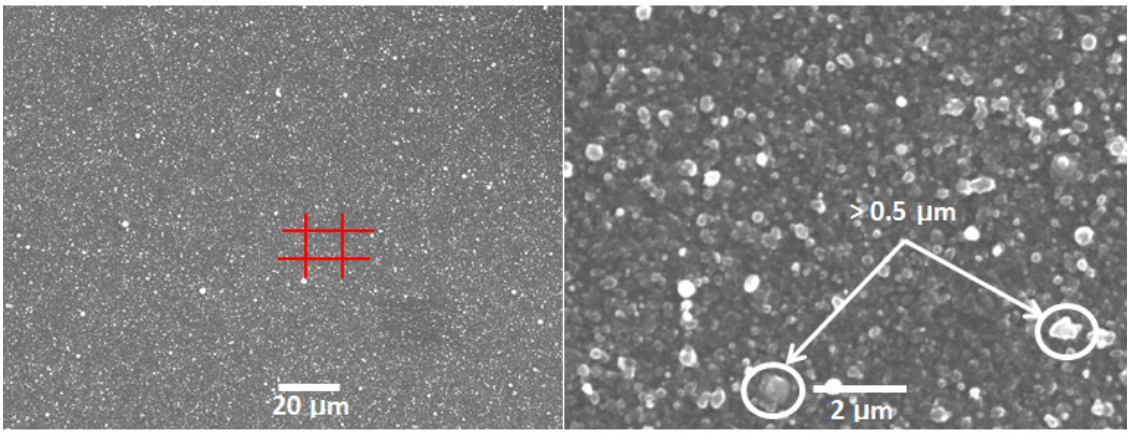

Figure 59: SEM images of the BAM film deposited using fs laser where the PLD parameters are: 5 cm distance between BAM target and Si substrate, 2.3 mJ pulse energy, 1000 Hz repetition rate: (a) Low magnification where the square shows 10x10 µm2; (b) High magnification where the circles showing particles > 0.5 µm size.

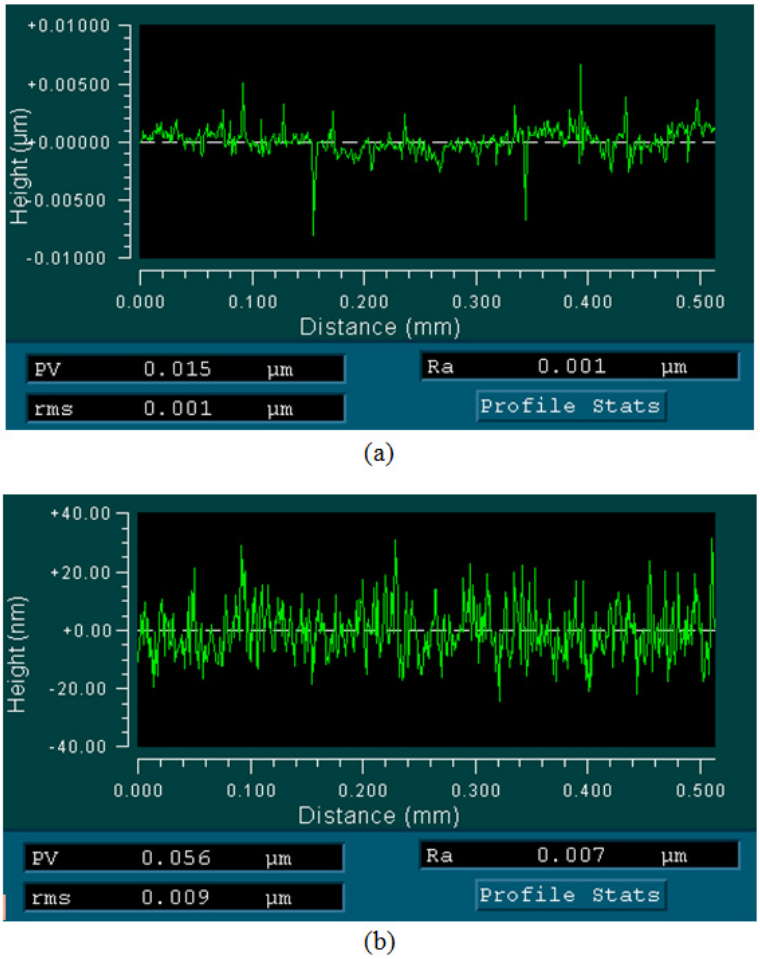

Figure 60: Surface profile using optical profilometer for sample g (a), and sample i (b) showing the surface roughness.

Table 9: Atomic percent of the desired films using XPS.

Sample	laser	B	Al	Mg
g	Nanosecond	77	12	10
i	femtosecond	83	8	9

The key performance characteristic of PLD is film thickness per unit time. Excimer lasers with ns-pulses ablated and deposited BAM for a film thickness in the range of 80 to 150 nm per hour depending primarily on the energy fluence. In contrast, fs-pulsed lasers offered much higher film thickness of 500 nm to 750 nm per hour for the same energy fluence. Three factors appear to contribute to the difference: pulse repetition rate, particulate formation and surface roughening of the target. Since fs-lasers operate at much higher frequencies (>100 times), it is expected that the film thickness could be higher than that of ns-lasers for a specified time. In addition, the reduction in particulate density of the film and surface degradation of target with fs-pulsed lasers enhanced film thickness. However, on a pulse basis, fs-laser deposits smaller amount of material than ns-pulse.

In comparison to ns-PLD for the same processing conditions, fs-PLD offers higher film thickness, better stoichiometry, more uniform film thickness and fewer particulates for BAM thin films. A comparative study of ablation using ns- and fs-lasers under similar energy fluences showed that the fs-pulses produce well-defined plasmas and are more efficient at producing a greater concentration of high-charge state and high-energy ions (Ref.36). The fs-laser plasma stretches in one dimension whereas the ns-laser plasma expands in three dimensions (Ref.37). The initial temperature rise within the irradiated region is also much more rapid in the case of fs-pulses leading to phase explosion as opposed to thermal evaporation of the transiently heated target surface in ns-pulses. In fs-ablation, the input energy is expended

by vaporization of the ablated volume, high degree of ionization and kinetic energies of the emitted species. For example, the kinetic energy of species in ns-PLD can be up to several 10 eV while it is up to 103 eV for fs-PLD. Thus, high-energy species in fs-pulsed laser ablation may induce self-sputtering, thermal spikes, etc. but aids in improving the film adhesion to the substrate and enhancing surface diffusion of adsorbed atoms/molecules. One unique feature observed in fs-PLD of superconducting thin films is the creation of nanoscale melt droplets in contrast to the micron-sized spheroidal particles from ns-PLD (Ref.38). Coulomb explosion coupled with multiphoton ionization are said to be the controlling mechanisms in the formation of nanostructures. Thus, the fs-PLD plasma exhibits nanoparticles in addition to high energy ions and atoms. The fs-laser deposited films were often found to be crystalline that could be attributed to surface diffusion of adatoms and resulting in increased crystallographic order.

7.5. Conclusion

The brick and bridge structures of $CaCO_3$ in natural nacre were mimicked in a superhard $AlMgB_{14}$ material by pulsed laser deposition. Both ns-pulsed and fs-pulsed lasers were capable of producing the desired sizes of these features. However, the fs-pulsed lasers were preferred due to shorter deposition time, uniform sized bridges, uniform brick thickness, better stochiometry and absence of large particulates. Although fs-laser appears to be the choice for producing $AlMgB_{14}$ thin films by PLD, ns-pulsed excimer lasers can also be accepted due to their well-established acceptance in the industry, reliability, ease of handling and relative low cost.

7.6. Acknowledgments

The authors sincerely acknowledge the financial support provided by the National Science Foundation under Grant No. CMMI-1067894 for this work. The authors also appreciate the scholarship provided by King AbdulAziz University and thank Mr. James Anderegg of the Ames Laboratory for assistance in XPS characterization of samples.

7.7. References

[1] B. Bhushan, Phil. Trans. R. Soc. A 367, 1445 (2009).

[2] M. A. Meyers, P. Y. Chen, Y. M. Lin, Y. Seki, Progress in Materials Science 53, 1 (2008).

[3] J.L. Arias, M.S. Ferna´ndez, Materials Characterization 50, 189 (2003).

[4] Z. Tang, N. A. Kotov, S. Magonov, B. Ozturk, nature materials 2, 413 (2003).

[5] G. M. Luz, J. F. Mano, Phil. Trans. R. Soc. A 367, 1587 (2010).

[6] E. Munch, M. E. Launey, D. H. Alsem, E. Saiz, A.P. Tomsia, R. O. Ritchie, Science 322, 1516 (2008).

[7] B. A. Cook, J. L. Harringa, T. L. Lewis, A. M. Russell, Scripta materialia 42, 597 (2000).

[8] B. A. Cook, J. L. Harringa, T. L. Lewis, A. M. Russell, Y. Lee, Journal of Advanced Materials 36, 56 (2004).

[9] R. Cherukuri, M. Womack, P. Molian, A. Russell, Y. Tian, Surface and Coatings Technology 155, 112 (2002).

[10] Y. Tian, A. F. Bastawros, C. C. H. Lo, A. P. Constant, A. M. Russell, B. A. Cook, Applied physics letters 83, 2781 (2003).

[11] M. Jelinek, V. Trtik, L. Jastrabik, edited by R. Kossowsky, M. Jelinek, J. Novak, Pulsed laser deposition of thin films, “Physics and Materials Science of High Temperature Superconductors, IV,” NATO science series, Volume 26, Part III, (Springer Netherlands, 1997) p. 215-231

[12] J. Dieleman, E. van de Riet, J. C. S. Kools, Jpn. J. Appl. Phys. 31, 1964 (1992).

[13] Z. Zhang, Y. Zhang, H. Gao, Proc. R. Soc. B 278, 519 (2010).

[14] http://www.kobelco.co.jp/english/titan/files/details.pdf (Accessed on 06/26/2012)

[15] M. A. Meyers, A. Y. Lin, P. Chen, J. Muyco, Journal of Mechanical Behavior of Biomedical Materials 1, 76 (2008).

[16] R.Z. Wang, Z. Suo, A.G. Evans, N. Yao, I.A. Aksay, J. Mater. Res. 16, 2485 (2001).

[17] G. Evans, Z. Suo, R.Z. Wang, I.A. Aksay, M. Y. He, J. W. Hutchinson, J. Mater. Res. 16, 2475 (2001).

[18] H. Gao, B. Ji, I. L. Jager, E. Arzt, P. Fratzl, Proceeding of the National Academy of Sciences of the United States of America 100, 5597 (2003).

[19] J.R. Cahoon, W.H. Broughton, A.R. Kutzak, Metallurgical and Material Transactions B 2, 1979 (1971).

[20] R. Morales, S. Seetharaman, V. Agarwal, J. Mater. Res. 17, 1954 (2002).

[21] Y. Tian, M. Womack, P. Molian, C. H. Lo, J.W. Andreegg, A. M. Russell, Thin Solid Films 418, 129 (2002).

[22] M. Stock, P. Molian, Journal of Vacuum Science and Technology A 22, 670 (2004).

[23] H. Sankur, J. T. Chung, Applied Physics A 47, 271 (1988).

[24] L. Landstrom, Zs. Marton, N. Arnold, H. Hogberg, M. Boman, P. Heszler, Journal of Applied Physics 94, 2011 (2003)

[25] M. Mendes, R. Vilar, Applied surface science 217, 149 (2003).

[26] E. W. Kreutz, J. Gottmann, phys. stat. sol. (a) 166, 569 (1998).

[27] Y. Watanabe, M. Tanamura, S. Matsumoto, Y. Seki, Jornal of applied physics 78, 2029 (1995).

[28] W. Siew, W. Lee, H. Wong, T. Yong, S. Yap, T. Tou, Appl Phys A 101, 627 (2010).

[29] L. Guan, D. Zhang, X. Li, Z. Li, Nuclear Instruments and Methods in Physics Research B: Beam Interactions with Materials and Atoms 266, 57 (2008).

[30] W. Zhaoyang, S. Liyuan, H. Lizhong, Vacuum 85, 397 (2010).

[31] Y.-L. Wang, W. Xu, Y. Zhou, L.-Z. Chu, G.-S. Fu, Laser and Particle Beams 25, 9 (2007).

[32] R. K. Singh, J. Narayan, Physical Review B 41, 8843 (1990).

[33] S. V. Pysarenko, A. V. Pan, S. X. Dou, IEEE transactions on applied superconductivity 21, 3179 (2011).

[34] J.P. Zheng, H.S. Kwok, Thin Solid Films 232, 99 (1993)

[35] H. S. Kim, H. S. Kwok, Appl. Phys. Lett. 61, 2234 (1992).

[36] Z. Zhang, P. A. VanRompay, J. A. Nees, P. P. Pronko, J. Appl. Phys. 92, 2867 (2002).

[37] X. Zenga, X. Mao, R. Greif, R. E. Russo, Ultraviolet femtosecond and nanosecond laser ablation of silicon: ablation efficiency and laser-induced plasma expansion (Lawrence Berkeley National Laboratory, 2004) http://www.osti.gov/bridge/servlets/purl/836676-ys4GaX/native/836676.pdf (Accessed on 06/26/2012)

[38] R. Eason, Pulsed Laser Deposition of Thin Films (John Wiley and Sons, Inc., Hoboken, New Jersey, 2007).

CHAPTER 8: LASER SHOCK PROCESSING ON MICROSTRUCTURE AND HARDNESS OF POLYCRYSTALLINE CUBIC BORON NITRIDE TOOLS WITH AND WITHOUT NANODIAMOND POWDERS

A paper published in *the Journal of Materials and Design,* Vol. 35, p. 235-242, (2012)

Roslyn Melookaran[26,27], Ammar Melaibari[1,28,29], Cheng Deng[1,4] and Pal Molian[1,4]

Abstract

High amplitude, short duration shock waves created by a 1064 nm, 10 ns Q-switched Nd:YAG laser were used to increase the hardness as well as build successive layers of nanodiamond on sintered polycrystalline cubic boron nitride (PcBN) tools. Multiple scans of laser shocking were applied. Scanning electron microscopy, Raman spectroscopy, Tukon microhardness tester, and optical surface profilometer were used to evaluate the microstructure, phase change, Vicker's microhardness and surface roughness. Results indicated that laser shock processing of plain PcBN changed the binder concentration, caused phase transition from cubic to hexagonal form, increased the hardness, and almost unaffected surface roughness. Laser shock wave sintering of nanodiamond powders on PcBN resulted in deagglomeration and layer-by-layer build-up of nanoparticles for a thickness of 30 lm inferring that a novel solid freeform technique designated as ''shock wave induced freeform technique

[26] Laboratory for Lasers, MEMS and Nanotechnology, Department of Mechanical Engineering, Iowa State University, Ames, IA 50011.
[27] Primary researcher and lead author.
[28] Dept. of Mechanical Engineering, King AbdulAziz University, Jeddah, Saudi Arabia.
[29] Co-author

(SWIFT)'' is being discovered for making micro-tools. Depending on the number of multiple laser shocks, the hardness of nanodiamond compact was lower or higher than that of PcBN. It is hypothesized that nanodiamond particles could serve as crack deflectors, increasing the fracture toughness of PcBN.

8.1. Introduction

Cubic boron nitride (cBN) is one of the hardest materials known to mankind, exceeded only by diamond. Unlike naturally-existing, covalently-bonded diamond, cBN is a synthetic material exhibiting both covalent and ionic bonds. Consequently cBN surpasses diamond in thermal and chemical stability while retaining high atomic density (1.68×10^{23} cm^{-3}) and maximum hardness of 70 GPa. Besides the cubic form, BN exists in four other allotropes: hexagonal BN (hBN), rhombohedral BN (rBN), explosive BN (eBN), and wurtzitic BN (wBN) [1]. The three phases – hBN, rBN and eBN – are softer with trigonal sp^2 bonded structures while the other two phases – cBN and wBN – are harder with tetrahedral sp^3 bonded structures. Furthermore, amorphous BN (highly disordered structure) and turbostratic BN (disordered, graphitic-like structure) were also found. Among all the forms of BN, cBN is the most thermodynamically stable phase at standard conditions [2] although it is formed from hBN under extreme pressures and temperatures [1].

One significant application of cBN is cutting tools used in machining of hard ferrous alloys [3]. Extensive works have been reported on the use of polycrystalline cubic boron nitride (PcBN) as high-performance cutting tools in the industry [4–7]. Although polycrystalline diamond (PCD) is much harder and more wear resistant, PcBN has superior thermal and chemical stability required for machining ferrous alloys. PcBN tools are made by mixing hBN

powders with a binding agent (usually a metal like Al or ceramic such as TiN), in a hydraulic press machine with six-way or two-way diamond anvils. The mixture is then sintered at high pressures (6–8 GPa) and high temperatures (1773–2273 K) [3, 8]. During sintering, the powder particles undergo both plastic deformation and chemical reaction with the binder in a complex fashion that is not fully understood [9, 10]. Depending on the grain size (1–20 μm) and type of binder and its volume fraction, the hardness of PcBN tools can vary from 30 GPa to 70 GPa. PcBN is also resistant to chemical attack up to 1500–1600 K in the presence of ferrous metals [11]. PcBN cutting tools are used in precision machining and finishing of hard-to-machine materials allowing for higher levels of productivity, accuracy and reliability in manufacturing [12, 13].

Despite their superior mechanical and physical properties and cutting performance, the PcBN tools suffer from lower toughness and higher production cost. Consequently its applications are limited to finish and semi-finish machining of hard materials. In order to extend PcBN's application to rough and interrupted machining such as milling, the microstructure and composition of PcBN must be modified to increase its toughness. In this paper, we present the potential use of laser shock treatment with and without nanodiamond powder to change the mechanical properties.

Laser shock processing (LSP) is a novel method of strain hardening the materials through compression; it has been successfully applied to increase the hardness and fatigue strength of metals such as aluminum alloys [14–16]. The process involves the use of a high intensity, nanosecond pulsed laser to deliver the high-amplitude stress waves through the target material. Shock waves are generated by laser vaporizing a thin layer of sacrificial material having a low heat of vaporization such as black paint deposited on the surface of target material

and forming plasma between the target and the transparent overlay such as glass. The confinement of plasma by the overlay enhances the amplitude and duration of the pressure pulse and increases the shock wave pressure levels thereby causing structural changes, residual stresses and densification in the target material. It may be noted that the sacrificial material protects the target material from melting and vaporization.

LSP has potential to make PcBN as one of high-performance, high-functionality materials. In addition, embedding or layering of nanodiamond (4–8 nm) in PcBN can further enhance hardness and toughness making it useful for rough and interrupted machining. Under the pressures of LSP (up to 5 GPa), nanodiamond powders can be sintered in cold condition. Nanodiamonds have increased surface area to volume ratio and exhibit higher surface reactivity than microcrystalline diamond. Applications for nanodiamond include deposition of wear and corrosion-resistant metal coatings, cooling fluids, and lubricants [17].

Recently there is a spur of research activities in developing cBN/ nanodiamond composites (both bulk sintered and thin films) for improving the electronic and mechanical properties. Synthetic PcBN was prepared by powder metallurgy with the addition of nanodiamond, titanium, aluminum and silicon at 5.5 GPa 1200 ^{o}C for 500 s [14]. Nanodiamond reacted with silicon, titanium and aluminum to form various compounds leading to superhardness, high heat resistance and high stability. There was no graphitization of nanodiamond during the sintering process due to the presence of silicon [18]. Another work dealt with the growth of cBN/nanodiamond composite thin films by plasma enhanced CVD for improved properties [19].

In this paper we report the effects of LSP on the microstructure, phase transition, hardness and surface roughness of PcBN cutting tool with and without the addition of

nanodiamond. A groove type of structure on PcBN by direct laser irradiation was created prior to the addition of nanodiamond powder. Fig. 61 shows a schematic of LSP of PcBN with a layering of nanodiamond powder. The rationale for using nanodiamond is twofold: (1) due to its fine size (4–8 nm), nanodiamond can fill in the voids between cBN crystals and the binder and thereby increasing the density of PcBN; (2) due to large surface area-to-volume ratio, nanodiamond can react easily with binders to form various carbides and thereby increasing the strength and hardness of PcBN or exist as individual particles offering toughness to PcBN.

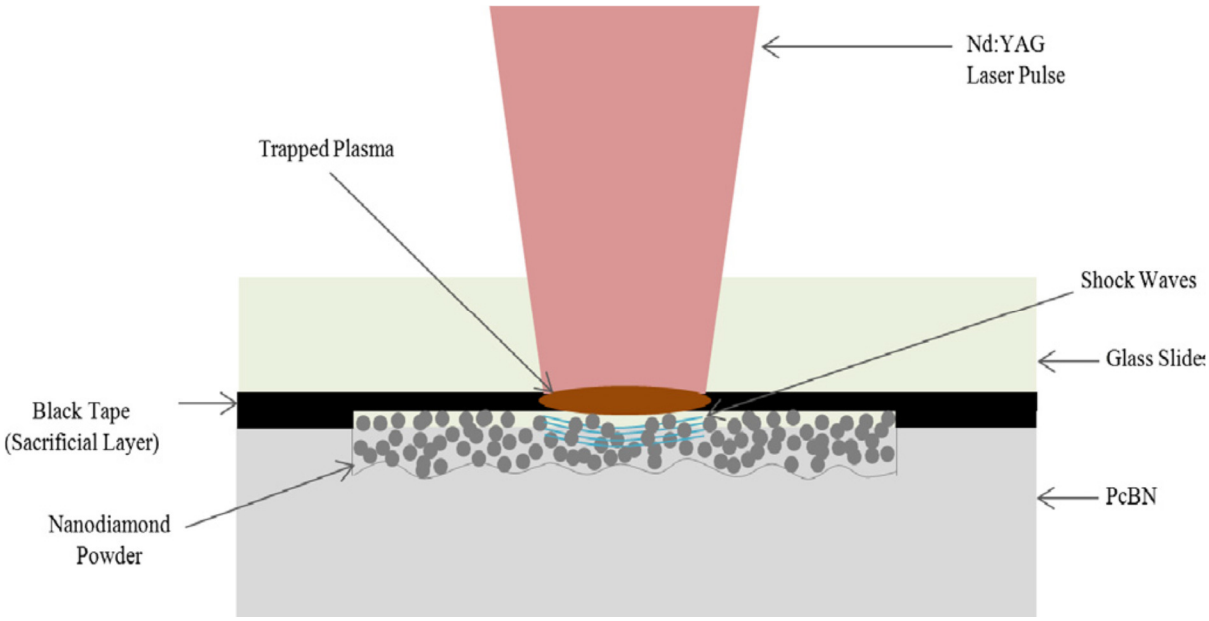

Figure 61: Schematic diagram of laser shock processing of PcBN with nanodiamond powder.

8.2. Experimental Details

The PcBN blanks with a nominal diameter of 50 mm (Grade HTM), received from Diamond Innovations, Inc. (Ohio, USA), consisted of 0.8 mm thick PcBN layer bonded to a tough 0.8 mm thick tungsten carbide (WCA13% Co) substrate. The PcBN layer is composed of 2 µm size cBN particles embedded in a TiN matrix. The composition of PcBN is 50% cBN,

45% TiN and 5% AlN by volume. The nanodiamond powders (90% purity, 4–8 nm in size, spherical/ elliptical particles produced by the detonation of explosives) were procured from Ukraine (sintal@yandex.ru). The surfaces of the nanodiamond particles contained many functional groups such as hydroxyl, carbonyl, carboxyl and ether-based resin.

A 1064 nm, Q-switched Nd:YAG laser (Quantel 481 near diffraction- limited beam) was employed to create high amplitude, short duration shock waves. The laser parameters were set at pulse width of 10 ns, average power of 2W and frequency of 10 Hz. A defocused beam of 1 mm diameter was used throughout the experimentation with a calculated peak power density of 2.55 GW/cm^2. Typical range of peak power density for laser shock processing is 1–5 GW/cm^2 [16].

The PcBN samples were subjected to LSP by applying a black tape (0.21 mm thick) as a sacrificial layer (to protect the sample's surface from direct ablation and melting) followed by placement of a transparent overlay (microscope glass slide, 1 mm thick). A thin layer of high vacuum grease was used to secure the glass slide on the sample. The overlay assists in increasing the shockwave intensity by confining the expanding plasma and thus the pressure developed propagates through material causing densification of the sample [14].

For PcBN samples without the addition of nanodiamond (B1 through B5 in Table 10), five different samples each with a size of 6.4 x 6.4 mm were prepared and laser shocked from one to five scans at a x–y positioning stage speed of 0.5 mm/s in x-direction and a movement of 0.75 mm in y-direction; such parameters allowed for a horizontal overlap of 95% and a vertical overlap of 25%. Increased overlap was preferred because it was reported that multiple shocks of a region would increase the plastically-affected depth [16].

Table 10: Sample designations and associated experimental conditions.

Designation	Sample	Treatment	Thickness of nanodiamond layer (µm)
A1	PcBN	Untreated	-
B1	PcBN	One time of LSP	-
B2	PcBN	Two times of LSP	-
B3	PcBN	Three times of LSP	-
B4	PcBN	Four times of LSP	-
B5	PcBN	Five times of LSP	-
C1	20 µm depth-grooved PcBN	One layer of nanodiamond and one scan of LSP	3 µm from the bottom of groove
C2	20 µm depth-grooved PcBN	Five layers of nanodiamond and one scan of LSP for each layer	31 µm from the bottom of groove
C3	20 µm depth-grooved PcBN	One layer of nanodiamond and five scans of LSP	14 µm from the bottom of groove
C4	20 µm depth-grooved PcBN	One layer of nanodiamond and 10 scans of LSP	13 µm from the bottom of groove

For the PcBN samples with nanodiamond powder, grooves were first produced for an area of 3.8 mm x 3.8 mm on the PcBN using the identical laser parameters as in LSP (no overlay and no sacrificial layer). The average depth of grooves based on 10 measurements was recorded as 20 ± 2 µm. After depth measurements were taken, nanodiamond powders were layered flush with the top of the sample surface and little above. The black tape (sacrificial layer) was then glued on the top of sample and around the grooved area to act as a shallow fence for nanodiamond powders. The glass slide was mounted on the sample using a thin layer of grease and then subjected to LSP. Finally, the samples were rinsed in acetone to remove the excess powders and residues of black tape. Samples C1 through C4 were prepared as listed in Table 10. For C1, one nanodiamond layer was added and then shock processed in one laser scan. For C2, LSP was repeated five times (five scans), each time adding a new layer of nanodiamond. For C3, one layer of nanodiamond was applied but LSP was repeated five times (five scans). For C4, one layer of nanodiamond was applied but LSP was repeated 10 times (10 scans). It may be noted the 0.2 mm thick black tape lasted for three scans of LSP after which it was replaced. The thickness of nanodiamond layer from the bottom of groove was

measured using an optical microscope with a resolution of 1 μm. Ten measurements were performed for each case and the average value was recorded.

Raman spectroscopy of LSP regions was performed to identify the phase transitions using Ar-ion laser with a 20 μm entrance slit width, 50mW laser power, and 488 nm operating wavelength. A scanning electron microscope (SEM) operating at 20 kV (Oxford EDS system JEOL 6060LV) in the secondary electron mode was then used to examine the microstructure of PcBN and uniformity of nanodiamond powder compaction. A Wilson Tukon microhardness testing machine was used to measure the Vickers hardness of LSP regions. The loading conditions were a 1 kg load and a dwell time of 10 s. The diagonals of indentations were measured using a Nikon Eclipse microscope coupled with a CCD camera at 1000x magnification. At least 10 hardness measurements were made per sample to get an average hardness value and a standard deviation. Finally surface roughness was evaluated using the Zygo New View 5000 series optical profilometer with 20x objective.

8.3. Results and Discussion

8.3.1. Laser shock processed PcBN samples (B2–B5)

Fig. 62 shows the microhardness test data of both untreated and laser shock processed samples. A maximum hardness of 4500 kg/mm^2 (45 GPa) was obtained in sample B2, with an increase in microhardness of 15% over untreated PcBN; such an increase in hardness could be attributed to a number of factors including plastic deformation of cBN particles, phase transition of hBN, development of residual stresses, stress fracturing of binder phases and reduction in porosity and other flaws due to densification. Maximum hardness was reached only after two scans of LSP. Although successive laser scans allow for increased strain

hardening and build-up of compressive residual stresses deeper into the surface which assist in increasing the hardness [14], there may be other deleterious effects such as removal or dissolution of binder materials and transformation of cBN to hBN that might have caused a loss in hardness. Let us now examine the evidence for hardness changes from SEM images and Raman spectroscopy data.

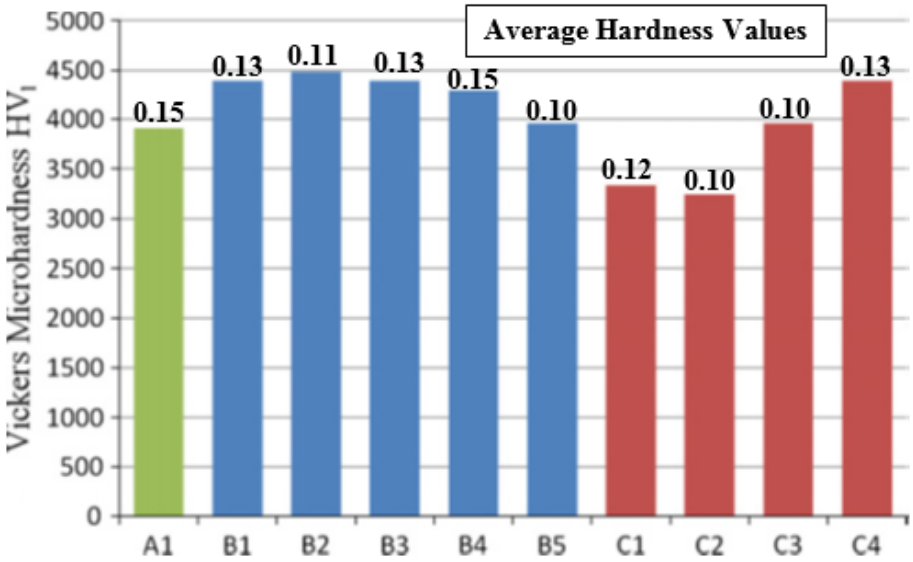

Figure 62: Average microhardness values of PcBN samples with and without nanodiamond. Coefficient of variation is listed above each bar.

SEM images of untreated and laser shock processed PcBN as a function of number of scans are presented in Figs. 63 and 64. The microstructure of untreated sample (Fig. 63) consists of 2 µm-sized particles of cBN (dark) and sub-lm sized particles of AlN (light) in a matrix of TiN (gray). The microstructure is homogenous and the binding phase is uniformly distributed in its volume. The micrographs do not reveal any detectable pores within this scale suggesting that the material is nearly fully densified. Although not shown here, PcBN is likely to contain structural defects namely dislocations and microtwins and TiB_2 at the interfaces and

grain boundaries based on transmission electron microscopy analysis of cBN/TiN systems [20, 21].

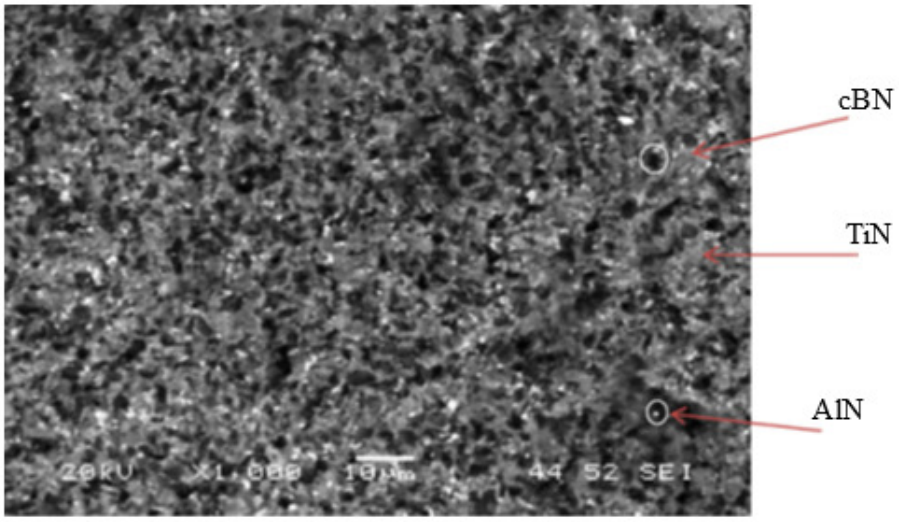

Figure 63: SEM image of untreated PcBN sample (A1).

After LSP, the particle size and volume fraction of cBN remained nearly same; however, there was a significant reduction in the amount of AlN (Fig. 64). In sample B5, AlN has almost disappeared indicating the following plausible explanations: one is the stress fracturing and dissolution of AlN in the TiN matrix to form a solid solution of TiN and AlN; other is the stress fracturing and removal of AlN leaving fine porosity. Both can contribute to the reduction in hardness. It can be seen from Fig. 62 that hardness first increases with number of shocks and then decreases upon further increase of shocks. There is an increased plastic deformation with increase in shocks. However, multiple shocks may break the binder particles bridging the cBN grains, thus reducing the hardness of the material. In addition, phase transformations result in hardness changes.

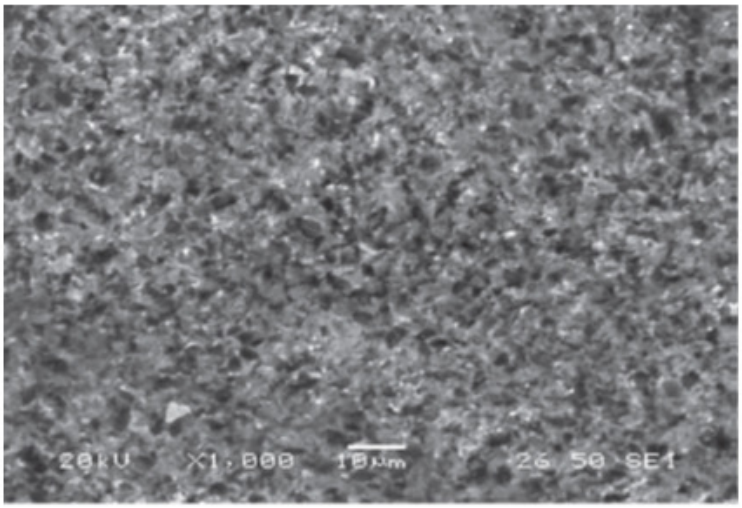

(a) Sample B2

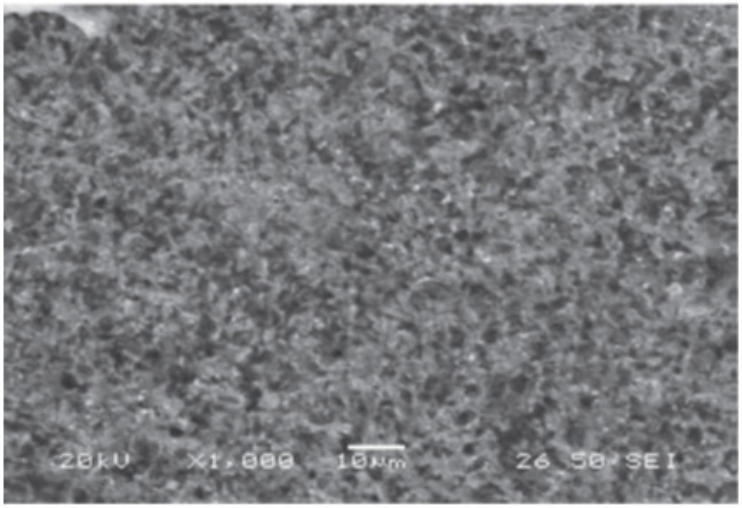

(b) Sample B5

Figure 64: SEM images of laser shock processed PcBN samples: (a) LSP two times (B2) and (b) LSP five times (B5).

Raman spectrum of untreated PcBN sample (Fig. 65) shows four Raman peaks: 1069, 1201, 1319, and 1579 cm^{-1}. The weaker intensity peaks and wider widths are typical of polycrystalline samples compared to single crystalline samples. The position of Raman peaks and their full width at half maximum (FWHM) in PcBN depends on the grain size, residual stresses, impurities, binder, extent of plastic deformation and defects. Peaks at 1069 and 1319

cm^{-1} are correlated with TO and LO phonon scattering that originates from the cBN phase. The peak positions of cBN are upshifted from the values corresponding to the single crystalline cBN, which typically have TO and LO peaks at 1056 and 1304 cm^{-1}, respectively. The upshifted and broadened peaks can be attributed to the plastic deformation which takes place during the sintering process [22], a reduction in the crystallite size during the sintering process [23] and the presence of impurities/defects which comes from the binder materials [24]. The 1201 cm^{-1} peak can be assigned to a boron-doped phase [25] which could be generated by some defects in the sample during the sintering process. The 1579 cm^{-1} peak is correlated with the eBN phase which typically has a peak around 1588 cm^{-1} [26].

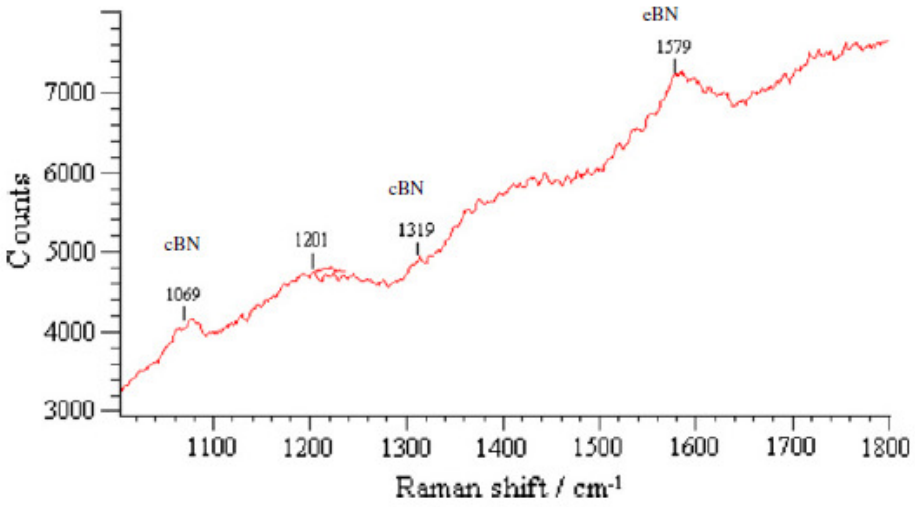

Figure 65: Raman spectrum of sample A1 (untreated).

After laser shocking two times (Fig. 66), the cBN peaks are downshifted slightly to 1067 and 1310 cm^{-1}. The position of Raman peaks can be used to characterize the residual stresses. Experiments have provided that a Raman shift of 3.39 ± 0.08 cm^{-1}/GPa for the TO Raman peak and 3.45 ± 0.07 cm^{-1}/GPa for the LO Raman peak [27]. Based on this data, LSP-induced residual stresses can be calculated in the range of 0.6–2.6 GPa. Such stress values are also observed in other processes such as CVD and PVD. For example, a plasma CVD process

induced 2–3 GPa residual stresses in cBN thin films which are even lower than those obtained with PVD films [19]. Analysis of diamond-indented single and polycrystalline cBN samples resulted in shifts of the Raman lines from their unstressed positions and indicated a compressive stress field with stresses ranging from 0.07 to 0.3 GPa [22].

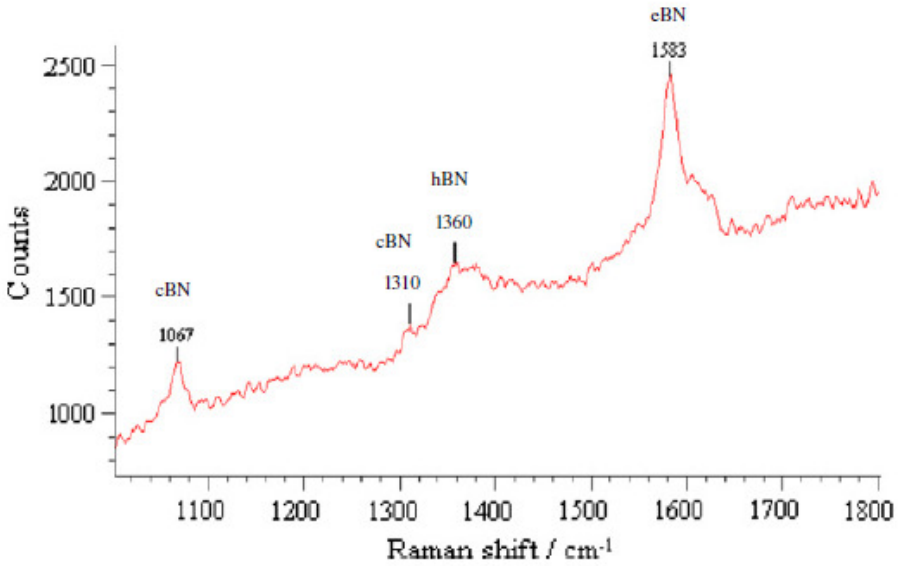

Figure 66: Raman spectrum of sample B2 (two times LSP).

In sample B2, the disappearance of the 1201 cm^{-1} peak and the presence of the 1360 cm^{-1} peak indicate a transformation of cBN to hBN which typically has a 1366 cm^{-1} peak [1]. It should be mentioned that the characteristic peak of hBN (1366 cm^{-1}) is much stronger than that of cBN because the scattering coefficient of hBN is two orders of magnitude higher than that of cBN [19]. The eBN peak was also upshifted and the peak became sharper. The reason for the upshift is not clear at the moment; however, the sharpness of the peak suggests an increase of the transformation of cBN to this phase. Increasing the number of laser scans seems to increase the transformation of cBN to hBN and eBN phases. In the Raman spectrum of the sample subjected to LSP five times (Fig. 67), the hBN and eBN peaks become sharper while

the cBN peak almost disappeared. Thus, the loss in hardness with five times LSP is primarily attributed to a change from hard cBN to soft hBN phase. It is hypothesized that multiple shock wave compression creates lattice strain and defects and results in the strain accumulation leading to conversion of cBN into hBN by some sort of diffusion mechanism.

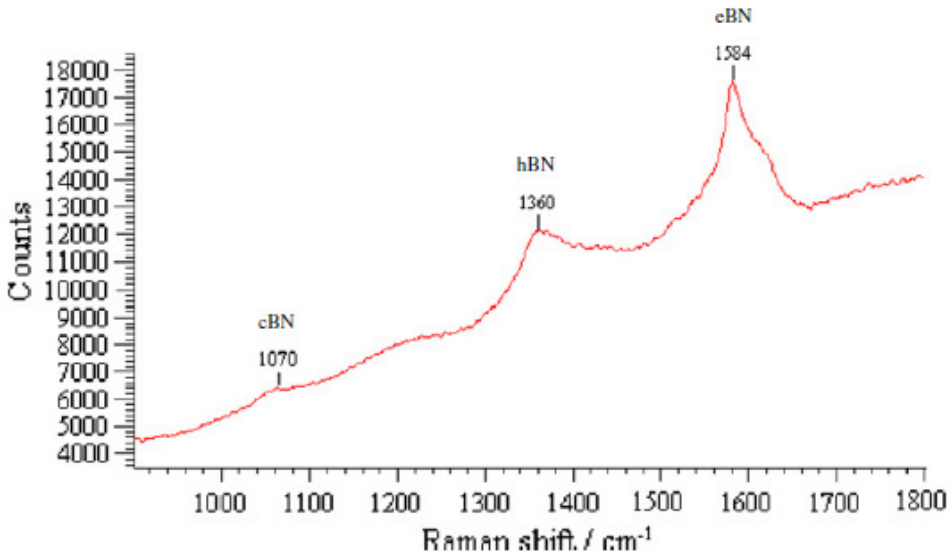

Figure 67: Raman spectrum of sample B5 (five times LSP).

Optical profilometer traces (Figs. 68 and 69) of LSP treated PcBN show that surface roughness parameters (Ra, rms, peak-to-valley) have slightly increased with the number of laser scans. Untreated PcBN has an even distribution of peaks and valleys with a Ra of 0.421 µm. With LSP scans, the Ra increased marginally and the formed surface has concentrated areas of peaks and valleys. The loss of AlN particles leaving a porous structure on the surface might have also contributed to the surface roughness.

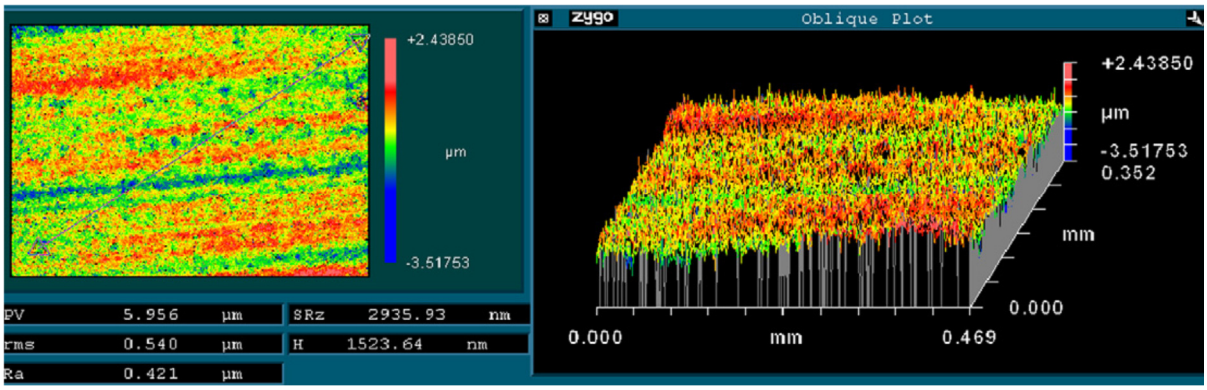

Figure 68: Optical profilometer trace of untreated PcBN (sample A1).

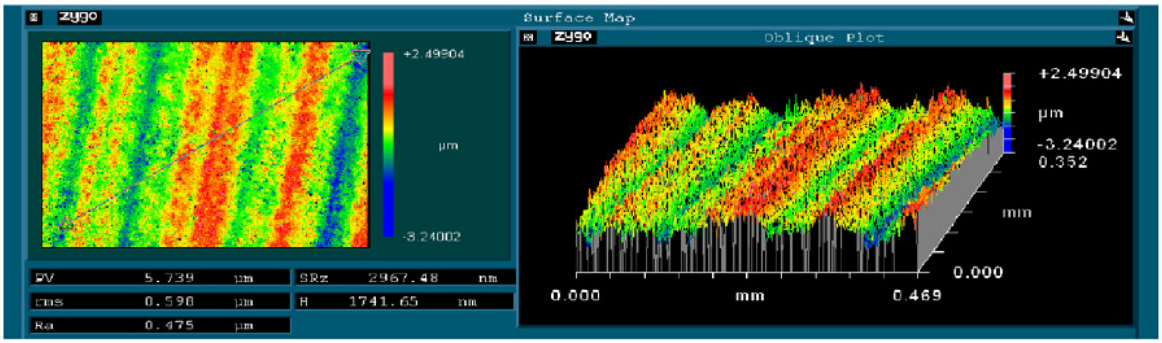

(a) Sample B2

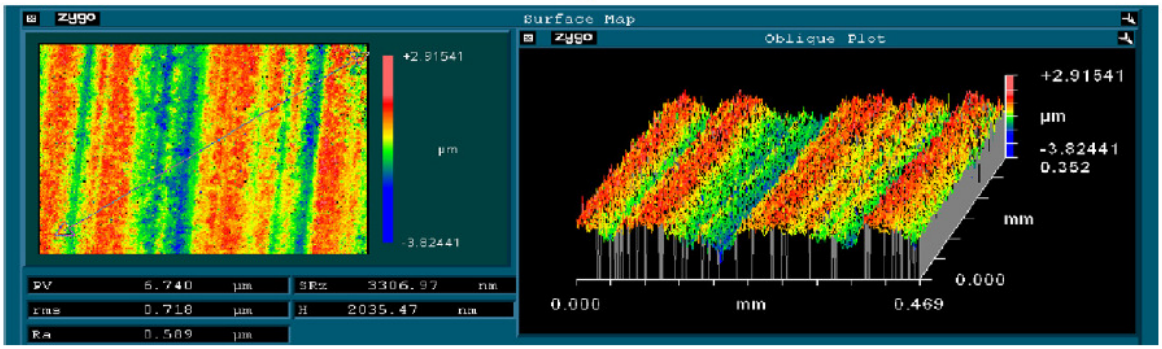

(b) Sample B5

Figure 69: Optical profilometer traces of LSP treated PcBN: (a) sample B2 and (b) sample B5.

8.3.2. Laser shock processed PcBN samples with nanodiamond

Table 10 shows that the thickness of nanodiamond deposit on PcBN by LSP depends on the number of scans and number of nanodiamond layer additions. It may be noted that without the groove formation, there is no bonding of nanodiamond on the PcBN substrate.

With only single layer nanodiamond powder, the average rate of deposition was about 3 μm per scan for up to five scans after which the number of scans do not appear to influence the deposit thickness. It is believed that significant amount of shock wave energy is to be expended initially to bind the nanoparticles in the grooves. However, rapid build-up of thickness occurs if nanodiamond powders are added in between scans. For example, sample C2 exhibits a total average thickness of 31 μm (11 μm above the baseline surface of the PcBN) in five scans. Multiple laser scans thus increased densification and reduced the amount of loose powders.

Microhardness test data shown in Fig. 62 indicates that best results were obtained with multiple LSP scans over the same area. In samples C1 and C2 (one scan per layer), the microhardness was lower due to lower densification of nanodiamond and agglomeration that skewed the microindentation process. However, the sample C4 processed with 10 scans had much improved densification, reduced agglomeration and better bonding for a net 12% increase in hardness over untreated PcBN. It may be noted that nanodiamonds are not hard unless fully consolidated. For example, plasma pressure compaction of detonation synthesized nanodiamond between 700 and 1200 ^{o}C under 65 MPa pressure yielded only porous pellets having a hardness of only 0.2 GPa [17]. Microhardness of high-purity detonation nanodiamond in 100% dense form was reported to be 30–35 GPa [28]. Nanodiamond compacts sintered from high purity, 25 nm size diamond crystals at high pressure of 8 GPa and temperature above 1500 ^{o}C produced hardness of 50 GPa [29].

PcBN usually fails in a brittle manner with rapid crack propagation throughout a stressed material. The resistance of PcBN to crack propagation can be significantly enhanced by the grain size and by adding various reinforcements such as secondary phase particles, whiskers and fibers. In the present study, we hypothesize that nanodiamond particles contribute

to weak interfaces and high residual stresses between cBN and nanodiamond as a result of their thermal expansion difference; this will allow the crack to be deflected away leading to improved toughness in PcBN.

SEM micrographs displayed in Fig. 70 illustrate that the agglomeration of nanodiamond is reduced upon multiple scans (compare C1 and C3). The pressure from the shock processing is great enough to break down the nanodiamond agglomerates, and disperse them more evenly over the area. Sample C2 exhibited similar sized agglomerates as in C1, but there was also varying heights in relation to the base of the groove. Sample C3 has the smallest and most evenly dispersed agglomerates.

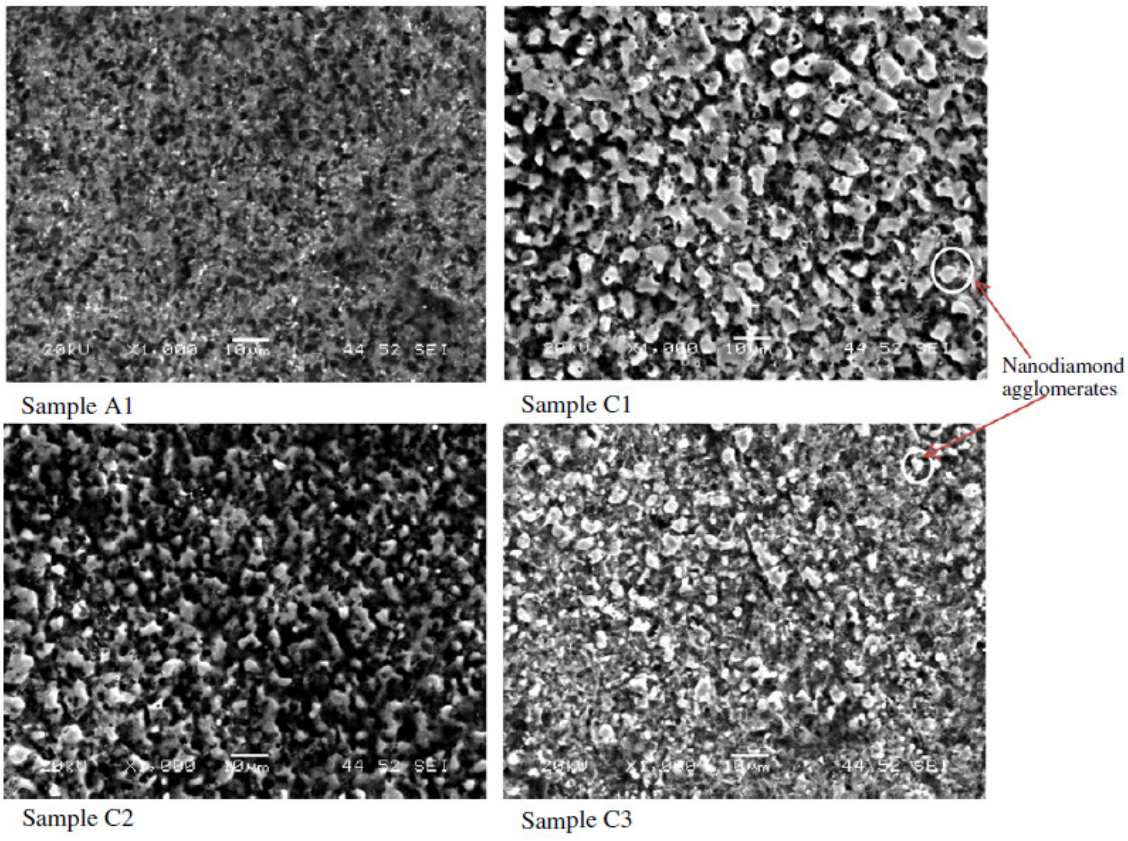

Figure 70: SEM images of laser shock hardened PcBN with nanodiamond powders.

Raman spectroscopy analysis of sample C1 revealed the presence of nanodiamond and different phases resulting from the reactions of nanodiamond and BN, as shown in Fig. 71. The 1329 cm^{-1} is attributed to nanodiamond [30]. The cBN peaks almost disappeared. The TO mode at 1048 cm^{-1} can be seen very broad, which is due to the possible increase in residual stresses, while the LO mode around 1304 cm^{-1} disappeared completely in the dispersion of the spectrum. The 1201 cm^{-1} peak, which is related to the boron- doped phase that existed in the untreated sample, can be still seen here. Another phase, such as boron carbonitride with a 1360 cm^{-1} (D bond) and 1600–1620 cm^{-1} (G bond) [31, 32], is also noted even though the D bond for this phase does not appear clearly on the spectrum. The 1397 cm^{-1} and 1601 cm^{-1} peaks show the C=N bonds. The 1700 cm^{-1} peaks, which are close to the theoretical carbonyl peak, could be an indication for the addition of oxygen, upon air exposure, to the C=N bond as in Aramid.

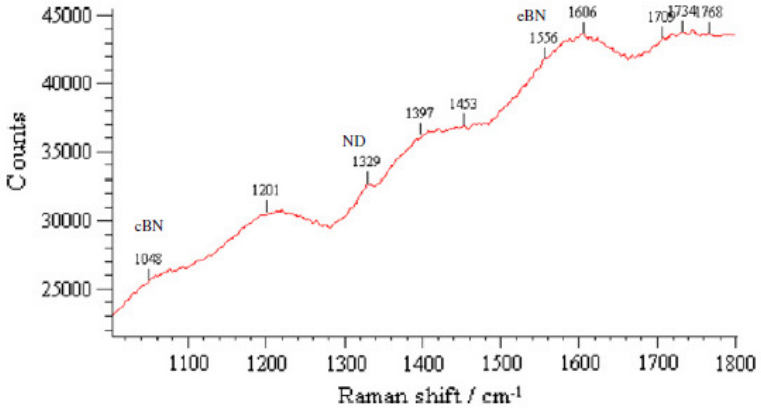

Figure 71: Raman spectrum of sample C1.

The observations for the case of one layer of nanodiamond with one scan are the same for the case of five layers of nanodiamond with one scan for each (Fig. 72). The peaks are shifted slightly since the residual stresses increased with each pass. Increasing the number of

scans on one layer of nanodiamond (Fig. 73) increased the transformation of cBN to hBN and nanodiamond to graphite. Note that, the peak at 1593 cm^{-1} can be a result of either an upshifted eBN peak, or the appearance of boron carbide. The C=B bond has a peak at 1590 cm^{-1} [33]. Studies on the microstructural characterization of diamond films deposited on cBN crystals by microwave plasma CVD revealed shifting of Raman peaks that is attributed to thermal stresses caused by the difference in lattice parameter and thermal expansion between diamond and cBN [34].

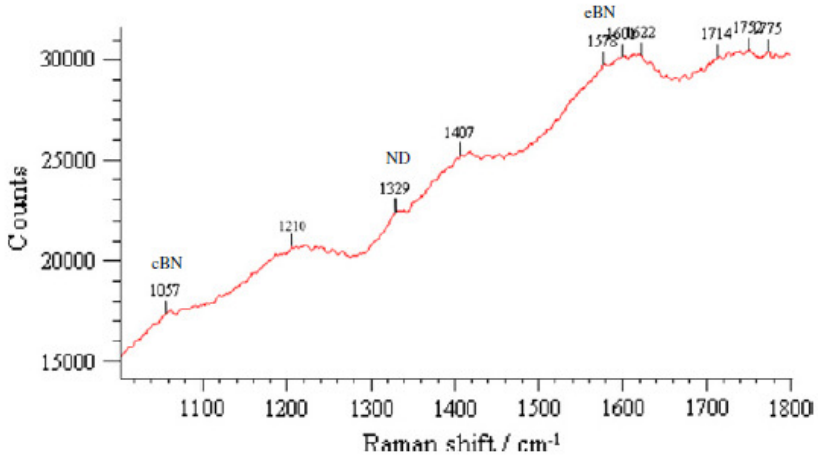

Figure 72: Raman spectrum of sample C2.

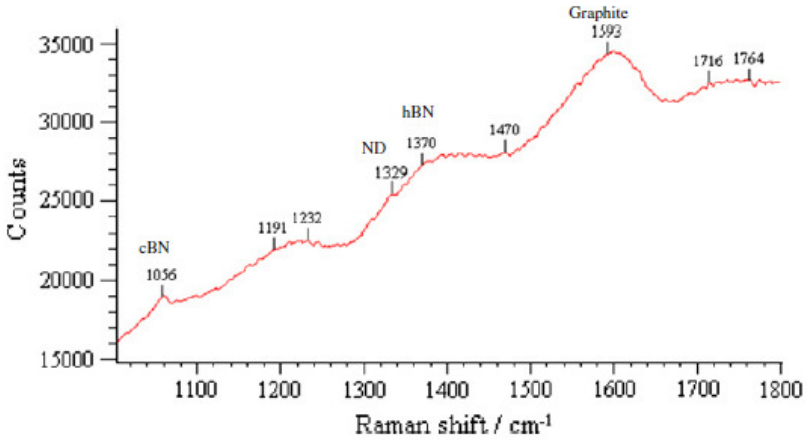

Figure 73: Raman spectrum of sample C3.

Groove formation coupled with nanodiamond addition and compaction by LSP has increased surface roughness in samples C1–C3 (Fig. 74). Sample C3 has the largest Ra value (0.688 µm) due to multiple bombardments while sample C2 has the highest peak to valley (PV) due to the addition of multiple layers of nanodiamond and uneven compaction.

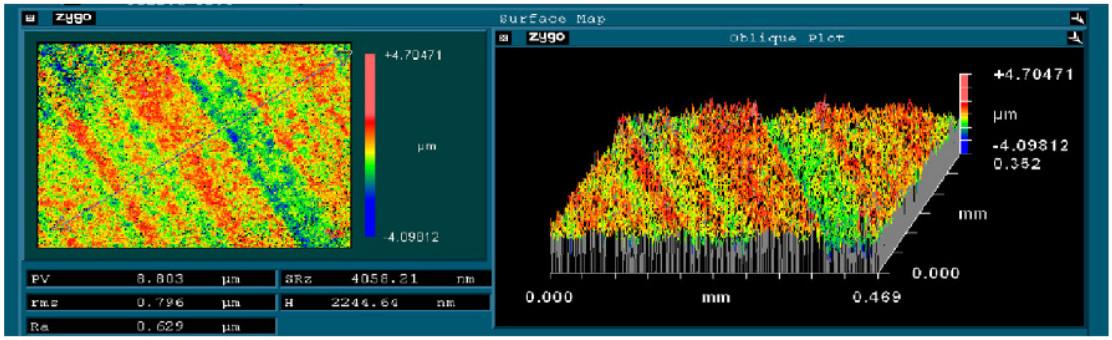

Sample C1

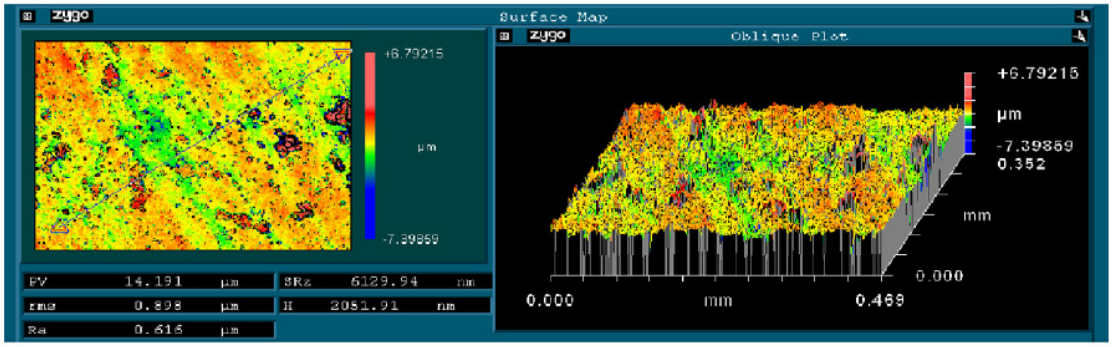

Sample C2

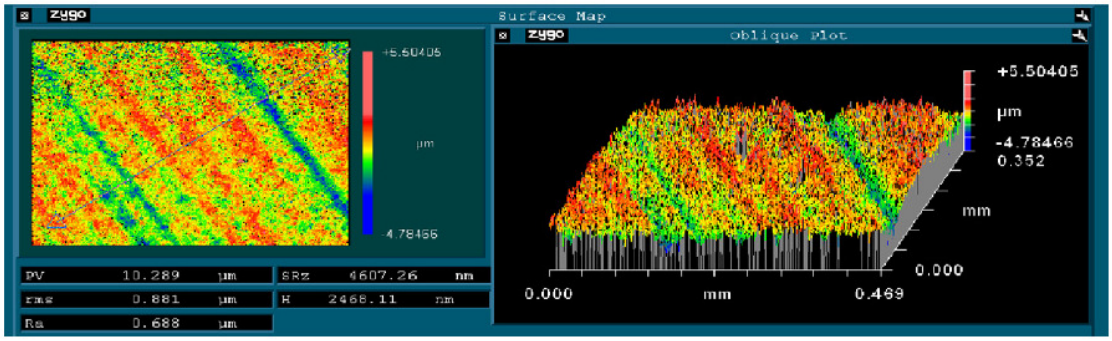

Sample C3

Figure 74: Optical profilometer traces of LSP treated PcBN with nanodiamond.

8.4. Conclusions

Laser shock processing of polycrystalline cubic boron nitride (PcBN) caused phase transformation and significant changes in hardness and microstructure. The key parameter that influenced the results was multiple shocks. A maximum of 15% increase in hardness was obtained with two scans under the non-optimized laser parameters. Laser shock sintering of nanodiamond powders on PcBN led to a potential solid freeform fabrication technique of building layer-by-layer to form a micro-diamond tool. The hardness of nanodiamond compacted by laser shock waves was 12% higher than that of PcBN. Multiple shocks not only increased the hardness but also broke down the agglomerates and improved densification. Thus, laser shock processing is a viable technique for increasing the hardness of PcBN and sintering of nanodiamond on PcBN.

8.5. Acknowledgments

This material is based upon work supported by the National Science Foundation under Grant No. CMMI-1029072. Roslyn, the lead author, likes to thank NSF's Research Experiences for Undergraduates for providing an opportunity to participate in the research project.

8.6. References

[1] Haubner R, Wilhelm M, Weissenbacher R, Lux B. Boron nitrides – properties, synthesis and applications. Struct Bond 2002;102:1–45.

[2] Solozhenko V. Thermodynamics of dense boron nitride modifications and a new phase P, T diagram for BN. Thermochim Acta 1993;218:221–7.

[3] Zhang J, Yu Q, Pang S, Meng S, Wang T, Hu J. Development and application of polycrystal cubic boron nitride cutting tool material. Key Eng Mater 2008;375– 376:168–71.

[4] Kurt A, Seker U. The effect of chamfer angle of polycrystalline cubic boron nitride cutting tool on the cutting forces and the tool stresses in finishing hard turning of AISI 52100 steel. Mater Des 2005;26(4):351–6.

[5] Sechi Y, Tsumura T, Nakata K. Dissimilar laser brazing of boron nitride and tungsten carbide. Mater Des 2010;31(4):2071–7.

[6] Bhaumik SK, Divakar C, Singh AK. Machining Ti–6Al–4V alloy with a wBN–cBN composite tool. Mater Des 1995;16(4):221–6.

[7] Jack DH. Ceramic cutting tool materials. Mater Des 1986;7(5):267–73.

[8] Casanova C, Balzaretti A, Voronin G, Jornada J. Experimental study of plastic deformation during sintering of cubic boron nitride compacts. Diamond Relat Mater 1999;8:1451–4.

[9] Novikov NV, Bondarenko VP, Kocherzhinskii YA. A study of plastic deformation of cubic boron nitride. J Superhard Mater 1985;2:17–20.

[10] Shulzhenko AA, Bozhko SA, Sokolov AN. Synthesis sintering and properties of cubic boron nitride. Naukova Dumka; Kiev 1993:255.

[11] Vel L, Demazeau G, Etourneau J. Cubic boron nitride: synthesis, physicochemical properties and applications. Mater Sci Eng B 1991;10(2):149–64.

[12] <http://www.cutting-tool.americanmachinist.com/guiEdits/Content/bdeee1/bdeee1_1.aspx>; 2011 [accessed 05.08.11].

[13] Cook M, Bossom P. Trends and recent developments in the material manufacture and cutting tool application of polycrystalline diamond and polycrystalline cubic boron nitride. Int J Refract Metal Hard Mater 2000;18:147–52.

[14] Montross S, Wei T, Ye L, Clark G, Mai Y. Laser shock and its effects on microstructure and properties of metal alloys: a review. Int J Fatigue 2002;24:1021–36.

[15] Peyre P, Fabbro R, Berthe L, Dubouchet C. Laser shock processing of materials, physical processes involved and examples of applications. J Laser Appl 1996;8:135–41.

[16] Ding K, Ye L. Laser Shock Peening. Performance and Process Simulation. CRC press; 2006. ISBN: 0849334446.

[17] Osswald S, Gurga A, Kellogg F, Cho K, Yushin G, Gogotsi Y. Plasma pressure compaction of nanodiamond. Diamond Relat Mater 2007;16:1967–73.

[18] Yucheng Z, Mingzhi W. Preparation of polycrystalline cBN containing nanodiamond. J Mater Process Technol 2008;198:134–8.

[19] Chong YM, Ma KL, Leung KM, Chen CY, Ye Q, Bello I, et al. Synthesis and mechanical properties of cubic born nitride/diamond thin films. Chem Vapor Depos 2006;12:33–41.

[20] Benko E, Stanisław J, Krolicka B, Wyczesany A, Barr T. CBN–TiN, cBN–TiC composites: chemical equilibria, microstructure and hardness mechanical investigations. Diamond Relat Mater 1999;8:1838–46.

[21] Ronga X, Tsurumi T, Fukunagab O, Yanoa T. High-pressure sintering of cBN– TiN–Al composite for cutting tool application. Diamond Relat Mater 2002;11(2):280–6.

[22] Erasmus RM, Comins JD, Fish ML. Raman and photoluminescence spectra of indented cubic boron nitride and polycrystalline cubic boron nitride. Diamond Relat Mater 2000;9:600–4.

[23] Bergman L, Nemanich RJ. Raman spectroscopy characterization of hard, widebandgap for semiconductors: diamond, GaN, GaAlN, AlN, BN. Annu Rev Mater Sci 1996;26:551–79.

[24] Sachdev H. Influence of impurities on the morphology and Raman spectra of cubic boron nitride. Diamond Relat Mater 2003;12:1275–86.

[25] Zinin PV, Kudryashov I, Konishi N, Ming LC, Solozhenko VL, Sharma SK. Identification of the diamond-like B–C phase by confocal Raman spectroscopy. Spectrochim Acta Part A 2005;61:2386–9.

[26] Olszyna A, Konwerska-Hrabowska J, Lisicki M. Molecular structure of E-BN. Diamond Relat Mater 1997;6:617–20.

[27] Sanjurjo JA, Lo´ pez-Cruz E, Vogl P, Cardona M. Dependence on volume of the phonon frequencies and their effective charges of several III–V semiconductors. Phys Rev B 1983;28:4579–84.

[28] <http://www.nanodiamond.com.ua/NANO.HTM>; 2011 [accessed 05.08.11].

[29] Osipov A, Nauyoks S, Zerda T, Zaporozhets O. Rapid sintering of nano-diamond compacts. Diamond Relat Mater 2009;18:1061–4.

[30] Sun KW, Wang JY, Ko TY. Raman spectroscopy of single nanodiamond: phonon-confinement effects. Appl Phys Lett 2008;92:15–8.

[31] Zhi CY, Bai XD, Wang EG. Raman characterization of boron carbonitride nanotubes. Appl Phys Lett 2002;80:19–22.

[32] Ci L, Song L, Jin C, Jariwala D, Wu D, Li Y, et al. Atomic layers of hybridized boron nitride and graphene domains. Nat Mater 2010;9:430–5.

[33] Kuhlmann U, Werheit H. Raman effect of boron carbide (B4.3C to B10.37C). J Alloy Compd 1994;205:87–91.

[34] Nistor L, Buschmann V, Ralchenko V, Dinca G, Vlasov I, Van Landuyt J, et al. Microstructural characterization of diamond films deposited on c-BN crystals. Diamond Relat Mater 2000;9:269–73.

CHAPTER 9: LASER/WATERJET HEAT TREATMENT OF POLYCRYSTALLINE CUBIC/WURTZITE BORON NITRIDE COMPOSITE FOR REACHING HARDNESS OF POLYCRYSTALLINE DIAMOND

A paper published in *the Journal of Materials Letters,* Vol. 89, P.123-125, (2012)
http://dx.doi.org/10.1016/j.matlet.2012.08.024

Ammar Melaibari[30, 31, 32], Pal Molian[1,33], and Pranav Shrotriya[1,4]

Abstract

We report a heat treatment technique that enabled the hardness of polycrystalline cubic/wurtzite boron nitride composite to reach that of polycrystalline diamond. The process consists of surface heating the composite using a continuous wave laser followed by tandem waterjet quenching of the laser beam path to cause stress-induced phase transitions. Visual examination indicated a change in optical transparency through a color change from black to white. Raman spectroscopy revealed the partial transformation of wBN to cBN and formation of amorphous boron. Vicker's microhardness test showed a dramatic increase in the nominal hardness from 40 GPa to 75 GPa.

Keywords: Heat treatment, Hardness, Boron nitride, laser.

[30] Laboratory for Lasers, MEMS and Nanotechnology, Department of Mechanical Engineering, Iowa State University, Ames, IA 50011.
[31] Dept. of Mechanical Engineering, King AbdulAziz University, Jeddah, Saudi Arabia
[32] Primary researcher and lead author
[33] Co-author

9.1. Introduction

Diamond, the natural or man-made material, has long been regarded as the "world's hardest material" where single crystalline (100) diamond and polycrystalline diamond exhibit Vicker's indentation hardness of 100 GPa [1] and 78 GPa [2] respectively. Cubic boron nitride (cBN) is the second hardest material produced only under synthetic conditions. The hardness of single crystalline cBN is anisotropic in nature with values ranging from 30 GPa in the [110] direction on the (001) plane to 43 GPa in the [100] direction on the same plane [3]. Polycrystalline cBN consisting of single crystals of cBN in a binder phase is much harder (39 GPa) than many of its single crystal counterparts due to random orientation of grains [3]. Wurtzite boron nitride (wBN) is another hard phase of boron nitride obtained by extreme (shock compression) conditions. Vicker's indentation hardness of wBN is reported as a varying number: 22.3 GPa, 35.6 GPa and 52.5 GPa [4].

wBN is usually mixed with cBN in 1:1 molar ratio and used to make composite poly-cBN/wBN cutting tool inserts. Such tools offer much higher fracture toughness and hardness than that of poly-cBN [4-6]. It may be noted that wBN and cBN have identical bond lengths, elastic moduli, and tensile/shear strengths [7]. It is believed that transformation toughening, a shear-induced phase transformation of wBN to hexagonal BN [4] during machining, may be responsible for increased toughness and consequently an increase in the longevity of poly-wBN/cBN tools.

Since chemical and thermal stability of wBN/cBN are superior to that of diamond, thermal or mechanical treatment of wBN/cBN to the hardness level of diamond is expected to generate huge industrial interest for tool wear and corrosion applications. By appropriate phase transition and grain size reduction, it is possible to increase the hardness of cBN/wBN to that

of (100) diamond [8, 9]. For example, a nanocomposite consisting of 14 nm sized cBN/wBN composite exhibited a Vicker's hardness of 85 GPa [8] illustrating the role played by the nanoscale size effect. Theoretical models predict that phase transition in wBN can cause its hardness to exceed single crystal diamond through phase transition. Using first-principle calculations, Pan et al [9] showed that the large normal compressive stresses under indentation conditions can force wBN to reach a hardness of 114 GPa which is well above that of single-crystal diamond. Such an increase was attributed to a "bond-flipping" structural phase transformation without any change in the crystal volume [9]. However there is no experimental proof for wBN's stress response to phase change for increased hardness.

9.2. Experimental Details

In the present work, a heat treatment technique that involved laser heating and waterjet quenching in tandem (Figure 75) was employed for a polycrystalline composite tool having 50%cBN-50%wBN and iron oxide as impurity. Cylindrical samples with a nominal diameter of 9.5 mm and height of 3 mm were synthesized from high-pressure, high-temperature processes. The composite contained many structural defects in the form of dislocations, stacking faults and point defects. The surfaces of samples were cleaned with acetone and methanol before being mounted on the X-Y positioning stage. The laser/waterjet (LWJ) system described in [10] was utilized. Heat treatment (no scribing or melting) was performed using a defocused beam of 1 mm spot at a laser power of 200 W and a speed of 68 mm/s. Multiple overlapping passes with an overlap of 50% were carried out to cover the 9.5 mm diameter surface. Following heat treatment, the samples were cleaned again with acetone and methanol and then subjected to metallographic and chemical analysis.

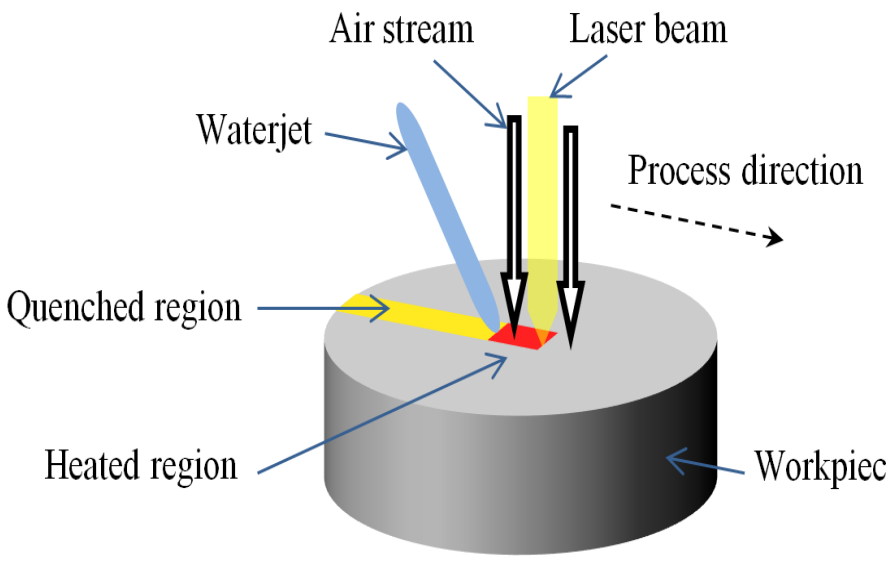

Figure 75: Schematic of LWJ process for heat treatment of wBN/cBN composite.

Optical and scanning electron microscopy revealed clean surfaces with no evidence of cracks suggesting that the heat treatment stresses did not exceed the fracture strength. There was also no change in the grain size. X-ray photoelectron spectroscopy (XPS) analysis was performed with a PHI 5500 spectrometer using Al Kα1 radiation with a 45° electron collection angle. Survey spectra were acquired in the range from 0 to 1100 eV at pass energy of 187 eV. The high resolution spectra of the surface constituents were acquired from untreated and heat treated samples with 58.7 eV pass energy.

9.3. Results and Discussion

A comparison of the spectra of both samples showed that the stoichiometric ratio of B and N remain unaltered after the heat treatment suggesting the absence of oxidation during the process. However there was an increase carbon concentration in the heat treated sample (Table

11) that was attributed to a result of the use of carbon-based adhesive to mount the sample in the heat treatment process.

Table 11: Atomic concentrations of elements in wBN/cBN samples

Sample	B	N	C	Fe	O
Before heat treatment	32.87	28.75	5.78	12.45	20.15
After heat treatment	23.23	19.66	20.01	14.75	22.36

Dispersive Raman spectroscopy analysis (Renishaw-inVia Raman Microscopy) was performed to identify the phase transitions using Ar-ion laser with a 20 μm entrance slit width, 50 mW laser power, and 488 nm operating wavelength. Figure 76a shows the spectrum of untreated cBN/wBN revealing the presence of both cBN/wBN phases. The 1302 cm^{-1} and 962 cm^{-1} peaks are assigned to cBN and wBN respectively. The two overlapped peaks at 1050 cm^{-1} belong to both phases; the high end at 1052 cm^{-1} to cBN and the low end at 1040 cm^{-1} to wBN. The two characteristic Raman peaks for cBN are in good agreement with what is well known: a TO mode at 1055-1057 cm^{-1} and LO mode at 1305-1306 cm^{-1}. It is generally difficult to identify the Raman peaks for wBN because of its small size (submicron) and shockwave method of production [11]. Many characteristic peaks at 950, 1015, 1053, 1075, 1246, 1280 and 1295 cm^{-1} were reported based on a number of theoretical and experimental observations [12-14] but usually not all these peaks are detectable. Unlike cBN, neither symmetry assignment of the individual modes nor LO/TO splitting information about wBN was provided. In the present work, only two peaks for wBN were noted. Figure 76b shows the Raman spectra of the sample after heat treatment where the peaks similar to that of untreated sample and a broader peak around 1200 cm^{-1} were observed. Broadening of peaks in the heat treated condition is probably caused by the compressive residual stresses. The peak with a hump

around 1180-1200 cm^{-1} is assigned to amorphous boron (B12) [15,16]. In the heat treated sample, the ratio of peaks corresponding to 1052 cm^{-1} (cBN) and 1040 cm^{-1} (wBN) becomes larger suggesting the partial transformation of wBN to cBN.

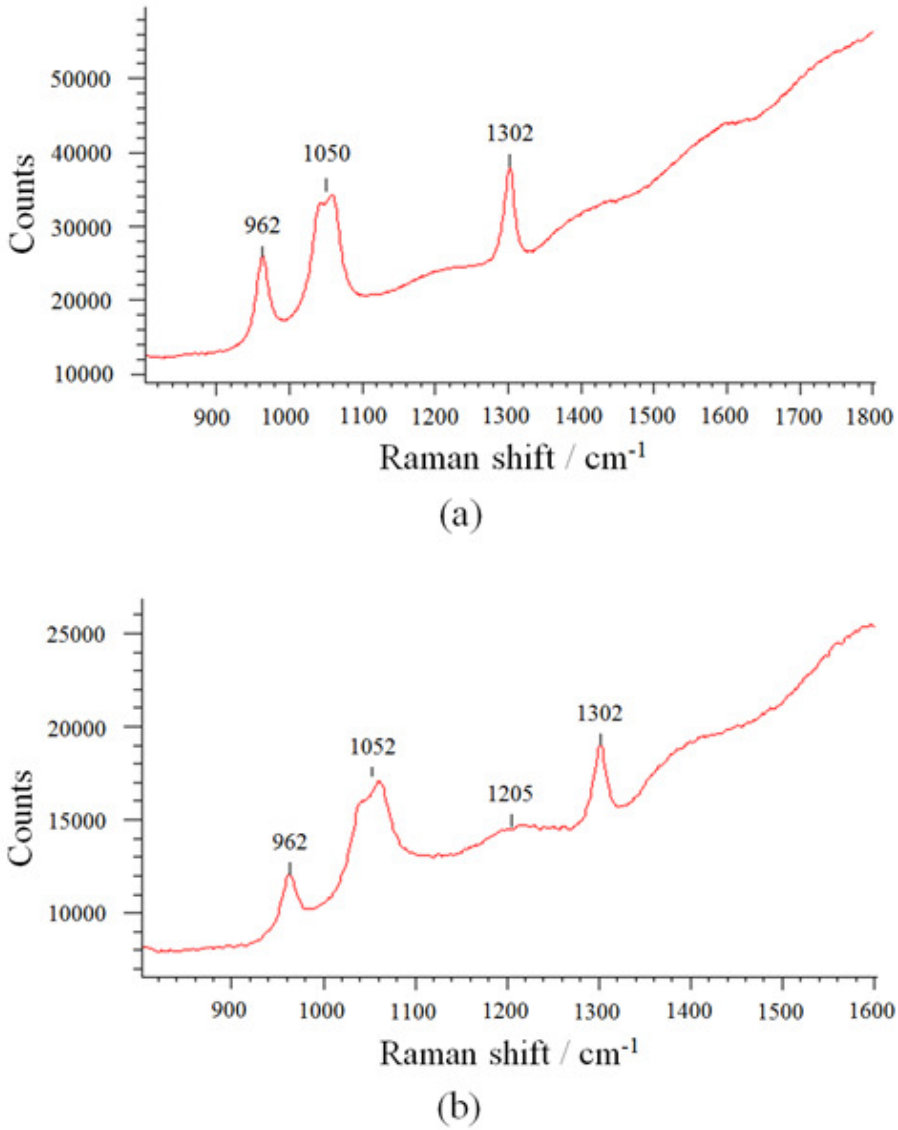

Figure 76: Raman spectra of wBN/cBN samples: (a) untreated (b) LWJ heat treated

Indentation hardness test was conducted using a Tukon microhardness tester with a Vicker's diamond pyramid indenter. The load was 1 kgf (9.81 N) and test duration was 30 sec.

Measurements were made using a high resolution (± 1 µm) optical microscope to ensure that no fracture had occurred and to measure the length of the diagonals of the indentations. Vicker's hardness was then calculated using the relationship: $HV = 1854\ L/d^2$ where L is the normal load (N) and d is the average length of the two diagonals (m) of the Vicker's indentation. Optical microscope and optical profilometer images of the indentations terrace were used to measure the diagonals (see the Supplemental material file). A number of hardness measurements were made to ensure the reliability of test data. Figure 77 shows the results of hardness test. The average hardness of the untreated sample is 40 GPa with a standard deviation of 10 GPa. The average hardness of heat treated sample is 75 GPa with a standard deviation of 14 GPa.

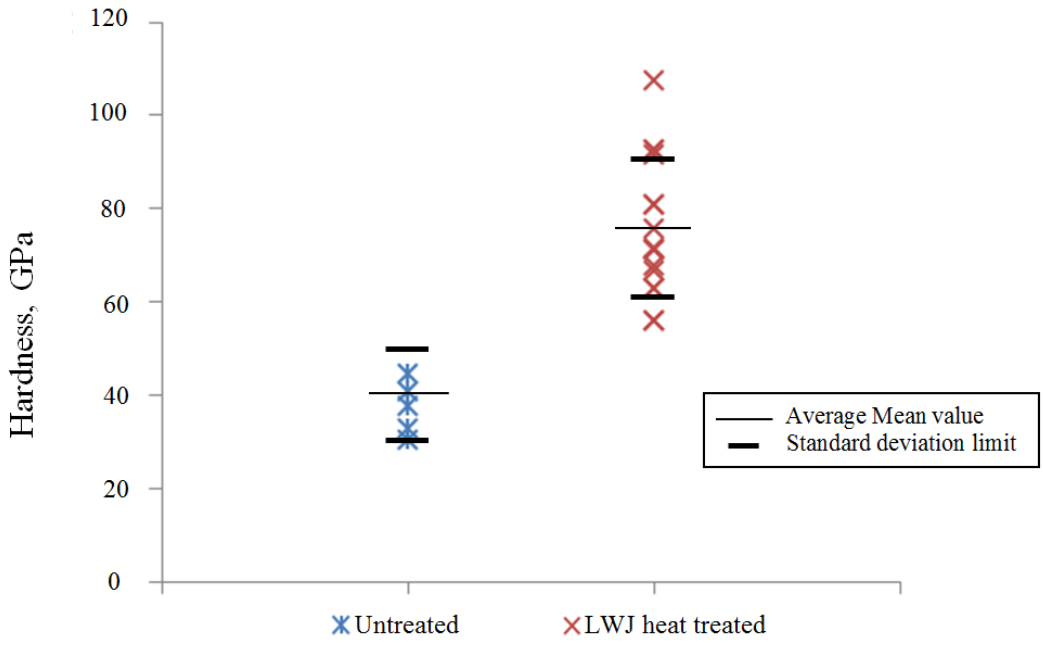

Figure 77: Vicker's indentation hardness test data

Visual examination of the heat treated sample revealed a color change from light-absorbing black/gray to transparent white. The color change is intriguing and may be explained by a change in crystal morphology. In following Sachdev's classification of the crystalline morphology of cBN according to color, size and transparency [11], a transparent cBN of white to amber color would have tetrahedral crystal morphology (as opposed to octahedral) with small grain size (submicron to 100 μm) and boron deficiency. It may be noted that the color is also caused by inclusions, dopants or defects. Thus there is a preferential crystal growth or reduction in defect density by the heat treatment.

Formation of amorphous boron and partial transformation of wBN are both temperature and stress-dependent. Surface temperature is computed using a thermal model based on heat conduction [17]:

$$T(0,t) = \frac{(1-R)I_0}{k\delta}\left[2\frac{\sqrt{\alpha\delta^2 t}}{\pi} + \exp(\alpha\delta^2 t)\, erfc\left(\delta\sqrt{\alpha t}\right) - 1\right] + T_0 \qquad (1)$$

Where R is the reflection energy losses; Io is the incident laser power density; k thermal conductivity; δ absorption depth; t laser beam interaction time; and α thermal diffusivity; T0 is the ambient temperature. The absorption depth of cBN is estimated from the complex refractive indices to be on the order of 10-5 m [18]. Thermal properties were obtained from [5,6] and listed in Table 12 along with LWJ parameters. Simple energy calculations are also presented at the end of the table.

Table 12: LWJ parameters, thermal properties of the samples, and the results of Thermal and Stress Analysis

Parameter	cBN/wBN
Laser Power, P	200 W
Spot Size, d	10^{-3} m
Power Density, I_0	2.55 (10^8) W/m^2
Beam interaction time, t	0.015 sec
Waterjet pressure, p	0.4 MPa
Absorption depth, δ	10^{-5} m
Reflection losses, R	20%
Thermal conductivity, k	40-50 W/m K (Ref. 5)
Density, ρ	3440 kg/m^3 (Ref. 5)
Specific heat, C_p	800 J/kg K (Ref. 6)
Thermal Diffusivity, $\alpha = k/\rho C_p$	1.64 (10^{-5}) m^2/sec
Linear thermal expansion, λ	3.6 (10^{-6})/K (Ref. 6)
Young's Modulus, E	890 GPa (Ref. 6)
Ambient temperature, T_0	300 K
Surface Temperature[a]	1660 K
Thermal diffusion distance[b], x	0.992 mm
Thermal stress at the surface[c], σ_T	3.48 GPa

[a]Equation (1)

[b]Thermal diffusion distance, $x = (4\alpha t)^{\frac{1}{2}}$

[c]Thermal stress, $\sigma_T = \lambda\, \Delta T\, E$

Under the conditions of 1660 K and 3.48 GPa, it is expected that a fraction of the metastable wBN would have undergone phase transition to the stable cBN. Both phases are also under stress and "bond flip" mechanism postulated in [9] can be invoked to support the observed increase in hardness. A partial transformation of wBN to the amorphous form at the grain boundaries would increase the resistance of dislocation motion which in turn increase the hardness.

9.4. Conclusion

The heat treatment technique of rapid laser heating of polycrystalline wBN/cBN composite to 1660 K followed by waterjet quenching of the laser beam path was able to increase the hardness of polycrystalline cBN/wBN by 88% to reach the hardness of polycrystalline diamond. Such an improvement will allow cBN/wBN composites to replace polycrystalline diamond which suffer from thermal and chemical instability in many applications. The superior hardness of the BN developed in this work coupled with its inherent high-temperature capability and chemical inertness would permit its utilization in numerous applications and surpass a wide range of ceramic materials including aluminum oxide, silicon nitride, SiAlON, boron carbide and silicon carbide.

9.5. Acknowledgments

The authors appreciate the scholarship provided by King AbdulAziz University and thank Mr. James Anderegg of the Ames Laboratory for assistance in obtaining the XPS characterization. Special thanks go to Dr. Volodymyr Bushlya, who kindly donated several boron nitride samples to us.

9.6. Appendix A. Supplementary Data

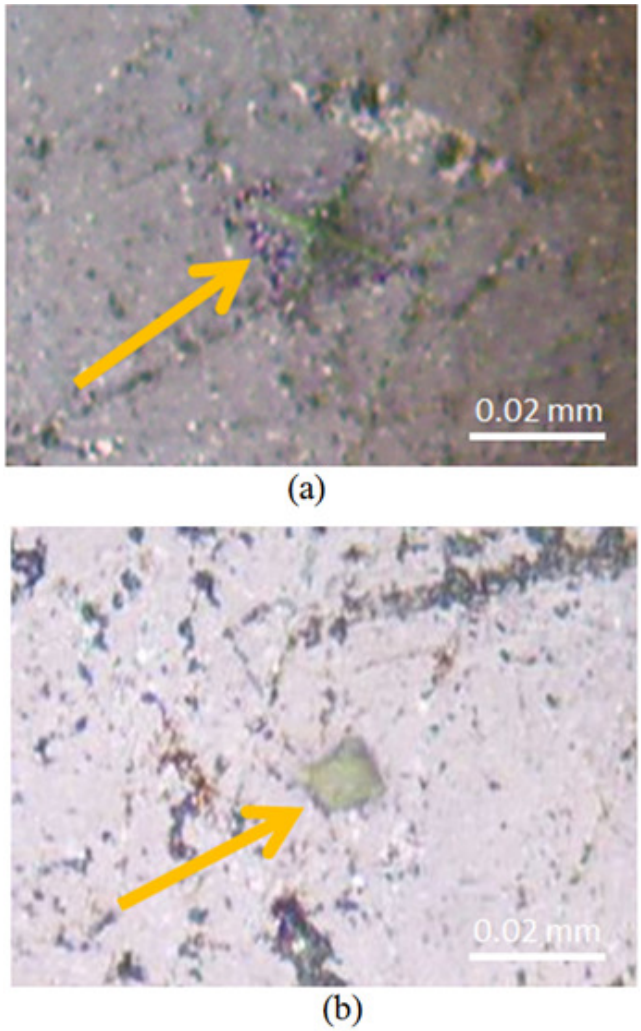

Figure 78: Optical microscope images of indentations: (a) untreated (b) LWJ heat treated.

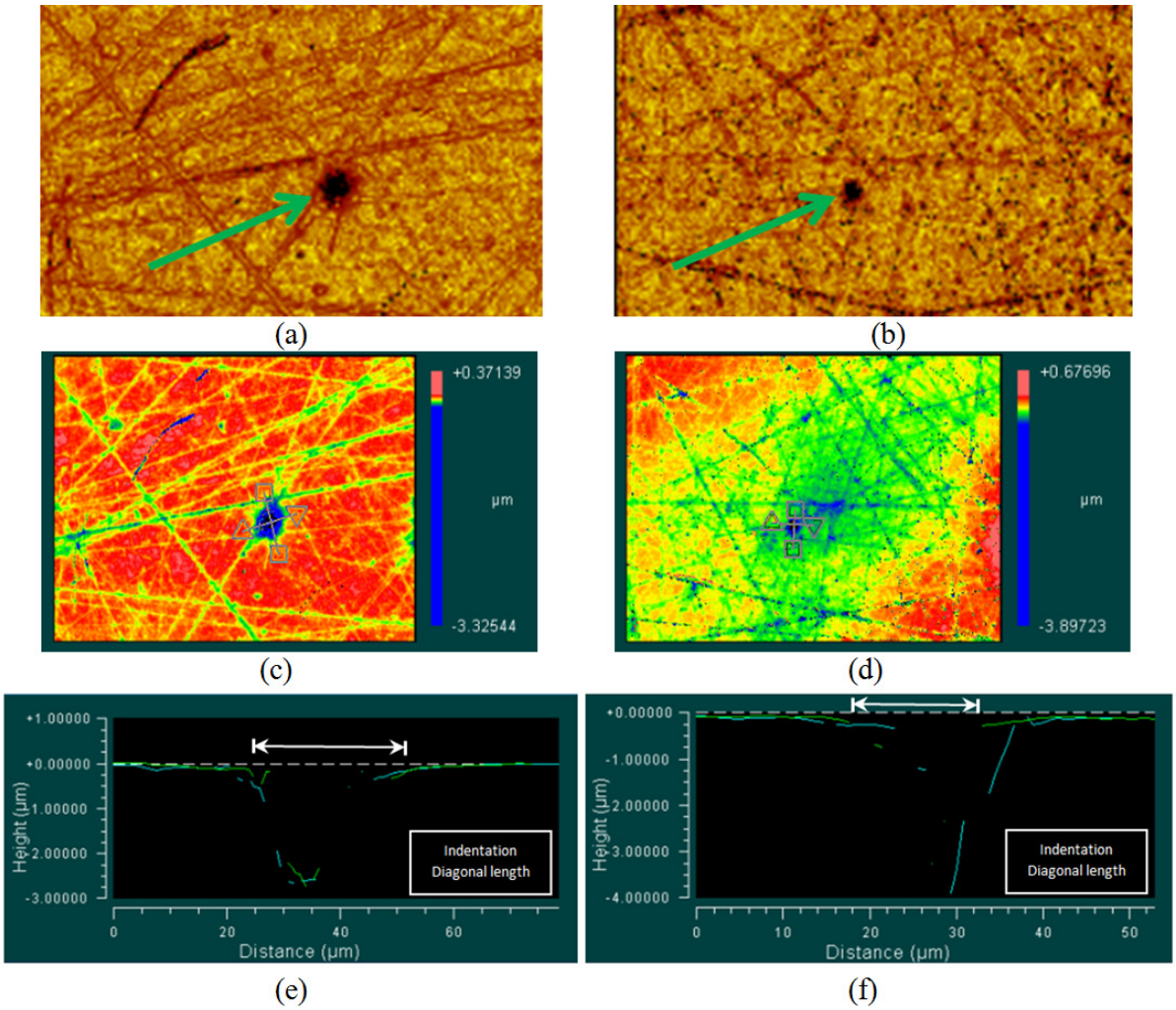

Figure 79: Profilometer images of two indentations: (a), (c), and (e) untreated sample; (b), (d), and (f) LWJ heat treated sample. (a) and (b) show profilometer's solid plot of the regions. (c) and (d) show the position of the line profiles which pass over the 10. diagonals of the indentations. (e) and (f) show the line profiles from which the diagonal length could be measured. Note the scales are different in (e) and (f).

9.7. References

[1] H. Li and R. C. Bradt, Diamond and Related Materials 1, 1161 (1992)

[2] M.K. Brun, M. Lee and F. Gorsler, Wear 104, 21 (1985)

[3] T.K. Harris, E.J. Brookes and C.J. Taylor, International Journal of Refractory Metals & Hard Materials 22, 105 (2004)

[4] R. R. Wills, International Journal of High Technology Ceramics 1, 139 (1985)

[5] S. K. Bhaumik, C. Divakar and A. K. Singh, Materials & Design 16:4, 221 (1995)

[6] C. Divakar, Metals Materials And Processes 12:2&3, 197 (2000)

[7] R. F. Zhang, S. Veprek and A.S. Argon, Phys. Rev. B 77, 172103 (2008)

[8] N. Dubrovinskaia, V. L. Solozhenko, N. Miyajima, V. Dmitriev, O. O. Kurakevych and L. Dubrovinsky, Appl. Phys. Lett. 90, 101912 (2007)

[9] Z. Pan, H. Sun, Y. Zhang and C. Chen, Physical Review Letters, 102, 055503 (2009)

[10] R. Molian, C. Neumann, P. Shrotriya and P. Molian, ASME Journal of Manufacturing Science and Engineering 130, 031008 (2008)

[11] H. Sachdev, Diamond and Related Materials 12, 1275 (2003)

[12] G.L. Doll, J. Edgar (Ed.), Properties of Group III Nitrides, Inspec, London, 1994, p. 241.

[13] K. Karch, F. Bechstedt, Phys. Rev. B 56, 7404 (1997)

[14] N. Ohba, K. Miwa, N. Nagasako, A. Fukumoto, Phys. Rev. B 63, 115207 (2001)

[15] Z. Wang, Y. Zhao, P. Lazor, H. Annersten and S. K. Saxena, Appl. Phys. Lett. 86, 041911 (2005)

[16] U. Kudlmann, H. werheit, T. Lundstram and W. Roberg, J. Phys. Chem. Solids 55:7, 579 (1994)

[17] B.S. Yilbas and S.Z. Shuja, Applied Surface Science 108, 167 (1997)

[18] T. Sumiyoshi, H. Tomita, A. Takahashi, M. Obara and K. Ishii, J. Appl. Phys. 79, 2831 (1996)

CHAPTER 10: EXTREME HARDNESS ACHIEVEMENTS IN BINDERLESS CUBIC BORON NITRIDE TOOLS

A paper published in the conference proceedings of *the 41st NAMRI/SME conference*,

Vol. 41, June 10-14 (2013)

Ammar A. Melaibari[34,35,36], Zhuoru Wu[1,37], Pranav Shrotriya[1,4], Pal Molian[1,4], Volodymyr Bushlya[4,38], Jinming Zhou[4,5], Jan-Eric Ståhl[4,5], and Igor Petrusha[4,39]

Abstract

Binderless cubic boron nitride tools are available in two forms: single phase cBN and dual phase wBN/cBN ("w" is wurtzite phase). In this work, a novel heat treatment process involving surface heating using a continuous wave CO^2 laser followed by tandem waterjet quenching of the laser beam path was applied to increase the hardness of both forms of boron nitride. Stress-induced phase transitions and nanometric grain sizes accompanying the rapid quench heat treatment enabled a hardness increase of 20% in single phase cBN (nominal 60 GPa) and 100% in dual phase wBN/cBN (nominal 75 GPa) that attest the ability of cBN to reach the hardness of polycrystalline diamond (65-80 GPa). The effects of laser heat treatment are identified by an examination of the changes in phase and microstructure by Raman spectroscopy, high resolution scanning electron microscopy and X-ray diffraction.

[34] Laboratory for Lasers, MEMS and Nanotechnology, Department of Mechanical Engineering, Iowa State University, Ames, IA 50011.
[35] Dept. of Mechanical Engineering, King AbdulAziz University, Jeddah, Saudi Arabia.
[36]Primary researcher and lead author.
[37] Co-author
[38] Division of Production and Materials Engineering, Lund University, Lund, 22363, Sweden.
[39] Department for Synthesis and Sintering of Superhard Materials, V.N. Bakul Institute for Superhard Materials, National Academy of Science of Ukraine, Kiev, 04074, Ukraine

Keyword: Binderless cBN, Composite wBN/cBN, Laser Heat Treatment, Hardness, Microstructure.

10.1. Introduction

Cubic boron nitride (cBN) in polycrystalline arrangement is a high-performance tool material in metal cutting industries for precision cutting and finishing of hardened alloy steels, titanium alloys, high-strength nickel superalloys and powder metal alloys [1], [2], [3], [4]. Despite polycrystalline diamond's (PCD) superior edge over cBN on mechanical properties, the chemical inertness and thermal stability of cBN at high temperatures made it highly preferable particularly for machining hard alloys. Research is needed to further enhance the mechanical properties of cBN and also find ways to improve the chemical and thermal stability of PCD. Such developments would make these superhard materials meet the stringent requirements of new applications and enhance their performance in established areas as well [5].

Some improvements in thermal and chemical stability of PCD have been achieved by: coating the tool surfaces with a stabilization layer to prevent direct contact between the PCD tool and workpiece; treating the workpiece prior to machining to decrease the chemical reactivity; and adding an ultrasonic vibration tool to reduce contact time and friction between the tool and workpiece [6], [7], [8]. However such methods are not quite acceptable because the coating reduces the inherent durability of PCD tool, the chemical treatment of workpiece changes its properties, and the addition of the ultrasonic tool affects the range of allowable cutting speeds.

The mechanical properties of cBN are currently improved by two ways: eliminating the binder phase and reducing the particle size of cBN. Harris et al reported that both binderless and fine particle cBN promoted the hardness [9]. The binder phase, which is typically aluminum or titanium nitride (15 to 50%), introduces diffusion barrier and reduces chemical wear in continuous machining of highly-alloyed hardened steels or superalloys; However, this could also lead to thermal strain cracks at high temperatures that degrade drastically the performance of the cBN tools [10], [11]. Binderless cBN is usually fine grained (< 500 nm) and well suited for interrupted and ultra-precision cutting due to three superior characteristics: hardness, high-temperature transverse rupture strength and thermal conductivity [12]. Binderless cBN is widely regarded as a breakthrough tool in high speed machining of titanium alloys [13]. There are two types of binderless cBN: one is a pure cBN and the other is a wurtzite/cubic boron nitride (wBN/cBN) composite. Wurtzite boron nitride (wBN) is a hard phase similar to cBN. A composite of wBN-cBN is obtained by sintering wBN powders at high pressures and temperatures (approx. 7 GPa and 1800 C) in the stability region of cBN. The cost of production of wBN/cBN is much lower than that of traditional cBN because the starting wBN powders can be produced in large quantities inexpensively by shock loading graphitic form of BN [4]. During the high-pressure, high-temperature sintering, a certain volume fraction of wBN transforms to cBN resulting wBN/cBN composite. The wBN/cBN compacts have a unique combination of high fracture toughness and hardness that enables these tools to be used under interrupted cutting conditions.

Although binderless cBN and wBN/cBN are very efficient in the finishing processes of milling and turning of hardened steels and titanium alloys, their hardness (40-50 GPa) is still well below that of PCD (65-80 GPa). Consequently a preliminary study of a novel

laser/waterjet heat treatment was conducted to find that the hardness of the wBN/cBN composite could reach the hardness of PCD [14]. The new discovery of rapidly quenched wBN/cBN composite matching the hardness of PCD can have vast implications in the tooling industry. Hence, in this paper, we made a detailed study of laser heat treated single phase cBN and dual phase wBN/cBN tools in order to identify the fundamental phase transition and microstructure refinement features that contribute to the hardness improvements.

10.2. Experiment

10.2.1. Materials

The workpiece materials used in this study were binderless single phase cBN with silicon nitride as the stress-relieving inclusion and binderless dual phase 50%wBN/50%cBN with iron oxide as the impurity. The dual phase tool contained many structural defects in the form of dislocations, stacking faults and point defects while the single phase tool has fewer defects [15], [16]. Both tools are round disks designated as RNGN09030T which gives diameter of 9.52 and thickness of 3.18 mm. they were synthesized by high pressure-high temperature processes (HP-HT).

10.2.2. Heat Treatment Tests

The heat treatment process involves laser heating and water-jet quenching in tandem (Figure 80) using the laser/waterjet (LWJ) system described in [17]. The surfaces of both tools were cleaned with acetone and methanol before being mounted on the X–Y positioning stage of the heat treatment process.

The heat treatment was performed using a continuous wave CO2 laser beam of 1 mm spot size and a speed of 68 mm/s. A low laser power of 200 W was used to prevent melting, scribing or cutting of boron nitride. The laser beam was immediately followed by waterjet stream of 400 kPa with a distance of 3.4 mm from the laser beam. Also, the laser beam was surrounded by a stream of air to prevent the laser-water interaction. Both single and multiple passes over the same region were carried out on the samples. After the heat treatment, the samples were cleaned again with acetone and methanol and then tested for Vicker's micro-hardness.

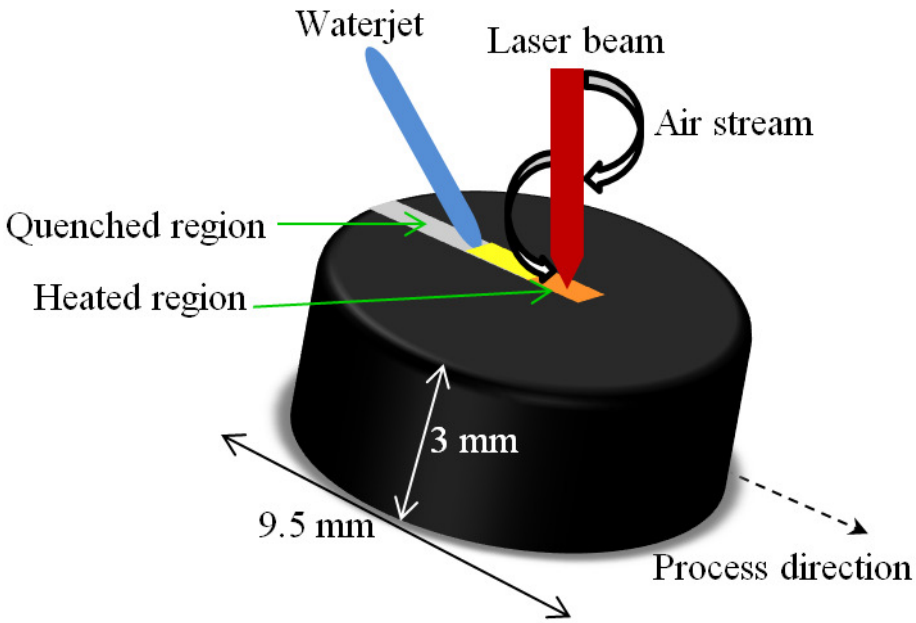

Figure 80: Schematic of LWJ heat treatment process.

10.2.3. Hardness Measurements

Indentation hardness tests were performed using a Tukon microhardness tester with a Vicker's diamond pyramid indenter. The load was set at 1 kgf (9.81 N) and test duration was made 30 sec. Measurements were made on the length of the diagonals of the indentations

using a high resolution (± 1 μm) optical microscope and optical profilometer to ensure that no fracture had occurred in the indentation zone. Vicker's hardness was then calculated using the relationship [18]:

$$HV = 1.8544\frac{L}{d^2} \quad (1)$$

Where L is the normal load (kgf) and d is the average length of the two diagonals (mm) of the Vicker's indentation. A number of hardness measurements (10 to 20) were made to ensure the reliability of test data.

10.2.4. Thermal Analysis

Green's function based approach was used to predict the temperature fields during the heat treatment operations (for more information about the green's function approach see [17], [19], [20], [21]). Temperature distribution, T(x,y,z,t), in the sample was determined by modeling the laser and waterjet as rectangular source and sink, respectively as shown schematically in Figure 80. Transient temperature distributions were obtained by the solution of following thermal diffusion equation:

$$c_p\rho\frac{\partial T}{dt} = k\nabla^2 T + q(x, y, t, I_h, I_c) \quad (2)$$

Where c_p is the specific heat, ρ is the density of the material, T is the temperature field and q(x, y, t, I_h, I_c) is the net heat input to the sample. The transient temperature distribution was determined using a Green's function approach as:

$$T(x,y,z,t) = \int_{0}^{\infty}\int_{-\infty}^{\infty}\int_{0}^{\infty} q(x_0, y_0 t_0, I_h, I_c)\,\theta(x, x_0, y, y_0, z, t, t_0)\,dy_0.dx_0.dt_0 + T_0 \quad (3)$$

Where θ(x, x_0, y, y_0, z, t, t_0) is the solution to the associated problem given by:

$$c_p \rho \frac{\partial T}{dt} = k\nabla^2 T + \delta(x - x_0)\,\delta(y - y_0)\,\delta\left(z - \frac{d}{2}\right)\delta(t - t_0) \qquad (4)$$

Where d is the thickness of the sample material, I_h, is the heating intensity (W/m^2), and I_c is the cooling intensity (W/m^2). Convective boundary conditions were used on the top surface where both laser heating and waterjet quenching takes place as well as on the sample edges ($x = \pm x_a$ and $y = y_b$). Insulated boundary conditions were assumed on the bottom surface ($z = -d/2$) and on the starting edge ($y = 0$).

It is important to note that Green's solution for this problem can be represented as a series of error functions or trigonometric functions. The error function representation accurately captures the steep gradients associated with transient heat source and sink for short time intervals but has slow convergence in matching the boundary conditions. On the other hand Eigen or the trigonometric function representation matches the boundary condition exactly, but has slow convergence in capturing the steep gradients associated with short duration transient response. We have utilized a hybrid approach for determining thermal solutions: error function representation for short duration and trigonometric series based Eigen function expansion for long duration when the gradients are not steep and can be captured with reasonable number of terms (<500).

10.2.5. Characterization

Dispersive Raman spectroscopy analysis (Renishaw-inVia Raman Microscopy) was performed to identify the phases before and after the heat treatment process using Ar-ion laser with a 20 μm entrance slit width, 50 mW laser power, and 488 nm operating wavelength.

General microstructure analysis of initial (untreated) sample was done on HRSEM LEO/Zeiss 1560 in high current mode which resolves most of the problems with sample charging but affects the resolution. Detailed analysis of both untreated and LWJ treated samples was done on HRSEM FEI Nova NanoLab 600.

XRD measurements in both θ/2θ and grazing angle setups were performed using a STOE Darmstadt Bragg-Brentano diffractometer operated at 40 kV and 40 mA using Cu Kα source.

10.3. Results

Visual examination of laser heat treated samples revealed a color change from light-absorbing black/gray to transparent white. Such an effect is ascribed to a change in crystal morphology following Sachdev's classification of the crystalline morphology of cBN according to color, size and transparency [22]. A transparent cBN of white to amber implies tetrahedral crystal morphology (as opposed to octahedral) with small grain size and loss of boron. It may be noted that the color may also be caused by inclusions, dopants or defects. The formation of transparent white of cBN provides some clues on the possible phase, stoichiometry and grain size changes in laser heat treatment.

Figure 81 shows the results of hardness tests of binderless, single phase cBN as a function of number of laser passes. The bar around each point shows the deviation of the hardness tests data. The maximum hardness increase was little more than 20% for 50 laser passes. Figure 82 shows a comparison of the size and shape of indentations of untreated and laser heat treated samples. There is extensive deformation around the indentation in untreated cBN due possibly to large grain size (3-5 microns) or the Si3N4 inclusions.

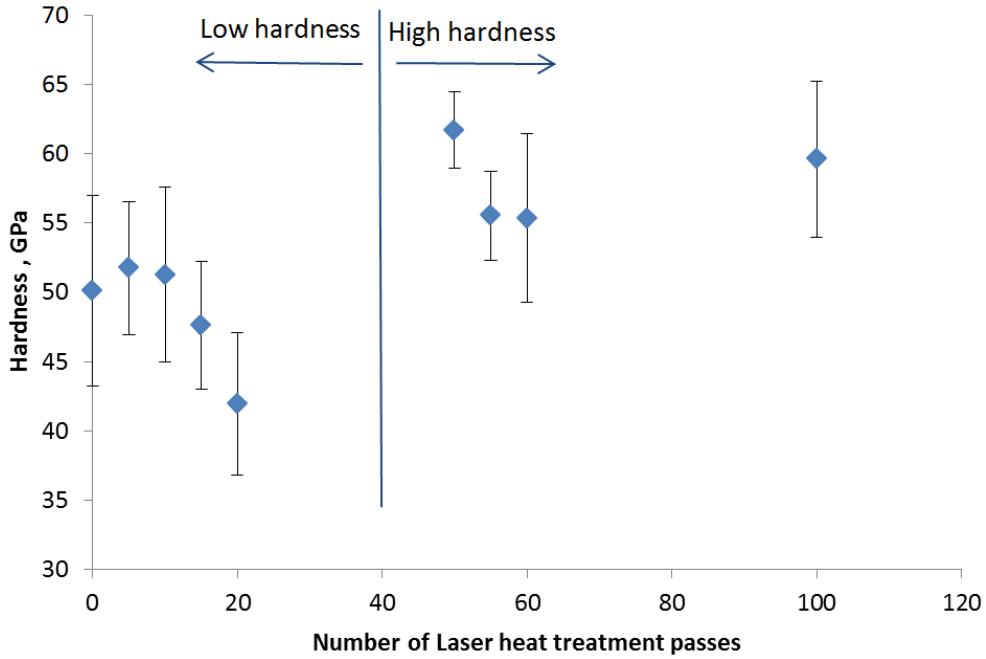

Figure 81: Vicker's indentation hardness test data of laser heat treated binderless, single-phase cBN.

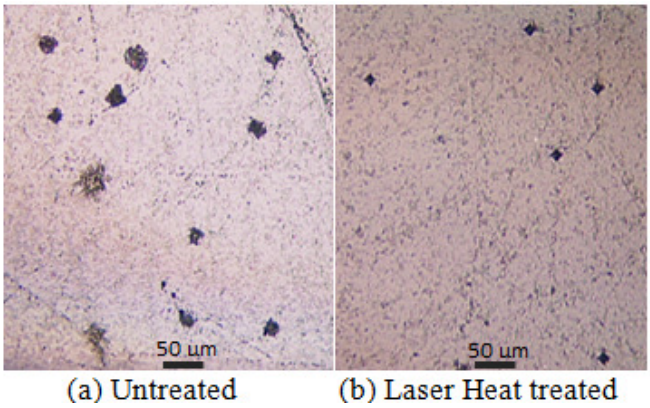

Figure 82: Vicker's indentations of binderless, single-phase cBN.

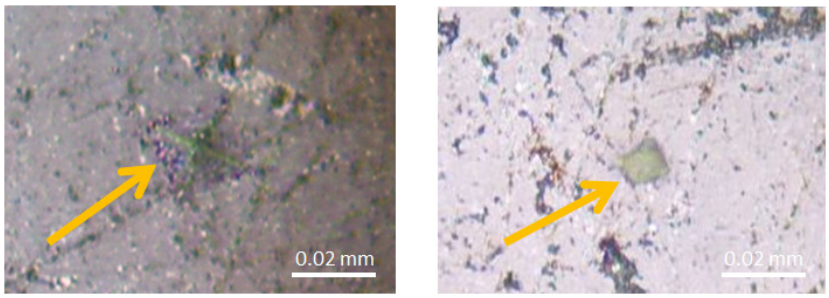

Figure 83: Optical images of indentations: (a) untreated (b) laser heat treated, dual phase wBN/cBN [14].

Figure 83 shows the optical microscope images of the indentations terrace before and after heat treatment of dual phase wBN/cBN. Figure 84 shows a statistical boxplot comparison between the results of hardness tests of single phase cBN after 50 laser passes (the maximum increase in hardness for the single phase cBN) and dual phase wBN/cBN after one pass. The laser treatment of the dual phase wBN/cBN has almost doubled the hardness and matched with that of PCD. It appears that the effect of heat treatment is more pronounced in wBN/cBN compared with single phase cBN. The average hardness was increased by 100% in wBN/cBN for a single pass and 20% in single phase cBN for 50 passes.

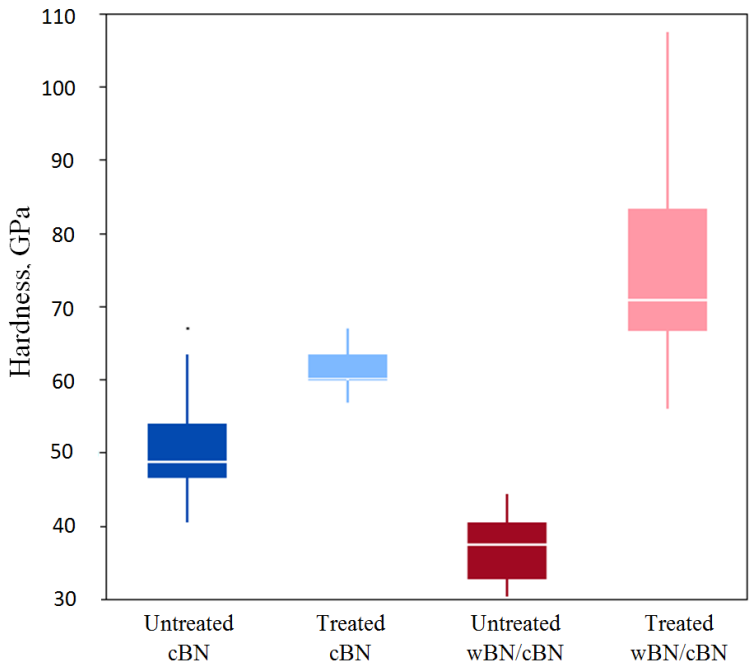

Figure 84:Vicker's indentation hardness test data of single phase cBN (50 laser passes), and dual phase wBN/cBN (single laser pass).

10.3.1. Temperature Distribution

The temperature distributions during the heat treatment process were computed to approximate the change in temperature along sample thickness. In both error function and

Eigen function expansions-based solutions for temperature field, quantities such as specimen dimension, cutting velocity, laser spot size, waterjet area, separation between laser beam and waterjet were chosen to exactly match the experimental conditions. The laser heating is approximated as a surface heat source whose intensity is given as:

$$I_h = a_s \frac{4P}{\pi b^2} \quad (5)$$

Where P represents laser power, b represents the diameter of the laser beam spot, and as represents the absorption coefficient. The absorption coefficient was chosen to be 0.75.

The temperature distribution along specimen thickness at the instant of maximum surface temperature is plotted in Fig 85. The surface of the sample is heated to a temperature of about 1700 K and 100 micrometer thick layer. The wBN to cBN and hBN to cBN transformations threshold temperatures are pressure dependent which are in the range of 1500-1800 K for the minimum required pressure.

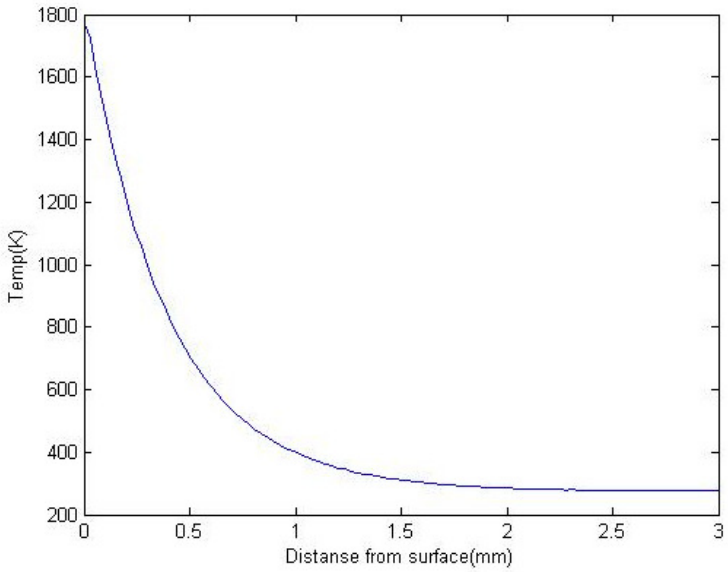

Figure 85: Predicted temperature distribution along the thickness of wBN/cBN specimen at the instant of maximum surface temperature during the heat treatment process.

10.3.2. Raman Analysis

The Raman spectrums of untreated and treated single phase cBN exhibit the two distinct peaks of cBN at 1307 cm^{-1} and 1058 cm^{-1} associated with the longitudinal (LO) and transverse (TO) optical phonon modes respectively [23]. An unidentified hump-like peak around 1206 cm^{-1} was also found. This peak can be assigned to amorphous boron (B_{12}) or a rich boron phase of BN [24], [25] at the grain boundaries. Increasing the number of heat treatment passes over the single phase cBN sample did not affect the Raman spectra in any significant way implying that there is no phase transition.

For the Raman analysis of the dual phase, it is generally difficult to identify the Raman peaks for wBN because of its small size (submicron) and shock-wave method of production [22]. Many characteristic peaks at 950, 1015, 1053, 1075, 1246, 1280 and 1295 cm^{-1} were reported based on a number of theoretical and experimental observations [26–28] but usually not all these peaks are detectable. The Raman analysis of the as received dual phase reveled the 962 and 1040 cm^{-1} peak for wBN. Figure 86 shows the Raman spectra of untreated and treated wBN/cBN samples. In both spectra the peaks of cBN (1302 and 1052 cm^{-1}) and wBN (962 and 1040 cm^{-1}) are present. The 1040 and 1052 cm^{-1} peaks are overlapped. The ratio of cBN to wBN peak in the overlapped region increased. Such an increase can be attributed to partial transformation of wBN→cBN [29]. In addition, the hump-like peak around 1200 cm^{-1} was increased. Due to the high reactivity of amorphous boron to oxygen, we postulate that the rich boron phase of BN along the boundaries of BN particles is increased.

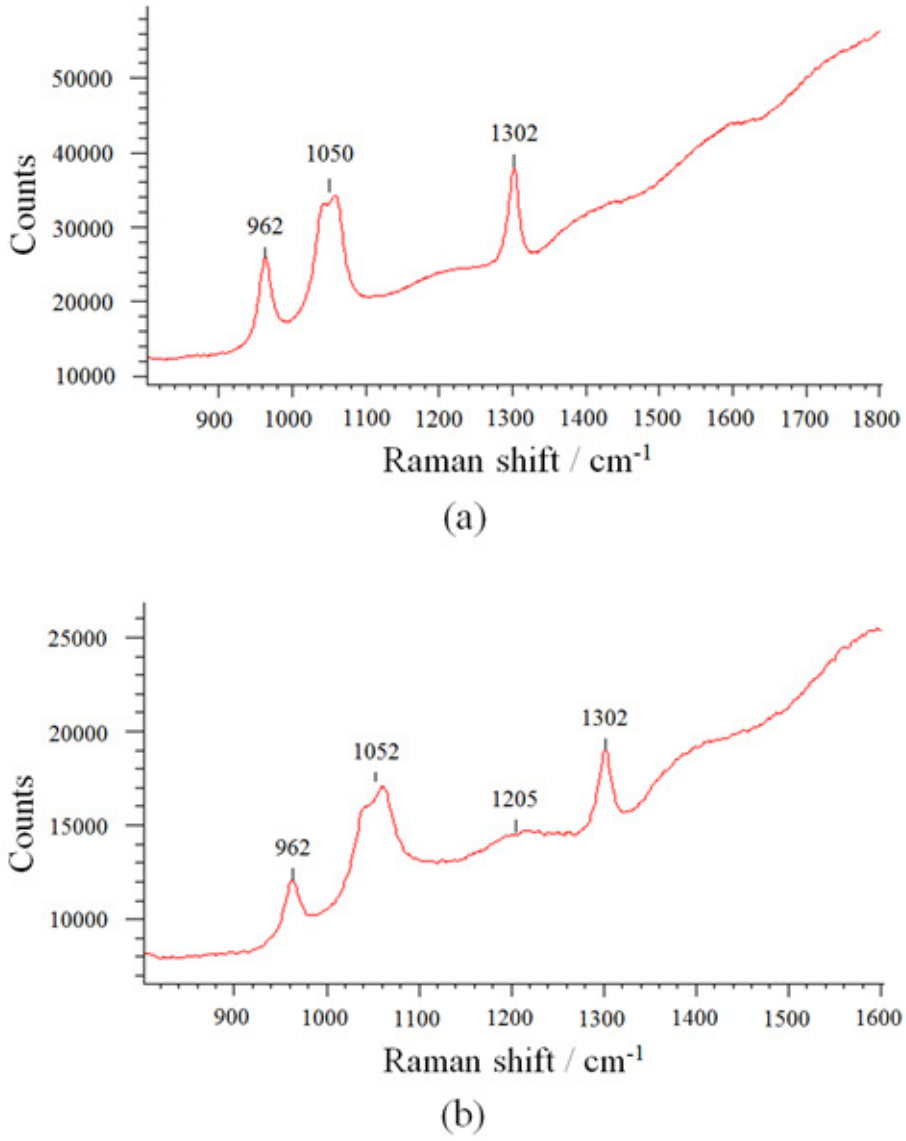

Figure 86: Raman spectra of untreated wBN/cBN (top), and laser treated wBN/cBN with 1 pass (bottom) [14].

10.3.3. HRSEM Analysis

Since the increase of hardness in the dual phase wBN/cBN composite is substantial when compared to single phase cBN, the analysis is only limited to the binderless, dual phase wBN/cBN. HRSEM analysis of the microstructure has revealed formation of nano-sized grains and significant cracking and fracture of wBN lamellas during laser heat treatment, which is elaborated in detail below.

10.3.3.1. Microstructure of the Sample Before Heat Treatment.

The microstructure consists of two types of structures with different size and morphology. The first type is lamellas of 0.5-2 μm in length and 0.15-0.2 μm in thickness (Figure 87). Majority of lamellas exhibit form changes of bending and fragmentation with displacement. Two features can be distinguished: regular band contract across the thickness (Figure 88) and interfaces at which the fragmentation takes place (Figure 87). The second type of structure is the independent grains with polyhedral faceting. Such polyhedral grains have the particle size of 0.1-0.2 μm (Figure 88). Their most common location is at the fragmentation sites and interfaces inside lamellas. Lamella/polyhedron and polyhedron/polyhedron interfaces have both straight-line boundaries which result in formation of pores (Figure 88).

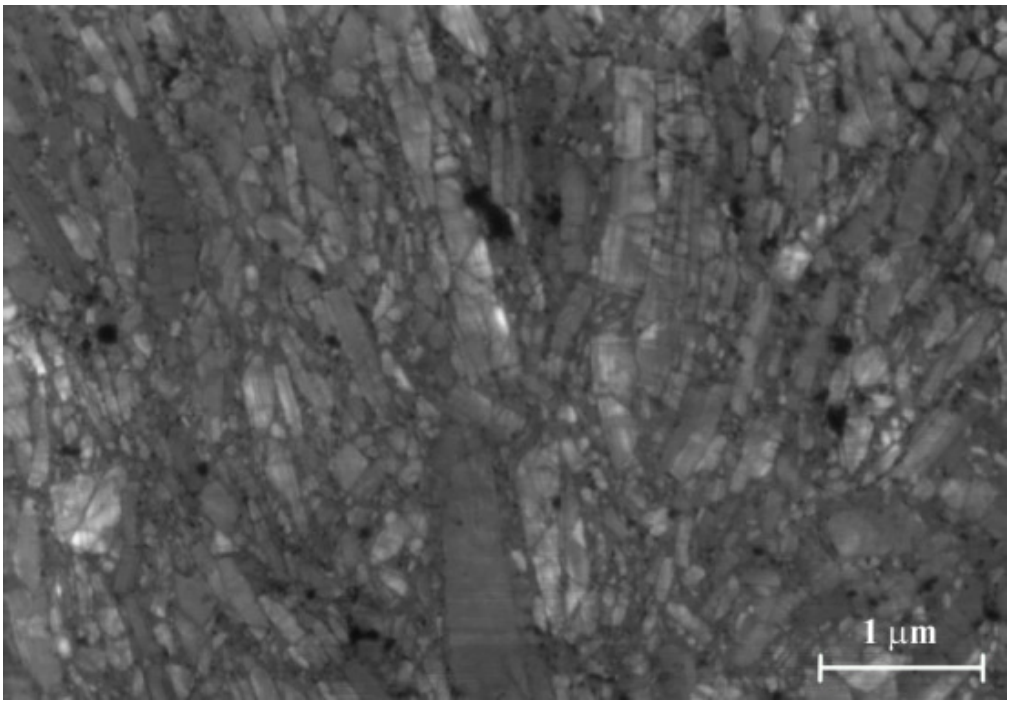

Figure 87: Microstructure of untreated wBN/cBN composite.

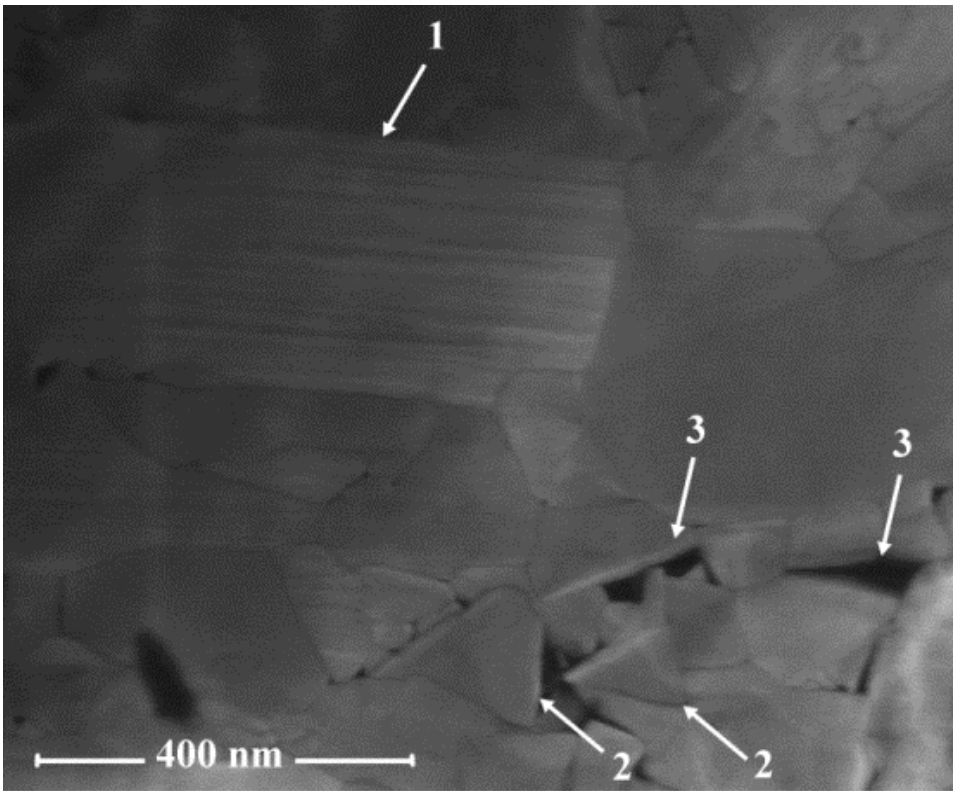

Figure 88: Detailed microstructure of untreated wBN/cBN composite: (1) Micro-band sub-structure of the lamellas; (2) Polyhedral grains at the fragmentation interfaces; (3) Pores due to polyhedral faceting.

The lamellas are originally the wurtzite BN grains fragmented during cold compaction prior to HP-HT (high pressure-high temperature) processing. Smaller polyhedral grains originate mainly during plastic fragmentation of lamellas under HP-HT conditions and evolve during recrystallization process. Such fragmentation takes place due both kink band nucleation and formation of interfaces via slip along prismatic and basal planes. Phase composition of the initial material is wurtzite BN, cubic BN and multilayer polytypes. Confirmation to the existence of these polytypes is the micro-band sub-structure of lamellas (Figure 88 and 89) which comprises of thin wBN and cBN plates as a result of layerwise wBN → cBN transformation (Figure 89).

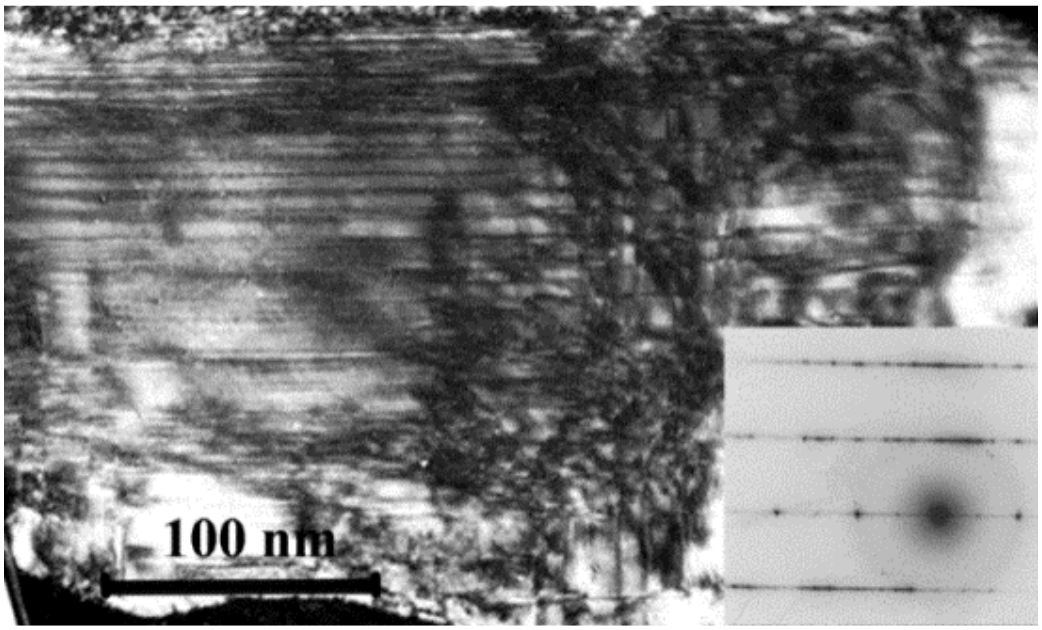

Figure 89: Dark field (in 002 wBN - 111 cBN joint reflection) TEM of micro-band sub-structure and corresponding SAED.

10.3.3.2. Microstructure of the Sample After Heat Treatment.

The microstructure consists of the same two grain types: lamellas and polyhedrons. Similar sub-structure as for untreated sample is also observed. The main differences as compared to the untreated microstructure are:

1) The smallest grains have smoothened faceting as opposed to straight-line faceting in untreated state. Solid interlayer is observed between such structural elements (grains) as well as between these grains and lamellas. In this case the lamellas also have well-developed topography of the facets. Cavities/pores at the interfaces of all such particles have smoothened shape as well.
2) Large lamellar particles exhibit cracking and fracture. Microstructural topography of such grains indicates formation of precipitates of 20-30 nm.

Three types of microstructural features can be distinguished (Figure 90 – type I, Figure 91 – type II and Figure 92 – type III).

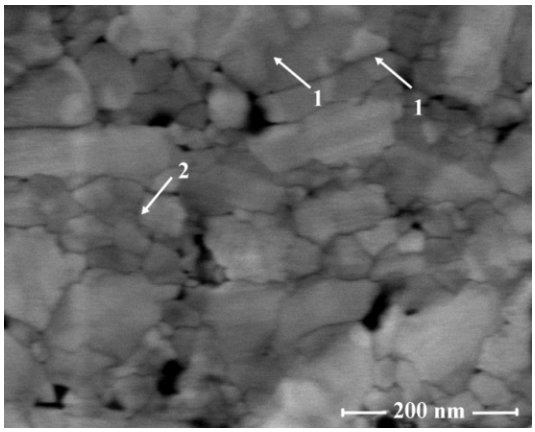

Figure 90: Type I of the heat treated microstructure: (1) Grain with precipitates on its surface; (2) Large region of formed nano-sized grains without polyhedral pores.

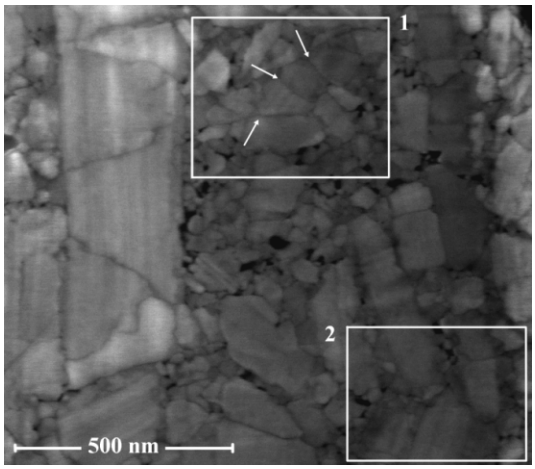

Figure 91: Type II of the heat treated microstructure: (1) Large region of polyhedral grains without pores; (2) Region of nano-sized grains of rounded shape.

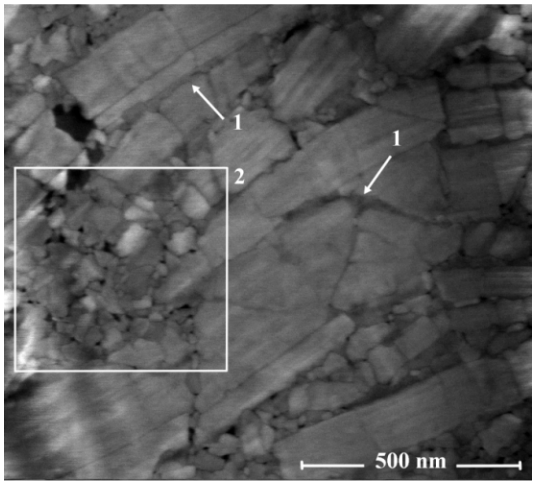

Figure 92: Type III of the heat treated microstructure: (1) Interlayer at grain boundaries; (2) Large of nano-sized grains of rounded shape.

10.3.4. XRD Analysis (Regular and Grazing-Angle)

Similar to HRSEM, XRD analysis is limited to the dual phase wBN/cBN material. The XRD analysis did not show any major differences before and after the treatment. In both cases, it shows that the composite is a multiphase material with wBN and cBN being dominant phases. Minor quantities of hexagonal (graphite-like) BN phase are also present, as well as impurities. In the traditional X-Ray analysis, the low attenuation coefficient of boron nitride leads to large penetration depth (up to 2-3 mm into the bulk thickness). In this case the relative surface contribution can become negligible. Hence, surface grazing angle XRD analysis was used because of its shallower penetration depth and surface sensitivity. By changing the grazing incidence (Figure 93), differences of the surfaces of untreated and treated samples can be detected. In our samples, the wBN peaks and the wBN+cBN peak are almost the same for treated and untreated samples and for different grazing angles; however, the cBN peak at 2θ=50.5 deg for different grazing angles is always higher implying a small increase in cBN.

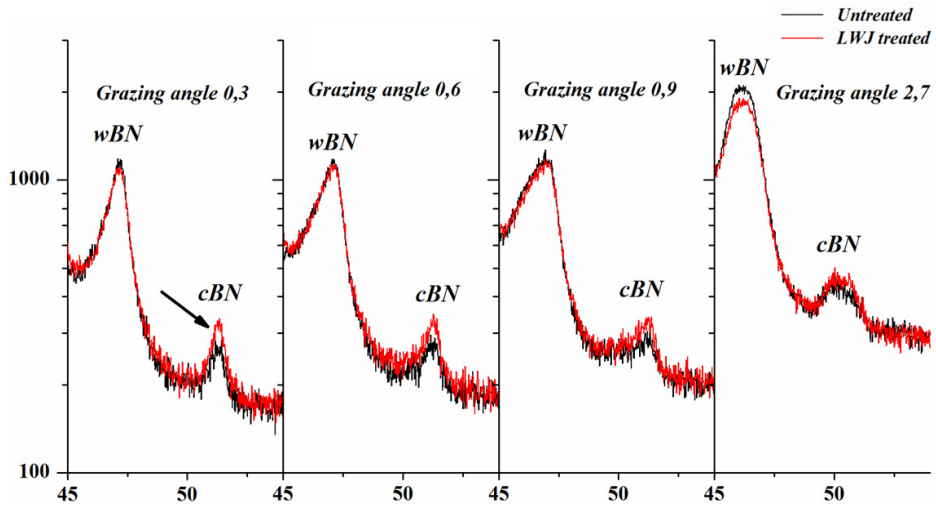

Figure 93: Grazing angle XRD indicating minor increase in cBN content on the heat treated surface.

10.4. Discussion

Several mechanisms can be attributed to the observed increase in hardness. First one is the formation of amorphous phase as noted by presence of the interfacial layer at grain boundaries (Figure 92). Such phase is expected to introduce the grain-boundary strengthening mechanism via inhibiting ease of dislocation movement across the boundary [30].

Second one is the formation of zones with nano-sized grains that are expected to increase the energy needed to move dislocations. Extensive fragmentation and cracking of the lamellas also reduces the effective grain size of the composite. The formation of the nano-sized grains between the larger lamellar grains could also introduce residual stresses.

Third is the increase in hardness due to the possible small amount of transformation of wBN→cBN as shown on Figure 86. While such a transformation requires similar to laser treatment temperatures of around 1200-1500^{o}C still much higher pressures of 6-8 GPa are needed [31], [32]. However, the presence of water, impurities, and inclusions could reduce the pressure needed for such transformation. The transformation of amorphous BN to cBN in the presence of water is reported to occur at 5.5 GPa [33]. wBN and cBN are similar in terms of hardness and the increase in hardness can be expected only through formation of finely dispersed cBN phase. Minor variation of wBN-to-cBN ratio due to laser treatment indicates that hardness improvement via such mechanism is minor as well.

It can be concluded that grain-boundary strengthening due to formation of interlayer amorphous phase, and significant reduction in grain-size of the material are the dominant mechanisms out of above three presented.

10.5. Conclusion

The laser-waterjet heat treatment increased the hardness of binderless cBN sample by 20% while it increased the hardness of binderless cBN/wBN sample by 100% reaching the hardness of polycrystalline diamond. The binderless dual phase is more affected by the treatment process and the treatment is only affecting the surface layer. A number of characterization techniques including Raman, HRSEM, and XRD analysis were used to identify the mechanisms responsible for the increase in hardness. A combination of amorphous phase formation at the grain boundaries and nano-sized grain formation are suggested as the mechanisms responsible for the increased hardness.

10.6. Acknowledgments

The authors appreciate the scholarship and financial support provided by King AbdulAziz University. Financial support from SSF/Proviking as well as in part Sustainable Production Initiative (SPI) is appreciated. Special thanks go to prof. G.S. Oleinik from Institute for Problems in Materials Science, Ukraine and Dr. S. Lehmann from Lund University, Sweden for assistance with TEM and grazing XRD respectively.

10.7. References

[1] Wang Z.G., Rahman M., Wong Y.S., 2005. Tool wear characteristics of binderless CBN tools used in high-speed milling of titanium alloys. Wear, 258: 752–758.

[2] Fujisaki K., et al., 2009. Development of ultra-fine-grain binderless cBN tool for precision cutting of ferrous materials. Journal of Materials Processing Technology, 209/15–16: 5646-5652.

[3] Zhang J., et al., 2008. Development & Application of polycrystal cubic boron nitride cutting tool material. Key Engineering Materials, 375-376: 168-171.

[4] Bhaumik S. K., Divakar C., Singh A. K., 1995. Machining Ti -6AI-4V alloy with a wBN-cBN composite tool. Materials & Design, 16/4: 221–226.

[5] Cook M. W., Bossom P. K., 2000. Trends and recent developments in the material manufacture and cutting tool application of polycrystalline diamond and polycrystalline cubic boron nitride. International Journal of Refractory Metals & Hard Materials, 18: 147-152.

[6] Brinksmeier, E., Gläbea, R. Osmer J., 2006. Ultra-precision diamond cutting of steel molds. Annals of the CIRP, 55/1: 551-554.

[7] Klocke, F., Demmer, A., Heselhaus, M., 2004. Material removal mechanisms in ultrasonic-assisted diamond turning of brittle materials. Int. J. Mater. Prod. Tech, 20/4: 231-238.

[8] Moriwaki, T., Shamoto, E., Song, Y. C., Kohda, S., 2004. Development of a elliptical vibration milling machine. Annals of the CIRP, 53/1: 341-344.

[9] Harris T.K., Brookes E.J., Taylor C.J., 2004. The effect of temperature on the hardness of polycrystalline cubic boron nitride cutting tool materials. International Journal of Refractory Metals & Hard Materials, 22: 105–110.

[10] Kato H., Shintani K., Sumiya H., 2002. Cutting performance of a binder-less sintered cubic boron nitride tool in the high-speed milling of gray cast iron. Journal of Materials Processing Technology, 127: 217–221.

[11] Luo, S. Y., Liao, Y. S., Tsai, T. Y., 1999. Wear characteristics in turning high hardness alloy steel by ceramic and CBN tools. J. Mater. Process. Technol, 88: 114-121.

[12] Shinya U., Hitoshi S., 2001. Properties and Cutting Performances of Binderless cBN Compact, High Pressure Conference of Japan, 42: 165.

[13] Zareena A, Rahman M and Wong Y.S., 2005. Binderless CBN Tools, a Breakthrough for Machining Titanium Alloys, J. Manuf. Sci. Eng., 127: 277.

[14] Melaibari A., Molian P., Shrotriya P., 2012. Laser/Waterjet heat treatment of polycrystalline cubic/wurtzite boron nitride composite for reaching hardness of polycrystalline diamond. Materials Letters 89: 123–125.

[15] Oleinik G.S., 2012. Structural transformations in the formation of superhard materials based on the wurtzitic boron nitride initial powders. Journal of Superhard Materials, 34/1:1-18.

[16] Petrusha I.A., Oleinik G.S., Danilenko N.V., 2000. Mechanisms of primary recrystallization in sintering of materials based on catalytically synthesized cBN powders. Journal of Superhard Materials, 22(6): 35-44

[17] Molian R, Neumann C, Shrotriya P, Molian P., 2008. Novel Laser/Water-Jet hybrid manufacturing process for cutting ceramics. ASME J. Manuf. Sci. Eng., 130: 031008.

[18] Jonsson B., Hogmark S., 1984. Hardness Measurement of Thin Films. Thin Solid Films, 114/3: 257-269

[19] Kalyanasundaram D., Shrotriya P., Molian P., 2010. Fracture mechanics-based analysis for hybrid laser/waterjet (LWJ) machining of yttria-partially stabilized zirconia (Y-PSZ). International Journal of Machine Tools & Manufacture. 50/1: 97-105.

[20] Kalyanasundaram D., Shrotriya P., Molian P., 2009. Obtaining a relationship between process parameters and fracture characteristics for hybrid CO2 Laser/Waterjet machining of ceramics. Journal of Engineering Materials and Technology-Transactions of the ASME. 131/1: 011005

[21] Molian R., Shrotriya P., Molian P., 2008. Thermal stress fracture mode of CO2 laser cutting of aluminum nitride. International Journal of Advanced Manufacturing Technology. 39/7-8: 725-733

[22] Sachdev, H., 2003. Influence of impurities on the morphology and Raman spectra of cubic boron nitride. Diamond and Related Materials, 12/8: 1275-86

[23] Bergman L., Nemanich R. J., 1996. Raman spectroscopy for characterization of hard, wide-bandgap semiconductors: Diamond, GaN, GaAlN, AlN, BN. Annu. Rev. Mater. Sei., 26: 551-79

[24] Wang Z., Zhao Y., Lazor P., Annersten H., Saxena S. K., 2005. In situ pressure Raman spectroscopy and mechanical stability of superhard boron suboxide. Appl. Phys. Lett., 86/4: 041911.

[25] Kudlmann U., werheit H., Lundstram T., Roberg W., 1994. Optical properties of amorphous boron. J. Phys. Chem. Solids, 55/7: 579- 587.

[26] Doll G.L., Edgar J. (Ed.), 1994. Properties of Group III Nitrides, Inspec, London.

[27] Karch K., Bechstedt F., 1997. Ab initio lattice dynamics of BN and AlN: Covalent versus ionic forces. Phys. Rev. B. 56/12:7404.

[28] Ohba N., Miwa K., Nagasako N., Fukumoto A., 2001. First-principles study on structural, dielectric, and dynamical properties for three BN polytypes. Phys. Rev. B. 63:115207.

[29] Pelletier M.J. (Ed.), 1999. Analytical Applications of Raman Spectroscopy, Blackwell Science.

[30] He W., Bhole S., Chen D., 2008. Modeling the dependence of strength on grain sizes in nanocrystalline materials. Sci. Technol. Adv. Mater., 9: 015003.

[31] Solozhenko V.L., Petrusha I.A., Svirid A.A., 1996. Thermal phase stability of rhombohedral boron nitride. High Pressure Research, 15: 95-103.

[32] Onodera, A., Sumiya H., Higashi K., Takahashi N., Oshima R., Saka H., Nobugai K., Kanamaru F., 1992. Phase relationships of boron nitride at high static pressures up to 15 GPa. High Temperatures - High Pressures, 24/1:45-54.

[33] Taniguchi, T., Kimoto, K., Tansho, M., Horiuchi, S., Yamaoka, S., 2003. Phase transformation of amorphous boron nitride under high pressure. Chem. Mater., 15: 2744-2751.

CHAPTER 11: ULTRAHARD BORON NITRIDE MATERIAL THROUGH A HYBRID LASER/WATERJET BASED SURFACE TREATMENT

A paper submitted for publication in *the journal of Acta Materialia*,

(2015)

Ammar A. Melaibari[40,41,42], Jingnan Zhao[1,43], Pal Molian[44,4], Volodymyr Bushlya[4,45], Jinming Zhou[4,6], Jan-Eric Ståhl[4,6], Igor Petrusha[4,46], and Pranav Shrotriya[1,4]

Abstract

We report a dual phase boron nitride (BN) material composed of 50% cubic and 50% wurtzite phases that has the same level of hardness as polycrystalline diamond. The dual phase BN material was initially synthesized from high pressure and high temperature consolidation of powder materials and subsequently, a laser/waterjet heat treatment (LWH) was applied to the material surface. The LWH process consisted of heating the sample surface using a continuous wave CO_2 laser beam followed by tandem waterjet quenching of the laser irradiated material. The indentation hardness of the as-synthesized material was measured to be nominally 37 GPa. After the heat treatment the indentation hardness increased to nominal values of 75 GPa reaching the hardness of polycrystalline diamond 65-80 GPa. Dispersive

[40] Laboratory for Lasers, MEMS and Nanotechnology, Department of Mechanical Engineering, Iowa State University, Ames, IA 50011.
[41] Department of Mechanical Engineering, King AbdulAziz University, Jeddah, Saudi Arabia.
[42]Primary researcher and lead author.
[43] Co-author
[44] Department of Mechanical Engineering, St. Cloud State University, St. Cloud, Minnesota, USA
[45] Division of Production and Materials Engineering, Lund University, Lund 22363, Sweden
[46] Department for Synthesis and Sintering of Superhard Materials, V.N. Bakul Institute for Superhard Materials, National Academy of Science of Ukraine, Kiev, 04074, Ukraine

Raman spectroscopy, high-resolution scanning electron microscope (HRSEM) and surface grazing XRD were used to characterize the BN phase signatures, grain size changes and phase transitions in both as-synthesized and heat treated material. Comparison of the as-synthesized and heat treated material microstructure revealed that heat treatment resulted in microstructure that consists of large grains; surrounded with regions of nano-grains between larger grains and; formation of solid interlayer along the grain boundaries. The increase in hardness was observed for LWH processing at laser fluence below 35 J/mm², and LWH processing above this value resulted in spallation of BN material from the surface. Raman spectrums of the material processed below the laser fluence of 35 J/mm² indicated that there are minimal phase transitions in the material; however, above that fluence, BN transformed into hexagonal phase resulting in surface damage through spallation. A combination of amorphous phase formation at the grain boundaries and grain size refinement are suggested as the mechanisms responsible for the LWH processing induced hardness increase.

Keywords: Ultrahard material; Boron Nitide; Laser Heat treatment; Microstructure; Composite wBN/cBN

11.1. Introduction

Ultra-hard materials that are chemically inert and thermally stable at high temperatures are desirable for enhancing machining and wear performance in demanding chemical and thermal environments. Single and polycrystalline diamonds are the hardest materials (Vickers hardness -75-100 GPa); however, at high temperatures, diamond loses its chemical inertness and thermal stability. In contrast, cubic boron nitride (cBN) has exceptional chemical and

thermal stability but has much lower hardness (35-45 GPa). Despite diamond's superior edge over cBN in hardness, the chemical inertness and thermal stability of cBN at high temperatures made it highly preferable particularly for machining hard alloys [1-4]. Increasing the hardness of BN to the level of diamond is expected to result in chemically and thermally inert ultrahard material that is suitable for range of demanding wear and machining applications.

A number of recent studies have investigated the formation, structure, and properties of cBN and have shown that it is possible to increase the hardness of dual phase boron nitride (Cubic and Wurtzite (cBN/wBN)) materials to that of diamond through nanotwinned grains [5] and selection of appropriate microstructures[6]. Using first-principle calculations, Pan et al [7] showed that the large normal compressive stresses under indentation conditions can force wBN to reach a hardness of 114 GPa through a volume-conserving/bond-flipping structural phase transformation. They proposed a two-stage shear deformation mechanism responsible for this unexpected result.

Dubrovinskaia et al [6] measured a maximum load-invariant hardness of 85 GPa and a high fracture toughness of 15 MPa$\sqrt{m}$ in cBN composites having nanoscale grain sizes (14 nm) coupled with the formation of dense hexagonal and cubic BN phases structures within the grains. The size effect of BN nanocomposites at 14 nm is at the transition between the strengthening due to stifled dislocation activity inside grains through the Hall–Petch effect and leveling off of plastic resistance due to increasing grain boundary shear [8, 9].

We report a dual phase boron nitride (BN) material composed of 50% cubic and 50% wurtzite phases that has the same level of hardness as polycrysalline diamond. The dual phase BN material was initially synthesized from high pressure and high temperature consolidation of powder materials and subsequently, a laser/waterjet heat treatment (LWH) was applied to

the material surface. The LWH process consisted of heating the sample surface using a continuous wave CO_2 laser beam followed by tandem waterjet quenching of the laser irradiated material. The microstructure and phase composition of the material are analyzed to identify the mechanism contributing to the hardness improvement. The influence of laser fluence on the LWH treatment is investigated to identify the thermomechanical conditions necessary for hardness improvement.

11.2. Experimental Approach

11.2.1. Sintering of Dual-phase Materials

The samples used in this study were produced by high pressure-high temperature (HP-HT) sintering of wBN powders obtained via detonation synthesis of hexagonal boron nitride (hBN) at presence of water. It is known [10] that wBN forms as a results of martensitic transformation of hBN, where the latice of the initial hBN transforms into a diamond-like latice of wBN with the following orintation relation (0 0 0 1)w ‖ (0 0 0 1)h, [$\bar{1}$ 1 0 0]w ‖ [$\bar{1}$ 1 0 0]h. The wBN particles have flake-like morphology which is related to the inheritance of the morphological shape of hBN phase during martensitic transformation. The size of the wBN particles in the basal plane normally reaches 1-3 μm, while the particle thickness is 0.1-0.3 μm. The particles, as a rule, possess the fragmented structure with azimuthal disorientation of the sub-structural elements [11].

Sintering was done on the Toroid type high pressure apparatus [12] at pressure of 7.7±0.3 GPa and temperature of 1750±50 ^{o}C, i.e. in the region of thermodynamic stability of cubic boron nitride (cBN). Duration of the HP-HT treatment was 45 sec. The sintering of wBN under conditions of high pressure in the given temperature range leads to the formation of

binderless dual phase microstructure as a result of incomplete wBN→cBN solid phase transformation [13]. The pressure-temperature conditions were selected such that the sintered material has 50±5% content of cBN phase which corresponds to a tool material known under trade name Hexanit-R. The material was sintered in the shape of round blanks and ground to the diameter of 9.52 and thickness of 3.18 mm which corresponds to standard tooling inserts RNGN09030T. The flat surfaces of the inserts were given the mirror finish using fine diamond grinding prior to Laser/Waterjet Heat (LWH) treatment experiments.

11.2.2. Laser/Waterjet Heat (LWH) Treatment Experiment

The LWH process involves laser heating and water-jet quenching in tandem (Figure 94) using the (LWJ) system that has been previously design and used for machining brittle ceramics [14-18]. The heat treatment was performed using a continuous wave CO_2 laser with power of 200 W and a process speed of 68 mm/s. The laser beam was immediately followed by waterjet stream of 400 kPa. Also, the laser beam was surrounded by a stream of air to prevent the laser-water interaction. To heat treat all the sample surface, the specimen surface was rastered with 50% overlap between adjacent passes. The laser heat treatment was performed with two different spot sizes (diameter of 1 mm and 0.8 mm) in order to achieve two different fluence levels: 35 J/mm² (low fluence) and 55 J/ mm² (high fluence)

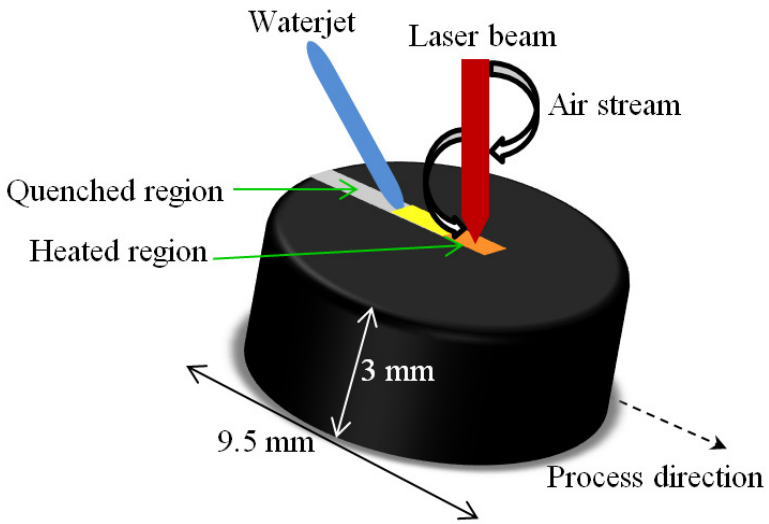

Figure 94: Schematic of LWH process.

11.2.3. Measurement of Micro-hardness

The hardness measurements were conducted following the procedures that ensure reliable measurements for material s with hardness close to diamond [19, 20]. The indentation hardness tests were performed using a Tukon microhardness tester with a Vicker's diamond pyramid indenters (cube-corner indenter with α=45° and 70° center-face angle). Measurements were made on the length of the diagonals and compared with the measurements of the depth of the indentations using a high resolution (± 1 µm) optical microscope and optical profilometer to ensure the accuracy of the data. A number of hardness measurements (20) were made to ensure the reliability and repeatability of the test data.

11.2.4. Microstructure and Phase Composition Characterization

The microstructure of the as-sintered and heat treated materials were characterized using high resolution SEM (HRSEM). General microstructure analysis of initial (untreated) sample was done on HRSEM LEO/Zeiss 1560 in high current mode which resolves most of

the problems with sample charging but affects the resolution. Detailed analysis of both untreated and LWJ treated samples was done on HRSEM FEI Nova NanoLab 600.

The phase compositions of the as-sintered and treated samples were characterized using grazing angle x-ray diffraction (XRD) and Raman spectroscopy. Quantitative XRD analysis was used for determination of the cBN and wBN content. The technique used is based on the measurement of intensities of closely located lines 200_c and 102_w for cubic and wurtzitic phases respectively [21]. The calculation of the volumetric content of cBN (αc) is done with the help of regression equation $\alpha_c = 1{,}71x - 1{,}17x^2 + 0{,}46x^3$, where parameter $x = I^c_{200} / \left(I^c_{200} + I^w_{102} \right)$ changes from zero to 1.

Dispersive Raman spectroscopy analysis (Renishaw-inVia Raman Microscopy) was performed to identify the phases before and after the heat treatment process using Ar-ion laser with a 20 μm entrance slit width, 50 mW laser power, and 488 nm operating wavelength. XRD measurements in grazing angle setups were performed using a STOE Darmstadt Bragg-Brentano diffractometer operated at 40 kV and 40 mA using Cu Kα source.

11.3. Experimental Results

11.3.1. As-sintered Material

Scanning electron micrograph of the as-sintered PCBN samples are plotted in Figure 95. The microstructure consists of two types of structures with different size and morphology. It also contained many structural defects in the form of dislocations, stacking faults and point defects [22, 23]. The first type is lamellas that are 0.5-2 μm in length and 0.15-0.2 μm in thickness. Majority of lamellas exhibit form changes of bending and fragmentation with displacement. Two features can be distinguished: regular band contrast across the thickness

and interfaces at which the fragmentation can take place. The second type of structure is the independent grains with polyhedral faceting. Such polyhedral grains have the particle size of 0.2-0.3 μm. Their most common location is at the fragmentation sites and interfaces inside lamellas. Lamella/polyhedron and polyhedron/polyhedron interfaces have both straight-line boundaries which result in formation of pores. The lamellas are originally the wurtzite BN grains that were fragmented during cold compaction prior to HP-HT (high pressure-high temperature) processing. Smaller polyhedral grains originate mainly during fragmentation of lamellas under HP-HT conditions and evolve during recrystallization process. Such fragmentation takes place due to both kink band nucleation and formation of interfaces via slip along prismatic and basal planes. Phase composition of the initial material is wurtzite BN, cubic BN and multilayer polytypes. Confirmation of the existence of these polytypes is the micro-band sub-structure of lamellas which comprises of thin wBN and cBN layers as a result of layerwise wBN → cBN transformation as shown in the transmission electron micrograph and associated selected area electron diffraction map in Fig 95.

Quantitative X-ray diffraction analysis indicated that volume content of cBN phase in the as-synthesized samples equaled 44%, which is close to the value targeted when selecting HP-HT conditions. The content was calculated from the above $\alpha_c = f(x)$ dependence which however did not consider the influence of material texturing [21].

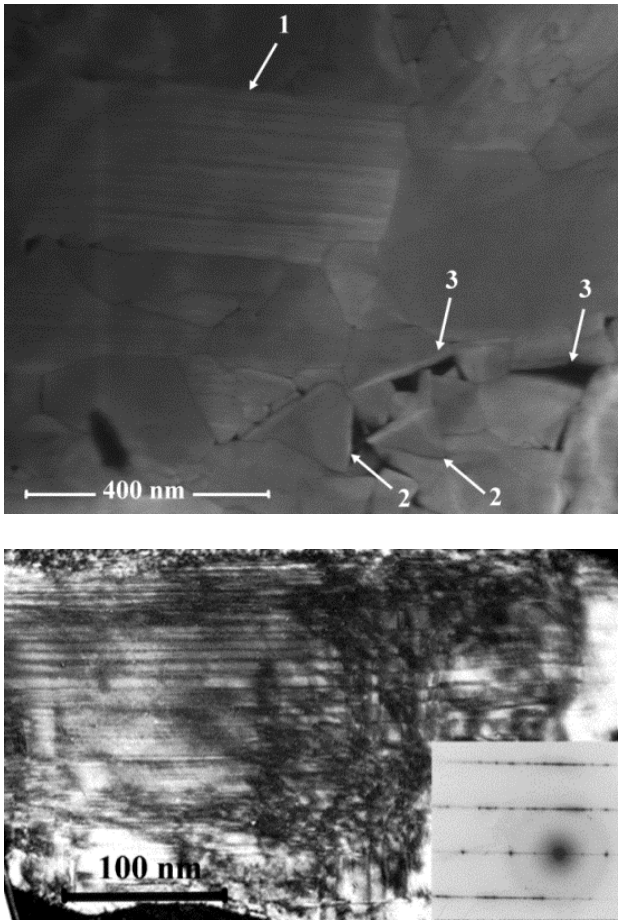

Figure 95: (top) Detailed microstructure of untreated wBN/cBN composite: (1) Micro-band sub-structure of the lamellas; (2) Polyhedral grains at the fragmentation interfaces; (3) Pores due to polyhedral faceting. (bottom) Dark field (in 002 wBN - 111 cBN joint reflection) TEM of micro-band sub-structure and corresponding SAED.

11.3.2. LWH Processing of BN Material

Visual examination of laser heat treated samples with low fluence revealed a color change from light-absorbing black/gray to transparent white. Such an effect is ascribed to a change in crystal morphology following Sachdev's classification of the crystalline morphology of cBN according to color, size and transparency [24]. A transparent cBN of white to amber implies tetrahedral crystal morphology (as opposed to octahedral) with small grain size and loss of boron. It may be noted that the color may also be caused by inclusions, dopants or

defects. The formation of transparent white of cBN provides some clues on the possible phase, stoichiometry and grain size changes in laser heat treatment.

In the high fluence treated sample, the LWH treatment resulted in surface damage through spallation of materials along the centerline of the laser beam path. In the damaged regions, the laser irradiated top surface was removed exposing the underlying material layers. Using an optical microscope (Leica M205 A stereo microscope), the depth of the spallation region was measured to vary between 1 to 3 microns. The undamaged surface surrounding the spallation area showed a similar color change from black/grey to transparent white as observed on the low fluence treated sample.

Representative SEM images of the LWH processed surface are shown in Figs 96 and 97. The microstructure consists of the same two grain types- lamellas and polyhedrons- as the untreated samples. Similar sub-structure as the untreated sample is also observed. The main differences as compared to the untreated microstructure are highlighted in the SEM images. As shown in the highlighted region 1 of Figs 96 and 97, the large lamella have sub-divided to form smaller lamellar grains of size 100-200 nm with smooth facets as opposed to straight-line faceting in untreated state. In addition, a distinct interlayer is observed at the boundary of some of the grains. Cavities/pores at the interfaces of all such particles have smoothened shape as well. As shown in the highlighted region 2 of Figs 96 and 97, microstructure in the as-received samples has been refined to form clusters of nanosized grains (sizes between 20-30 nm) that are sandwiched between larger grains.

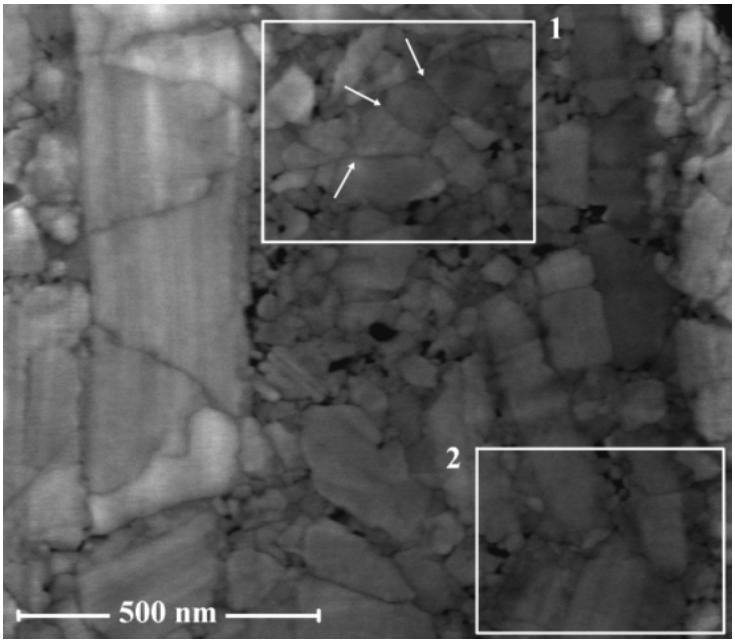

Figure 96: HRSEM of the LWJ treated microstructure showing the lamellas with the smoothened faceting and: (1) Region of polyhedral grains without pores with solid interlayer at the grain boundary; (2) Regions of nano-sized grains of rounded shape between larger grains.

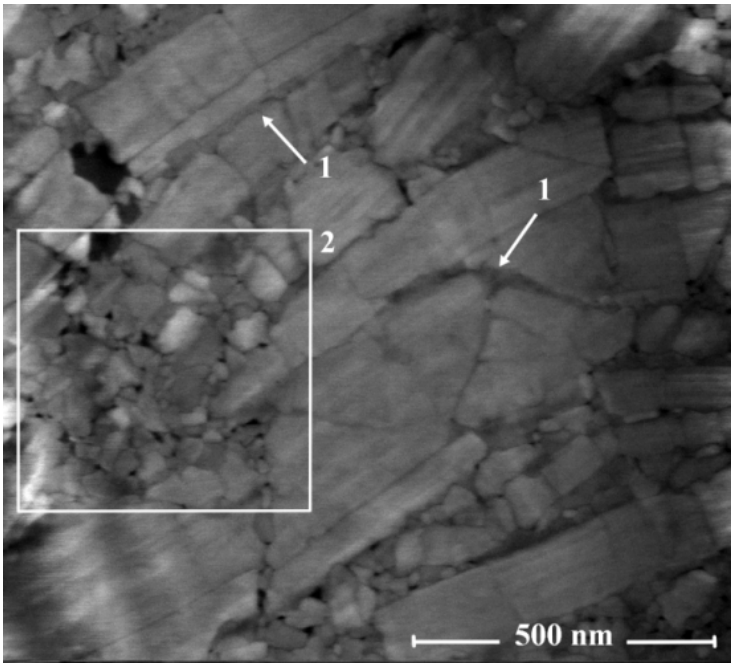

Figure 97: HRSEM of the LWJ treated microstructure showing the smaller lamella grains with: (1) Interlayer at grain boundaries; (2) agglomeration of nano-sized grains of rounded shape.

11.3.3. Hardness Measurements

Results of the hardness experiments on the untreated, low fluence treated and high fluence treated samples are plotted in Fig 98. On the high fluence treated samples the hardness measurements were conducted at the bottom of the spalled area as well as on the undamaged surface. As shown in Fig. 98, the hardness of the as-synthesized surface was found to be 37 ±5 GPa, while the hardness of the laser treated surface was found to be 72± 10 and 75±16 GPa for the low fluence and undamaged high fluence treated surfaces, respectively. The LWJ has almost doubled the hardness in the low energy fluence treatment and the undamaged surface on the high energy fluence treated samples. In the damaged regions on the high fluence treated sample, the hardness was found to be 32 ± 11 GPa which is similar but slightly lower than the hardness of the as-synthesized material. Another indicator of the increased hardness of the LWH treated samples was the damage to indenters used for hardness measurements. In the initial tests, two diamond indenters with α=45º center-face angle were broken performing these hardness tests. Hence, an indenter with center-face angle α= 70º was used for the hardness measurement in order to reduce the chance of breaking another diamond indenter. The nominal hardness values measured with both indenters were found to be consistent but the scatter in hardness values was found to be greater with lower face angle indenter. The nominal value as well as the total range and dispersion of the measured values are plotted in Fig.98 to show the LWH treatment results in a statistically significant difference of the measured hardness values.

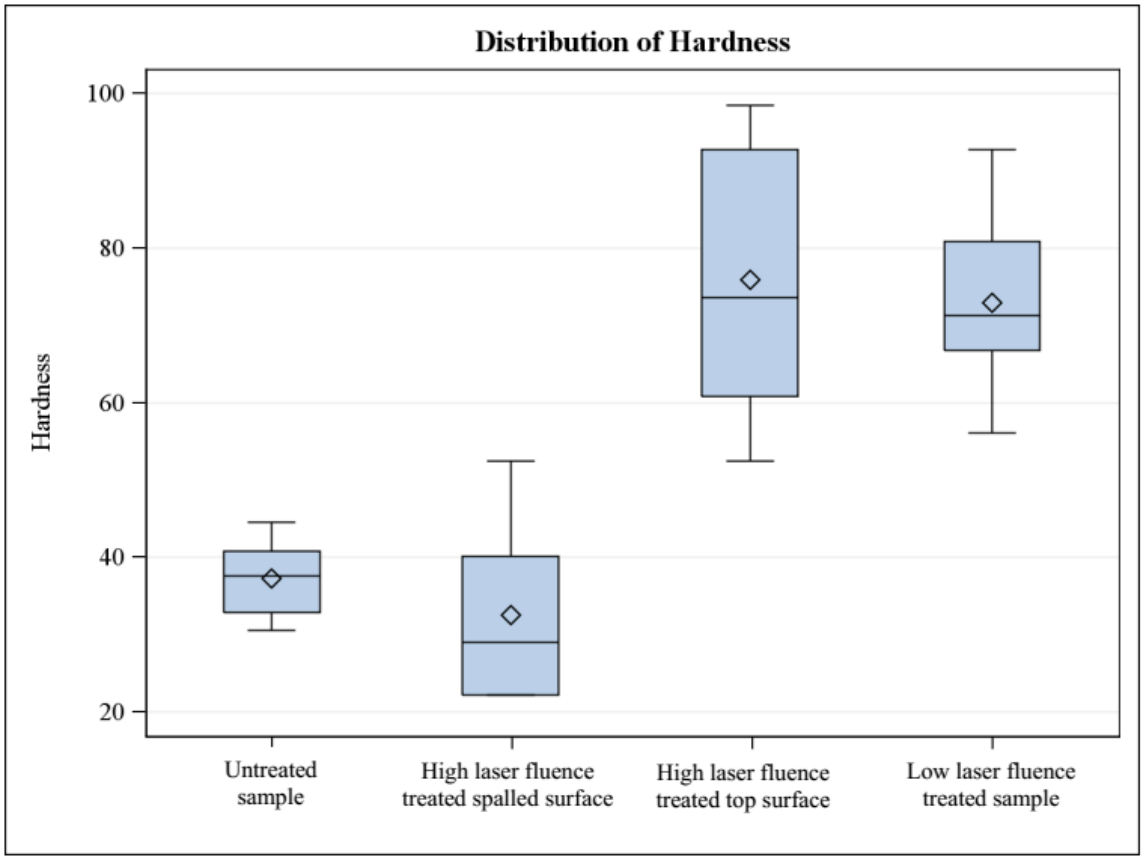

Figure 98: Vicker's indentation hardness test data of dual phase wBN/cBN using high and low energy fluence.

11.3.4. Raman Spectroscopy and X-ray Diffraction Characterization

11.3.4.1. Surface Grazing Angle XRD Analysis

The XRD analysis did not show any major differences before and after the treatment on the surfaces that have shown increase in hardness. XRD analysis was not performed on the damaged surfaces. In the traditional X-Ray analysis, the low attenuation coefficient of boron nitride leads to large penetration depth (up to 2-3 mm into the bulk thickness). In this case the relative surface contribution can become negligible. Hence, surface grazing angle XRD analysis was used because of its shallower penetration depth and surface sensitivity. The diffraction patterns obtained for different grazing angles are plotted in Figure 99 to characterize

the differences between untreated and treated samples. As shown in Fig 99, the wBN peaks are either almost the same for treated and untreated sample at all the different grazing angles. However, the cBN peak at 2θ=50.5 deg for different grazing angles is always higher for LWH treated samples implying a small increase in cBN.

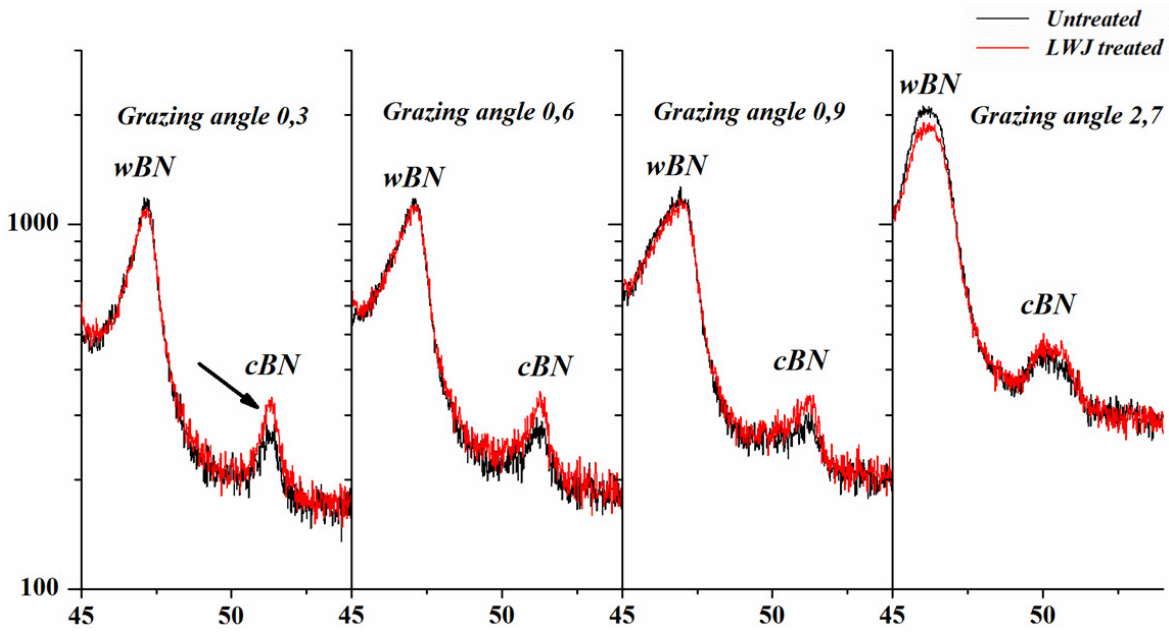

Figure 99: Grazing angle XRD indicating minor increase in cBN content on the heat treated surface.

11.3.4.2. Raman Analysis

The Raman spectrums obtained for untreated surface, damage free treated surface and damaged surface exposed due to spalling damage are plotted in Figure 100. The Raman spectrum of untreated sample exhibits the two distinct peaks of cBN at 1307 cm-1 and 1058 cm^{-1} associated with the longitudinal (LO) and transverse (TO) optical phonon modes respectively [25]. The cBN peaks at 1058 cm^{-1} overlaps with one of the wBN peaks. The Raman analysis of the untreated sample also revealed the 962 and 1040 cm^{-1} peak for wBN. It is generally difficult to identify the Raman peaks for wBN because of its small size (submicron)

and shock-wave method of production [26]. Many characteristic peaks at 950, 1015, 1053, 1075, 1246, 1280 and 1295 cm^{-1} have been reported based on theoretical and experimental observations [27-29] but usually not all of these peaks are detectable. The Raman spectra of treated and undamaged samples also show the peaks of cBN (1302 and 1052 cm^{-1}) and wBN (962 and 1040 cm^{-1}). However, the ratio of cBN to wBN peak in the overlapped region appear to be increased after LWJ treatment. Such an increase may be attributed to partial transformation of wBN→cBN [23]. In addition, an unidentified hump-like peak around 1205 cm^{-1} is also observed. This hump-like peak can be assigned to amorphous boron (B_{12}) or a rich boron phase of BN [30, 31] which may correspond to the solid interlayers observed at the grain boundaries in the HRSEM images. Due to the high reactivity of amorphous boron to oxygen, we expect that boron-rich phase of BN are more likely to be present along the boundaries of BN particles.

In the surfaces exposed due to spallation of the laser treated material, the characteristic peaks from cBN and wBN are observed. However, the ratio of the wBN peaks to cBN peaks is even smaller than that observed in damage-free surfaces, suggesting an increased transformation of wBN to cBN under high fluence treated surfaces. In addition, the hexagonal boron nitride (hBN) peak at 1362 cm^{-1} peak indicates a transformation of cBN→hBN where hBN typically has a 1366 cm^{-1} peak [26]. The volumetric increase associated with cBN→hBN may have resulted in spallation of surface layer off the surface since hBN volume is larger than cBN.

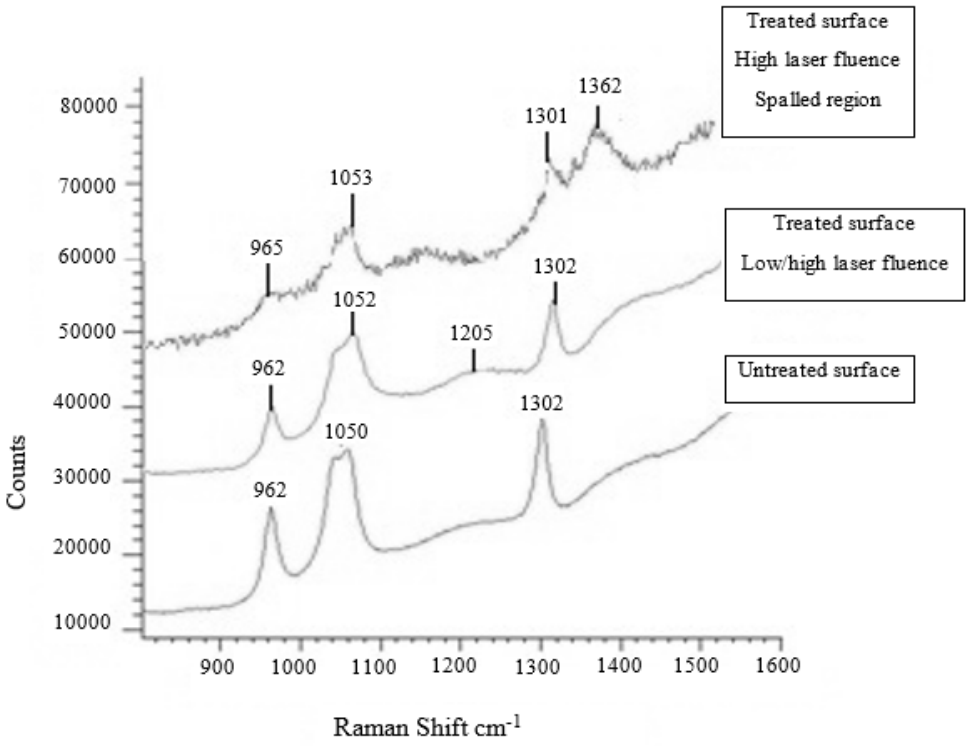

Figure 100: Raman spectra of untreated sample (bottom spectrum), low laser fluence treated sample (middle spectrum), and peeled off region in the high laser fluence treated sample (top spectrum).

11.4. Discussion

The average hardness of the untreated samples is almost doubled with the LWJ treatment with low energy fluence and on the undamaged surfaces of the samples treated with high energy fluence. Finite element analysis was applied to estimate the thermomechanical loads applied to the sample during the LWH processing. An axisymmetric finite element model was used to model the localized heating due to incidence of laser beam followed by the quenching of the heated material surface due to the water-jet. Water quenching leads to rapid decrease of temperature in the circular zone heated by low-power laser therefore the heating and subsequent cooling associated with LWH processing can be modeled as an axis symmetric

problem. The Gaussian profile of the laser beam is approximated as a surface heat source whose intensity at distance r from center is given as:

$$I_h(r) = a_s I_o e^{\left(\frac{-2r^2}{w^2}\right)}$$

where as represents the absorption coefficient, represents laser intensity at center of beam, w represents the diameter of the laser beam. The absorption coefficient was chosen to be 0.75 [8]. The laser intensity at the center of the beam was calculated based on the laser fluence used in the laser heat treatment experiment. The duration of laser spot interaction with sample surface was calculated to equal the duration that a laser beam is incident at a material point during experiments. Thermal quenching due to the waterjet was modeled using convective heat transfer coefficient of 10,000 W/ m^2 K such that the sample surface is rapidly cooled down to water temperature on the action of waterjet [15, 16]. Finite element analysis package ABAQUS was utilized to compute the temperature and stress fields for both low and high laser fluence experiments. The finite element mesh was refined till the computed temperature and stress field became independent of the element size.

During LWH surface treatment, the temperature of the surface increased rapidly during laser heating and attained a maximum value at the end of the laser irradiation. After the laser heating, the sample surface was rapidly cooled due to the waterjet quenching. The computed temperature field in the samples at the end of laser irradiation is plotted in Figs 101(a) and (b), for low fluence and high fluence laser processing experiments, respectively. The localized heating of the sample surface also led to development of large compressive stresses in the laser heated area. The radial stress field in the sample at the end of laser irradiation is plotted in Figs 102 (a) and (b), for low

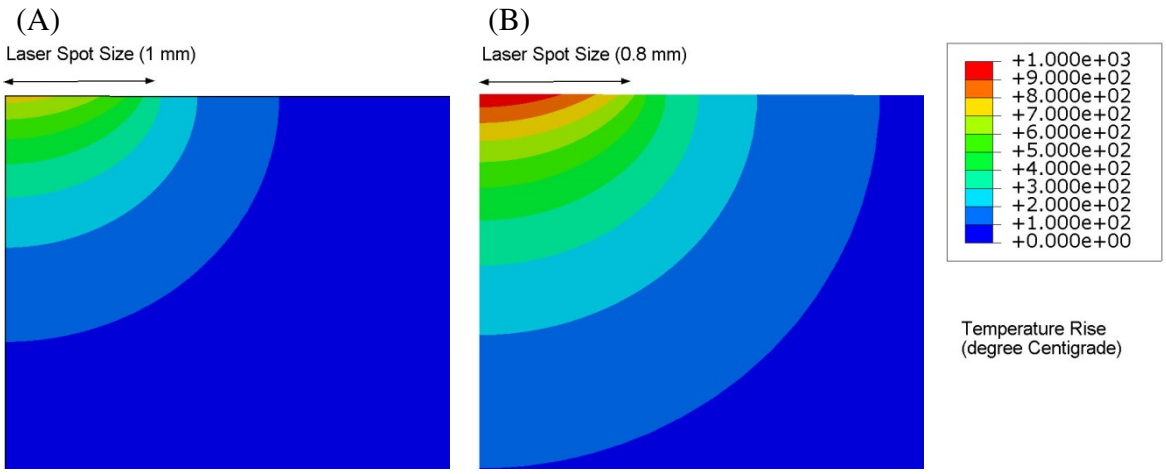

Figure 101: Temperature distribution at the end of laser irradiation during LWH processing: (A) sample treated at low laser fluence (35 J/mm^2); and (B) sample treated at high laser fluence (55 J/mm^2).

fluence and high fluence laser processing experiments, respectively. The stress field in the sample dissipated as the sample is rapidly cooled down with the waterjet. The numerical results show that during LWH treatment at low fluence conditions, the treated surface is heated to approximately 900-1000 K (700 – 800 °C) and subjected to maximum biaxial compressive stress of 1 GPa. While the sample processed at high fluence conditions are subjected to maximum temperatures of 1200 –1300 K (900 – 1000 °C) and maximum biaxial compressive stress of 1.5 GPa. The numerical results indicate the microstructural changes in the material are caused by heating the sample surface above 900 K under a biaxial compressive stress of 1 GPa. The rapid cooling of the sample surface may result in quenching the surface and thus refining the microstructure. In addition to microstructure refinement, the laser heating may also result in transformation of cBN (sp^3 phase) to hBN (sp^2 phase) and the volumetric expansion associated with the phase transformation results in surface damage. The average hardness of damaged surface was found to be lower than the hardness of the original material (untreated). The hBN phase has a relative smaller hardness than cBN and wBN [26]. Therefore, the observed reduction of hardness in the damaged region can be result of the

presence of hBN phase. Numerical results on the high fluence LWJ treatment indicate that phase transformation occurs only when the surface layers are heated above 1200 K. In order to achieve high hardness over the whole surface, the LWJ treatment should heat the sample surface between 900 -1200 K as heating above the higher temperature results in surface damage.

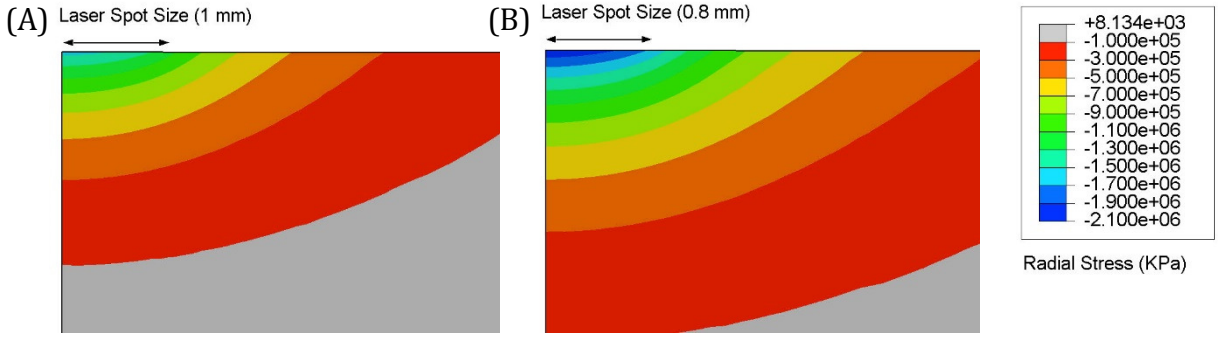

Figure 102: Maximum radial stress during LWJ treatment: (A) Stress distribution in sample treated at low fluence (35 J/mm^2); and (B) Stress distribution in sample treated at high fluence (55 J/mm^2).

Several mechanisms can be attributed to the observed increase in hardness. First one is the formation of amorphous phase at the grain boundaries as noted by presence of the interfacial layer at grain boundaries (Figs 96 and 97). Such phase is expected to introduce the grain-boundary strengthening mechanism via inhibiting ease of dislocation movement across the boundary[32]. Second one is the microstructure refinement that results in formation of zones with nano-sized grains that are expected to increase the energy needed to initiate and propagate deformation. The subdivision of the lamella grain has also reduces the effective grain size of the composite. The formation of the nano-sized grains between the larger lamellar grains results in a refined microstructure with fewer pores “defects” as compared to as-received materials.

The hardness of wBN samples may be increased through transformation of wBN to finely dispersed cBN. But this mechanism is expected to have a minimal influence in the observed increase in surface hardness because the phase composition of the LWH treated material does not change as shown on Figs 99 and 100. Additionally, the thermo-mechanical conditions during LWH processing are not conducive for transformation from wurtzite to cubic phase material. Such a transformation (wBN -> cBN) requires temperature around 1200-1500^{o}C and high pressures of 6-8 GPa [33]. The presence of water, impurities, and inclusions could reduce the pressure needed for such transformation as transformation of amorphous BN to cBN in the presence of water is reported to occur at 5.5 GPa [34] but transformation is not expected at the temperature and stress magnitudes applied during the LWJ processing.

Therefore, it can be concluded that grain-boundary strengthening due to formation of interlayer amorphous phase, and significant reduction in grain-size of the material are the dominant mechanisms underlying the observed hardness increase.

11.5. Conclusion

Laser-waterjet treatment composed of tandem laser heating and waterjet quenching is utilized to increase the hardness of dual phase boron nitride based material such that treated surface matches the hardness of polycrystalline diamond. Microstructural and phase characterization reveal that combination of amorphous phase formation at the grain boundaries and nano-sized grain formation may be the mechanisms responsible for the increased hardness. The LWJ treatment is able to achieve the microstructure refinement associated with hardness increase for laser fluence over a narrow range 35-55 J/mm^2. LWH treatment with laser fluence above this range results in spallation damage due to formation of hexagonal boron nitride

through phase transformation. Numerical analysis of the LWH treatment shows that the microstructure refinement is associated with heating the surface above 900 K and rapidly quenching the surface.

11.6. Acknowledgment

The authors appreciate the scholarship and financial support provided by King AbdulAziz University. Financial support from SSF/Proviking as well as in part Sustainable Production Initiative (SPI) is appreciated. Special thanks go to prof. G.S. Oleinik from Institute for Problems in Materials Science, Ukraine and Dr. S. Lehmann from Lund University, Sweden for assistance with TEM and grazing XRD respectively.

11.7. References Cited

[1] Bhaumik, S.K., C. Divakar, and A.K. Singh, *Machining Ti-6Al-4V alloy with a wBN-cBN composite tool.* Materials & Design, 1995. **16**(4): p. 221-226.

[2] Fujisaki, K., H. Yokota, N. Furushiro, Y. Yamagata, T. Taniguchi, R. Himeno, A. Makinouchi, and T. Higuchi, *Development of ultra-fine-grain binderless cBN tool for precision cutting of ferrous materials.* Journal of Materials Processing Technology, 2009. **209**(15-16): p. 5646-5652.

[3] Wang, Z.G., A. Rahman, and Y.S. Wong, *Tool wear characteristics of binderless CBN tools used in high-speed milling of titanium alloys.* Wear, 2005. **258**(5-6): p. 752-758.

[4] Zhang, J., Q. Yu, S. Pang, S. Meng, T. Wang, and J. Hu, *Development & application of polycrystal cubic boron nitride cutting tool material*, in *Advances in Machining and Manufacturing Technology Ix*, Y. Yao, X. Xu, and D. Zuo, Editors. 2008. p. 168-171.

[5] Tian, Y., B. Xu, D. Yu, Y. Ma, Y. Wang, Y. Jiang, W. Hu, C. Tang, Y. Gao, K. Luo, Z. Zhao, L.-M. Wang, B. Wen, J. He, and Z. Liu, *Ultrahard nanotwinned cubic boron nitride.* Nature, 2013. **493**(7432): p. 385-388.

[6] Dubrovinskaia, N., V.L. Solozhenko, N. Miyajima, V. Dmitriev, O.O. Kurakevych, and L. Dubrovinsky, *Superhard nanocomposite of dense polymorphs of boron*

nitride: Noncarbon material has reached diamond hardness. Applied Physics Letters, 2007. **90**(10).

[7] Pan, Z., H. Sun, Y. Zhang, and C. Chen, *Harder than Diamond: Superior Indentation Strength of Wurtzite BN and Lonsdaleite.* Physical Review Letters, 2009. **102**(5).

[8] Melaibari, A., P. Molian, and P. Shrotriya, *Laser/waterjet heat treatment of polycrystalline cubic/wurtzite boron nitride composite for reaching hardness of polycrystalline diamond.* Materials Letters, 2012. **89**: p. 123-125.

[9] Veprek, S., A.S. Argon, and R.F. Zhang, *Design of ultrahard materials: Go nano!* Philosophical Magazine, 2010. **90**(31-32): p. 4101-4115.

[10] Kurdyumov, A., N. Ostrovskaya, V. Pilipenko, and A. Pilyankevich, *Structural changes occurring in boron nitride during shock compression in the presence of water.* Soviet Powder Metallurgy and Metal Ceramics, 1978. **17**(9): p. 714-717.

[11] Oleinik, G., V. Volkogon, Y.A. Fedoran, S. Avramchuk, A. Kravchuk, and A. Kotko, *Influence of the wurtzitic boron nitride initial structural state on the formation of the granular structure of the wBN based materials. I. Structural characteristics of particles of the initial wBN powders.* Journal of Superhard Materials, 2013. **35**(6): p. 331-338.

[12] Khvostantsev, L., L. Vereshchagin, and A. Novikov, *Device of toroid type for high pressure generation.* High Temp.-High Pressures, 1977. **9**(6): p. 637-639.

[13] Oleinik, G., V. Volkogon, Y.A. Fedoran, S. Avramchuk, A. Kravchuk, and A. Kotko, *Influence of the wurtzitic boron nitride initial structural state on the formation of the granular structure of the wBN-Based materials. II. Structural transformations in the microstructure formation of the samples of materials based on various types of wBN.* Journal of Superhard Materials, 2014. **36**(1): p. 1-8.

[14] Kalyanasundaram, D., G. Shehata, C. Neumann, P. Shrotriya, and P. Molian, *Design and validation of a hybrid laser/water-jet machining system for brittle materials.* Journal of Laser Applications, 2008. **20**(2): p. 127-134.

[15] Kalyanasundaram, D., P. Shrotriya, and P. Molian, *Obtaining a Relationship Between Process Parameters and Fracture Characteristics for Hybrid CO(2) Laser/Waterjet Machining of Ceramics.* Journal of Engineering Materials and Technology-Transactions of the Asme, 2009. **131**(1).

[16] Kalyanasundaram, D., P. Shrotriya, and P. Molian, *Fracture mechanics-based analysis for hybrid laser/waterjet (LWJ) machining of yttria-partially stabilized zirconia (Y-PSZ).* International Journal of Machine Tools & Manufacture, 2010. **50**(1): p. 97-105.

[17] Molian, R., C. Neumann, P. Shrotriya, and P. Molian, *Novel laser/water-jet hybrid manufacturing process for cutting ceramics.* Journal of Manufacturing Science and Engineering-Transactions of the Asme, 2008. **130**(3).

[18] Molian, R., P. Shrotriya, and P. Molian, *Thermal stress fracture mode of CO2 laser cutting of aluminum nitride.* International Journal of Advanced Manufacturing Technology, 2008. **39**(7-8): p. 725-733.

[19] Fischer-Cripps, A., *Measurement of Hardness of Very Hard Materials*, in *Nanomechanical Analysis of High Performance Materials*. 2014, Springer. p. 53-62.

[20] Fischer-Cripps, A.C., S.J. Bull, and N. Schwarzer, *Critical review of claims for ultra-hardness in nanocomposite coatings.* Philosophical Magazine, 2012. **92**(13): p. 1601-1630.

[21] Kurdyumov, A., V. Malogolovets, N. Novikov, A. Pilyankevich, and L. Shulman, *Polymorphic modifications of carbon and boron nitride.* Metallurgiya, Moscow, 1994: p. 318.

[22] Oleinik, G.S., *Structural transformations in the HP-HT formation of monophase superhard materials based on carbon and boron nitride dense phases.* Journal of Superhard Materials, 2011. **33**(4): p. 217-238.

[23] Oleinik, G.S., *Structural Transformations in the Formation of Superhard Materials Based on the Wurtzitic Boron Nitride Initial Powders.* Journal of Superhard Materials, 2012. **34**(1): p. 1-18.

[24] Sachdev, H., *Influence of impurities on the morphology and Raman spectra of cubic boron nitride.* Diamond and Related Materials, 2003. **12**(8): p. 1275-1286.

[25] Bergman, L. and R.J. Nemanich, *Raman spectroscopy for characterization of hard, wide-bandgap semiconductors: Diamond, GaN, GaAlN, AlN, BN.* Annual Review of Materials Science, 1996. **26**: p. 551-579.

[26] Haubner, R., M. Wilhelm, R. Weissenbacher, and B. Lux, *Boron nitrides - Properties, synthesis and applications*, in *High Performance Non-Oxide Ceramics Ii*, M. Jansen, Editor. 2002. p. 1-45.

[27] Karch, K. and F. Bechstedt, *Ab initio lattice dynamics of BN and AIN: Covalent versus ionic forces.* Physical Review B, 1997. **56**(12): p. 7404-7415.

[28] Ohba, N., K. Miwa, N. Nagasako, and A. Fukumoto, *First-principles study on structural, dielectric, and dynamical properties for three BN polytypes.* Physical Review B, 2001. **63**(11).

[29] Ohba, N., K. Miwa, N. Nagasako, and A. Fukumoto, *First-principles study on structural, dielectric, and dynamical properties for three BN polytypes (vol 63, art no 115207, 2001).* Physical Review B, 2008. **77**(12).

[30] Kuhlmann, U., H. Werheit, T. Lundstrom, and W. Robers, *OPTICAL-PROPERTIES OF AMORPHOUS BORON.* Journal of Physics and Chemistry of Solids, 1994. **55**(7): p. 579-587.

[31] Wang, Z.W., Y.S. Zhao, P. Lazor, H. Annersten, and S.K. Saxena, *In situ pressure Raman spectroscopy and mechanical stability of superhard boron suboxide.* Applied Physics Letters, 2005. **86**(4).

[32] He, W., S.D. Bhole, and D. Chen, *Modeling the dependence of strength on grain sizes in nanocrystalline materials.* Science and Technology of Advanced Materials, 2008. **9**(1).

[33] Solozhenko, V.L., I.A. Petrusha, and A.A. Svirid, *Thermal phase stability of rhombohedral boron nitride.* High Pressure Research, 1996. **15**(2): p. 95-103.

[34] Taniguchi, T., K. Kimoto, M. Tansho, S. Horiuchi, and S. Yamaoka, *Phase transformation of amorphous boron nitride under high pressure.* Chemistry of Materials, 2003. **15**(14): p. 2744-2751.

CHAPTER 12: GENERAL CONCLUSION

Conclusion

The utilization of ultra-hard materials in more products and by more industries is held back by the difficulties to process and shape them. Though, unconventional machining techniques in general have more potential in processing ultra-hard materials since these processes do not rely solely on the mechanical properties of the material. Among all unconventional processes, laser processing hold a special advantage in dealing with ultra-hard materials due to the diversity of laser processing. It includes machining, thin film deposition, and treatment. The studies presented in this dissertation investigate some of the new developments in laser processing of ultra-hard materials, and initiate some new trends.

In the process of laser machining of ultra-hard materials, the controlled crack propagation mechanism was investigated using LWJ system through: 1) studying the effect of different fluid mediums on the process; 2) optimizing the process parameters by modeling the governing mechanism of the process; 3) effectively changing the crack direction in controlled manner. Also, the micromachining of ultra-hard thin film using short pulse duration (picosecond) was investigated.

In PLD of ultra-hard thin film, the feasibility to mimic the “brick-bridge-mortar” of Nacre’s microstructure using PLD was explored. A comparative study of PLD using nano- and femto-second lasers initiated -for the first time- the utilization of the inherent problem of PLD; particulate formation. Controlling the density and the distribution of particulates on the film can be used to create the bridges in our design to mimic the microstructure as well as texture the film surface which can be used in other applications.

Laser shock processing of ultra-hard materials was studied as laser treatment process to increase the hardness of material like BN with or without nano-diamond. In addition, LWJ treatment of ultra-hard materials was proposed for the first time to increase the hardness of hard materials like BN to reach the hardness of diamond. LWJ treatment process was investigated experimentally, and the hardness improvement mechanisms were explored.

Future work

Even though the new developments in laser machining, micromachining, treatment, and deposition of ultra-hard materials have been discussed in these research projects with a great details, they are still in the early stage and can be extended to different directions:

1. The work done on mimicking the nacre microstructure and the picosecond micromachining need to be continued in order to create multiple layers of the bio-inspired structured material. Then, the material can be tested and analyzed to capture the proposed improvements in its mechanical properties. Creating such a material would validate the design and open the door for improving the mechanical properties of other materials as well.
2. The work done on controlling the particulate formation in PLD process can be extended to other materials and used in different products where texturing of surfaces are needed. I want to explore the applicability of PLD with controlled particulate in different thin film industries like in solar cells.
3. The work done on PLD can be combined with the work done on LWJ treatment to produce thin films of ultra-hard ceramics that can be LWJ treated to improve the thin films. This can be used to improve the film mechanical properties which has its own

applications. On the other hand, treated films will provide a better platform to study and analyze treated ultra-hard material. It has been difficult to analyze the surface of LWJ treated samples without interference from the bulk of the material.

4. The work done on LWJ treatment of BN can be further tested in machining application. BN is commonly used as tool insert for turning and milling applications. Therefore, testing the effect of the LWJ treatment on the efficiency and performance of these tools is the logical next step.
5. The work done on LWJ treatment can be modeled to verify how much contribution from each of the proposed mechanisms lead to the hardness improvement. This is important to optimize the microstructure for hardness improvement for this material as well as other materials in the future.
6. The work done on LWJ treatment may affect the thermal and optical properties as well. Further thermal and optical analysis are needed to explore the full potential of the process and the feasibility to apply the process on other materials.
7. The work done on LWJ treatment has the potential to be applied to other materials that has a lamellas of stable and metastable phases. I would like to explore the feasibility of applying the process on zinc oxide, silver iodide, cadmium sulfide, cadmium selenide, silicon carbide, aluminum nitride, gallium nitride, and diamond (Lonsdaleite).